



Delft University of Technology

Offshore VSC-HVDC Networks

Impact on Transient Stability of AC Transmission Systems

van der Meer, Arjen

DOI

[10.4233/uuid:ea19a35c-96e3-4734-82bb-f378d262cbc0](https://doi.org/10.4233/uuid:ea19a35c-96e3-4734-82bb-f378d262cbc0)

Publication date

2017

Document Version

Final published version

Citation (APA)

van der Meer, A. (2017). *Offshore VSC-HVDC Networks: Impact on Transient Stability of AC Transmission Systems*. [Dissertation (TU Delft), Delft University of Technology]. <https://doi.org/10.4233/uuid:ea19a35c-96e3-4734-82bb-f378d262cbc0>

Important note

To cite this publication, please use the final published version (if applicable).
Please check the document version above.

Copyright

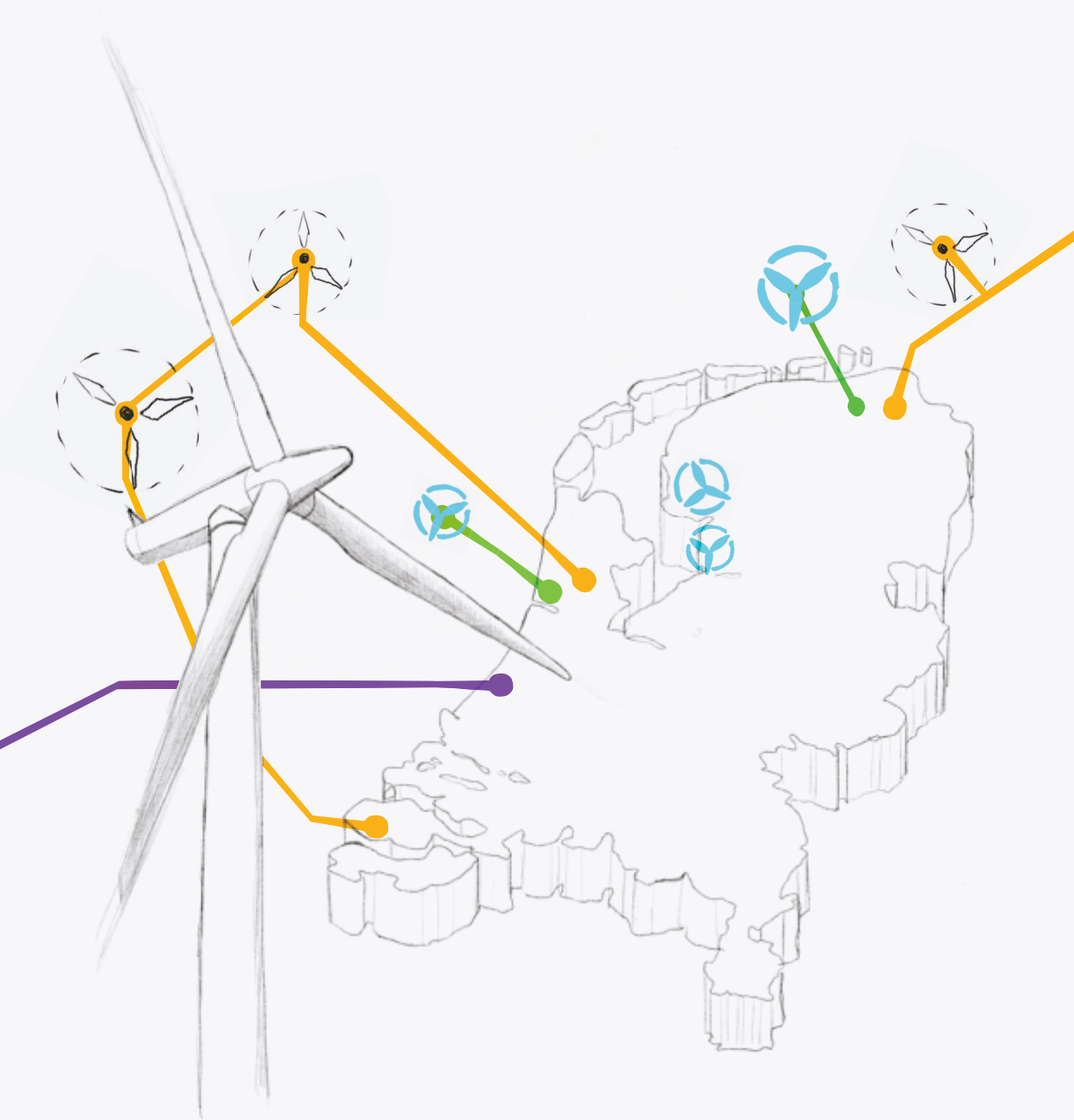
Other than for strictly personal use, it is not permitted to download, forward or distribute the text or part of it, without the consent of the author(s) and/or copyright holder(s), unless the work is under an open content license such as Creative Commons.

Takedown policy

Please contact us and provide details if you believe this document breaches copyrights.
We will remove access to the work immediately and investigate your claim.

Offshore VSC-HVDC Networks

Impact on Transient Stability of AC Transmission Systems



Offshore VSC-HVDC Networks

Impact on Transient Stability of AC Transmission Systems

Proefschrift

ter verkrijging van de graad van doctor
aan de Technische Universiteit Delft,
op gezag van de Rector Magnificus prof.ir. K. C. A. M. Luyben,
voorzitter van het College voor Promoties,
in het openbaar te verdedigen op dinsdag 12 september 2017 om 10:00 uur

door

Arjen Anne VAN DER MEER,

Elektrotechnisch ingenieur,
geboren te Dokkum, Nederland.

Dit proefschrift is goedgekeurd door
promotoren: Prof.ir. M. A. M. M. van der Meijden en Prof.dr.eng. J. A. Ferreira en
co-promotor: dr.ir. M. Gibescu

Samenstelling promotiecommissie:

Rector Magnificus	voorzitter
Prof.ir. M. A. M. M. van der Meijden	Technische Universiteit Delft, promotor
Prof.dr.eng. J. A. Ferreira	Technische Universiteit Delft, promotor
dr.ir. M. Gibescu	Technische Universiteit Eindhoven, co-promotor

Onafhankelijke leden:

Prof.dr. P. Palensky	Technische Universiteit Delft
Prof.dr. S. J. Watson	Technische Universiteit Delft
Prof.dr. K. Uhlen	Norwegian University of Science and Technology
Prof.dr. R. Iravani	University of Toronto

This research described in this thesis was financially supported by Agentschap NL, an agency of the Dutch Ministry of Economic Affairs, under the project North Sea Transnational Grid (NSTG). NSTG was a joint project of Delft University of Technology and the Energy Research Centre of the Netherlands (<http://www.nstg-project.nl/>).

Cover design by Ellen-Claire Boomsma-Hulsegge

Published and distributed by: Arjen Anne VAN DER MEER
E-mail: arjen@vdrmeer.org
WWW: <https://vdrmeer.org/>

ISBN 978-94-6299-652-6

Keywords: Transient Stability, VSC-HVDC, co-simulation, offshore wind

Copyright © 2017 by Arjen Anne VAN DER MEER

All rights reserved. No part of the material protected by this copyright notice may be reproduced or utilised in any form or by any means, electronic or mechanical, including photocopying, recording or by any information storage and retrieval system, without written permission of the author.

Printed in The Netherlands by Ridderprint B.V. (<https://www.ridderprint.nl>)

to my beloved colleague Nakisa Farrokhseresht

Contents

Summary	1
Samenvatting	5
1 Introduction	9
1.1 Context	9
1.1.1 Gradually Increasing RES Penetration	9
1.1.2 High-Voltage Direct Current Transmission	11
1.1.3 Grid Integration of Offshore Wind Power and VSC-HVDC	12
1.1.4 Simulation Aspects of VSC-HVDC and offshore WPPs	13
1.2 Research Challenges and Problem Definition	14
1.3 Research Objectives and Approach	17
1.4 Scientific Contribution	19
1.5 Research Framework	20
1.6 Outline of the Thesis	21
2 Operational Aspects and Modelling Requirements	23
2.1 Operation of VSC-HVDC Transmission	23
2.1.1 Historical notes on HVDC Transmission	23
2.1.2 VSC-HVDC Components and Terminal Layout	25
2.1.3 VSC operation and control principles	28
2.2 Deployment and Operating Characteristics of Offshore Wind Power	31
2.2.1 Operation of Wind Turbines	31
2.2.2 Wind Power Plants	37
2.2.3 Wind power as a primary source	39
2.3 Transnational Offshore Networks by VSC-MTDC	41
2.3.1 HVDC-side operation and control	41
2.3.2 Offshore Network Topology Options	43
2.4 Potential impacts of VSC-HVDC and Modelling Requirements	44
2.4.1 Fault Response of VSC-HVDC and WTGs	45
2.4.2 Dynamic Behaviour of VSC-HVDC and Grid Code Requirements	46
2.4.3 Modelling and Simulation Needs	49

3	Modelling of VSC-HVDC and Wind Power Plants	53
3.1	VSC-HVDC representation and control	53
3.1.1	Model Assumptions and Grid Interface	53
3.1.2	Vector Control	55
3.1.3	Per Unit System	55
3.1.4	Phase-Locked Loop Model	57
3.1.5	Inner Current Controller	60
3.1.6	Current Limiter and Rate Limiter	62
3.1.7	Outer Controllers	64
3.1.8	Direct Control	66
3.1.9	Power balance model	67
3.2	Wind Turbine Generator Model	67
3.2.1	Input-Output Representation	68
3.2.2	WTG Network Interface	68
3.2.3	Aerodynamic Model	69
3.2.4	Shaft Representation	69
3.2.5	Pitch Controller	70
3.2.6	Active-Power Controller (d-axis Controller)	71
3.2.7	Voltage-Amplitude Controller (q-axis controller)	72
3.3	Fault Ride-Through of VSC-HVDC Connected Offshore Wind Parks	72
3.3.1	Power Reduction Methods	73
3.3.2	Implementation into Onshore and Offshore VSC Control	76
4	VSC-MTDC modelling for Transient Stability Simulation	79
4.1	Introduction	79
4.2	Simulation Framework	81
4.2.1	Stability-type simulation	81
4.2.2	EMT-type simulation	85
4.3	Quasi-stationary VSC-MTDC model	88
4.3.1	AC-side Grid Interface and Controls	88
4.3.2	DC grid interface and Power Balance Model	90
4.3.3	State-Space Model of VSC-MTDC for Stability Studies	91
4.3.4	Inclusion of VSC-HVDC into Power Flow Analysis	93
4.4	Improved State-Space Modelling by Multi-Rate Techniques	94
4.5	Reduced-order State-Space MTDC Model	95
4.6	Simulation Studies	96
4.6.1	Simulator Validation Against PSS [®] E and PSS [®] NETOMAC	96
4.6.2	Validity of the Quasi-Stationary Model	99
4.6.3	Comparison between Transient Stability Models	100
4.7	Summary and Conclusions	103
5	Simulation of VSC-MTDC by Hybrid Methods	107
5.1	Introduction	107
5.2	Literature Overview and Contribution of this Chapter	108
5.2.1	Literature Overview on Co-Simulations	108

5.2.2	Literature Overview of Hybrid Stability and EMT simulations	111
5.2.3	Contribution of this Chapter	113
5.3	Hybrid EMT-type and Stability-type Simulation	114
5.3.1	Overview of Interfacing Techniques	114
5.3.2	Implementation of Existing Interfacing Techniques in this Thesis	115
5.4	Interface Technique Improvements in this Thesis	125
5.4.1	Thévenin Impedance recalculation during faults	125
5.4.2	The External System Priority Interaction Protocol	126
5.4.3	Improved Angular Magnitude filtering	127
5.4.4	Improved External System Priority IP during ac-side events	127
5.4.5	Interaction Protocol Improvements Under Small Time Step-Size Conditions	128
5.5	Simulation Studies	129
5.5.1	Simulation Setup	129
5.5.2	Application of existing interfacing techniques	134
5.5.3	Interface Technique Improvements for VSC-HVDC	138
5.5.4	Application of the Advanced Interfacing Techniques to VSC-MTDC	143
5.6	Summary and Conclusions	145
6	Stability Assessment of Hybrid AC/VSC-HVDC Networks	149
6.1	Introduction	149
6.2	Study Approach and Simulation Setup	150
6.2.1	Approach	150
6.2.2	Scenario Selection	154
6.2.3	System Description	156
6.2.4	Parameter Selection and Case Study Setup	162
6.2.5	Response Variable Treatment	165
6.3	Case Study 1: Stability Impacts of FRT and Post-FRT of VSC-HVDC links	166
6.3.1	Stability impacts of VSC-HVDC FRT	166
6.3.2	Stability impacts of active power recovery	168
6.3.3	Effect of VSC-HVDC connected offshore wind power penetration	168
6.3.4	Influence of Converter-Interfaced Onshore Generation	170
6.4	Case Study 2: Stability Impacts of a Future Offshore VSC-HVDC Grid	171
6.4.1	Effect of post-fault active power recovery on onshore dynamics	171
6.4.2	Radial versus meshed HVDC topology	171
6.5	Case Study 3: Stability Support by VSC-MTDC	173
6.5.1	Robust direct voltage control of MTDC transmission	173
6.5.2	Stability support assessment	174
6.5.3	Computational considerations	176
6.6	Summary	177
7	Conclusions and Recommendations	179

7.1	Conclusions	179
7.1.1	Development of VSC-HVDC models for FRT analysis	179
7.1.2	Combined EMT and stability-type Simulation Framework	180
7.1.3	Improved Monolithic Modelling and Simulation Techniques for Transient Stability Studies	180
7.1.4	Advanced Hybrid EMT and Stability Simulation of VSC-HVDC	181
7.1.5	Stability impacts of multi-terminal VSC-HVDC transmission	182
7.2	Recommendations for Further Research	182
7.2.1	Quasi-stationary Modelling of VSC-HVDC	182
7.2.2	Hybrid Simulations	183
7.2.3	Stability Support of VSC-HVDC	183
A	Iterative Procedure for Systems of Non-Linear Equations	185
A.1	Fixed-point iteration	185
A.2	Newton-Raphson Algorithm	185
B	Reference Frames, Space Vectors, Phasors	187
B.1	Sinusoidal quantities	187
B.2	Common Transformations for Three-Phase Systems	187
B.2.1	Clarke transformation	187
B.2.2	Park transformation	188
B.2.3	Space Vectors	189
B.2.4	Space Vector Representation of Reference Frame Transform- ations	190
B.2.5	The Arbitrary Reference Frame	191
B.3	Complex Phasors	192
C	Test Network Data	197
C.1	Extended Single Machine Infinite Bus System	197
C.2	IEEE 9-Bus System	198
	Nomenclature	201
	List of Publications	209
	Bibliography	212
	Acknowledgements	221
	Cirriculum Vitae	223

Summary

Motivation

Renewable energy sources are essential ingredients for the ongoing transition towards a sustainable society. It is expected that a substantial part of the future electricity production will be fuelled by wind power. High-voltage direct current based on voltage sourced converter technology (i.e., VSC-HVDC) is anticipated to become the major type of transmission for offshore wind parks. VSC-HVDC comes with significant technological advantages: controllable power flows, advanced ancillary services, black start capabilities, and the possibility of multi-terminal operation could support large-scale commissioning of wind parks located far offshore.

Our society, however, also highly depends upon the availability of electricity. It is important but also challenging to integrate renewables into the electricity network while preserving the high level of reliability, controllability, and stability we are experiencing today. The foreseen large-scale connection of offshore wind power by VSC-HVDC may impact various of these aspects, which need to be considered in prospective grid integration studies.

Objectives and Approach

This Ph.D. thesis assesses the electrotechnical consequences of (multi-terminal) VSC-HVDC connected offshore wind parks on the dynamics of the onshore power system. These interactions can occur at several time frames of interest ranging from μs (lightning, switching) to seconds (short-circuits, park disconnection) or longer (generation/load balancing). This work addresses rotor angle stability (i.e., 0.1 – 5 s), covering large geographic areas with many transmission lines, cables, and electric machines. The dynamics of such large systems are commonly incorporated into stability-type simulations. Unfortunately, such simulators are not well-suited to handle VSC-HVDC transmission. Developing accurate and generalised dynamic VSC-HVDC models without affecting the computational agility of stability-type simulations is the main goal.

To study the stability impacts of VSC-HVDC transmission, this thesis starts with a survey of the relevant operational characteristics of VSC-HVDC and offshore wind parks and the occurrence of mutual interactions with the onshore transmission system. Subsequently, time-domain VSC-HVDC models will be developed, thereby respecting the assumptions common to transient stability assessment. The efficacy of model simplifications, multi-rate methods, and hybrid electromagnetic transient(EMT)/stability-type simulations are investigated in detail.

The modelling and simulation improvements allow stability assessment of large-scale

transmission systems containing extensive multi-terminal VSC-HVDC networks. This is done by deterministically assessing the impact of various operation and control functions using a test network, first, and subsequently by extrapolating the findings to a more realistic case study containing the Northwestern European power system and a VSC-HVDC-based transmission network in the North Sea. 3 future scenarios have been selected, varying in wind conditions and HVDC network topology.

Generalised Modelling of VSC-HVDC for Stability-Type Simulations

The protection and control during onshore short-circuits (i.e., fault ride-through) are the main operational challenges of offshore wind parks connected by VSC-HVDC. The involved operating modes affect the transient stability, specifically for high levels of wind power. This calls for a careful dynamic representation of the VSC-HVDC network into stability simulators. Taking an averaged VSC model as a starting point, a generic model implementation of multi-terminal VSC-HVDC networks into stability-type simulations has been developed. Although this general model succeeds in covering all relevant system dynamics, its computational performance is prohibitive for large-scale system studies. HVDC model simplifications provide a remedy for this at the expense of reduced response accuracy. Multi-rate modelling, which considers the HVDC part of the system by using a smaller time step-size for numerical integration, is an excellent solution to the simulation challenge. Execution times are up to 5 times faster than the initial dynamic model while accuracy requirements are satisfied.

Hybrid Simulation of VSC-HVDC

The HVDC part of the system requires the highest level of modelling detail. Alternative to the monolithic approach taken earlier, the network can be split into an AC part, simulated by the same stability-type simulation, and a VSC-HVDC part, which is incorporated into a separate EMT simulator. At the boundaries of both parts of the system voltages and currents are exchanged during runtime. A *hybrid simulation* platform has been developed and validated against commercially available tools. This work presents several contributions to previously published interfacing techniques to make them better compatible with VSC-HVDC transmission. The resulting simulation platform has shown to be flexible and computationally efficient: even on small test networks the hybrid approach shows a 40% speed improvement as compared to a full EMT simulation.

Stability Impacts of VSC-HVDC Connected Offshore Wind Power

The analysis of the stability impacts shows a significant relation between the post-fault active power recovery and the AC rotor angle response, notably when the share of conventional generation is small (i.e., high wind conditions). This is verified by the Northwestern European case study. Simulations show that the fault ride-through duty is relieved when the offshore grid is operated as multi-terminal. Moreover, the propagation of fault dynamics can be partly mitigated by modifying the overall control strategy, which comes at the price of more severe direct voltage excursions. At the AC side, additional reactive current injection shows up to 33% improvement in critical clearing times, a measure for the level of transient stability. The effect of the VSC-HVDC network topology on transient stability is marginal.

Recommendations for Future Research

The model and simulation improvements foster large-scale AC/VSC-HVDC grid integration studies. Directions for further research include 1) optimised numerical implementations, 2) refined HVDC model simplifications, 3) assessing the compatibility with adaptive time step-size simulations, and 4) applying quasi-standardised interfacing techniques.

The stability impacts are addressed by deterministically choosing a set of input parameters whereas other system properties are assumed fixed. Especially wind conditions and the corresponding unit commitment appear to significantly impact transient stability. The main recommendations to strengthen the conclusions are 1) to include the assessment of wind speed fluctuations during the time frame of interest, 2) the application of a stochastic approach to determine the wind turbine loadings, 3) to model the dynamic behaviour of neighbouring power systems more accurately, and 4) to search for alternative key performance indicators for transient stability, aside from critical clearing times of generators.

Samenvatting

Motivatie

Hernieuwbare energiebronnen zijn essentiële bouwstenen voor de transitie naar een duurzame samenleving. Naar verwachting zal windenergie een aanzienlijk deel uitmaken van de toekomstige elektriciteitsproductie. Hoge gelijkspanning gebaseerd op voltage sourced converter technologie (VSC-HVDC) kan worden gezien als de voornaamste transmissietechnologie voor offshore windparken. VSC-HVDC heeft significante technologische voordelen: regelbare vermogensstromen, ondersteunende diensten, opstartfaciliteiten en de mogelijkheid tot multi-terminalbedrijf kunnen bijdragen aan de grootschalige realisatie van windparken ver op zee.

Onze samenleving is echter ook afhankelijk van de beschikbaarheid van elektriciteit. Het is belangrijk en uitdagend om hernieuwbare energiebronnen te integreren in het net en tegelijkertijd de hoge mate van betrouwbaarheid, regelbaarheid en netstabiliteit te waarborgen. De verwachte grootschalige inpassing van wind op zee door middel van VSC-HVDC kan een aantal van deze elementen beïnvloeden, wat uitvoerig zal moeten worden onderzocht in netintegratiestudies.

Doelstelling en Aanpak

Dit proefschrift onderzoekt de elektrotechnische gevolgen van wind op zee, verbonden door middel van (multi-terminal) VSC-HVDC, op het dynamische gedrag van het elektriciteitsvoorzieningsstelsel op land. De relevante interacties vinden plaats in een tijdsspanne van μs (blikseminslag, schakelverschijnselen) tot seconden (kortsluitingen, windparkafschakeling) en langer (vermogensbalans). Dit werk behandelt de rotorhoekstabiliteit ($0.1 - 5\text{ s}$), die zich uitstrekt over grote geografische gebieden met veel transmissielijnen, kabels en elektrische machines. De dynamica van grote transmissiesystemen wordt normaal gesproken beschouwd aan de hand van stabiliteits simulaties. Helaas zijn deze simulatoren ongeschikt voor VSC-HVDC-transmissie. Het ontwikkelen van nauwkeurige en algemeen toepasbare dynamische modellen van VSC-HVDC zonder daarbij aan de simulatiesnelheid te tornen is het hoofddoel van dit proefschrift.

Om de invloed van VSC-HVDC-transmissie op de netstabiliteit te onderzoeken wordt er gekeken welke operationele karakteristieken van VSC-HVDC en offshore windparken relevant zijn en wanneer er wederzijdse interacties met het onshore elektriciteitsvoorzieningsstelsel optreden. Aansluitend worden tijdsdomeinmodellen van VSC-HVDC ontwikkeld, waarbij de gebruikelijke stabiliteitsaannames in acht worden genomen. De doelmatigheid

van de modelsimplificaties, de multi-rate-methodes en hybride elektromagnetische transiënten (EMT)/stabiliteitssimulaties wordt in detail doorgelicht.

De modelleer- en simulatieverbeteringen maken het mogelijk de stabiliteit van groot-schalige transmissiesystemen met uitgebreide multi-terminal VSC-HVDC netwerken te berekenen. Dit wordt gedaan door deterministisch de invloed van verscheidene bedrijfsvoerings- en regelfuncties te bestuderen aan de hand van een testnetwerk, om de resultaten vervolgens te extrapoleren naar een realistischer casus die onder andere het Noordwest-Europese netwerk en een toekomstig net op zee omvat. Drie toekomstige scenarios zijn geselecteerd, variërend in windcondities en de topologie van het HVDC-net op zee.

Generieke modellering van VSC-HVDC voor Stabiliteitssimulaties

De beveiliging en regeling tijdens onshore kortsluitingen, zgn. fault ride-through, is een van de voornaamste operationele uitdagingen voor VSC-HVDC-verbonden wind op zee. De regelstrategieën beïnvloeden transiënte stabiliteit, vooral bij condities met veel wind. Dit noopt tot een precieze dynamische representatie van een net op zee in stabiliteitssimulatoren. Startend met een versimpeld eenfasemodel van VSC's wordt een generieke implementatie van multi-terminal VSC-HVDC netwerken in stabiliteitssimulaties ontwikkeld. Alhoewel alle relevante systeemdynamica in dit veralgemeniseerde model zit ingebed zijn de numerieke prestaties beperkend voor grootschalige systeemstudies. Modelreductie aan de HVDC-zijde verhelpt dit deels ten koste van de algehele nauwkeurigheid. Multi-rate modellering, waarbij de HVDC-zijde van het systeem in een interne integratieroutine wordt ingepast, vormt een uitstekende oplossing voor het simulatievraagstuk. Simulatielooptijden zijn tot vijf maal korter in vergelijking tot het initiële dynamische model terwijl aan de nauwkeurigheidseisen wordt voldaan.

Hybride Simulatie van VSC-HVDC

De hoogste mate van detail is nodig voor het HVDC-deel van het systeem. Als alternatief voor de monolithische benadering zoals eerder beschreven kan het netwerk gesplitst worden in een AC-deel, gesimuleerd door de stabiliteitssimulatie, en een VSC-HVDC-deel dat ingepast wordt in een afzonderlijke EMT-simulator. Op het scheidingspunt van beide afzonderlijke systeemdelen worden gedurende de simulatie spanning- en stroomwaarden uitgewisseld. Dit concept wordt onderzocht door middel van een zelfontwikkelde hybride simulator die gevalideerd wordt tegen commerciële softwarepakketten. Dit werk beschrijft een aantal bijdragen om eerder gepubliceerde koppeltechnieken beter aan te passen aan VSC-HVDC. Het resulterende simulatieplatform blijkt flexibel en rekenkundig efficiënt; zelfs bij kleine testnetwerken werd een snelheidswinst van 40 % behaald vergeleken met een volledige EMT-simulatie.

Stabiliteitsgevolgen van Netintegratie van Wind op Zee door VSC-HVDC

De analyse van stabiliteitseffecten laat een sterke relatie zien tussen het terugkomen van het vermogen na foutafschakeling en de rotorhoekreactie in het AC-netwerk, in het bijzonder wanneer het aandeel conventionele opwekkers laag is (hoge windpenetratie). Dit is geverifieerd door een casus waarin het Noordwest-Europese netwerk gemodelleerd wordt. Uit

simulaties blijkt dat de fault ride-through-taak wordt verlicht indien het net op zee als een multi-terminal HVDC-net wordt bedreven. Daarnaast kan het voortplanten van de slecht gedempte foutoscillaties door het HVDC-net deels worden verholpen door het aanpassen van de gelijkspanningsvermogensregeling, deels ten koste van iets hogere piekspanningen. Het blijkt dat additionele blindstroominjectie aan de AC-zijde leidt tot één derde verbetering in kritische kortsluittijden, die een maatstaaf zijn voor de mate van transiënte stabiliteit van het systeem. Het effect van de topologie van een net op zee (radiaal versus vermaasd) op de transiënte stabiliteit is marginaal.

Aanbevelingen voor Vervolgonderzoek

De modelleer- en simulatieverbeteringen bevorderen grootschalige netintegratiestudies van VSC-HVDC. Aanbevelingen voor vervolgonderzoek omvatten 1) geoptimaliseerde numerieke implementaties, 2) verbeterde modelsimplificaties voor HVDC, 3) het bestuderen en aanpassen voor variabele tijdstapgroottes en 4) het toepassen van gestandaardiseerde koppelmethodes voor hybride simulaties.

De stabiliteitsimplicaties worden beschouwd met een deterministische aanpak door een aantal ingangsparameters te kiezen terwijl andere onveranderd blijven. Uit dit onderzoek blijkt dat in het bijzonder windcondities en de inzet van het productievermogen een aanzienlijke invloed hebben op de transiënte stabiliteit. De voornaamste aanbevelingen om tot meer universele conclusies te komen zijn door 1) de windfluctuaties mee te nemen in de tijdspanne die relevant is voor transiënte stabiliteit, 2) een stochastische benadering toe te passen op de productie van windparken, 3) de dynamische verschijnselen van gekoppelde transmissiesystemen nauwkeuriger te modelleren, 4) naast kritische kortsluittijden ook alternatieve indicatoren voor transiënte stabiliteit te selecteren.

Chapter 1

Introduction

1.1 Context

The characteristics of the power system will change in the coming decades. The increasing level of renewable energy sources (RES) calls for more flexibility in maintaining the balance between electricity generation and usage. RES are commonly grid-connected by power electronic devices and it is foreseen that the roll-out of converter-interfaced generation and transmission will continue. Despite fostering the much needed flexibility in the transmission system, power electronics exhibit behaviour during faults that differs from ordinary electrical machines. It is manifest to study this in detail to eventually maintain the reliability of the future sustainable power system [1]. This needs rethinking about the fashion – from methods to simulation platforms – in which planning and grid integration studies are performed.

1.1.1 Gradually Increasing RES Penetration

Our society is extremely dependent on machines and systems that use electricity, oil, coal, or gas as their primary supply for energy [2]. It is hard to imagine a world without the devices that make us commute to and fulfil our jobs, help us relaxing afterwards, substitute manual labour, and even save our lives. Figures from the International Energy Agency show an increase in primary energy supply from 6106 Mtoe in 1971 to 13371 Mtoe in 2012 [3]. 1 Mtoe (i.e., million of tonnes of oil equivalent) equals 11.630 TWh. For comparison, the annual Dutch electricity demand is around 114 TWh, which amounts to 9.8 Mtoe [4].

Economic growth and electricity demand often go hand in hand. Figure 1.1 shows the worldwide GPD, (i.e., gross domestic product) and electricity demand in kWh per capita. We can discern a clear (non-causal) relation between the GPD and electricity demand over the past 4 decades. Hence, economic growth fuels the electricity demand. Although economic growth is hugely dependent on the overall political situation, it is in general foreseen the growth persists in the coming decades [5]. Alongside the economic aspects fostering electricity demand there is also a continuous trend towards further electrification of our society, notably cars, storage, heating, and even navigation and avionics [6]. It is hence evident the increasing electricity demand will persist throughout our lifespan – and our reliance on it, too.

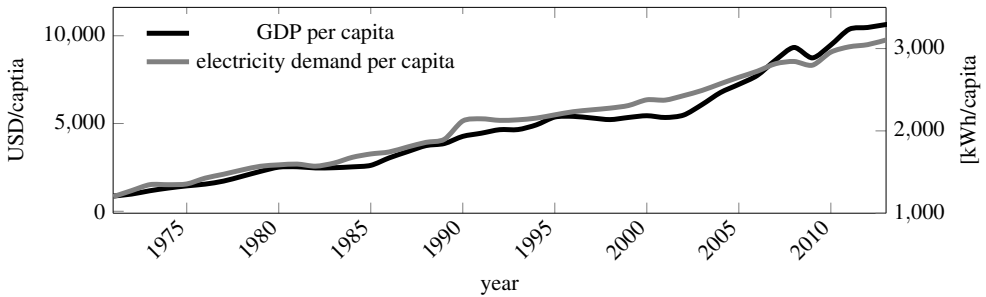


Figure 1.1: *World's growth and energy demand* [7].

The current fashion in which the primary sources for electrical power generation are utilised is far from sustainable. In 2013, 77.8 % of the worldwide electricity production came from fossil fuels (67.2%) or nuclear sources (10.6%) [3, 8]. Aside from the greenhouse gas production from fossil fuels [9], these resources are finite and mining is commonly centred around fixed geographical locations, some governments of which are not particularly stable. Against the background of the Paris climate agreements being signed (i.e., [10]) and various promising renewable energy outlooks, some of which even envisage a 100% renewable electricity production for 2050 [11], the future looks rosier for a transition towards a more sustainable society.

Wind power is envisaged as a crucial instrument to achieve a more sustainable energy resource portfolio. Windmills, for centuries the work horse of the Dutch industry, got their electrotechnical counterparts in the 1980s when the wind turbine industry grew mature across Europe. Advancements in rotor blade, foundation, and tower design as well as the incorporation of variable speed generators and power electronic interfaces led to upscaling their ratings to the MW range. Their arrangements in large wind parks, or wind *farms*, allow them to behave as one single generation entity: a wind power plant (WPP).

The Dutch *energieakkoord voor duurzame groei* (i.e., energy agreement for sustainable growth) is an agreement between the government, industries, labour unions, and non-governmental organisations [12]. It encompasses a whole spectrum of legally binding arrangements ranging from sustainability to economic growth and (energy) infrastructure. The deployment of wind power is a large component, constituting these agreements, i.e., one of the pillars. It is foreseen to foster the roll-out of existing agreements between the government and provinces to upgrade and extend the onshore wind power portfolio to 6000 MW in 2022–2024. Aside from that, the agreements imply an operational offshore wind power fleet amounting to 4450 MW in 2023.

In the Netherlands, spatial restrictions and (related) legislative issues make it hard to deploy large amounts of wind power onshore. The energy yield of a WPP is, theoretically, proportional to the cubic of the wind speed and it is hence from an energy perspective lucrative to deploy large amounts of wind power far from the coastline. The variable nature of the primary source is an important parameter to be considered in both short-term (day-ahead) production planning [13] and long-term grid expansion planning [14].

The liberalisation of the European electricity sector, which rolled out over the past decades, constitutes other significant bounds on the deployment of offshore wind power. First, wind power producers are considered just like other electricity production parties, and are penalised in case power sold at the electricity market cannot be produced, or vice versa.

Second, the liberalisation facilitates the planning of (transnational) connections between markets, even overseas (e.g., NorNed, BritNed, and COBRACable).

1.1.2 High-Voltage Direct Current Transmission

High-voltage direct current (HVDC) transmission is key in achieving large-scale cross-border electricity trade. The functionality requirements for achieving transnational offshore transmission predominantly amount to the application of submarine cables, the minimisation of transmission losses, the ability to control the power flow from one side to the other, and adequate protection devices [15]. AC submarine cables have the demerit of generating capacitive currents, which severely limits the transmission capacity and may require (costly) reactive power compensation. Especially for long connection distances HVDC is commonly the only technologically feasible solution despite the AC/DC conversion losses. Aside from this HVDC enables control over the power flow, which is an excellent feature given the trade requirements.

Major developments in the field of power electronics lead to the availability of reliable insulated-gate bipolar transistors (IGBT) in the kV range. IGBTs combine the high forward current of BJTs (i.e., bipolar junction transistors) with the switching characteristics of MOSFETs (i.e., metal-oxide semiconductor field-effect transistors) [16]. Unlike thyristors, which are used for line commutated converter (LCC) HVDC, IGBTs have *turn-off* capability, allowing the device to modulate any desirable switching pattern and hence voltage. A particular (stacked) series arrangement of such IGBTs comprises a voltage sourced converter (VSC). VSC-HVDC enables application in weak or even passive systems. Especially for offshore purposes, for instance a WPP that needs to be connected to the shore, this feature is invaluable.

VSC-HVDC systems have favourable control characteristics. In contrast to LCC-HVDC where the current (and hence power flow) direction can be reversed by reversing the polarity of the DC cable, VSC-HVDC can control the current flow (and reverse it) by regulating the DC side voltage. This potentially allows the connection of an arbitrary number of VSCs in parallel by multi-terminal VSC-HVDC systems (VSC-MTDC). The currently ongoing development and deployment of modular multi-level converter (MMC) technology for new VSC-HVDC schemes enhance the controllability of VSC-HVDC schemes even further.

VSC-HVDC links are, however, also costly investments compared to LCC-HVDC and AC transmission expansion. The COBRACable for instance, a 700 MW link that is currently in the construction phase, is estimated to cost around EUR 600 million [17]. The 1000 MW BritNed cable, based on LCC-HVDC cost EUR 600 million whereas the Randstad 380 kV North Ring is estimated at EUR 690 million for over 5 GW additional transmission capacity [18]. Relatively speaking, the grid connection of offshore WPPs is even more expensive. BorWin1, the first VSC-HVDC connected offshore WPP, entailed a total of EUR 340 million investments for the onshore VSC, the offshore platform and VSC, and the cable connection [19]. It is important to seek for synergies between transnational transmission system expansion, WPP deployment, and other offshore energy-related activities.

The technological benefits of VSC-HVDC on one hand and the careful economic considerations on the other hand gives rise to the development of VSC-MTDC structures offshore: To alleviate the additional investment costs that must be borne when connecting an offshore WPP by VSC-HVDC, the offshore infrastructure can be extended towards an adjacent transmission system in the planning phase. In this way this VSC-MTDC link also acts as a

transnational interconnection in case the WPP connection is not fully utilised. This principle has been subject of many research and development projects throughout the past decade, and has lead to various visions and working groups regarding the design of and deployment towards such a *transnational offshore grid* (technology, network topology of offshore grid, implementation in market mechanism) [20–25].

1.1.3 Grid Integration of Offshore Wind Power and VSC-HVDC

Integrating VSC-HVDC connections and WPPs – onshore and offshore – into the AC transmission system is considered one of the main challenges of the coming decades [26, 27]. Despite the excellent controllability of VSCs their physical behaviour is very different from that of conventional rotating machinery (e.g., discontinuous behaviour during faults, limited short circuit power, no inherent inertia response). Especially when the relative penetration of such converter interfaced generation is high this might pose serious threats to the operation of the power system as a whole.

Transmission system operators (TSOs) therefore devise grid connection requirements for newly installed generating units by grid codes. Ideally speaking, these requirements oblige the connecting partner to make its device or plant compatible with the behaviour of the grid it connects to. This will be elaborated upon in Chapter 2, but common requirements are fault ride-through, voltage support, active power recovery, frequency support, or even inertia emulation by WPPs and VSCs.

One of the more specific aims of grid connection requirements is conserving the stability of the power system as a whole. A joint IEEE/Cigré task force on stability terms and definitions proposed a definition for power system stability [28], reading

“Power system stability is the ability of an electric power system, for a given initial operating condition, to regain a state of operating equilibrium after being subjected to a physical disturbance, with most system variables bounded so that practically the entire system remains intact.”

and subsequently clustered power system stability into 3 main branches:

- **rotor angle stability:** associated with the ability of interconnected rotating machines to remain in synchronism with each other, either after a severe disturbance (i.e., transient stability) or during natural perturbations (i.e., small-signal stability);
- **frequency stability:** associated with the ability to maintain the system frequency within defined boundaries, maintaining the overall power balance between electricity generation and consumption;
- **voltage stability:** associated with the maintenance of acceptable voltages during normal operation or after disturbances.

In practice, these three types of stability are interrelated, depending on the operating conditions of the network. It is significant to consider the influence of VSC-MTDC on all of these primary types of stability, and, subsequently, to what extent VSCs can support the stability of the system. We will primarily focus on the first aspect: the influence of VSC-MTDC on rotor angle stability.

1.1.4 Simulation Aspects of VSC-HVDC and offshore WPPs

Grid extensions, deployment of large power plants, and connection of industrial loads foreseen in the far future requires knowledge about their implications on the existing power system. This is as a rule addressed by planning and grid integration studies performed today, which are predominantly supported by software experiments. VSC-HVDC and offshore WPPs are no exception to this practice.

The planning phase is dominated by demonstrating the socio-economic feasibility of the connection, taking a holistic approach. Connections, power systems, and plants are traditionally modelled in the energy domain by a reduced level of detail. For technical aspects such as reliability and security of supply more detail is usually needed to test success criteria; at least including a sufficient topological representation of the power system. The solution algorithms for these studies are mainly linear in nature.

Short-circuit rating and voltage profile testing commonly need a fundamental frequency projection of the network representation. Load-flow studies for instance comprise a non-linear set of algebraic relations to represent the power system, and hence need an iterative solution algorithm. Grid code requirements touching the stability aspects of transmission systems require a more thorough representation of the physical interactions between devices in the network, which need to be addressed in the time-domain.

Device or connection-specific phenomena are typically over-voltages, unit protection, inrush phenomena, power electronic switching, and so forth. Their influence stretches across the near electric vicinity of the connection of interest. The level of modelling detail required for studying these phenomena is substantial: electromagnetic interactions of every device near the region of interest must be addressed properly. Electromagnetic transients (EMT) simulators covers these needs and allow moderately sized networks to be assessed by a high level of detail. The numerical integration routines that calculate the dynamic interactions generally require time step-sizes in the order of tens of μs .

Network-level aspects are phenomena such as transient stability, frequency response, voltage control, stabilising functionality, fault ride-through, etc. Their nature is historically related to interactions between electric power production facilities, which mainly have a mechanical nature, and their corresponding conversion to electrical power, mainly by rotating machinery. These electromechanical interactions are mainly perceived in the system frequency and voltages; their influence spreads much further than EMT-based interactions whereas the required level of modelling detail is considerably lower. The corresponding studies are executed by stability-type simulations, which consider the system by splitting it into a network part, which is modelled by algebraic relations, and a dynamic part, which is described by differential equations.

Wind power plants, VSC-HVDC connections, and AC transmission systems each have their own particular spectrum of controls, phenomena, and corresponding time constants. This is shown by a typical time-scale versus power system phenomenon characteristic in figure 1.2. It can be seen that each subsystem has its own characteristic set of operating features, which would ideally speaking culminate in a dedicated set of tools to study a particular grid integration aspect. The advent of bulk VSC-HVDC transmission gives rise to re-evaluating the applicability of EMT and stability-type simulations, which have predominantly been designed to serve AC power system analysis.

The assumptions stability-type and EMT-type simulations are founded on, have evolved over decades. The limited computation power at the start of the digital computing era for power systems constituted the main bounds for the respective simulation paradigms: a strict

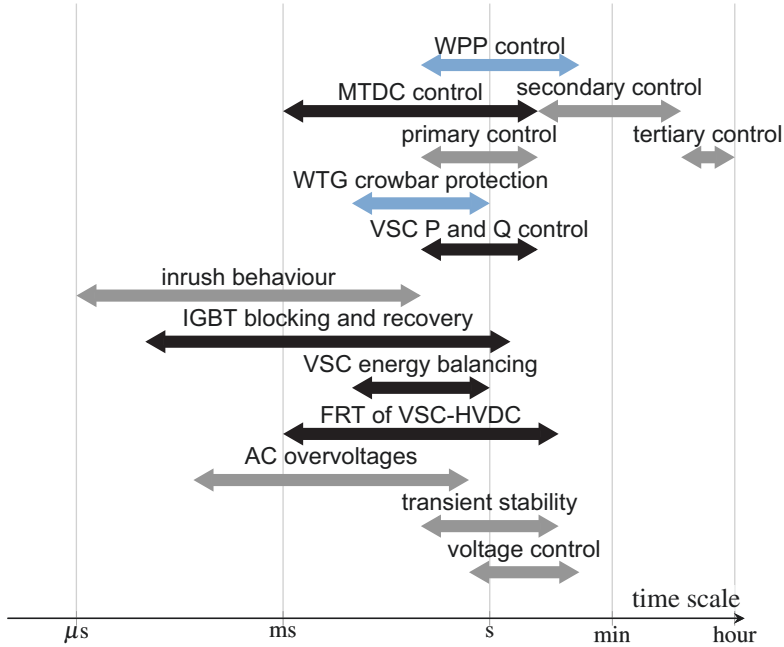


Figure 1.2: Time scale versus phenomenon of interest showing the overlap between transient stability and VSC controls and protection. (adapted from [29]). Types of controls and phenomena: \longleftrightarrow (AC), \longleftrightarrow (HVDC), and \longleftrightarrow (wind).

trade off between system size and simulation accuracy had to be made. The choice to assess EMT and electro-mechanic phenomena by different modelling and simulation methods was therefore comparatively natural. Notwithstanding the evolution of the computational power, which roughly doubles each two years according to Moore's law and even led to real-time computing of EMT, this separation still exists today and poses a tremendous modelling and simulation challenge of the next generation power system.

1.2 Research Challenges and Problem Definition

The deployment of WPPs, onshore and offshore, and their connection via VSC-HVDC networks involve significant challenges for various (sub-)domains of power engineering. On the planning level, the challenges include a trade-off between investment costs, legislative boundaries, and operational benefits [30]. Looking from an operational angle, the continual balancing between supply and consumption becomes an important aspect to consider, especially for high RES penetrations. These are issues related to power system behaviour in normal operation and (quasi) steady-state, which are the boundary conditions for this work.

This thesis deals with the analysis of large-scale electrical power systems in which transnational offshore transmission networks based on HVDC technology are an integral part. In particular, the main focus of the analysis is on the transient stability of such networks. That is, the behaviour during and shortly after fault conditions. On this level, the challenges are very different compared to the planning level and have a more physical-technical nature.

In particular:

- DC fault current interruption for VSC-MTDC networks such as circuit breaker design and selectivity of protection ;
- operation and control during and after AC-side faults: e.g., fault ride-through (FRT), active power recovery, ancillary services;
- IGBT forward current limiting; and
- power flow control and the corresponding direct voltage balancing.

These issues are strongly related to the time-bound vulnerability of the power electronic components involved and the relatively small energetic capacity available in the HVDC system for balancing variations in active power in-feed. The latter brings about a boundary to the HVDC control system by means of a small time constant inside the *plant* to be controlled.

VSC-HVDC networks thus interact with AC networks using their controls and protective equipment. In terms of grid integration aspects, i.e., making such networks compatible with the existing power system for a wide range of operating characteristics, it is relevant to consider:

1. the elements that set up these interaction, i.e., the operation and control of VSC-HVDC transmission schemes;
2. how AC-side events influence the operation of the VSC-HVDC network, especially FRT of offshore WPPs; and
3. how VSC-HVDC-side phenomena impact the AC network operation, control, and stability.

It is expected that large fossil-fuelled synchronous generators will be gradually replaced by renewable energy generation. Among others, a significant role will be played by (offshore) wind power interfaced by HVDC transmission. As synchronous generators to a large extent determine the dynamic behaviour of today's power system, it is expected that this behaviour will change considerably. Currently, not much is known about the transient stability of such networks. This constitutes the first problem addressed in this thesis, and is formulated with the following research question (RQ1):

"Given the gradual substitution of conventional generation by renewables such as VSC-HVDC connected large-scale offshore wind power, how does VSC-HVDC transmission interact with the onshore system, and what is the impact on the transient stability of interconnected AC systems?"

To answer this research question satisfactorily we first need more detailed information about VSC-HVDC networks, which translates into the following sub research questions:

1. What are realistic network connection schemes for offshore VSC-HVDC transmission?
2. Which operation and control options do we have to consider for the transient stability impacts of VSC-HVDC transmission?

3. What are the phenomena of interest for the AC/VSC-HVDC interactions and transient stability?
4. What are the connection requirements of interest for the AC/VSC-HVDC interactions and transient stability?
5. How do the main control schemes of VSC-HVDC transmission interact with wind power plant control mechanisms, mainly during FRT?
6. What is a realistic scenario to assess transient stability impacts (i.e., unit commitment, grid extensions, wind penetration, among others)?

The first four background questions will be answered by a state of the art analysis of the operation and control of VSC-HVDC and offshore wind power. The latter two background questions will be answered by simulation studies taking the data availability for the 2025 time horizon as a boundary condition.

It is commonplace to study the transient stability of large power systems by quasi steady-state simulations. Network quantities (voltages and currents) are represented by phasors, whereas only the rotating machines and other dynamic devices are represented by differential equations. Such tools are based on a well-established framework of assumptions that allow the simulation of very large networks with moderate computational complexity. The inclusion of power electronic converters, and in particular arbitrary DC network topologies, into these simulation tools does not fit well into this framework. This is mainly caused by the time scale in which this equipment operates, which is much faster compared to conventional generation. This is the second problem addressed in this thesis, which we formulate by RQ2:

“Provided the necessity to employ stability-type simulations to investigate the dynamic interaction of VSC-HVDC networks with large-scale onshore transmission systems, how can VSC-MTDC transmission be incorporated without compromising simulation speed and accuracy?”

Similar to the first research question, we first require answers to more specific sub-questions:

1. How can the AC/VSC-HVDC interactions relevant to transient stability be modelled in the time domain?
2. How can VSC-HVDC schemes be modelled into stability-type simulations in an structured manner, while retaining the desired modelling accuracy?
3. How can the adapted and developed models be simplified and what are the implications?
4. Given the modelling assumptions, fault ride-through implementation, and control strategies of VSC-HVDC, how can averaged EMT models be interfaced universally with transient-stability simulation tools?

The first sub-question will be answered by qualitatively comparing the capabilities of time-domain simulation tools with the time-frame of the foreseen interactions. Generalised HVDC modelling, its simplifications, and the development of dedicated interfacing techniques are based on mathematical modelling for time-domain simulations and subsequently comparing differences between various implementations both quantitatively and qualitatively.

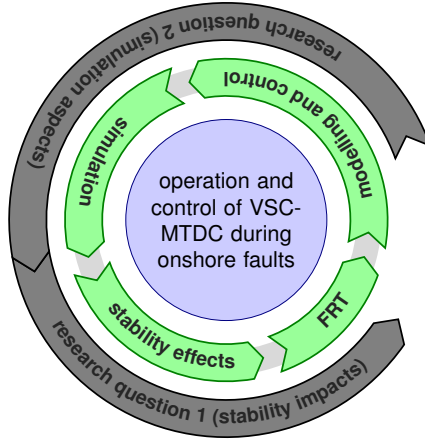


Figure 1.3: *Scope, technical aspects, and research questions of this thesis*

1.3 Research Objectives and Approach

The main scope of this thesis is the operation and control of offshore transnational grids, using VSC technology, during and after disturbances originating from the onshore power system. Several technical aspects of VSC-MTDC revolve around this, as shown in figure 1.3. These can hardly be considered separately. For a correct modelling of FRT for instance, we need to establish which phenomena potentially cause stability impacts. On the other hand, assessing the impact itself needs a suitable simulation platform. The various functionality requirements may on their turn clash with the modelling requirements, and so on. We hence need to make assumptions and carefully motivate them or test their plausibility later on.

Grid codes commonly require generating units to stay connected during AC disturbances (the fault ride-through requirements) and state which additional control actions to take during and after disturbances. Grid codes differ from TSO to TSO but the bottom line is that especially FRT-related requirements operate in the transient stability time frame (see also figure 1.2). We assume onshore FRT capability of VSC-MTDC, connecting offshore WPPs or otherwise, as the main operating feature to be considered for addressing the research questions. FRT involves quick control actions and coordination, discontinuous behaviour of the VSCs, and prompt changes in active power in-feed into the onshore power system. It will be shown that FRT can be achieved in several manners, depending on the topology of the VSC-MTDC network and the type of wind turbine generator (WTG) the WPP comprises.

The dynamic behaviour of the VSC-MTDC as an integral system is partly driven by state transitions of individual components, which exhibit a non-linear and discontinuous nature. For rotor angle stability purposes, the problem can therefore be best addressed in the time-domain. At the outset of this research, no standardised set of numerical models for simulating the dynamics of WPPs, VSCs, or VSC-MTDC was available. Based on normal operating conditions, FRT functionality, and literature VSC-MTDC models will be constructed and tested on exemplary test networks.

Although we acknowledge the importance of DC-side faults for both the operation of

VSC-MTDC and its potential stability impacts, we will not consider such events for the following reasons. First, the VSC-HVDC links that are currently in operation are point-to-point, predominantly for the grid connection of offshore WPPs. In such cases, disconnection of DC-side events is achieved at both AC-sides, diminishing the importance to interrupt at the DC-side. Second, HVDC circuit breakers are still under development so their exact interruption behaviour is not fully known, and their implementation in MTDC networks need sophisticated protection algorithms [31]. Third, the HVDC cable discharging time constants are small and cause large over-currents, necessitating very fast interruption times [32]. So fast that, as seen from the AC-sides, we assume the DC side interruption to be similar to blocking the VSC active and reactive power in-feed, while quickly re-dispatching the power across the unaffected VSC terminals in the MTDC network. Under this assumption we can apply averaged-value modelling of VSCs, i.e., representing the AC and DC sides of the VSC by variable voltage or current sources.

The averaged VSC-MTDC models and controls will be established for EMT simulations and implemented into MATLAB/SIMULINK and the EMT-type tool PSS[®]NETOMAC. The high numerical complexity of EMT type simulations make them unsuitable for the analysis of large networks. Studies focusing on the behaviour of power electronic converters would require EMT type simulations. Instead, stability type simulations based on algebraic network equations are applied to investigate the transient stability of large systems. The inclusion of VSC-MTDC into such platforms is addressed under the assumption of applying a fixed time step-size for numerical integration. This focus is driven by the grid data availability – the AC transmission system was available in PSS[®]E, employing a fixed time step-size – while implementation in a variable time step-size tool caused numerical instabilities. Three implementations into a stability type simulation are assessed in this thesis: 1) a state-space representation of the VSC-MTDC system, 2) a reduced-order model neglecting various small time constants at the DC side, and 3) a multi-rate implementation of the generalised state-space model of the VSC-MTDC system. Multi-rate implies the inclusion of a dynamic model using its own inner numerical integration loop, usually with a much smaller time step-size, while leaving the time step-size of the overall simulation untouched.

It is then examined if and how EMT and stability type simulations can be combined to keep the numerical complexity moderate (to study large systems) and on the other hand offer the ability to include multi-terminal HVDC systems. This leads to the refined development of so-called *hybrid* simulation methods, in which the part requiring high detail is simulated using the EMT technique with a small time step-size, and the remainder is simulated by the stability technique with a much larger time step-size. Special attention will be paid to the way in which both simulation types are coupled (i.e., the interfacing techniques). A proof of concept is implemented in MATLAB first and subsequently in Python to enhance generality.

For both monolithic and hybrid simulation approaches the accuracy and speed will be compared to a reference EMT simulation. This is done qualitatively by considering the time-domain behaviour, and quantitatively by measuring computation times and numerical deviations from the reference simulation.

The simulation and modelling improvements established for the monolithic approach are then applied to study the transient stability of interconnected power systems with an integrated meshed HVDC structure. The control mechanisms of VSCs during normal operation and disturbances have a determining effect on the ability of the system to maintain stability. Therefore, these control methods will be analysed and applied in detail. (Different) benchmark systems are used to investigate the impact on transient stability under variation

of the level of HVDC-connected wind generation, WTG types, FRT implementation, and other converter interfaced generation. After having obtained a qualitative understanding of the interactions on the benchmark systems these findings will be tested deterministically on a scenario that comprises a realistic (dynamic) representation of the North-West European transmission system for the 2025 time-horizon. These simulations are executed by PSS®E using the multi-rate implementation as explained under point 3 above.

1.4 Scientific Contribution

The first set of research questions cannot be answered before answering the second. That is, the modelling and simulation challenge precludes a straightforward and adequate assessment of rotor angle stability of large-scale power systems with offshore VSC-MTDC. Yet, the described approach assures that all stability-specific technical aspects are adequately (i.e., accurately and computationally feasible) included into the numerical models. The scientific emphasis of this thesis is hence on the second research question.

The operation principles of VSCs, WTGs, as well as their arrangement in point-to-point connections and offshore WPPs respectively has been researched and developed over the past decade. There is a wide consensus in the scientific and industrial community on how to numerically model and incorporate wind turbine generators into stability-type simulations. The individual WTG modelling has recently been standardised by the International Electrotechnical Commission (IEC), [33] whereas their WPP-level representation is currently under consideration by the same working group 27 [34]. Numerical models of VSC-HVDC links (point-to-point) are only implemented in some tools and are primarily vendor-specific and their applicability is subject to network parameters and event type. This thesis contributes to the current state-of-art by proposing a *generalised dynamic representation of multi-terminal VSC-HVDC networks*, which is flexibly applicable for either islanded (weak) grids such as WPPs or for integration into transmission systems. The generalised VSC-MTDC model supports numerous AC voltage control schemes, various FRT implementations, direct voltage control mechanisms, and handling of various AC current limiting schemes. The model is systematically implemented into PSS®E: arbitrary VSC-MTDC network topologies and control strategies can be configured, initialisation is obtained using the sequential AC/DC power flow algorithm, and dynamic data files are generated automatically.

The numerical properties (modelling accuracy and simulation speed) of the generalised VSC-MTDC model are tested by implementing it into an in-house developed stability type simulation. It will be demonstrated that further improvements are necessary for grid integration studies taking into account large-scale offshore wind connected through HVDC. To increase the computational performance, we will propose two innovations: one that simplifies the DC-side to a single node with an equivalent capacitance, and one that applies multi-rate techniques to isolate the numerical solution of the VSC-MTDC model from the remainder of the stability simulation. That is, implementations 2) and 3) listed in section 1.3. These improved models provide insight in how the speed/accuracy trade-off can be achieved and under which circumstances.

The main scientific contribution of this thesis lies in the thorough analysis and further development of a hybrid simulation environment, which embeds an EMT-type simulation into the stability-type simulation. The in-house development provides an invaluable understanding of the interaction between the two type of simulations up to the level of numerical

integration and related computational aspects. It will be shown that integrating VSC-HVDC into hybrid simulations requires improvements to the interfacing techniques that are currently state-of-the-art. The main innovations are:

1. updating the passive components of equivalent sources during faults;
2. extrapolative filtering of equivalent source quantities such as angles and voltage magnitudes;
3. interaction protocol allowing interpolative filtering of equivalent source quantities; and
4. a special interaction protocol for accurate phasor determination after disturbances in the stability part of the hybrid simulation.

The systematic application of ride-through mechanisms for several types of WTGs has been extensively investigated in literature. This thesis contributes to the existing body of work by

1. implementing the FRT methods into the controls of the developed VSC-MTDC model;
2. combining several types of FRT mechanisms for WPPs consisting of mixed types of WTG;
3. investigating the interaction with other grid code requirements such as (onshore) active power recovery after fault clearance; and
4. assessing the impact of AC-side grid properties such as inertia, grid strength, and type of generation on the applicability of the FRT options.

Considering FRT in a broader context here furnishes us with not only a better understanding of the interaction between VSCs and AC systems but also with new insights in possibly conflicting grid code requirements.

Developments with respect to the deployment of large-scale offshore wind power plants point toward the application of multi-terminal VSC-HVDC. This work contributes to the investigation of the operational characteristics of such schemes, most importantly during and after disturbances. Considering the proposed MTDC control and (post-)FRT methods on one hand, and the various limiting schemes and reactive power support methods adopted from literature on the other hand, the impact of VSC-MTDC on onshore transient stability is assessed. The case study concluding this thesis focuses primarily on Western Europe and the North-Sea region in particular. The stability studies conducted for this thesis are amongst the first applied for this region using this particular level of detail.

1.5 Research Framework

The Dutch government foresees the deployment of 4450 MW wind power in the Dutch part of the North Sea by 2023. Long term plans for the entire North Sea cover up to 60 GW wind power capacity by 2030 (high scenario of [35]). The economical, societal, and technical challenges of connecting offshore wind at such a large scale requires careful attention of each of these aspects by research and development conducted today. The North Sea Transnational Grid (NSTG) research project investigated the expected gradual shift from

conventional generation onshore to a generation portfolio largely driven by offshore wind power. The economical and technical impacts of connecting this huge amount of offshore wind power to the grid were studied. Special attention was paid to the structure (topology), the transmission technology to be adopted, the operation and control, and the market integration of such a grid.

The NSTG research project was funded under the EOS-LT framework (i.e., *Energie Onderzoek Subsidie Lange Termijn*) issued by Agentschap NL (now RVO, Rijksdienst Voor Ondernemend Nederland). It was a research collaboration between Delft University of Technology and the Energy Research Centre of the Netherlands [36]. Both parties gained substantial knowledge about offshore wind power in the related We@Sea consortium [37], the recommendations of which pointed towards the further investigation and development of multi-terminal HVDC transmission for various levels of detail [38]. The overall lead of the NSTG research project was in the hands of ECN, which also governed the regular reporting to Agentschap NL. A study advisory board consisting of various industrial partners assembled on a yearly basis to provide feedback to the intermediate results. The project ran from October 2009 to June 2013 and encompassed a total budget exceeding EUR 1 million.

The research comprised the following main topics: the techno-economic evaluation of connection options, MTDC network operation, control, and optimisation, grid integration, and a cost-benefit analysis. These topics were covered in work packages, drawing up in total 3 Ph.D. projects, all conducted by TU Delft. Aside from this thesis these were:

- *Multi-Terminal DC Networks - System Integration, Dynamics and Control* [39];
- *Transmission Expansion Planning Under Increased Uncertainties - Towards Efficient and Sustainable Power Systems* [14];

The first Ph.D. project (i.e., [39]) mainly centred on controlling and operating a transnational grid under normal (non-disturbed) operating conditions, whereas [14] concentrated upon long-term planning and $N - 1$ security aspects of the *combined* AC/HVDC transmission system. This thesis adds value by considering the operation and control of the combined mainland AC and transnational offshore grid during and immediately after disturbances. The control proposed for normal operation has been inspired by [39], whereas the results from [14] have been adopted as a one of the starting points for the scenarios of the transient stability simulation studies.

1.6 Outline of the Thesis

This thesis follows the line of reasoning described in section 1.3 as closely as possible. We will first elaborate on the second main research question before we actually assess stability impacts. Each chapter starts with an abstract referring to the main scientific publications the contents are based upon. Each chapter ends with a summary of the main findings. The outline of this thesis is shown in figure 1.4.

After this introduction we will in Chapter 2 continue with an overview of relevant notions on the operation, control, simulation, and grid integration of offshore wind generation and VSC-MTDC. This paves the path for developing numerical models for the relevant components, and provides bounds and assumptions for the scenarios of Chapter 6.

Chapter 3 will describe the numerical models for VSCs – onshore and offshore – HVDC submarine cables, the relevant wind turbine generators, and their arrangement in WPPs. We

Chapter 2

Operational Aspects and Modelling Requirements

This chapter discusses in detail the construction and operational characteristics of VSC-HVDC links, both point to point and MTDC, and wind power plants. The massive deployment of these systems as large-scale power plants will impact the dynamic characteristics of the power system. These impacts need to be assessed through stability-type simulations. Grid code requirements aim to maintain compatibility between (converter-interfaced) generation and conventional components. It will be shown that the model requirements for VSC-HVDC links clash with the simulation requirements for transient stability assessment.

2.1 Operation of VSC-HVDC Transmission

2.1.1 Historical notes on HVDC Transmission

Ever since the war of the currents back in the 19th century, our present transmission system consists largely of alternating current equipment. Technologically, this has for a very long time been the *de facto* type of transmission, as power generators were rotating machines and conversion to higher voltage levels was highly efficiently done by power transformers. DC transmission did not have such a conversion mechanism without engaging mechanical devices, requiring considerable maintenance. The invention of mercury arc valves in the early 20th century allowed a non-mechanical conversion between AC and DC, which led to several interconnections between distribution systems. Over the next decades this technology was scaled up to high voltage level, enabling transport capacities in the GW range. The availability of thyristor valves in the kV range for several hundreds of A in the 1970s resolved a myriad of issues related to mercury-arc valves (e.g., reliability, blocking capability, maintenance and spatial requirements) [40]. During the course of the next four decades the majority of commissioned HVDC links employed thyristor technology, and mercury-arc valve based converters were gradually replaced by thyristor bridges – the last one in 2012 [41].

Figure 2.1 shows three common (thyristor-based) HVDC system configurations: mono-

polar, bipolar, and a symmetrical monopole. A typical point-to-point link consists of a (rectifying) sending-end *converter station* that connects by means of one or two *poles* to the (inverting) receiving-end converter station. Depending on geographical conditions and spatial requirements, a pole is connected either by overhead lines or (submarine) cables.

The type of system configuration is a design choice depending on diverse criteria. An asymmetrical monopole configuration as in figure 2.1a for instance, needs a suitable return path for the current. Environmental conditions such as soil resistance, biotic interference, or existing infrastructure in the direct proximity of the electrodes may cause undesired side effects and necessitate a metallic return path instead. The transmission capacity is doubled in case a bipolar configuration is adopted (figure 2.1b). Moreover, the negative pole provides a return path and inserts 50% redundancy in case one of the two poles fails. Alternatively, the system can be operated as a *symmetrical monopole*, as shown in figure 2.1c. This configuration, which is also adopted for the NorNed cable [42], introduces more flexibility in grounding the DC-side. It also considerably reduces the DC voltage stresses on the converter transformers. The symmetrical monopole configuration is commonly applied for VSC based HVDC.

The HVDC converter station comprises harmonic filter banks (both AC and DC), reactive power control switchgear, converter transformers, a valve hall, and protection and pole reversal switchgear. The converter itself is usually composed of a pair of 6-pulse *Graetz* bridges as shown in figure 2.1a. These bridges are connected in parallel on the AC side to reduce harmonics and in series on the DC side to increase the voltage level. Depending on the operating voltage, each *phase arm* consists of a multitude of stacked thyristor *valves*.

At present the majority of HVDC connections is operated by thyristor valves. Unlike diodes, thyristors can delay the forward conduction instance by triggering a pulse at their gates, the *delay angle* α . By controlling α the voltage and hence the current through the DC circuit can be regulated. Subsequently the AC side voltages determine the instances at which the current commutates from one valve to the other (in a 12 pulse configuration every 30°). Thyristor based HVDC transmission is hence commonly referred to as line-commutated converter (LCC) HVDC. The employed operating mechanism of delay angles and current commutation inherently implies that the fundamental components of line currents lag the voltages. Thus, an LCC needs a relatively strong network to commute against and draws reactive power irrespective of the conduction angle α .

HVDC transmission offers various advantages over its AC counterpart. First, HVDC allows bulk transmission using less conductors compared to AC (one or two for HVDC compared to three for AC). Bulk transmission and long distances often go hand in hand. HVDC circuits do not need or generate reactive power; this is an immense benefit as compared to AC lines or cables, which need careful reactive power compensation measures along their path. The second advantage of HVDC is their controllability. As mentioned, active power can be controlled by setting the delay angle of the thyristor bridges. The power through AC transmission can be only partly controlled by phase shifting transformers or switched series impedances. Finally, the HVDC equipment influences the short-circuit characteristics and determines the dynamic behaviour of the connection. This enables linking asynchronous areas and to some extent separation of the respective system dynamics.

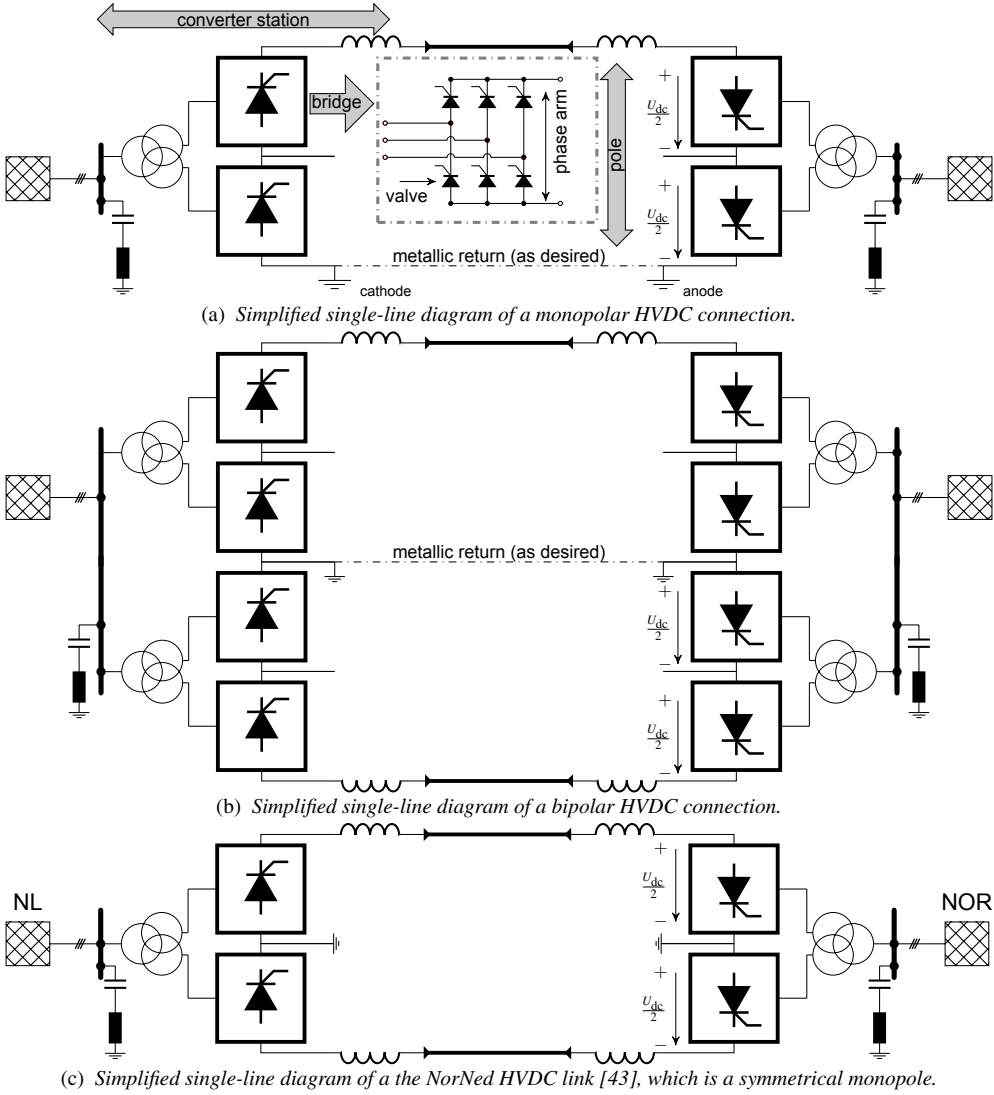


Figure 2.1: Common HVDC point-to-point system configurations.

2.1.2 VSC-HVDC Components and Terminal Layout

In the 1990s, a new type of semiconductor became available at high-voltage levels, the IGBT [44]. Contrary to thyristors, IGBTs offer turn-off capabilities at relatively high switching frequencies (in the kHz range). This allows sophisticated pulse width modulation (PWM) techniques for setting the AC waveform switching pattern. With PWM, the AC terminal voltage can be practically set at any desired value between the positive pole voltage and the negative pole voltage, constituting a voltage sourced converter.

A typical VSC terminal layout is shown in the connection diagram of figure 2.2. From AC (left) to DC (right) it comprises the point of common coupling (PCC), the converter transformer ($R_t + jX_t$), harmonic filters (C_f), the converter phase reactor X_c , the VSC unit

alongside its DC-side capacitors and overvoltage protection, and the DC-side terminals. In this particular scheme a symmetrical monopole configuration with rigid grounding is applied (see figure 2.1c).

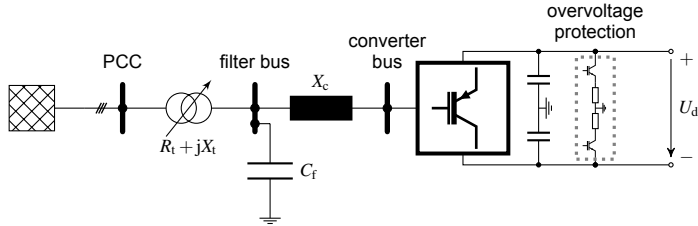


Figure 2.2: *Single-line diagram of a VSC terminal.*

The grid operator commonly defines the connection requirements at the PCC. Voltage profiles, reactive power set points, and capability diagrams refer to network quantities at this location. The PCC also determines the legal boundary between the grid operator and the HVDC system owner.

The operating voltage of the converter differs generally from the nominal voltage of the grid and transformation is hence needed. The converter transformer is thus a crucial element in the design of a converter unit. First, depending on the system layout, it has to withstand DC stresses under normal operating conditions. For VSCs DC stresses are less of an issue as it is customary to operate the HVDC side in a symmetrical monopole configuration [45]. Second, the converter transformer can be exposed to harmonic distortion. Harmonic issues are more severe for LCC as the converter transformers are rigidly connected to the converter bridges. Filters must hence be installed at the grid side of the transformer. Harmonic filters for VSCs are normally installed at the converter side of the transformer, and thereby relieving the harmonic distortion. As a result, normal power transformers can be utilised, two and three winding transformers alike [46].

The main duty of the AC filters is to form a low-pass filter in concordance with the phase reactor, thereby attenuating the PWM switching harmonics. The switching pattern depends on the power electronic topology of the converter itself, among others. For a two-level VSC, for instance, a common switching frequency is 2 kHz [47]. This brings about the 40th as the lowest harmonic in the converter current to be attenuated. The physical filter component size shrinks with increasing tuning frequency. Hence, spatial requirements for filter equipments are more relaxed compared to LCC. More refined (cascaded) converter topologies generate a near-sinusoidal voltage. This reduces the filtering needs even further and VSCs using the latest technology are even operated without any harmonic filters.

The phase reactor has two main objectives: it is part of a low-pass harmonic filter as described above and it comprises an impedance the current through which can be controlled. The latter makes it an indispensable element of a VSC station, potentially allowing the VSC to independently exchange active and reactive power with the AC grid.

The key element of the VSC station is the converter itself, which, usually by a bridge configuration of IGBT valves and freewheeling diodes, allows the modulation of AC waveforms from the DC voltage by applying a particular switching pattern to the IGBTs. Figure 2.3 shows the most elementary type of VSC: the two-level converter topology, which was applied to the first generation VSCs at high-voltage level [44]. Each phase arm (i.e., S1 ... S6) consists of a number of stacked IGBT valves that are fired simultaneously. Each valve has

a freewheeling diode in anti-parallel to prevent flyback across the inductive elements connected in series of the circuit shown in figure 2.3 . With this converter topology, each AC phase is either connected to the positive or the negative pole. PWM lends itself very well for synthesising a three-phase sinusoidal voltage waveform at the AC terminals.

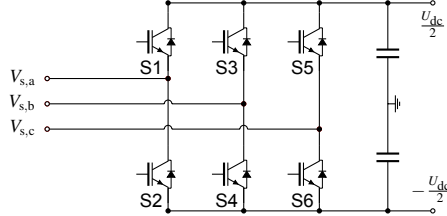


Figure 2.3: Three-phase diagram of a two-level VSC terminal.

The relatively long (i.e., 1 s) turn on and turn off times of IGBTs inhibit the application of high carrier frequencies. This calls for a trade-off between limiting the harmonic distortion and reducing the switching losses. At 1950 Hz these losses amount to 3% per VSC [48, 49], so 6% over a point-to-point connection. Neutral point clamped VSCs insert additional freewheeling diodes between the neutral point (ground) and halfway a phase arm, thereby enabling the neutral point as an extra switching level alongside $U_{dc}/2$ and $-U_{dc}/2$. This reduces the harmonic distortion and allows the PWM to operate at a lower carrier frequency to reduce switching losses.

A significant technological innovation was the advent of modular multi-level converters (MMC) at high power levels [50, 51]. An MMC based VSC is built up by series connected MMC *submodules*, as shown in figure 2.4. A half-bridge MMC submodule consists of two IGBTs and freewheeling diodes in parallel with a capacitance. By switching S1 and S2 appropriately, the output of an MMC module is either short circuited, open circuited (blocked), or connected to the capacitance. By stacking the MMC modules and applying a specialised modulation scheme, a near-sinusoidal waveform can be synthesised at the AC terminals [52]. This facilitates a significant reduction in switching frequency, as low as 115 Hz [53], reducing the VSC switching losses to around 1% per terminal. All (currently three) main manufacturers of VSC-HVDC links have the MMC concept in their portfolio marketed under various brand names:

- ABB: HVDC Light® [54]
- Siemens AG: HVDC PLUS® [55]
- General Electric (formerly Alstom Grid): MaxSine™ [56]

It is foreseen that MMC will be further optimised and developed. Main challenges include the attenuation of circulating currents in the VSC, MMC submodule capacitor voltage balancing [57], and operation and control during grid disturbances [58, 59].

The power electronic components of a VSC are vulnerable to overvoltages and over-currents, especially the IGBTs. Overvoltages can have a transient nature (e.g., lightning, switching phenomena), which last for s and are commonly handled by protective equipment such as surge arresters. The direct voltage is however also used as a balancing mechanism to control the power inflow and outflow of the HVDC link. Hence, overvoltages can also have a quasi-dynamic, operation-driven nature. The overvoltage protection for such situations is

implemented by resistors that are interfaced to the DC poles by a IGBTs, and is designed such that the rated converter power can be dissipated for a limited duration. These *dynamic braking resistors* are a vital part of the fault ride-through operation of a VSC-HVDC link. Further details on their modelling and implementation will be treated in section 3.3.1.

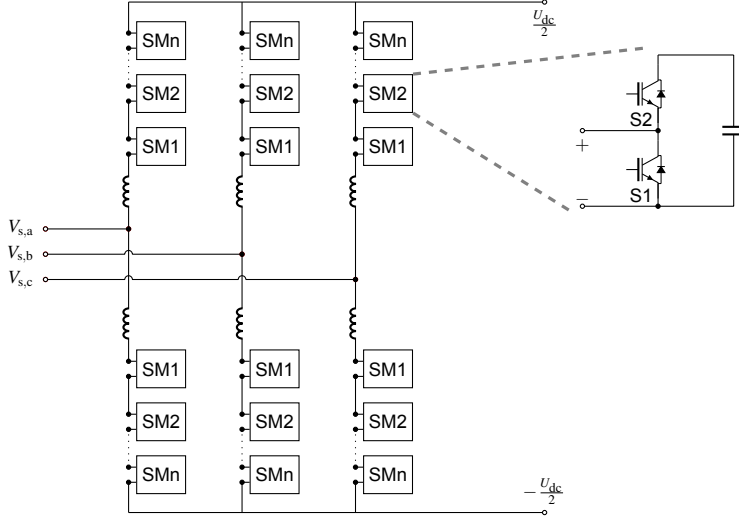


Figure 2.4: Circuit diagram of a three-phase n -level MMC terminal; on the right a simplified diagram of a half bridge submodule.

2.1.3 VSC operation and control principles

The power electronic components (IGBTs and diodes) and their layout in a VSC (two-level, multi-level, MMC) enable the generation of AC waveforms from the direct voltage at the DC terminals. As long as the desired AC voltage does not exceed the positive or negative pole voltage, any set of three-phase voltages can be modulated. We assume a two-level topology for introducing the operation and control principles of a VSC, and will reflect at a later stage on the implications for different topologies.

The maximum phase-to-neutral voltage that can be modulated at the VSC terminals equals the pole voltage

$$\hat{V}_{c,Ln} = \frac{U_{dc}}{2} \quad (2.1)$$

in which $\hat{V}_{c,Ln}$ is the peak value of the converter voltage and U_{dc} the DC-side pole-to-pole voltage. V_c is established by applying sinusoidal PWM, so we can write for the phase voltage

$$V_{c,a} = \hat{m} \cos(\omega_m t + \phi_m) \frac{U_{dc}}{2} + \text{higher harmonic terms} \quad (2.2)$$

where m is the amplitude of the modulation signal, ω the modulation frequency in rad/s, and ϕ the phase angle of the modulation signal in rad. Taking (2.1) into account the maximum modulation index for which (2.2) holds equals 1. We do not consider over-modulation in this thesis. Within these boundaries there are thus three degrees of freedom to set the AC voltage:

magnitude, frequency, and phase angle. For quasi-stationary considerations of device-grid interactions it is common to assume a fundamental frequency projection of network quantities, neglecting higher harmonics. This allows representation by quasi-stationary complex phasors. For the phase-to-phase VSC terminal voltage this leads us to

$$\underline{V}_c = \frac{m U_{dc}}{2} \quad (2.3)$$

with

$$\underline{m} = \frac{\sqrt{3}\hat{m}}{\sqrt{2}} e^{j\phi_m} \quad (2.4)$$

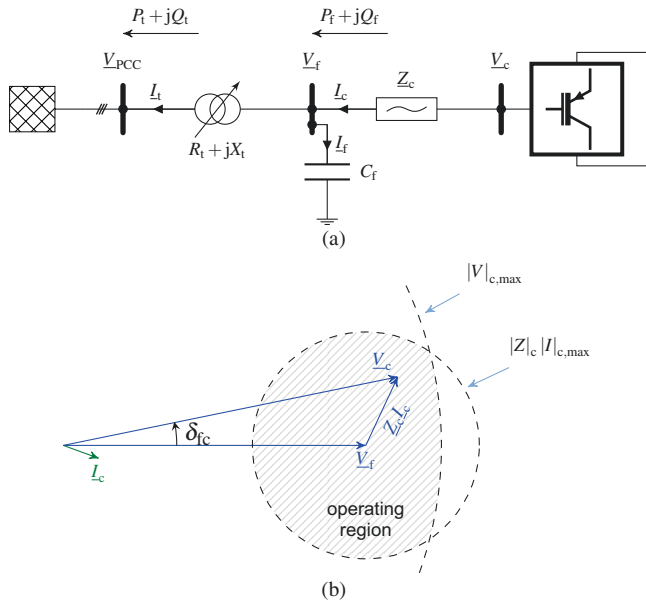


Figure 2.5: Single-line diagram of a VSC terminal. a) Mathematical notation and b) phasor diagram with operating region.

The main operating philosophy of VSCs can best be illustrated using Figure 2.5a, showing a single-line electrical diagram of the VSC terminal and its phasor diagram respectively. Our focus is on the active and reactive power exchange over the phase reactor, i.e.,

$$P_f + jQ_f = \underline{V}_f \underline{I}_c^* \quad (2.5)$$

which expands to

$$P_f + jQ_f = \frac{R_c \left[|V|_c |V|_f \cos \delta_{fc} - |V|_f^2 \right]}{|Z|_c^2} + \frac{X_c |V|_c |V|_f \sin \delta_{fc}}{|Z|_c^2} + j \frac{X_c \left[|V|_c |V|_f \cos \delta_{fc} - |V|_f^2 \right]}{|Z|_c^2} + j \frac{R_c |V|_c |V|_f \sin \delta_{fc}}{|Z|_c^2} \quad (2.6)$$

with δ_{fc} the angular difference between \underline{V}_c and \underline{V}_f . Assuming a phase reactor consisting only of an inductive part ($R_c = 0$), this relation becomes more friendly and converges to the power flow formulae

$$P_f = \frac{|V|_c |V|_f \sin \delta_{fc}}{X_c} \quad (2.7)$$

$$Q_f = \frac{|V|_c |V|_f \cos \delta_{fc} - |V|_f^2}{X_c} \quad (2.8)$$

The VSC's power output can hence be controlled by controlling the voltage drop over \underline{Z}_c and, thereby, \underline{I}_c .

The converter voltage \underline{V}_c can be modulated almost arbitrarily, with the main bounds the current limit of the converter valves, i.e., $|I|_{c,\max}$ and the maximum voltage that can be synthesised for a particular direct voltage, i.e., $|V|_{c,\max}$. The phasor diagram of figure 2.5b shows these boundaries as circles around the tip of \underline{V}_f and the origin respectively. The encapsulated area constitutes the operating region for a given \underline{V}_f and U_{dc} . Each point in this operating region implicates a one-to-one mapping between \underline{V}_c and $P_f + jQ_f$, allowing setting active and reactive power independently.

The phase reactor accounts for a relatively weak coupling between P_f and $|V|_c$ and between Q_f and δ_{fc} . The active power can hence largely be controlled by using δ_{fc} as a control variable, whereas the reactive power output can be controlled using $|V|_c$ as a control variable. This control concept is commonly referred to as *direct control* and is applied for VSCs connected to weak or islanded power systems (i.e., power synchronisation control [60]).

Pure direct control, however, does not fully separate the active power control from the voltage or reactive power control – the cross-coupling that appears in (2.7) is not accounted for. Under most circumstances, especially onshore transmission systems, *vector control* can be applied. Vector control stems from motor drives and relies on the concept of synchronising a control reference frame to the grid voltage (either at the PCC or the filter bus). The control system then consists of two independently operating parts. A d-axis part that accounts for the active power control and a q-axis part that operates with a 90° phase shift and is associated with the reactive power control.

The mathematical modelling and the design of VSC controls are generally speaking done using space vectors. How space vectors relate to phasors and sinusoidal quantities is discussed in Appendix B. The implementation of vector control in this work is treated in chapter 3.

2.2 Deployment and Operating Characteristics of Offshore Wind Power

2.2.1 Operation of Wind Turbines

Principle of Energy Conversion

In essence, wind turbine generators capture the kinetic energy contained in the mechanical displacement of air by converting it into rotational motion. This mechanical rotation subsequently drives an electrical generator, which allows arbitrary further utilisation of the wind as a primary source. WTGs exist in miscellaneous shapes and types, and can be differentiated by the various properties [61, 62]:

- wind extraction (rotating blades, kites, electrostatic)
- axis orientation (horizontal versus vertical)
- rotor speed (fixed versus variable)
- electrical generator (converter interfaced, rigid grid coupling)
- tower foundation (rigid versus floating)
- collector grid connection (AC versus DC)

Some properties are interrelated and exclude the utilisation of other combinations. Notwithstanding the industrial and academic interest—and increasing market penetration—of the various sub-categories of WTGs, the horizontal-axis, AC connected WTGs with concrete tower foundations are dominant in the generation fleet. We hence assume these as a basis for further analysis.

Figure 2.6 highlights the main operational components of a WTG. The aerodynamic part consists of rotor *blades* that can be turned in longitudinal direction by a *pitch controller*. Each blade is attached to the *spinner*, which on its turn is connected to the horizontal turbine *shaft*. Depending on the type of *generator*, the *gear box* caters for a proper rotor speed conversion. Both mechanical and electromechanical conversion steps take place in the *nacelle* compartment, which is attached to the turbine *tower* through a *yaw system*. Depending on *meteorological measurements*, the yaw system turns the spinner/nacelle combination parallel to the wind direction. The electrical grid connection is generally close to the tower base by means of a (two or three winding) power transformer.

The wind power undergoes three main conversion steps inside a WTG: 1) kinetic to rotation, 2) rotation to rotation (gear box and shaft), and 3) rotation to electrical. Each of these steps will be described using the schematic overview of these steps shown in figure 2.7.

Wind Power Extraction

Consider a fictitious thin disc of air with area A_R and volume V_{air} moving in horizontal direction towards the WTG with speed v_w . The kinetic energy inside this disc equals

$$E_{wind} = \frac{1}{2} \rho_{air} V_{air} v_w^2 = \frac{1}{2} \rho_{air} A_R v_w^3 \int dt \quad (2.9)$$

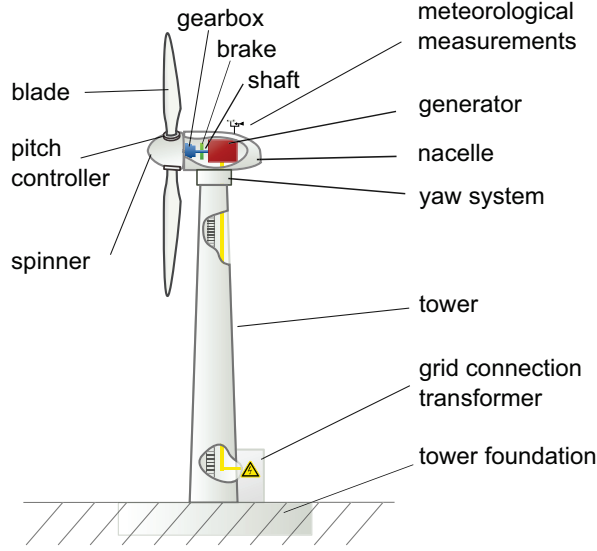


Figure 2.6: Wind turbine overview (adjusted from [63]).

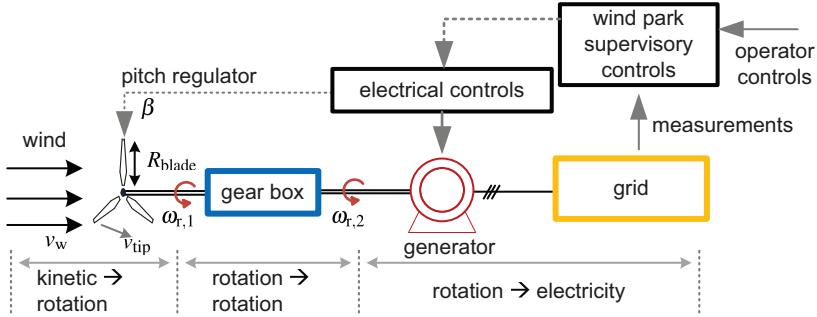


Figure 2.7: Schematic representation of a wind turbine generator (adjusted from [62]).

where ρ_{air} is the density of air 1.225 kg/m^3 and A_R the area swept by the rotor blades. The power that potentially can be extracted is the time derivative of (2.9), yielding

$$P_{\text{wind}} = \frac{1}{2} \rho_{\text{air}} A_R v_w^3 \quad (2.10)$$

However, extracting all the energy from the wind implies that the air would stop flowing at the other side of the wind turbine, accumulating air at the rear of the WTG. This is impossible and thus the wind speed will be reduced to a value lower than v_w instead. Albert Betz showed in 1926 that the maximum proportion of power that under ideal circumstances can be harvested from the wind is $\frac{16}{27}$, hence the Betz constant $C_{\text{betz}} = 0.593$. In general this results in the following expression for the aerodynamic power absorbed from the wind and exerted as mechanical power at the rotor shaft

$$P_R = \frac{\rho_{\text{air}}}{2} C_p A_R v_w^3 \quad (2.11)$$

In which C_p is the efficiency coefficient (i.e., the ratio between P_R and P_{wind}), with $C_{p,\text{max}} = C_{\text{betz}}$. The operation of the WTG can be optimised by 1) employing a larger rotor diameter to increase its swept area A_R , 2) designing lofty towers as wind speed increases with increasing hub height, and 3) by sophisticated rotor blade design, bringing C_p closer to $C_{p,\text{max}}$. Contemporary rotor blade design permits optimised C_p just a few percent below the Betz constant.

For quasi-stationary conditions (i.e., negligible turbulence, constant v_w , no torsional shaft oscillations), C_p depends on a couple of variables such as the rotor speed (and thus tip speed), the angle of attack set by the yaw system, and the pitch angle β , being the angle between the rotor axis and the rotor blade. For a given β , C_p is a highly non-linear function of the *tip speed ratio* λ between the rotor tip speed v_{tip} and the wind speed, being

$$\lambda = \frac{v_{\text{tip}}}{v_w} = \frac{\omega_R R_{\text{blade}}}{v_w} \quad (2.12)$$

where R_{blade} is the radius of the swept area A_R . C_p has an optimal value at λ_{opt} , commonly in between $\lambda = 6$ and $\lambda = 10$ [62]. For variable speed WTGs, this set point can be obtained by controlling ω_R for a particular v_w . The shape of the C_p curve as well as λ_{opt} vary with the pitch angle β . The resulting $C_p(\lambda, \beta)$ curves can be accurately calculated by the blade element method and are usually provided by wind turbine manufacturers. Figure 2.8 shows an example $C_p(\lambda, \beta)$ plot for a Vestas V90 WTG.

System studies commonly apply an analytical approximation of $C_p(\lambda, \beta)$, which is obtained by curve fitting. In line with [62], we assume a non-linear approximation of the $C_p(\lambda, \beta)$ curves by

$$C_p = c_1 \left(c_2 / \lambda_i - c_3 \beta - c_4 \beta^{\frac{3}{2}} - c_5 \right) e^{-c_6 / \lambda_i} \quad (2.13)$$

where c_1 to c_6 are constants, and

$$\frac{1}{\lambda_i} = \frac{1}{\lambda + 0.08\beta} - \frac{0.035}{\beta^3 + 1} \quad (2.14)$$

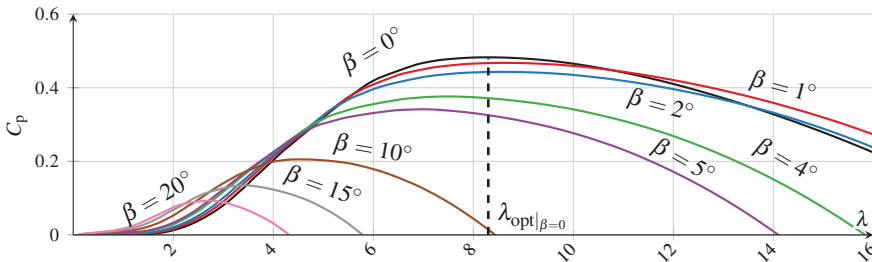


Figure 2.8: Example $C_p(\lambda, \beta)$ curve using approximated data of a Vestas V90 wind turbine.

Electromechanical Conversion

Generally speaking, the blade rotation speed of modern WTGs is in the order of 5–14 rpm. This is far less compared to the nominal rotation speed of electrical generators (e.g., around 1500 rpm for 2 pole pairs). Increasing the number of (electro)magnetic pole pairs, applying a gearbox, or both can resolve this issue. Increasing the number of pole pairs increases the design complexity and hence costs [64], whereas a gearbox is bulky, increases losses, and, as compared to other WTG components, potentially prone to failures. The representation of the shaft in simulation studies depends on the specific use case, and ranges from disregarding shaft dynamics completely to adopting detailed multi-mass shaft representations for torsional oscillations [65].

Another significant design consideration is the choice of electrical generator and its connection scheme, determining whether the WTG operates at fixed rotor speed or variable rotor speed. From a power engineering point of view, the industry distinguishes between 4 main classes of wind turbines as shown in Figure 2.9. Type 1 and 2 are referred to as fixed speed while type 3 and 4 operate at variable shaft speed.

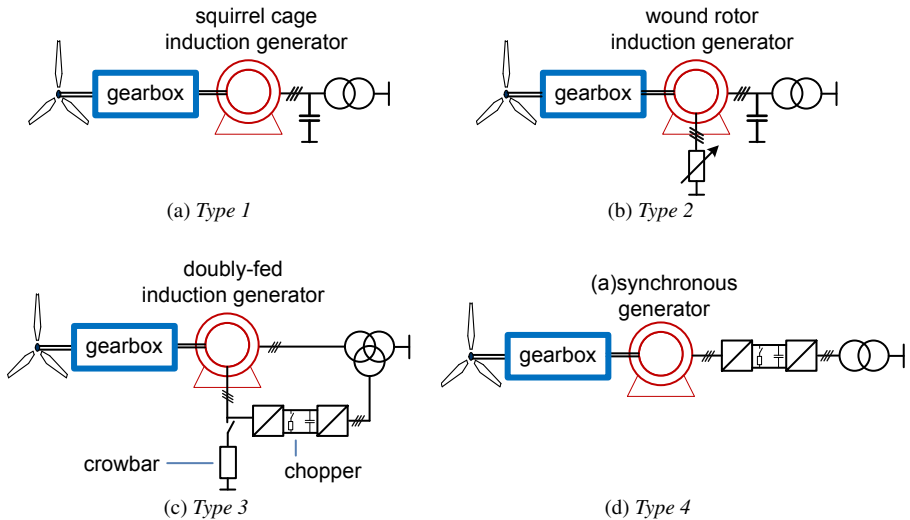


Figure 2.9: Common (electrical) types of wind turbine generators. (a): squirrel cage induction generator, operation at fixed rotor speed; (b): Wound-rotor induction generator with variable rotor resistance, nearly fixed speed; (c): Doubly-fed induction generator, variable speed; and (d): full-converter interfaced generator, operating at variable speed.

Type 1 - squirrel case induction generator (SCIG): Until the early 1990s the only WTG available. The application of an induction machine without slip rings implies a stiff coupling between the rotating stator field and the mechanical shaft (see also figure 2.9a). Power generation can hence only take place in a limited speed range, typically a few % above the nominal shaft speed n_s . From an aerodynamic point of view, no active blade angle adjustment was available at the time, and rotor blades were designed such that $C_p(\lambda)$ decreases at high wind speeds, automatically limiting the power output of the wind turbine (i.e., passive stall control). These considerations drastically impede the flexibility of the WTG to optimise the power extraction from the wind. Moreover, induction machines always draw reactive

power from the grid. Hence compensation devices, usually passive components, have to be installed at the PCC. Despite all these limitations, type 1 WTGs showed high fidelity rates and the did not require expensive power electronics to operate.

Type 2 - wound-rotor induction generator: The limited speed range and the related limited controllability of the operating conditions for type 1 WTGs can be partly mitigated by connecting variable resistors to the rotor circuit through slip rings. By controlling the rotor resistance, the linear region of the speed-torque characteristic of the induction generator could be widened. This characterises the type 2 WTG. Moreover, blade angle control (i.e., pitch control) was typically added to aerodynamically reduce the WTG output during high wind conditions.

Type 3 - doubly-fed induction generator (DFIG): A further extension to the application of wound-rotor induction machines is to excite the rotor circuit by an external voltage source (see figure 2.9c). The rotor circuit of such a double-fed induction generator is connected to the stator terminals through a back-to-back converter arrangement and a choke inductor or three winding transformer. The DC link itself is equipped with a chopper for overvoltage protection and a crowbar on the rotor side for overcurrent protection (the fault response of DFIGs will be discussed in section 2.4.1). The rotor-side converter acts as a variable frequency voltage source for the rotor circuit, operating at *slip frequency*, i.e.,

$$\omega_{\text{slip}} = \omega_s - \omega_R = s\omega_s \quad (2.15)$$

where

$$s = \frac{\omega_s - \omega_R}{\omega_s} \quad (2.16)$$

is the *slip* of the induction generator, and ω_s is the synchronous frequency. Using this setup, the angle and magnitude of the rotor currents are actively controlled; so is the rotor-side contribution to the air gap flux and eventually the developed electrical torque.

In steady state the active power distribution between the stator and rotor circuits depends on the slip, i.e.,

$$P_{\text{ag},s} = \frac{1}{(1-s)} P_{\text{shaft}} \quad (2.17)$$

$$P_{\text{ag},R} = \frac{s}{1-s} P_{\text{shaft}} = -sP_{\text{ag},s} \quad (2.18)$$

in which $P_{\text{ag},s}$ and $P_{\text{ag},R}$ are the stator and rotor side air gap power flows respectively. Controlling the electrical torque hence implicitly allows regulating the WTG shaft speed. A typical operating region for DFIG based WTGs is $-0.3 \leq s \leq 0.3$, which limits the rating of the rotor side converter to 30% of the rated WTG power, and thus reducing manufacturing costs.

Variable speed operation offers two main advantages. First, the WTG can operate continuously around the optimum tip speed ratio λ_{opt} , allowing a higher annual energy yield. Second, the WTG's shaft system is partially decoupled from the electrical grid, which operates at fixed frequency. Wind gusts and for instance shaft oscillations are handled and eventually damped by the control system of the rotor side converter and do not have an immediate effect on the turbine output power—in contrast with fixed speed WTGs.

There exist various methods for controlling DFIG based wind turbines [66,67], of which stator flux oriented vector control has become commonplace and is assumed for this thesis [68]. Akin to vector control of VSC-HVDC, one converter controls the active power, the rotor side converter, and one controls the direct voltage of the DC link, the grid side converter. The active power can be controlled through the rotor side converter because its d-q control reference frame is aligned with the air gap flux. The reactive power at the PCC can be controlled by both the rotor-side and grid-side converters [69].

Type 4 - full converter interfaced generator (FCG): The back-to-back concept used for the DFIG can also be applied to interface the entire electrical generator to the grid by power electronics. Various generator types and corresponding shaft setups exist; the overarching concept is referred to as type 4 or full converter generator (FCG, figure 2.9d), [70]. For the operation and construction of the WTG this has the following implications:

1. The converter completely decouples the mechanical rotation from the electrical frequency;
2. The number of magnetic poles in the stator circuit is high, potentially avoiding the need for a gearbox, leading to the *direct-drive* concept; and
3. The excitation of the rotor field by permanent magnets;

which are especially beneficial for offshore applications: owing to the absence of slip rings, brushes, and a staged drive train the WTG requires substantially less maintenance. The current flagships of various wind turbine manufacturers (see table 2.1) primarily apply the FCG concept using permanent-magnet synchronous machines. From the type 4 WTGs, only the Vestas V164-8.0 uses a gearbox in the drive train, whereas the others apply direct drive technology. From table 2.1 the Senvion 6.2M152 is the only WTG using the DFIG concept.

As indicated the back-to-back arrangement of FCGs is similar to DFIGs. The generator-side converter operates at variable frequency and has the duty to control the DC-side voltage and the stator voltage of the synchronous machine, whereas the grid-side converter accounts for the tracking the optimal power extraction based on the rotor frequency [71]. Alternatively the grid-side converter can control the DC voltage and the generator-side converter the optimal power point [72].

vendor	Siemens	GE	Vestas	Enercon	Senvion	Lagerwey
type	SWT-8.0-154	Haliade* 150-6MW	V164-8.0	E-126	6.2M152	L136-4.0
hub height	site-specific	100 m	site-specific	135 m	97–124 m	120 – 166 m
rotor diameter	154 m	150 m	164 m	127 m	152 m	136 m
rated power	8 MW	6 MW	8 MW	7.58 MW	6.15 MW	4 MW
offshore	yes	yes	yes	no	yes	no
WTG type	4	4	4	4	3	4
generator	PM-SG	PM-SG	PM-SG	PM-SG	DFIG	PM-SG
shaft	DD	DD	gearbox	DD	gearbox	DD

Table 2.1: *Indicative overview of multi-MW wind turbines and their main attributes. PM:permanent magnet, SM: synchronous machine, DD:direct drive (source: vendors' web-sites).*

Maximum power point tracking: Both the rotating inertia (machine, drive train, rotor blade) and the electrostatic capacitance in the DC link are used as energy storage elements to allow maximum power point tracking (MPPT). The principle of MPPT is illustrated in figure 2.10, which shows the per unit shaft speed versus power curves for various wind speeds. The WTG would draw wind power at optimal efficiency when following the dashed red line. Below the cut-in wind speed the power output is obviously zero; above nominal shaft speed or wind speed, the pitch regulator adjusts β to maintain the rated power output. This power curve is commonly adopted in variable speed WTGs (either as algebraic functions or as lookup tables [73, 74]), acting as a reference signal for the torque controllers. In contrast, fixed speed WTGs have a very limited ω_R range and are commonly designed for a limited spectrum of optimal wind speeds [75], depending on the gearbox construction.

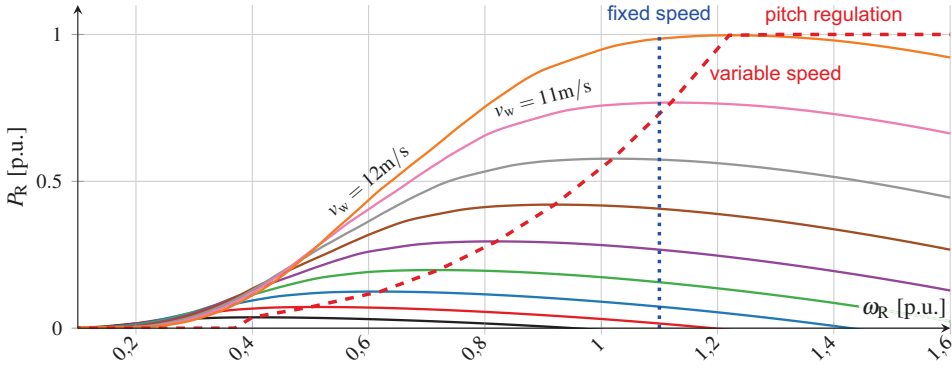


Figure 2.10: Per unit power versus shaft speed curve for wind speeds ranging from 4 m/s (solid, black) to 12 m/s (solid, orange), based on the $C_p(\lambda)$ of figure 2.8. The optimal ω_R - P_R characteristic crosses the optimal power extraction points per wind speed (dashed, red). The limited operating range of fixed speed WTGs is also illustrated (dotted, blue).

2.2.2 Wind Power Plants

Grid connection and grouping of WTGs

Wind turbines can be installed and operated alone or in clusters acting as one single generation entity, a wind power plant (WPP). Figure 2.11 shows the various connection options and the terminology commonly applied by legislative bodies and grid operators. The term WPP, which is used in this thesis, has recently been replaced by *power park module* (PPM) for harmonisation purposes. Offshore the only economical option is to cluster wind turbines owned and operated by one market party. Leaving some exceptions aside, clustering of WTGs is done by connecting the WTGs to a radial medium voltage AC *collection grid* by means of step-up transformers. The actual layout, e.g., cable routing, switchgear placement, and redundancy measures, is commonly subject to a complex optimisation procedure, which is outside the scope of this thesis. The collection grid terminates at an interface point at which the current is either transformed to a higher voltage and rectified (for a *DC connected PPM*) or transformed to a high voltage and connected to the onshore interface point by an AC submarine cable (i.e., for *offshore PPMs*). An interface point is a *connection point* in

case it acts as a boundary between asset owners according to connection agreements. The connection point is generally the location at which the WPP owner must comply to the grid code set out by the network operator. In the Netherlands, Germany, and the UK for instance, the network operator is responsible for the grid connection to the *offshore connection point*. In contrast, in the US the connection point would be onshore.

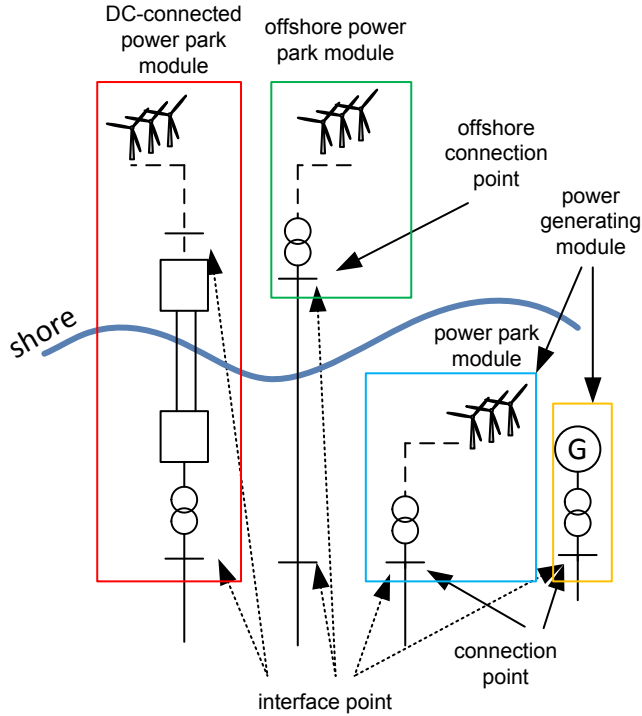


Figure 2.11: Overview of wind power plant connection options and common terminology.

Location of Coupling Point

The location of the PCC determines the electrical location at which the grid code is enforced by the TSO; some TSOs even have distinct onshore and offshore grid codes [76]. The location significantly impacts the manner in which the grouped set of WTGs must behave as a single WPP entity. That is, the functionality needed for the supervisory controls at park level (figure 2.7) and the need for compensation devices. Some of the onshore requirements (frequency control, low-voltage ride through, post-fault active power recovery) require control actions offshore. This also affects the required level of detail for modelling and simulation (discussed in section 2.4.2).

WPP aggregation applied in this thesis

The level of modelling complexity is predetermined by the interactions of interest. As indicated in the introduction of this thesis system-level interactions such as transient stability, frequency response, and load rejection use a quasi-stationary approach. Including each WTG

as a separate dynamic model is the most detailed solution but infeasible from a computational perspective. Therefore, for these type of studies the individual WTGs are usually being aggregated to equivalent models scaled to WPP-level. This approach relies on the following assumptions:

1. Favourable wind conditions exist across the WPP site (wake effect neglected, turbulences are smoothed out, wind gust model accounts for spatial dispersion of WTGs) [77],
2. the individual WTGs have a near equal operating point on the ω_R – P_R curves.
3. the collector grid can be represented by an equivalent impedance representing the losses [78]
4. The plant level controls have equal latencies for all connected WTGs.

For the transient-stability time-frame of interest (0.1–10 s) we assume the wind speed fixed, which implies that all WTGs work on the same point in the ω_R – P_R curve. In [77] it was shown that especially for large electrical disturbances this (assumption 2 above) is plausible.

2.2.3 Wind power as a primary source

Wind is abundantly available as a free and sustainable primary power source. The nature of wind is, however, variable and only to some degree predictable. Figure 2.12 shows graphs that are commonly used to characterise wind power and WTGs' output power. The variability is illustrated by figure 2.12. It shows hourly average wind speeds for the Gemini offshore wind park site, which is currently under construction 60 km north of Schiermonnikoog. The histogram of figure 2.12a gives insight in the distribution of the hourly wind speeds that appeared in 2007, clearly following the Weibull distribution that is natural to wind.

The wind duration curve of figure 2.12c shows the hourly wind speeds in decremental order. This gives us a valuable understanding into the total hours the wind speed is above a certain value. For the indicated v_w of 12 ms^{-1} and higher for instance, a typical rated wind speed value for WTGs, the number of full-load hours is 1900 (out of 8760 hours/year). Using the example power curve in figure 2.12d, which is derived from figure 2.10, the power output duration curve of the WTG can be calculated (i.e., figure 2.12e). Similar to the hourly duration curve, this figure shows the per unit power availability of the WTG in decremental order. Throughout the year 2007, the WTG would have operated for at least 2100 hours at 90% of its rated power, and 1900 hours at rated power. The total capacity factor of the WTG, being the ratio between the cumulative energy harvested divided by the cumulative energy that would have been harvested at full utilisation, is in this example 45%.

Despite the fact that above considerations are done using averaged wind speed time series with a resolution far beyond the dynamic simulations done for this thesis, they provide us with a general notion on which kind of wind speed to consider for transient stability studies. For that we need to take into account the following:

- transient and frequency stability issues are expected to crop up during high-wind conditions. The relative participation of converter interfaced generation in the power mix is then considered highest.

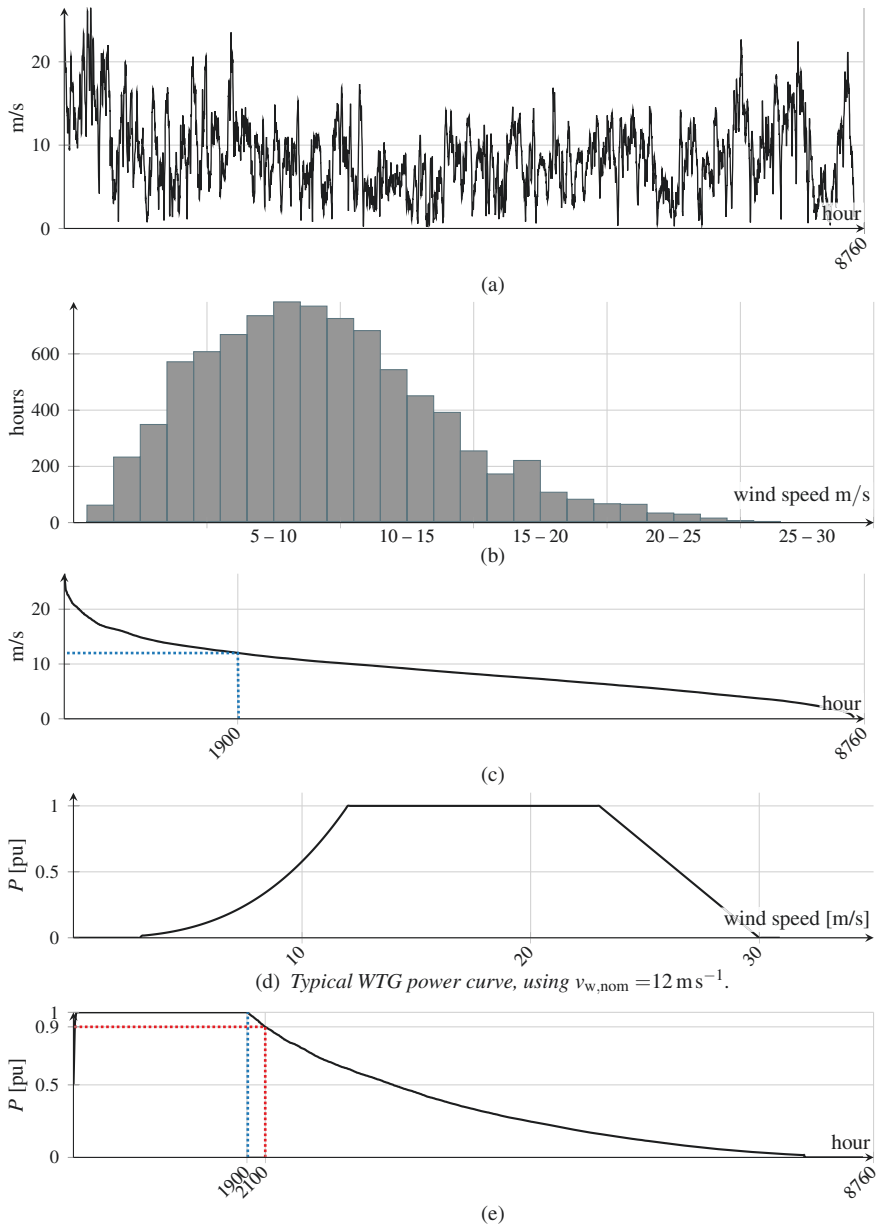


Figure 2.12: Wind characteristics for the Gemini offshore wind park location, 120 m above sea level based on re-analysis data (Data provided by Sander+Partner GmbH, Switzerland). a) Hourly wind speeds, b) Histogram of hourly wind speeds, c) wind duration curve, d) example WTG power curve, e) wind power output duration curve.

- low voltage ride-through of VSCs and WTGs are especially challenging during full or near-full utilisation.

Hence, the transient stability and fault-ride through analysis done in the following chapters

are especially relevant for high-wind conditions. Taking for instance 90% of the rated power as "high wind" would in the above analysis account for 24% of the annual operation. Likewise, taking 80% of the rated power would account for 27% of the time, etc. Keeping in mind that a particular operating point is only valid for certain wind conditions, we maintain a plausible trade-off between realism and worst case conditions for stability and FRT (i.e., full operation) by selecting a utilisation of the WPP of 90% and higher.

operation and control of Transnational Offshore Networks

2.3 Transnational Offshore Networks by VSC-MTDC

2.3.1 HVDC-side operation and control

The characteristics of VSC-HVDC are favourable for deploying multi-terminal networks: the AC-side power can be controlled by adjusting the terminal voltage, which on its turn is synthesised by forced commutation. This allows, by means of the direct voltage, the electrostatic energy inside the DC system to be applied as a control input variable. As a result the active power direction can be changed by altering the current direction without the prerequisite of reversing polarity, as is the case for LCCs.

The electrostatic energy in the HVDC part is stored in both the capacity distributed over the submarine cables and auxiliary capacitors installed at the DC side of the VSC (C_{dc} in figure 2.2). VSCs are subsequently connected in parallel amongst the HVDC network, using the direct voltage U_{dc} as a common measure for the energy balance across the HVDC side. From an operational viewpoint, this implies that AC/DC active power exchange can conveniently be regulated according to a $P_{dc} - U_{dc}$ characteristic, on the condition that a proper balancing mechanism is accounted for. To illustrate this control principle, we start with the application of such characteristics to a point-to-point link and project the implications to different VSC-HVDC network topologies afterwards.

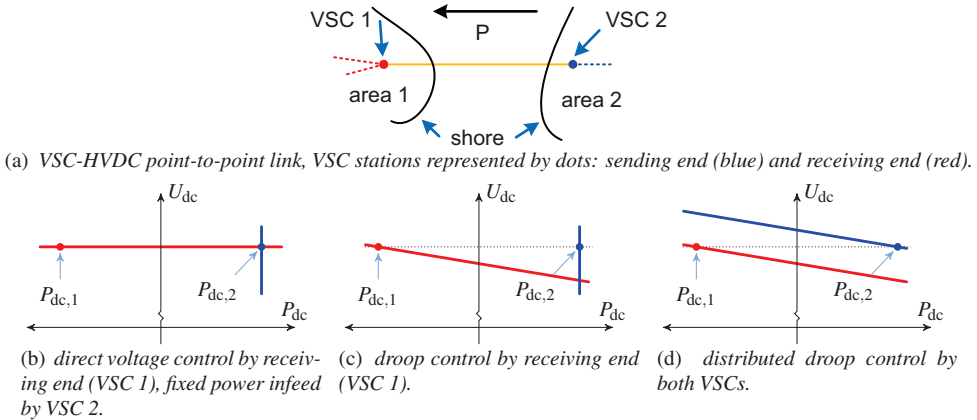


Figure 2.13: Elementary HVDC control principles.

Figure 2.13a shows a point-to-point VSC-HVDC link between two otherwise unconnected areas 1 and 2. The scheduled active power exchange (P) flows from VSC 2 to VSC 1, which are the sending and receiving ends respectively. For VSC 2, P_{dc} is positive, whereas P_{dc} is negative for VSC 1. Three elementary control methods exist for such a situation [79]:

- direct voltage control by the receiving end VSC (figure 2.13b)
- droop control by the receiving end VSC (figure 2.13c)
- distributed voltage control by both VSCs (figure 2.13d)

Direct voltage control implies that the receiving end VSC accounts for the balancing need in the HVDC system by maintaining a fixed U_{dc} . In steady state the VSC hence operates across a horizontal line in the $P_{dc} - U_{dc}$ diagram [80]. The sending end on its turn transfers power to the HVDC side regardless of U_{dc} (i.e., a vertical line in the $P_{dc} - U_{dc}$ diagram). This line can be shifted horizontally by the operator of area 2. Rigidly controlling the direct voltage is predominantly applied in situations where the power in-feed from the sending end is variable [81], whereas the direct voltage must be maintained within tight boundaries.

Droop control by the receiving end VSC, as shown in figure 2.13c, also ensures that power imbalances in the HVDC system are caught accordingly by VSC 1. Yet its steady state characteristic is a droop line: every active power in-feed level by VSC 2 results in a unique U_{dc} . VSC 2 hence determines the power whereas the droop characteristic of VSC 1 determines the common direct voltage.

A more general implementation of droop control can be seen in figure 2.13d, in which both sending and receiving end VSCs operate according to a steady-state droop characteristic. This potentially allows a very flexible way of active power management. Like primary and secondary frequency control in AC systems, in which the system frequency forms the key balance indicator, HVDC droop control allows several VSCs to share power imbalances such as fluctuating wind power, AC side frequency response [82], and load rejection / converter outages. After reaching a new steady direct voltage, the active power in-feed of each VSC can be managed by shifting its droop line up or downwards in the $P_{dc} - U_{dc}$ plane – very similar to the classical secondary control for AC systems [83]. The mathematical foundations and understanding of setting these characteristics on VSC and network level [84], embedding droop control into a centralised MTDC voltage controller [85, 86], and using these cascaded schemes to minimise for instance losses [87], have been subject of numerous research efforts over the past decade.

Depending on the operational requirements, the aforementioned elementary control methods can be combined to more generic $P_{dc} - U_{dc}$ diagrams [88]. For instance, the operator could offer direct voltage control between certain power boundaries, desire to set a fixed power exchange under specific circumstances, or to need to quickly switch between sending and/or receiving end operation. Such functionality is taken account of by the voltage margin method (VMM), which stems from the current margin method for LCC-HVDC and was first proposed for a back-to-back gate turn-off thyristor based HVDC link [89]. It relies on a voltage margin in the $P_{dc} - U_{dc}$ diagram, which allows the VSCs to operate in fixed power mode unless the voltage reaches a certain level and one of the VSCs turns to voltage control mode (See figure 2.14). This offers redundancy in case the voltage-controlling VSC fails. The applicability of the VMM for MTDC networks and WPP connections has been extensively analysed for several conditions and time-frames of interest [90, 91]. Although the VMM is still considered for MTDC, there is a wide consensus that the flexibility gained by the VMM often comes at the price of complex VSC-level controls and unfavourable direct voltage dynamics.

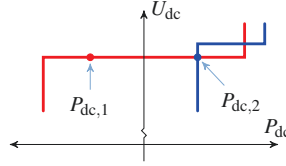


Figure 2.14: Voltage margin method by both VSCs.

2.3.2 Offshore Network Topology Options

The choice for a particular HVDC network topology determines to a large extent technical aspects such as the applicability of a certain active power management method, the implementation of grid code requirements, extendability, and protection requirements. Table 2.2 gives an overview of the features and particulars of each elementary type of HVDC network. Only the bottom two configurations are multi-terminal. From an operational viewpoint the main differences between the configurations are:

- a WPP can only deliver power to the HVDC part, so unidirectional infeed;
- the WPP power is variable in nature, so the power infeed $P_{dc,2}$ in say figure 2.13b is permanently shifting horizontally and cannot be set to a fixed value. Droop control can hence not be applied here.
- offshore loads such as oil platforms would have the same issue, but with reversed power direction.
- droop control (figure 2.13c) is applicable for all other implementations, but its true strengths (e.g., modularity of active power control, redundancy in control) are revealed for generic multi-terminal network topologies.
- the effectiveness of ancillary service provision, for instance for embedded HVDC, is partly determined by the AC network characteristics (e.g., coupling strength through the AC transmission system, inertia, grid strength at AC connections) [92–94]
- multi-infeed connections are potentially prone to interacting VSC controllers [95,96].
- later HVDC side grid extensions have to be compatible with the initial design, mainly the VSC power ratings and their controls [97,98].

As for wind power integration, fault ride-through, and impact on onshore system dynamics, some of the HVDC network topologies are more relevant than others. FRT is a challenge for every type of HVDC connection, but first and foremost when the power of one of the VSCs is uncontrollable (i.e., WPPs). The effect of FRT on the AC dynamics, the main operational focus of this thesis, is most stringently manifesting itself for 1) a point-to-point WPP connection, 2) three terminal VSC-HVDC, and 3) generic VSC-MTDC. Therefore, we will apply these three fundamental schemes for both the development of simulation techniques and for scrutinising the impact on transient stability.

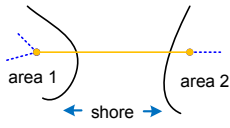
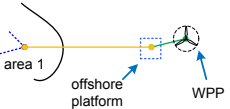

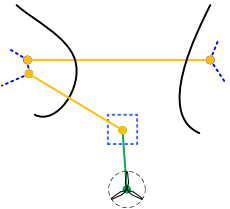
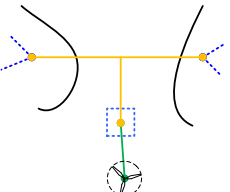
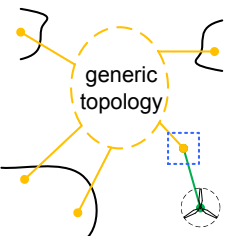
configuration	features	example applications
	point-to-point link <ul style="list-style-type: none"> • bi-directional power flow; • ancillary service provision at both sides. 	<ul style="list-style-type: none"> • COBRACable [99], • Estlink 1 [100], • East-West interconnector [101]
	WPP connection <ul style="list-style-type: none"> • unidirectional power flow 	Offshore WPPs in the North Sea region
	embedded VSC-HVDC <ul style="list-style-type: none"> • bi-directional power flow 	<ul style="list-style-type: none"> • INELFE [102], • ALEGrO [103], • France-Italy interconnector
	multi-infeed VSC-HVDC <ul style="list-style-type: none"> • bi-directional • unidirectional 	Planned grid extensions in Northern Germany
	3-terminal VSC-HVDC <ul style="list-style-type: none"> • interlinked WPP • extended WPP connection 	COBRACable extension [104]
	generic VSC-MTDC <ul style="list-style-type: none"> • multi-terminal, • various types of infeed 	<ul style="list-style-type: none"> • Zhoushan project [105], • North Sea: feasibility phase [24] • Dogger Bank Modular Island [25]

Table 2.2: Main properties and example applications of VSC-HVDC network topologies

2.4 Potential impacts of VSC-HVDC and Modelling Requirements

With transient stability being the main scope of this thesis, we aim at studying events having a large geographical impact with dynamics in the range of 0.1–10 s, see also figure 1.2. As mentioned, the characteristics of VSC-MTDC (controls, power electronic switching, protection) couple dynamics to transient stability effects. To define simulation and modelling

requirements that manifest this coupling, we will take the following approach. First the response of VSCs and WTGs to faults will be described, which provides an understanding of which controls and phenomena act in the transient stability frame of interest. In general, faults are considered the main inciters for which transient stability issues arise. TSOs aim to align plant behaviour with the power system phenomena, the requirements of which are set out in grid codes. The relevant requirements for this thesis are discussed in more detail below. Ultimately, the whole spectrum of device behaviour, their controls and grid code implementation puts forward the desired simulation and modelling requirements.

2.4.1 Fault Response of VSC-HVDC and WTGs

In this section we qualitatively discuss the response of various building blocks of the offshore transmission system connecting WPPs to the onshore power system, focusing on symmetrical AC short circuits. This is significant for further determining the simulation and modelling needs.

VSC-HVDC response to short circuits

Response of VSCs to ac faults Overcurrents occur predominantly in the event of short-circuits at either side of the VSC. For DC-side faults, the IGBTs are blocked and the VSC acts as a three-phase diode bridge. Although the freewheeling diodes are designed to withstand such fault currents, the VSC becomes completely uncontrollable and cannot support in interrupting the fault [106]. Full-bridge MMCs resolve this issue by completely disabling conduction mode of the submodule diodes [107]. For AC-side faults things are different. The IGBTs cannot withstand the fault current and need to be adequately protected. On valve level, IGBTs are swiftly blocked in case the forward current exceeds the rated current, thereby severely disrupting the voltage balance across the module capacitors (for MMC) or the overall direct voltage (for two-level VSCs). It is hence crucial to maintain controllability by implementing this forward current limit properly into the VSC-level controls.

Response of VSC-HVDC connected WPPs to onshore faults For normal operation the VSC acts as a voltage controlled current source. For voltage dips with a very low retained voltage the VSC fails to maintain its desired active power as the current set point violates the IGBT limit. For VSC-HVDC connected WPPs the offshore VSC uses direct control, and acts as a slack source for the collection grid, drawing all the power from the WTGs into the HVDC link. This influx does not halt at the moment of onshore fault ignition, creating a power imbalance in the HVDC link and hence overvoltages. The dominant time constant of the DC link voltage is defined by the equivalent parallel capacitance

$$C_{dc,eq} = C_{cable} + \sum_{i=0}^N C_{dc,i} \approx \frac{\tau_{dc}}{U_{dc,nom}^2} \sum_{i=0}^N S_{rated,i} \quad (2.19)$$

where i is the VSC index, N the amount of VSCs in the link, and S_{rated} the rated power of the VSC. C_{dc} is commonly designed to match $\tau_{dc} = 20$ ms [108], a trade-off between control bandwidth, and the technical and economical feasibility at nominal voltage. Subsequently, the overvoltages are not just severe, they also leave very little time to counter the imbalance. Conceptually, three methods exist to ride through an onshore fault, i.e.,

1. Drain away the excess energy by for instance the dynamic braking resistor discussed

in section 2.1.2;

2. reduce the power infeed by the offshore VSC by mirroring the onshore voltage to the offshore VSC;
3. reduce the power delivered by the wind turbines by WPP-level communication and/or frequency control.

The implementations of these concepts and their inclusion into the VSC and WTG models will be dealt with in more detail in section 3.3. Except when engaging the dynamic braking resistor the prefault power is not instantly available for active power recovery after fault clearance. The DC voltage must be re-established and the individual WTGs will change to a different operating point during the ride through measures. The fault response of the DC-connected power park module as well as its post-fault recovery act particularly in the transient stability time frame.

DFIG response to faults and rotor circuit protection

During faults in the collection grid or beyond, DFIGs behave similarly to normal asynchronous generators, and cause significant fault currents in the stator, and hence through the air gap coupling inside the rotor [75]. To protect the rotor side converter against such overcurrents yet remain connected to the grid, the WTG is assumed to have a semi-conductor interfaced small resistor (or pure star) connection installed in the rotor circuit, the *crowbar* [109]. It is engaged during voltage dips at the stator terminals, allowing an additional short-circuit path to flow for the rotor-side current. A similar circuit is usually installed in the DC link to resist DC overvoltages during external faults [110] (i.e., *chopper* in figure 2.9c).

FCG fault response

On WTG level, the full scale converter has to stand up to the same fault-ride through challenge as the VSC-HVDC links. Overvoltages occur when the power balance inside the back-to-back link cannot be preserved, mainly occurring during AC-side voltage dips. The DC link hence contains a chopper to drain away a surplus of electrostatic energy. Contrary to DFIGs however, where the fault current can be a multitude of the rated WTG current, the maximum fault current of FCGs is limited to the IGBT rating. This completely separates the generator-side dynamics from the grid-side behaviour both during normal and faulted operation, and substantially reduces the modelling needs for FRT behaviour [70].

2.4.2 Dynamic Behaviour of VSC-HVDC and Grid Code Requirements

Need for grid connection requirements

System operators generally want to prevent unforeseen interactions between existing and newly connected generator plants. To better understand this figure 2.15 illustrates a typical synchronous generator response after a 0.2 s voltage dip. During the fault, the generator has to bear significant stator overcurrents and it can only deliver a small proportion of the generator power to the grid. As a result the rotor shaft will accelerate. After fault clearance the network voltage oscillates back to pre-fault operating conditions. The amplitude of this

oscillation depends on several parameters such as the grid strength, dip duration, and generator design. In general the grid voltage follows a lower, worst-case boundary indicated by the dashed blue line. Underneath this bound the generator typically endures a pole slip or completely runs out of step. It is hence essential that during the recovery region no further power unbalances may occur in the system, active and reactive power alike.

VSCs and WTGs act on the power infeed at the grid interface, both directly (controls) and indirectly (limiting, protection) thus impacting the transient stability. Table 2.3 provides a non-exhaustive overview as to what extent stability aspects are influenced by the protection and control of WTGs and VSC-HVDC. The growing penetration of RES and converter interfaced generation in general thus dramatically changes the dynamic characteristics of the power system. The fault response of converters and conventional generators are dissimilar: the converters' overcurrent capabilities are more restrictive while voltage recovery can be almost instantaneous. However, especially the former can lead to disconnection during faults, potentially leading to cascaded disconnection of plants.

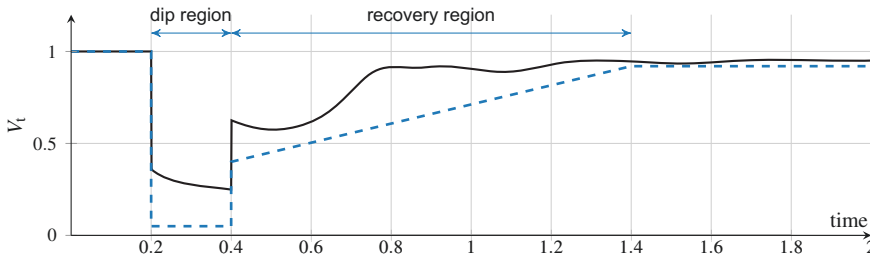


Figure 2.15: Typical synchronous generator fault response and the lower bound of the voltage amplitude (dashed, blue).

stability type	small signal	voltage	frequency	transient
FRT	—	—	++	++
MTDC control	++	+	+	++
I_{lim}	—	—	+	++
crowbar	—	—	+	++
post-FRT	+	+/-	+	++
V_{ac} control	+	++	—	+/-
aRCI	—	++	+	+

Table 2.3: Influence of a particular control mode on stability. —: very little influence, ++: very high impact, I_{lim} :overcurrent protection.

Grid Code Requirements Relevant to Transient Stability

To prevent undesired disconnections and cascaded system-level effects system operators devise grid codes, which stipulate for each particular operational aspect or grid-side event the demanded response, control response, bounds, etc. For transient stability the most important ones are 1) fault ride-through, 2) dynamic voltage support, and 3) active power recovery

of plants. Figure 2.16 shows typical characteristics power generating modules shall comply to at their point of common coupling. Over the past decade the overarching European TSO (ENTSO/e) succeeded to define a generic grid code for both DC connected WPPs and power generating modules (i.e., AC connected). These define such characteristics at meta-level while the respective system operator can fine tune these to their specific grid needs.

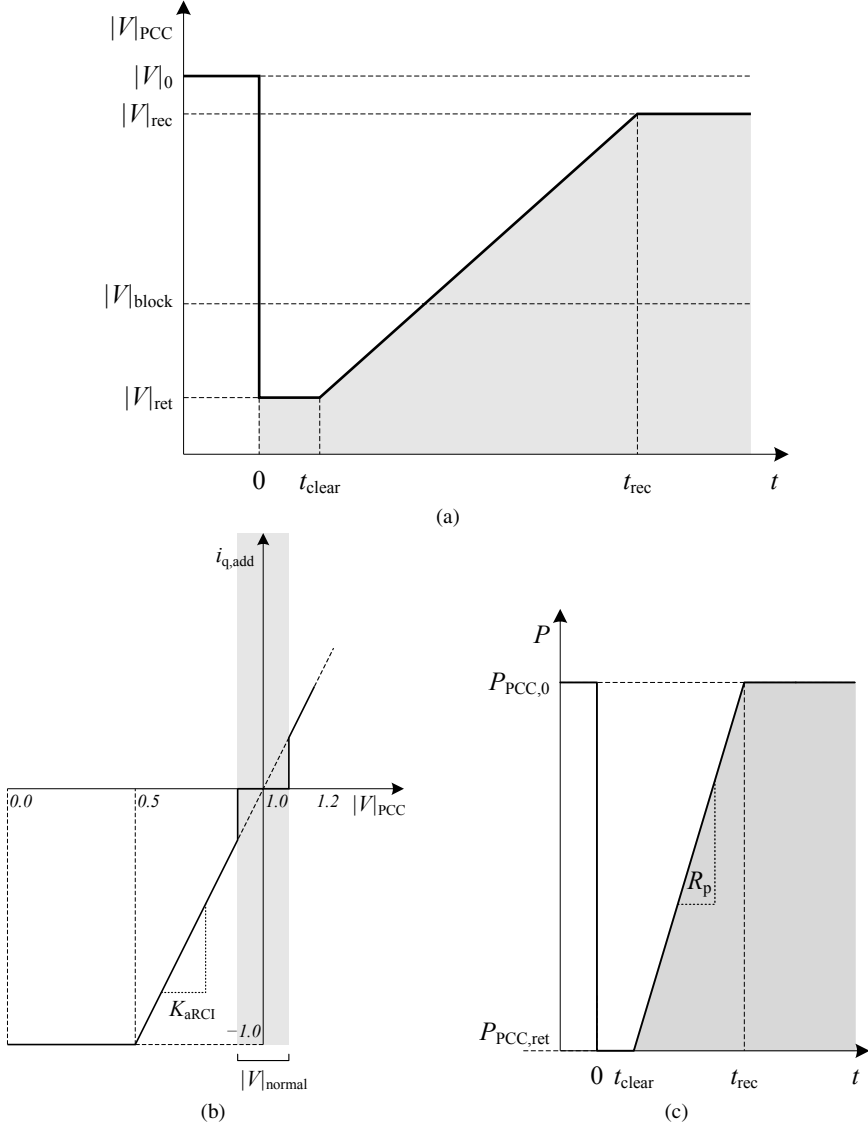


Figure 2.16: Grid code requirements most relevant to the transient stability problem. a) low-voltage ride-through, b) voltage dependent additional reactive current injection, c) post-fault active power recovery.

Fault ride-through (FRT): Figure 2.16a shows the time versus $|V|_{PCC}$ curve to which the power generating module must conform. As long as the terminal voltage keeps above

the solid line it must remain connected (taking $t = 0$ s as fault ignition instance). If the voltage enters the grey area the plant is allowed to disconnect. The curve commonly consist of two parts, one that resembles the deep dip region (i.e., from $t = 0$ s to t_{clear}) and one that encompasses the recovery region of figure 2.15 (i.e., t_{clear} to t_{rec}). TSOs have also the flexibility to define a voltage threshold under which the plant is allowed to suspend its power output (i.e. $|V|_{\text{block}}$) or temporarily disconnect during the recovery phase (not shown).

Additional Reactive Current Injection (aRCI): The basic philosophy behind aRCI is to provide reactive power thus boosting the voltage level at the PCC, and potentially preventing the own and neighbouring power generating modules from disconnecting from the grid (i.e., entering the grey area in figure 2.16a) [111, 112]. We include aRCI according to the characteristic shown in figure 2.16b. It shows the reactive current ($i_{q,\text{add}}$) that is added to the prefault reactive current setpoint. The controller only acts outside the dead band indicated by the grey surface, and $i_{q,\text{add}}$ is inversely proportional to the voltage dip depth by a factor K_{aRCI} . The use and boundary conditions of aRCI still is an ongoing research topic [113, 114], the applications and implementations differ per system operator, and no high-level requirements are defined by ENTSO/e at the moment.

Post-fault Recovery Rate: A swift post-fault restoration of the balance between generation and load is vital for the transient and frequency stability of the power system. From this viewpoint, power generation modules shall hence restore their power output as quickly as possible, at least before the automatic generation controls of conventional plants take measures. As for VSC-HVDC links and WTG during FRT operation, these have to resolve the internal active power balance between the sending and receiving ends. Such severe conditions involve the activation of pitch or stall control of WTGs and non-linear overvoltage protection. After fault clearance, the prefault power may hence not be immediately available.

In order to manage these clashing characteristics often minimum active power recovery rates are demanded by the system operators [115]. This is shown in figure 2.16c, which states the maximum time allowed (i.e., t_{rec}) to restore at least a substantial proportion of the active power output of the plant. In this thesis this requirement is implemented by a minimum ramping rate (i.e., R_p) in the active power part of the vector controller.

2.4.3 Modelling and Simulation Needs

In section 2.4.1 we discussed how WTGs and VSCs respond to short circuits and how various control modes that accomplish grid code compliance interact with the power system, mainly in the transient stability region. The time-scales of control modes and their potential impact provide the modeling needs for simulation. Taking table 2.3 as a starting point the modelling needs for transient stability assessment are as follows:

rotor angle response: needed for adequate transient stability analysis. The critical clearing times of the main generators must be calculable as well as the correct topological representation of the AC transmission system are of huge importance. The dynamics of excitation and governing systems shall be adequately represented, at least for the appropriate time frame (≈ 5 s). Generators can be modelled in a simplified manner as long as the electromechanical interactions are represented correctly (typically 5th order Parkian models). WPPs can be represented aggregatedly as discussed in section 2.2.2. VSCs need to model their active and reactive power regulator dynamics.

three-phase AC faults: main initiators for transient stability issues and severe rotor angle

control/mode	time-scale	simulation needs
rotor angle response	0.1–10 s	stability-type
3-phase faults	1 ms–5 s	stability-type
FRT of VSCs	0.1 ms–1 s	EMT and stability-type
MTDC control	1 ms–5 s	EMT and stability-type
current limiting	1 ms–5 s	stability-type
active power recovery	0.1–5 s	stability-type
AC voltage control	0.1–10 s	stability-type
aRCI	1 ms–2 s	stability-type

Table 2.4: *Simulation needs for the control modes and network phenomena relevant to transient stability.*

deviations. The geographical impact is large and hence affects the interaction of many devices and components. If the focus of the study is system-level, generators can be represented as discussed for the rotor angle response. The DC to AC interaction of VSC-HVDC links must be properly included. An averaged converter grid interface is a common assumption, especially when the DC voltage remains in its normal operating region there is no need to include the power electronic topology into the grid interface model. Type 3 WTGs can be represented by a reduced order model but the crowbar behaviour must still be exhibited [68, 116].

fault ride-through of VSC-HVDC: the implementation of the FRT capability needs at least the DC overvoltage protection to be adequately modelled, which in turn needs an electromagnetic transient representation of the DC-side equipment.

MTDC control: stipulates the DC-side interaction between VSCs, and hence the propagation of dynamics from one AC system to the other. The dynamics and the absolute value of the direct voltage must be included. Depending on the control method the voltage response (and hence the MTDC network) can be modelled aggregatedly [117, 118].

current limiting: The current limit of the individual IGBT valves cannot possibly be represented due to the involved calculation complexity. We hence assume that the current limiter inside the vector controller can fulfil this duty. This limiter acts on the outputs of the active and reactive power controllers.

active power recovery: operates in the transient stability and frequency stability time-frame of interest. For vector controllers the minimum recovery time is implemented as a rate limiter in the active power controller, which is only engaged at fault clearance.

AC voltage control: maintains the voltage or reactive power at the point of common coupling and has a dominant effect during non-FRT operation. Commonly represented by either PI controllers or predefined $V - Q$ setpoints.

additional reactive current injection (aRCI): operates in the transient and voltage stability time-frame of interest, based on the implementation. The implementation as a proportional controller is modelled inside the reactive power regulator of the VSCs and WTGs.

The above-mentioned modelling ingredients need to be implemented into a dynamic simulation paradigm that suits the specific needs of the research. For this thesis we considered the options EMT or stability-type simulations. Table 2.4 depicts the time-scale range based

on the modelling needs and the corresponding simulation requirements. It turns out that especially in case the HVDC system is part of the model the grid needs to be modelled by electromagnetic transients, culminating into the need for an EMT-type simulation to properly address the rotor angle response for hybrid AC-HVDC systems. EMT simulations are however unsuitable for studying large-scale transmission systems. In the following chapters we will define the VSC-HVDC and WTG models that are needed to scrutinise this clash of simulation accuracy and efficiency requirements.

Chapter 3

Modelling of VSC-HVDC and Wind Power Plants

Following the operational aspects of VSC-HVDC and WPPs described previously, this chapter deals with the modelling and control of VSC-HVDC and WTGs necessary for time-domain simulations. Using models from literature we will set out the implementation of grid code requirements by attaching a fault ride-through controller on top of the control system for normal operating conditions ¹. The chapter will approach the modeling and control from a DC-connected power park module angle; system-wide aspects and stability modelling are treated from Chapter 4 onward.

3.1 VSC-HVDC representation and control

3.1.1 Model Assumptions and Grid Interface

As discussed in section 2.1.2, generally two types of VSC topologies can be distinguished at transmission voltage: The two-level type and (modular) multilevel type converters. Both have their own characteristics with respect to modulation techniques, filtering requirements, converter protection, and control approach. The presented model for system studies is based on the following assumptions.

AC harmonic generation: In this VSC model, the PWM switching frequency is assumed to be infinitely high, i.e., the reference voltage dictated by the VSC control scheme is immediately conveyed to the VSC terminals. This enables representation of the VSC by a three-phase voltage source that generates fundamental-frequency sinusoidal voltages only. A reasonable assumption for (large-scale) power system integration studies, which usually consider balanced three-phase circuits.

Operating region PWM enables a very flexible manner of synthesising the AC-side voltage to control the current through the VSC interface inductor and/or transformer. The current limit of the VSC and the direct voltage constitute the operating region as discussed in section 2.1.3 and shown in figure 2.5b. We assume the direct voltage to exceed the AC-side voltage setpoint indefinitely, and can hence safely disregard the diode behaviour of the AC/DC grid

¹the material of this chapter is based on [AC , Z , AA]

interface model.

DC side grid connection: At the DC terminals, the VSC is assumed to be connected to two submarine cables (symmetrical monopole). Moreover, relatively large capacitors are installed in parallel to the VSC at the DC terminals, which is considered essential for the DC-side operation of the VSC. In practise, the direct voltage is influenced by the switching behaviour of the converter, causing switching harmonics on top of the DC voltage. Meanwhile the control scheme maintains the direct voltage, regulates the AC-side power exchange, or works as a rigid AC voltage source. In either case, the VSC exhibits current source behaviour at the DC-side. As no converter valves need to be modelled under aforementioned assumptions, the energy exchange between AC and DC is provided by the active power balance between AC and DC, modelled by a current injection at the DC terminals, see figure 3.2.

converter protection: Contrary to electrical machines, which still shape the power system of today, VSCs have very strict over-current constraints. As related in section 2.4.1 the current limit is enforced on component level (IGBT), converter level (current setpoint limiting), and on meta-level by the network operator (power setpoints may not exceed VSC rating). As IGBT valves are not modelled individually in this thesis, the overcurrent limit is modelled at control level.

AC side grid connection: The control strategy, particularly vector control, requires the connection of a considerably large inductor in series with the AC terminals of the VSC. This enables the VSC to generate an angular difference between the grid voltage and the terminal voltage. This inductance may be either the step-up transformer, a phase reactor, or both. As the VSC model generates a balanced set of three phase voltages, no zero-sequence currents are assumed to flow through the VSC star point. Therefore, a series inductance is assumed to adequately represent the interface of the VSC with the grid.

As compared to figure 2.5a, above considerations allow a couple of simplifications in the representation of the VSC, i.e., filtering equipment can be disregarded, the grid interface can be modelled by time-varying sources, and the current limit can be adopted upstream in the control system. This leads to the grid representation shown in figure 3.1, the structure and notation of which will be used for the model description discussed in the remainder of this section.

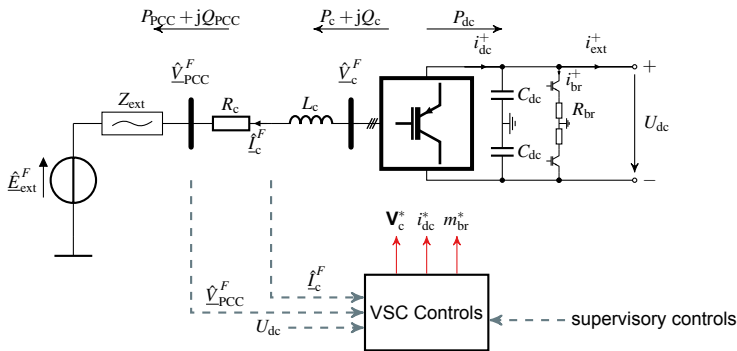


Figure 3.1: Single-phase equivalent of VSC grid interface and the used notation of network quantities.

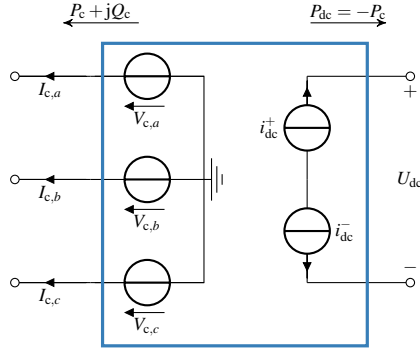


Figure 3.2: The equivalent source representation of the voltage sourced converter.

3.1.2 Vector Control

As discussed in sec 2.1.3, mainly two control principles exist for VSCs, vector control and direct control, mainly dependent on the type of grid connection. In both cases the grid interface can be assumed equal. The main advantage of vector control is the controllability of the VSC's power output. Active and reactive power can be controlled independently, which eventually allows the implementation of numerous control strategies, ranging from terminal voltage control to, for instance, frequency/inertia emulation.

The vector control method is based on a cascaded control structure consisting of fast inner controllers, which synchronise with the grid and control the ac current, and relatively slow outer controllers, which control active and reactive power and/or the terminal voltage. The described models are adjusted versions of the models presented in [119] and [120]. The general structure applied for this thesis is depicted in figure 3.3. It roughly comprises three parts:

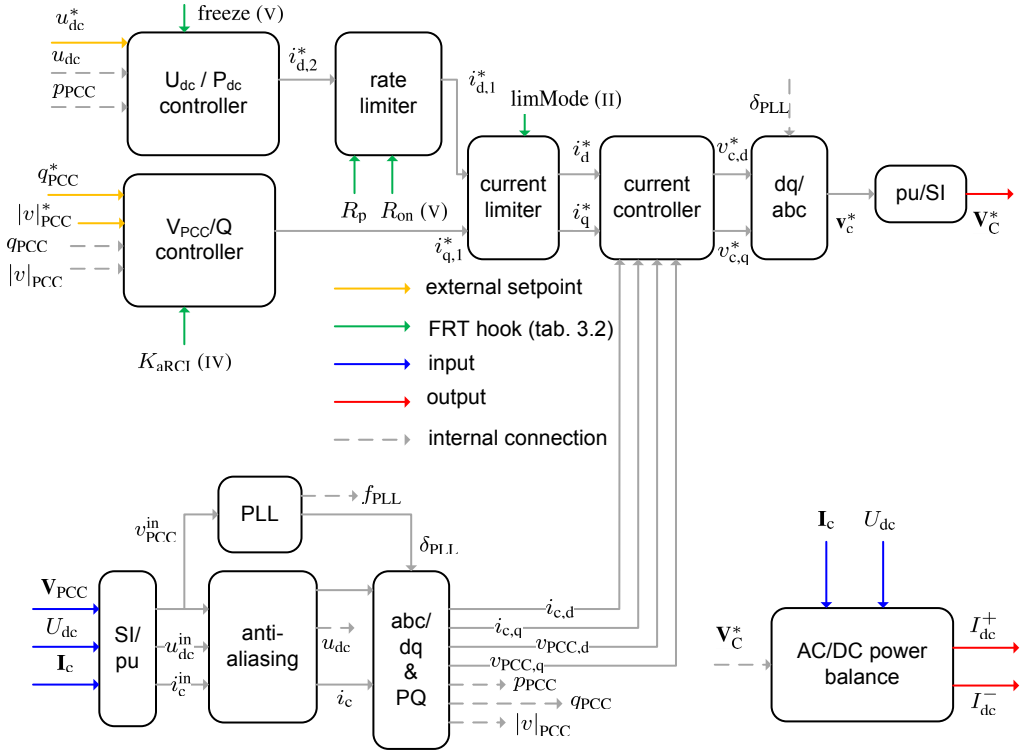
1. a measurement part that accounts for per unit transformations, filtering, and synchronisation with the terminal voltage through a PLL (bottom left).
2. the power balance model that emulates the coupling between the AC and DC sides of the VSC (bottom right)
3. a cascaded control scheme that forms the core of the vector controller (top).

3.1.3 Per Unit System

The VSC controls are implemented in the $d - q$ reference frame and are designed and tuned according to the per unit system of the VSC. The order in which the measurement and transformation blocks in figure 3.3 can be arbitrary – e.g., interchanging the PLL with the per unit transformation does not have influence on the overall dynamic characteristics. Yet it is most natural to synchronise the VSC reference system against the measured point-on-wave values of PCC voltage and then performing additional transformations.

The per unit system adopted in this thesis serves to the following functionality needs:

- 1 pu current and voltage correspond to rated current and voltage respectively.



- 1 pu power implies operation at rated power.

The former two are particularly desirable for implementing the operating limits of the VSC. If we let

$$V_{\text{VSC,base}} = \frac{\sqrt{2}}{\sqrt{3}} V_{\text{nom,LL}} \quad (3.1)$$

and

$$I_{\text{VSC,base}} = \frac{2}{3} \frac{S_{\text{VSC,rated}}}{V_{\text{VSC,base}}} \quad (3.2)$$

The $\alpha - \beta$ transformation yields

$$\begin{aligned} \hat{v}_{\text{PCC}}^F &= \frac{\hat{V}_{\text{PCC}}^F}{V_{\text{VSC,base}}} = \frac{\hat{V}_{\text{PCC}} e^{j(\omega t + \phi_{\text{PCC}})}}{\frac{\sqrt{2}}{\sqrt{3}} V_{\text{nom,LL}}} \\ &= \frac{\sqrt{2} |V_{\text{PCC}}|}{\sqrt{2} V_{\text{nom,LL}}} e^{j(\omega t + \phi_{\text{PCC}})} \end{aligned} \quad (3.3)$$

which has unity magnitude at nominal voltage. Similarly for the AC terminal current holds

$$\begin{aligned}
\hat{i}_c^F &= \frac{\hat{i}_c^F}{I_{VSC,base}} = \frac{\sqrt{2} \frac{|S|_c}{\sqrt{3}V_{c,LL}}}{\frac{S_{VSC,rated}}{\sqrt{3}V_{nom,Ln}}} e^{j(\omega t + \varphi_c)} \\
&= \frac{|S|_c V_{nom,Ln}}{S_{VSC,rated} |V|_{c,Ln}} e^{j(\omega t + \varphi_c)}
\end{aligned} \tag{3.4}$$

which has amplitude 1 in case the modulated voltage magnitude equals the nominal voltage and the converter operates at rated power. From (3.3) and (3.4) follows $S_{VSC,base} = 2/3 S_{VSC,rated}$.

As for the DC quantities of the VSC, it is desirable to let the rated DC voltage coincide with 1 pu voltage in the VSC control system. Hence $U_{dc,base} = U_{dc,rated}$, the rated voltage of the entire HVDC system.

3.1.4 Phase-Locked Loop Model

As mentioned before, vector control enables independent control of active and reactive power at the PCC. This control feature is a result of the synchronisation method provided by the phase-locked loop, which synchronises a rotating $d-q$ reference frame with the voltage measured at the PCC. We will first describe the grid interface by space vectors and then derive the corresponding PLL implementation. Consider a symmetrical and balanced (i.e., $v_a + v_b + v_c = 0$) set of sinusoidal, fundamental frequency three-phase voltages,

$$\mathbf{V} = \begin{bmatrix} v_a \\ v_b \\ v_c \end{bmatrix} = \hat{v} \begin{bmatrix} \cos(\omega_s t + \phi) \\ \cos(\omega_s t + \phi - \frac{2\pi}{3}) \\ \cos(\omega_s t + \phi + \frac{2\pi}{3}) \end{bmatrix} \tag{3.5}$$

with \mathbf{V} the vector of instantaneous values of the phase voltages v , \hat{v} their peak value, ω_s the instantaneous value of the external system frequency in rad/s, and ϕ the phase angle of the concerned voltages in rad. Generally speaking, ω_s may vary in time due to, for instance, disturbances. Therefore, (3.5) can be written as

$$\mathbf{V} = \hat{v} \begin{bmatrix} \cos(\theta_s + \phi_v) \\ \cos(\theta_s + \phi_v - \frac{2\pi}{3}) \\ \cos(\theta_s + \phi_v + \frac{2\pi}{3}) \end{bmatrix} \tag{3.6}$$

with

$$\theta_s = \int_0^t \omega_s dt \tag{3.7}$$

and $\hat{v} = V\sqrt{2}$

Above assumptions are reasonable for stability studies, in which the power system is usually represented by its single line equivalent and therefore only positive sequence quantities are of interest. As a result we can write one of the phase voltages as a function of

the other two, i.e. $v_a = -(v_b + v_c)$, enabling the representation of a balanced set of three phase voltages by an equivalent two-axis system, with axis α and β [120, 121]. This is often referred to as the *space vector representation* of \mathbf{V} , $\underline{\hat{v}}^F$, defined by

$$\begin{aligned}\underline{\hat{v}}^F &= v_\alpha + jv_\beta = \frac{2}{3} \left(v_a + v_b e^{\frac{j2\pi}{3}} + v_c e^{-\frac{j2\pi}{3}} \right) \\ &= \hat{v} e^{j(\theta_s + \phi_v)}\end{aligned}\quad (3.8)$$

or, in matrix notation

$$\underline{\hat{v}}^F = \begin{bmatrix} v_\alpha \\ v_\beta \end{bmatrix} = \begin{bmatrix} \hat{v} \cos(\theta_s + \phi_v) \\ \hat{v} \sin(\theta_s + \phi_v) \end{bmatrix}\quad (3.9)$$

$\underline{\hat{v}}^F$ can be interpreted as a vector rotating in the counterclockwise direction with respect to the stationary reference frame at angular speed ω_s . A commonly used transformation is the d-q transformation. Here, $\underline{\hat{v}}^F$ is rotated in the clockwise direction by

$$\begin{aligned}\underline{\hat{v}}^C &= \underline{T}^{F \rightarrow C} \underline{\hat{v}}^F = \underline{\hat{v}}^F e^{-j\theta_s} \\ &= \hat{v} e^{j\phi_v} = v_d + jv_q\end{aligned}\quad (3.10)$$

where $\underline{\hat{v}}^C$ is stationary in the d - q reference frame. In the stationary, α - β reference frame, the grid quantities around the VSC terminals are related by

$$L_c \frac{d\underline{\hat{i}}_c^F}{dt} = \underline{\hat{v}}_c^F - \underline{\hat{v}}_{PCC}^F - \underline{\hat{i}}_c^F R_c \quad (3.11)$$

in which v , i , R , and L are all in the VSC per unit system. The apparent power delivered by the VSC at the PCC is now given by

$$\begin{aligned}\underline{\hat{s}}_{PCC} &= \underline{\hat{v}}_{PCC}^F \underline{\hat{i}}_c^{F,*} \\ &= \underline{\hat{v}}_{PCC}^C \underline{\hat{i}}_c^{C,*} \\ &= (v_{PCC,d} + jv_{PCC,q})(i_{c,d} - ji_{c,q})\end{aligned}\quad (3.12)$$

with for the active power

$$\begin{aligned}p_{PCC} &= \Re \left\{ \underline{\hat{v}}_{PCC}^C \underline{\hat{i}}_c^{C,*} \right\} \\ &= (v_{PCC,d} i_{c,d} + v_{PCC,q} i_{c,q})\end{aligned}\quad (3.13)$$

and for the reactive power

$$\begin{aligned}q_{PCC} &= \Im \left\{ \underline{\hat{v}}_{PCC}^C \underline{\hat{i}}_c^{C,*} \right\} \\ &= (-v_{PCC,d} i_{c,q} + v_{PCC,q} i_{c,d})\end{aligned}\quad (3.14)$$

According to (3.12), the calculated power does not depend on θ_s (because of the complex

conjugate term) and hence the relation holds for an arbitrary rotation angle. Vector controlled devices use this property extensively. For VSCs the reference angle is regulated such that $v_{PCC,d} = \hat{v}_{PCC}^F$. Consequently, (3.13) and (3.14) reduce to

$$\begin{cases} p_{PCC} = v_{PCC,d} i_{c,d} \\ q_{PCC} = -v_{PCC,d} i_{c,q} \end{cases} \quad (3.15)$$

so active and reactive power can be controlled independently by regulating $i_{c,d}$ and $i_{c,q}$, provided that $v_q = 0$. This entails that the d - q reference frame must continuously be aligned with \hat{v}_{PCC}^F . This can be achieved by a phase-locked loop (PLL). A PLL tracks the terminal voltage by controlling an internal oscillator that produces an artificial space vector

$$\begin{aligned} \hat{w}^s &= w_\alpha + jw_\beta \\ &= \hat{w} (\cos \delta_{PLL} + j \sin \delta_{PLL}) \end{aligned} \quad (3.16)$$

where

- \hat{w} the per unit amplitude of the rated system phase-to-ground voltage
- δ_{PLL} the reference angle calculated by the PLL control scheme

The duty of the PLL is to control δ_{PLL} in such a way that the \hat{w}^F overlaps \hat{v}^F in the stationary reference frame. To obtain this, the angle between these two rotating vectors is approximated by calculating the cross product $\mathbf{w}^F \times \mathbf{v}^F$ by

$$\begin{aligned} \mathbf{w}^F \times \mathbf{v}^F &= \begin{vmatrix} 1 & 1 & 1 \\ w_\alpha & w_\beta & 0 \\ v_{PCC,\alpha} & v_{PCC,\beta} & 0 \end{vmatrix} = \mathbf{k} (w_\alpha v_{PCC,\beta} - v_{PCC,\alpha} w_\beta) \\ &= \hat{w} \hat{v}_{PCC} \sin \Delta \gamma_{PLL} \end{aligned} \quad (3.17)$$

where $\Delta \gamma_{PLL}$ is the angular difference between $\delta_v = \theta_s + \phi_{PLL}(0)$ and δ_{PLL}

For small phase angle deviations yields $\sin \Delta \gamma_{PLL} \approx \Delta \gamma_{PLL}$. This enables calculation of the error signal directly from the cross-product given in (3.17). The overall control scheme, also referred to as the d - q - z type PLL [122], is shown in figure 3.4.

When the PLL is locked ($\delta_{PLL} \approx \theta_s + \phi_{PLL}(0)$), a measured change in the phase angle is in fact the integrated change in system frequency, i.e., $\Delta \gamma_{PLL} = \frac{1}{s} \Delta \omega_s$. Taking variation in the measured frequency $\Delta \omega_{PLL}$ as output and $\Delta \omega_s$ as input, the response of the PLL is given by

$$\frac{\Delta \omega_{PLL}}{\Delta \omega} = \frac{G(s)}{s + G(s)} \quad (3.18)$$

with s the Laplace operator and $G_p(s)$ the transfer function of the tracking controller. A commonly used bandwidth is $\alpha_{PLL} = 25 \text{ rad s}^{-1}$ [123, 124]. If, as a first approach, $G_p(s) = k_{p,PLL}$ is chosen, this results in $k_{p,PLL} = 25$. figure 3.5 shows the response to the PLL that tracks a 50 Hz voltage source. Despite a correct tracking of the system frequency, we can observe

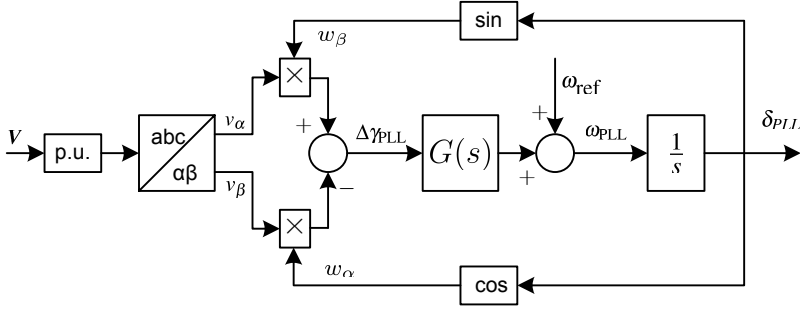


Figure 3.4: d - q - z type phase locked loop as implemented in the VSC model

that a relatively large steady state control error remains. This is awkward for the entire control structure of the VSC, as the d -axis of the converter reference frame must be aligned with the point of common coupling voltage. Therefore, $G_p(s)$ must contain an integrative part as well (i.e. $G_p(s) = K_{p,PLL} + \frac{1}{\tau_{i,PLL}s}$). figure 3.6 shows the response of the PLL to the same event, now with $\tau_{i,PLL} = 400$.

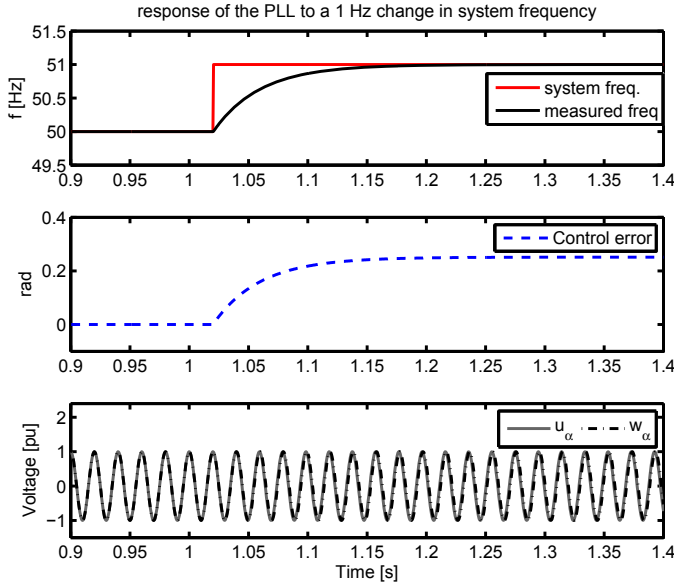


Figure 3.5: Response of the PLL to a 1 Hz change in system frequency.

3.1.5 Inner Current Controller

Once phase locked, the VSC can independently control active and reactive power by tracking $i_{c,d}$ and $i_{c,q}$. This is achieved by controlling the converter voltage output \hat{v}_c^C . In this way, the VSC behaves as a current controlled voltage source. In the converter's d - q reference frame, the converter reactor's current dynamics are given by

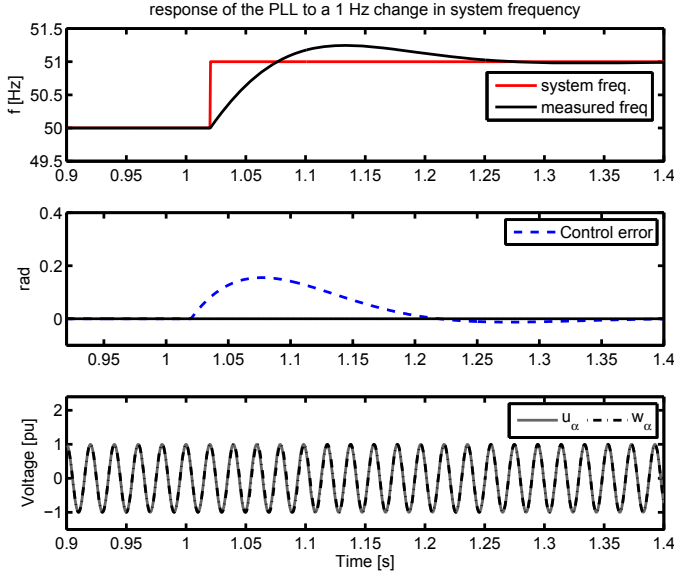


Figure 3.6: response of the PI controlled PLL to a 1 Hz change in system frequency.

$$L_c \frac{d\hat{i}_c^C}{dt} = \hat{v}_c^C - \hat{v}_{PCC,c}^C - R\hat{i}_c^C - j\omega_{PLL}L_c\hat{i}_c^C \quad (3.19)$$

where

- ω_{PLL} is the frequency (in rads^{-1}) at the PCC, measured by the PLL as described previously;
- L_c is the inductance of the phase reactor in perunit;
- $\hat{v}_c^C = v_{c,d} + jv_{c,q}$ is the output voltage of the VSC.

The model assumes an idealised representation of the modulation scheme (infinite switching frequency, sufficiently high U_{DC}). This is mainly expressed by the fact that the VSC voltage \mathbf{v}_c follows the reference value given by the controller (\mathbf{v}_c^*) without any delay or distortion, i.e.,

$$\hat{v}_c^F = (v_{c,d}^* + jv_{c,q}^*) e^{j\delta_{PLL}} \quad (3.20)$$

in space vector notation. The rightmost term of (3.19) introduces a mutual coupling between the d axis and the q axis. Therefore, the multi-variable system to be controlled has a mutual dependency between the control variables. Instead of treating it as an input disturbance, this issue can be dealt with by including this cross coupling as a feed-forward term \hat{x}_c^C , which leads us to

$$\hat{x}_c^C = \hat{v}_c^C - j\omega_{PLL}L_c\hat{i}_c^C \quad (3.21)$$

By substitution of (3.21) into (3.19) two mutually independent systems are obtained

$$L_c \frac{d\hat{i}_c^C}{dt} = \hat{x}^C - \hat{v}_{PCC}^C - R_c \hat{i}_c^C \quad (3.22)$$

That is, the converter current can now be tracked by controlling \hat{x}^C , and thus \hat{v}_c^C . Therefore, \hat{x}^C is selected as

$$\hat{x}^C = G_i(s) \left(\hat{i}_c^{C,ref} - \hat{i}_c^C \right) + H_{lp}(s) \hat{v}_{PCC}^C + R_c \hat{i}_c^C \quad (3.23)$$

where

- $G_i(s) = k_i + \frac{1}{\tau_i s}$ the transfer function of a proportional-integral controller;
- H_{lp} the transfer function of a low-pass filter, i.e., $H_{lp}(s) = \frac{\alpha_p}{s + \alpha_p}$; and
- $\hat{i}_c^{C,ref}$ are the reference values for the active and reactive currents, $i_{c,d}^*$ and $i_{c,q}^*$ respectively.

The VSC output voltage reference is then given by

$$\hat{v}_c^{C,ref} = G_c(s) \left(\hat{i}_c^{C,ref} - \hat{i}_c^C \right) + H_{lp}(s) \hat{v}_{PCC}^C + j\omega_{PLL} L_c \hat{i}_c^C + R_c \hat{i}_c^C \quad (3.24)$$

By substituting (3.23) into (3.22) and assuming $R_c \ll \omega_{PLL} L_c$ we obtain an expression for the closed loop behaviour of the inner current controller

$$\hat{i}_c^C = \frac{G_c(s)}{L_c s + G_c(s)} \hat{i}_c^{C,ref} + \frac{s}{(L_c s + G_c(s)) (s + \alpha_p)} \hat{v}_{PCC}^C \quad (3.25)$$

with α_p the bandwidth of the low-pass filter $H_{lp}(s)$. From (3.25), it can be concluded that \hat{i}_c^C follows its reference with zero steady state error, even when $G_c(s)$ represents a proportional controller. Moreover, the right term of (3.25) has zero gain for steady state, which means that the PCC voltage has no influence on the converter current in steady state. Feedforwarding this voltage is not a strict necessity – its absence can be accounted for by properly initialising the integrator term in $G(s)$. Variations in \hat{v}_{PCC}^C can instead be treated as an input disturbance for $G_c(s)$.

The parameters of the inner current controller were chosen heuristically such that the rise time of the inner current controller is around 1.5 ms.

3.1.6 Current Limiter and Rate Limiter

In this VSC model, the converter current is limited by the control scheme. This is achieved by monitoring the actual converter current set points that have been set by the outer controllers, and then comparing it to the converter current rating, denoted in pu by $|i|_{c,lim}$. If the amplitude of the current set point, $|\hat{i}_{c,1}|^{ref} = \sqrt{i_{d,1}^{*2} + i_{q,1}^{*2}}$ exceeds the rated converter current, the reference value can be altered in generally three ways: reactive current priority, active current priority, and proportional current limiting. These are depicted in figure 3.7 and summarised below.

Reactive current priority: The q-axis reference receives priority above the active current reference value (figure 3.7a). The main reasoning behind this is that injecting reactive power

boosts the voltage at the VSC terminals. As the current limit is predominantly reached during faults, it giving $i_{d,1}^*$ precedence potentially keeps the VSC and nearby plants out of the grey region of the $t - |V|_{PCC}$ diagram (i.e., figure 2.16a) thus remaining grid-connected.

Active current priority: The d-axis reference gets precedence above the reactive part of the current (figure 3.7b). This is mainly applied in cases where availability of active power is key. This is for instance when the VSC fulfils a crucial role in the DC voltage control, or when not delivering active power is severely penalised—even temporarily.

Proportional current limiting: Here, the limiting duty is equally shared between the active and reactive part of the current reference (figure 3.7c).

Engaging the current limiter not only leads to discontinuities in the response of the overall control scheme, it also makes it futile to perform linearised approaches. Moreover, the current references are outputs of the outer controllers in the cascaded scheme, which commonly contain integrators. Careful anti-windup limiting is therefore significant for the response, notably during faults.

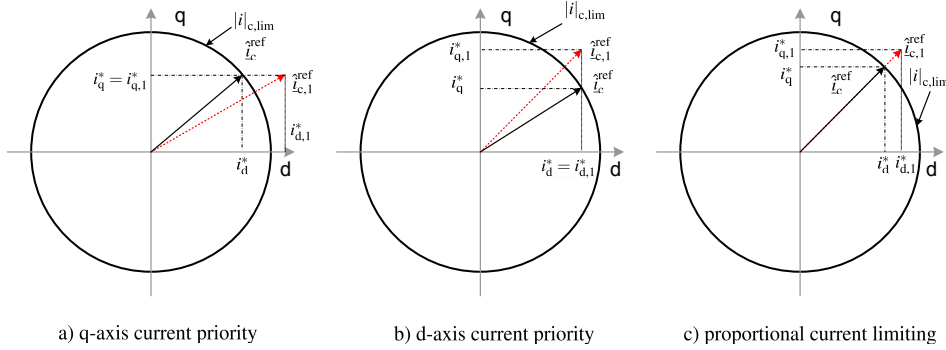


Figure 3.7: Converter limiting strategies applied to the VSC model of figure 3.3

In addition, the model assumes a rate limiter in the d-axis part of the controller only (i.e., for active power recovery requirements). It is supposed to engage during the recovery phase after fault clearance (i.e., $R_{on} = 1$). The active power output of the VSC must be restored with a minimum recovery rate R_p . The block diagram as applied for EMT modelling is shown in figure 3.8, which is equal to the implementation inside Simulink [125]. When $R_{on} = 1$, the R_p is set to ∞ and the rate limiter block is virtually bypassed. In order to calculate the differential of $i_{d,1}^*$ the implementation of the rate limiter needs the value of the simulation time step-size Δt . Though it was not encountered in this work, this can become a potential issue in case this value cannot be obtained by means of the simulation API.

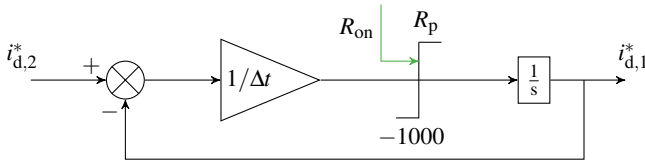


Figure 3.8: Block diagram of the d-axis rate limiter. Subscripts 2 and 1 refer to the outputs of the outer controller and rate limiter respectively.

3.1.7 Outer Controllers

The current set points (i.e., $i_{c,d}^*$ and $i_{c,q}^*$) are provided by the outer control loops, which indirectly control active power exchanged between the AC and DC network, and the reactive power delivered at the VSC terminals.

The actual implementation and settings of the controllers very much depend on the characteristics of the DC network, the strength of the ac network, and auxiliary control strategies required by for instance the TSOs.

Active current controller

The active current controller can have various implementations, ranging from direct voltage control to frequency support and inertia emulation. We will focus on the implementation of the direct voltage (droop) controller. The direct voltage is closely related to active power exchanged with the AC grid. Assuming a lossless converter, the pole to neutral direct voltage is maintained by the relation

$$\begin{aligned} \frac{C_{dc}}{2} \frac{dU_{dc}}{dt} &= i_{dc}^+ - i_{ext}^+ \\ &= \frac{P_{VSC,n}}{U_{dc}} - \sum_{n=1}^{m,n \neq k} \frac{P^{k \rightarrow n} + P_{loss}^{k \rightarrow n}}{\Delta U_{dc}^{k \rightarrow n}} \end{aligned} \quad (3.26)$$

where

- C_{dc} is the (per pole) ancillary capacitance at the DC side in F;
- U_{dc} is the bipolar direct voltage in V;
- i_{dc}^+ is the positive-pole direct current injected into the part by the model in A as per the active power balance between AC and DC side;
- i_{ext}^+ is the positive-pole current flowing into the DC network;
- m is the number of VSCs connected to the (multi-terminal) DC system;
- k is the converter of interest;
- $P^{k \rightarrow n}$ is the active power transported from VSC k to VSC n in MW;
- $P_{loss}^{k \rightarrow n}$ are the resistive series losses in the DC cables between VSC k and n in MW; and
- $\Delta U_{dc}^{k \rightarrow n}$ is the voltage drop between VSC k and n in V.

The active power transfer can thus be controlled by tracking the direct voltage to a reference value (e.g., $P_{DC,1}$ in figure 2.13b). In the presented model this is achieved by setting $i_{d,2}^*$ by a proportional integral controller according to

$$\begin{aligned} i_{d,2}^* &= G_{dc}(s) (u_{dc}^* - u_{dc}) \\ &= \left(k_{dc} + \frac{1}{\tau_{dc}s} \right) (u_{dc}^* - u_{dc}) \end{aligned} \quad (3.27)$$

In a similar fashion the active power (e.g., $P_{DC,2}$ in figure 2.13b) can be controlled by tracking target values of P_{dc} or P_{PCC} . Direct voltage droop control, as shown in figure 2.13d, has a slightly different structure as it is often part of a cascaded control system, the outer parts of which fall under the umbrella of the energy management system. The strategy is to imitate the primary and secondary control of AC systems, in which the direct voltage takes the role of frequency, and the individual VSCs operate on a droop line. In line with figure 2.13d, the implementation of the droop control on VSC level is shown in figure 3.9. If the direct voltage changes, the VSC shall take its (proportional) share in restoring the DC side power balance. The resulting error is then controlled by a PI controller similar to (3.27). P_{dc}^* and u_{dc}^* are in this configuration typically set by external supervisory controllers, which shift the droop line in either direction. The droop constant D is given in per unit but should comply to the droop designed at DC grid level. Setting this droop and optimising the voltage reference levels (i.e., location of the droop line) falls outside the scope of this thesis.

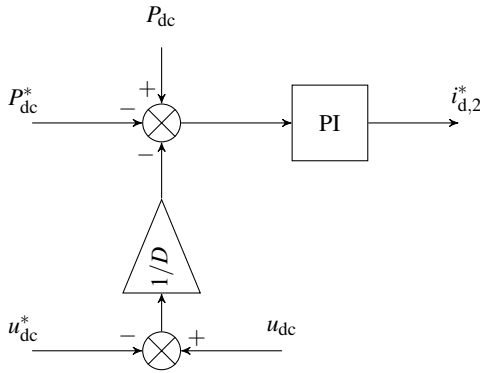


Figure 3.9: Block diagram of the droop controller at VSC level

Reactive current control loop

When the VSC is phase locked, the delivery of reactive power is provided by the relation

$$Q_{PCC} = -v_{PCC,d} i_{c,q} = -|\hat{v}|_{PCC} i_{c,q} \quad (3.28)$$

That is, increasing the q -axis current delivered by the converter results in reducing the reactive power exchanged with the grid. When designing a controller that tracks a certain reactive power set point, this issue has to be taken into account by an additional minus sign. In this thesis a continuous proportional-integral controller is employed

$$\begin{aligned} i_{q,1}^* &= -G_q(s) (Q^* - Q_{PCC}) \\ &= -\left(k_q + \frac{1}{\tau_q s}\right) (Q^* - Q_{PCC}) + K_{aRCI} \left(|\hat{v}|_{PCC}^* - \sqrt{v_{PCC,d}^2 + v_{PCC,q}^2}\right) \end{aligned} \quad (3.29)$$

where k_q and τ_q are the proportional gain and integrator time constants of $G_q(s)$ respectively, and Q is the per-unit reactive power delivered to the external grid at the PCC. k_{aRCI} is the additional reactive current injection gain that is set by the FRT controller discussed in section

3.3.2. The gain is 0 during normal operation and it is assumed that aRCI is always based on the voltage dip depth (i.e., not on the reactive power error).

Alternatively, the reactive current controller can control the PCC voltage. This can be achieved by rearranging (3.28) to

$$v_{\text{PCC},d} \approx |\hat{v}|_{\text{PCC}} = -\frac{Q_{\text{PCC}}}{i_{c,q}} \quad (3.30)$$

which implies that positive reactive power would boost the terminal voltage whereas negative reactive power suppress the voltage. This is in line with what can be expected from the sign convention chosen in figure 3.3. In this model, the PCC voltage can be controlled by

$$\begin{aligned} i_{c,q}^* &= G_v(s) \left(|\hat{v}|_{\text{PCC}}^* - \sqrt{v_{\text{PCC},d}^2 + v_{\text{PCC},q}^2} \right) \\ &= \left(k_v + k_{\text{aRCI}} + \frac{1}{\tau_v s} \right) \left(|\hat{v}|_{\text{PCC}}^* - \sqrt{v_{\text{PCC},d}^2 + v_{\text{PCC},q}^2} \right) \end{aligned} \quad (3.31)$$

in which k_v and τ_v are the proportional gain and integrator time constants. As with the reactive power controller, k_{aRCI} is set only during FRT conditions.

As mentioned, all control loops are equipped with anti-windup limiters in order to comply with the current limiter block. It must be noted that the selection of the control parameters hugely depend on the strength of the connected grid, the required bandwidth of the downstream controllers, and the control strategy required by the grid code. The parameters of the continuous voltage controller have been picked in such a way that a rise time of approximately 100 ms was achieved.

3.1.8 Direct Control

A prerequisite for vector control is the existence of a relatively strong AC grid such as the European mainland transmission system. Therefore, the control method for offshore applications is different. The control system can not depend on the synchronisation loops, as the VSC itself has a huge impact on the terminal voltage. In this thesis we apply direct control as shown in figure 3.10. Like vector control we can distinguish three main parts: the measurement blocks (bottom left), the voltage and angle control blocks (top), and the active power balance model (bottom right).

The PLL has been replaced by a simple oscillator that allows the transformation of the control set points to the stationary reference frame. The frequency controller dictates a fixed terminal voltage angle ϕ_c^* . During FRT operation however, this controller is triggered to quickly increase the angle, and thereby the voltage frequency. The voltage controller has the same structure as the one implemented in the vector control scheme. During FRT operation, however, this controller behaves differently. It will then use the direct voltage as an input to decrease and control the voltage amplitude and thereby limit the active power infeed into the HVDC system.

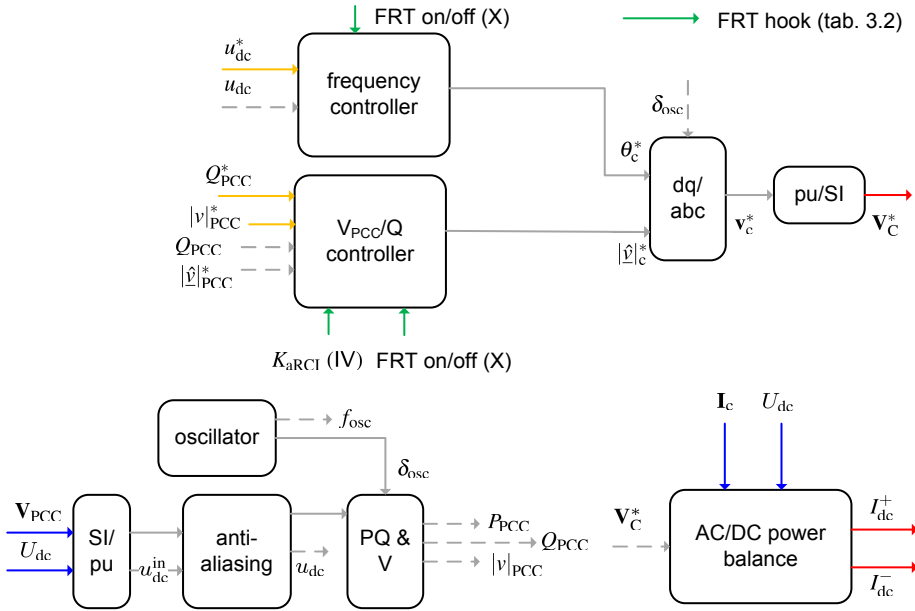


Figure 3.10: Direct control scheme of the averaged VSC as implemented in this thesis.

3.1.9 Power balance model

The AC/DC power balance controller is equal for both the vector and the direct control scheme. Its duty is to set the DC side current infeed according to the current measured at the AC terminals, the terminal voltage setpoints, and the present value of the direct voltage. The active power at the AC terminals of the VSC is given by

$$P_c = V_{c,a}^* I_{c,a} + V_{c,b}^* I_{c,b} + V_{c,c}^* I_{c,c} \quad (3.32)$$

where V^* and I are the modulated phase voltages and line currents respectively. The losses depend on the type of valves and their arrangement inside the VSC, the data of which is often not publicly available. Therefore, we assume a lossless converter. The power delivered to the DC-side must equal the power drawn from the AC side, i.e., $P_{dc} = -P_c$. As the voltage of the DC poles is known from the network model we can subsequently write for the DC side current injections

$$I_{dc}^+ = I_{dc}^- = \frac{P_{dc}/2}{U_{dc}/2} = -\frac{P_c}{U_{dc}} \quad (3.33)$$

assuming a symmetrical distribution of the power and voltage across both DC poles.

3.2 Wind Turbine Generator Model

As discussed in section 2.2.1 the vast majority of the currently installed wind generation fleet is of type 3 or 4. These WTGs come with a partially or fully rated converter to interface with the grid. In this section we present a type 4 WTG model that simplifies the dynamic

behaviour such that

- it accurately implements the dynamics that are most prominent for stability studies
- it applies averaged modelling for the grid interface
- it allows studying FRT for offshore applications

Type 4 WTGs have a back-to-back converter interface between the stator and the connected network. Owing to the excellent controllability of these converters, (fast) transients that occur at the generator side are not conveyed to the network side of the converter [71]. This allows us to represent the full converter generator (FCG) by a three phase voltage source for EMT-type simulation or a positive-sequence current source in TS simulations, both dictated through vector control. The description of the model is based on an RMS-type interface to the grid. It has however been implemented in both EMT-type environments (PSS[®]NETOMAC, Matlab/Simulink) and stability-type simulations (PSS[®]NETOMAC).

3.2.1 Input-Output Representation

The presented model is a quasi-steady state representation of a FCG. Akin to the two-level VSC model it is valid under the following assumptions:

- The network can be represented by a balanced set of three-phase voltages and currents. These voltages and currents do only contain a fundamental frequency component, i.e. no harmonics are present. Under these assumptions, only positive-sequence currents and voltages exist and network and machine elements can be represented by their single-phase equivalent. Therefore, a complex-phasor representation of voltages and currents can be used.
- No saturation occurs in the WTGs or their interfacing transformers
- The PWM controllers operate in their linear region.
- The DC-link voltage inside the FCGs remains constant. Inclusion of the DC link and its corresponding protection mechanism into the model is explained in .
- The blades are regulated by an active pitch controller. Active-stall and passive-stall control are not considered.
- The d - q reference frame is continually aligned with the terminal voltage amplitude. Under this assumption, no phase-locked loop has to be included into the model.

The overall scheme of the WTG model is shown in figure 3.11.

3.2.2 WTG Network Interface

The WTG is interfaced with the network through a variable current source. This interface can be subdivided into three parts:

Measured network quantities and phasor rotation: the terminal voltage and delivered apparent power of the previous time step or iteration are used as an input for the WTG model. This is realised by aligning the d -axis with the terminal voltage phasor \underline{V}_n . This

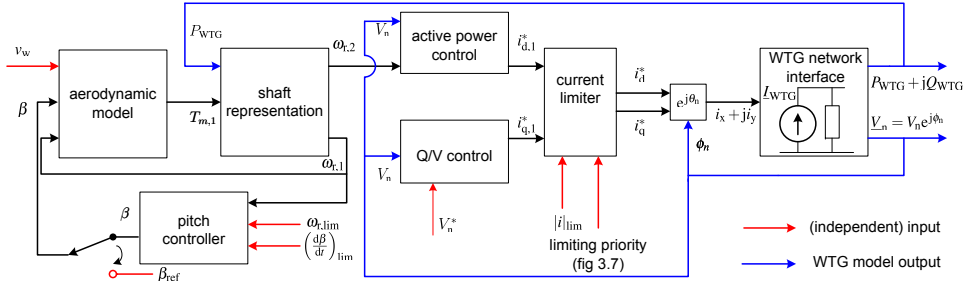


Figure 3.11: Input-Output representation of the WTG model.

constitutes the frame of reference for the internal controllers, which is shown in figure 3.12. The active power output is then defined as $P_{WTG} = v_d i_d$.

Calculate output quantities and backward phasor rotation: The output of the WTG controllers are $i_{d,1}^*$ and $i_{q,1}^*$. Under the assumption that the d - q reference frame is continually aligned with the terminal voltage phasor, these quantities can be rotated counterclockwise by an angle θ_n to provide $I_{WTG} = I_x + jI_y$.

Network solution: The current injection I_{WTG} is actually based on input quantities obtained from the previous time step or iteration. Without an appropriate iterative procedure, this leads to numerical oscillations, specially during short circuits. This can be solved by including a first-order delay on both input and output of the WTG control system.

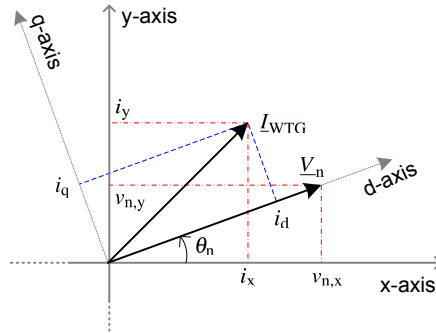


Figure 3.12: Complex phasor representation of the WTG terminal-quantities.

3.2.3 Aerodynamic Model

The aerodynamic representation of the wind turbine is based on normalised quasi-stationary C_p - λ - β -curves discussed in section 2.2.1, applying β , v_w , and ω_r as inputs, and providing the shaft torque $T_{m,1}$ as output.

3.2.4 Shaft Representation

The shaft of the wind turbine can either be modelled by a stiff-shaft model (also: single-mass model) or a two-mass model. A stiff-shaft representation links the mechanic circuit to the electric circuit by the swing equation

$$\frac{d\omega_{R,1}}{dt} = \frac{T_{m,1} - T_e}{2H} = \frac{T_{m,1} - \frac{P_R}{\omega_s}}{2H} \quad (3.34)$$

where $T_{m,1}$ the per unit mechanical shaft torque provided by the aerodynamic model, ω_s the per-unit grid frequency and H the combined inertia constant of the turbine blades and the shaft in s. The two-mass model links the electric part of the WTG model with the mechanic part by a flexible shaft representation. This model treats the rotor blades and the shaft as two separate inertias. The dynamic behaviour can be described by

$$\frac{d\omega_{R,1}}{dt} = \frac{T_{m,1} - K_s \gamma}{2H_r} \quad (3.35)$$

$$\frac{d\omega_{R,2}}{dt} = \frac{K_s \gamma - T_e}{2H_m} \quad (3.36)$$

$$\frac{d\gamma}{dt} = 2\pi f_s (\omega_{R,1} - \omega_{R,2}) - D_\gamma \gamma \quad (3.37)$$

with $\omega_{R,1}$ the per-unit rotational speed of the rotor-blades, $T_{m,1}$ the per-unit mechanical torque acting on the shaft by the rotor blades, K_s the stiffness constant of the shaft in $^\circ/\text{s}$, γ the angular displacement of the shaft in $^\circ$, H_r the inertia constant of the rotor blades in s, $\omega_{R,2}$ the per-unit rotational speed of the generator side of the shaft, T_e the per-unit electric counter torque, H_m the shaft inertia constant in s, and D_γ the damping constant of the shaft oscillations in s^{-1} .

In order to achieve an oscillation frequency of 1.67 Hz with a damping time constant of 2.5 s [74, 126], the following parameters have been chosen

$$H_r = 0.5 \text{ s}$$

$$H_m = 2.5 \text{ s}$$

$$K_s = 0.4 \text{ deg}^{-1}$$

$$D_\gamma = 0.0025 \text{ s}^{-1}$$

Both shaft representations have their advantages and disadvantages. For instance, the two-mass model introduces an additional active power output swing when the WTG is subjected to a network disturbance. On one hand, this is more realistic since the blades are flexible. On the other hand, controls can well suppress these oscillations and therefore, a single-mass equivalent commonly suffices, even for stability studies [127]. The equivalent inertia constant H can be calculated from the two-mass model by

$$H = H_r + H_m \quad (3.38)$$

3.2.5 Pitch Controller

The pitch controller adjusts the angle of attack of the rotor blades in such a way that the mechanical torque can be controlled. This can be done by the pitch regulator, which is either a hydraulic mechanism, engaged induction motors, or a servomechanism. In this WTG model, the pitch controller increases the pitch angle in case the rotor speed exceeds a

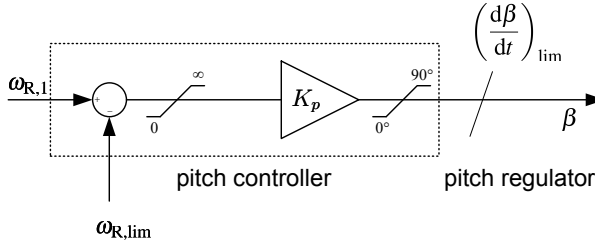


Figure 3.13: The pitch controller and regulator through a servo mechanism.

threshold value $\omega_{R,lim}$. The general structure is provided in figure 3.13. $\left(\frac{d\beta}{dr}\right)_{lim}$ and $\omega_{R,lim}$ can be used as input variables. Initially, these equal $\left(\frac{d\beta}{dr}\right)_{lim} = \pm 8 \text{ deg/s}$ and $\omega_{R,lim} = 1.2 \text{ pu}$ [128]. For wind power curtailment, the pitch controller may be used as well. This can be done by changing from ordinary local pitch regulation to external pitch regulation [129]. This is shown in figure 3.11 as β_{ref} .

3.2.6 Active-Power Controller (d-axis Controller)

Under the assumption that the direct voltage of the DC-link inside the WTG remains constant, the wind power can instantly be delivered from the stator-side converter to the grid-side converter. In some wind turbines, the active power setpoint is provided by maximum power point tracking or a lookup table [77]. In this WTG model, the active power output setpoint is laid down by an active-power setpoint curve, which is shown in figure 3.14. The power curve contains five sections:

I: For $\omega_{R,2} < 0.4$, the active-power setpoint P_{WTG}^* equals 0 as $\omega_{R,2}$ is below the operating range of the WTG and hence wind energy cannot be extracted efficiently.

II: For $0.40 \geq \omega_{R,2} < 0.41$ the output power setpoint increases proportionally from 0 to 0.05 per unit.

III: For $0.41 \geq \omega_{R,2} < 1$ the output power setpoint is proportional to $\omega_{R,2}^3$, which is in line with (2.10).

IV: For $1 \geq \omega_{R,2} < 1.01$ the power setpoint proportionally increases from 0.73 per unit to 1 per unit. This (steep) part of the power curve is intended to prevent unstable behaviour between the transition from stage III to stage V as well as to limit thrust forces on the rotor.

V: For $\omega_{R,2} \geq 1.01$, the power setpoint is set equal to 1 per unit. When this power cannot be delivered, $\omega_{R,2}$ automatically decreases and the control system returns to stage IV.

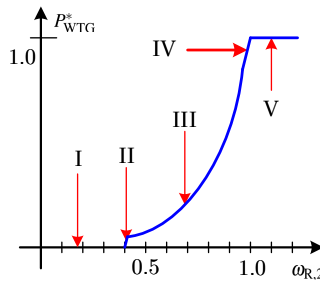


Figure 3.14: Active-power setpoint curve based on maximum power point tracking.

3.2.7 Voltage-Amplitude Controller (q-axis controller)

The terminal voltage amplitude is controlled by a proportional-integral controller similar to the vector controller of the VSC. For the q-axis current setpoint holds

$$i_q^* = K_v (V_n^* - V_n) + \frac{1}{\tau_v} \int (V_n^* - V_n) dt + V_n(0) \quad (3.39)$$

It should be noted that inside a wind park, especially offshore, many devices try to control either reactive power or voltage amplitude [130, 131]. Eq. (3.39) can easily be changed to obtain reactive power control instead. In case the park controller controls the reactive power output, the q-axis controller only consists of a feed-forward term

$$i_q^* = -\frac{Q^*}{V_n} \quad (3.40)$$

in which Q^* is sent by the wind park controller through a communication link. Q^* is not an entirely independent variable since it is constrained by physical limits and grid-code requirements. We assume the individual WTGs to operate at unity power factor, i.e., $Q^* = 0$.

3.3 Fault Ride-Through of VSC-HVDC Connected Offshore Wind Parks

Riding through onshore grid faults poses a major challenge to the design of the VSC-HVDC connection [132]. During a severe voltage dip in the AC network, the power that the grid-side VSC (GSVSC) can deliver will suddenly decrease. Since the power generated by the WTGs is still being rectified by the wind park side VSC (WPVSC), the direct voltage will quickly rise to an unacceptably high level. Therefore, active power generated by the wind power plant must be decreased within a very short time interval, approximately 20 ms, depending on wind park size and DC-link capacitance. Riding such a VSC-HVDC link through an onshore fault is expected to cause significant effects on the dynamics in the onshore system. It is hence manifest to discuss the potential countermeasures, the applicability, and implementation for each type of WTG before scrutinising the stability impacts.

Fault ride-through methods for WPPs connected to the grid through VSC-HVDC have been investigated in detail in [133–137]. In [133] several power reduction methods are compared. It was concluded that a combination of ride-through methods should always be used in order to survive a severe voltage dip at the grid side. It was not mentioned what kind of wind turbine generators had been used during the study, however. In [134], fault ride-through capabilities of a VSC-connected WPP consisting of type 1 WTGs was investigated and it was shown that a combination of voltage reduction and frequency increase in the offshore collection grid led to adequate fast reduction of the active power injected into the DC circuit. In [135] and [136], power reduction is achieved by the application of fast communications between WPVSC and wind turbine. Ride through of a wind park containing only DFIG based WTGs using frequency increase was studied in [137].

3.3.1 Power Reduction Methods

Depending on the HVDC link capacitance, only a few milliseconds are available for active power reduction at WPVSC (see also Eq. 2.19). It must be noted that, though costly, extra capacitors can be installed to increase the time available to achieve correct fault ride-through of the wind park. Some power reduction methods require extra control loops within the WTGs. Reduced power exchange with the onshore network can be detected by the WPVSC by either a signal from the GSVSC through a communication link or by an elevated direct voltage at the wind park side of the DC-link. Combinations of fast power reduction methods are summarised in [133] and implemented in the models used in this work. This thesis focuses on power reduction methods on a conceptual level (i.e., operational aspects, qualitative effect on grid dynamics), hence detailed technical requirements of specific grid codes are not considered. Details of the implementation of the various FRT mechanisms are given below, alongside their advantages and disadvantages.

WPP Frequency Increase

Frequency variation of the offshore WPP is a promising solution since the power infeed to the HVDC link can be quickly reduced for each WTG type. SCIGs have a natural frequency response as the generator slip quickly decreases by raising the frequency by only a few percent, causing the active power output to drop near zero. DFIG and FCG based wind turbines do not respond naturally to a frequency deviation as their controls are designed to inject a fixed power into the network independent of the network frequency. Like VSCs, a PLL is applied that aligns the internal reference frame of the controller to the network voltage in a short time interval. Therefore, an additional control loop must be implemented into the existing converter controls that adds a droop characteristic as presented in [138]. The reaction time of DFIG and FCG wind turbines, which is eminent to engage their frequency power droop, is restricted by the PLL bandwidth.

Figure 3.15 shows the DFIG and the FCG droop-regulator implementation. During frequency increase, the reference torque T_e acquired by maximum power point tracking is decreased by a factor P^* , which results in the torque reference T_e^* . The per unit droop K_{ft} depends on the actual WPP configuration and should be high for the case of DFIG or FCG based WTGs that are installed in a wind park together with SCIGs.

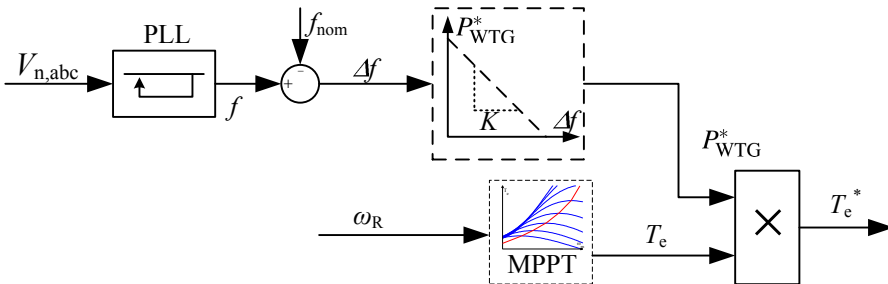


Figure 3.15: Frequency control support of FCG and DFIG wind turbines during increased offshore AC frequency

On the WPVSC side, the frequency increase is realised by adding an additional phase angle θ_c^* to the generated AC voltage vector. This is triggered by an abnormal direct voltage.

As can be seen in figure 3.16 frequency increase is obtained here by controlling an additional phase angle θ_c according to

$$\theta_c = K_f(U_{dc} - U_{dc}^*) + \frac{1}{\tau_f} \int (U_{dc} - U_{dc}^*) dt \quad (3.41)$$

with k_f and τ_f , the proportional frequency controller gain and integrator time constant respectively, u_{dc} the HVDC link direct voltage, and u_{dc}^{ref} the direct voltage set point for FRT operation, which is equal to the per unit nominal direct voltage in this case. The additional phase angle θ_c^* is added to the nominal frequency phase angle $\delta_{\text{osc}} = 2\pi f_{\text{osc}} t$ to obtain the reference phase angle, and thus frequency for the converter modulator. Controller gains strongly depend on the wind park configuration as highly FCG and DFIG penetrated wind parks have a well defined frequency response (by droop constant K), whereas the frequency response of SCIGs is dependent on slip and thus on operating point. After direct voltage recovery, the frequency controller is disabled and the WPVSC returns to normal operation.

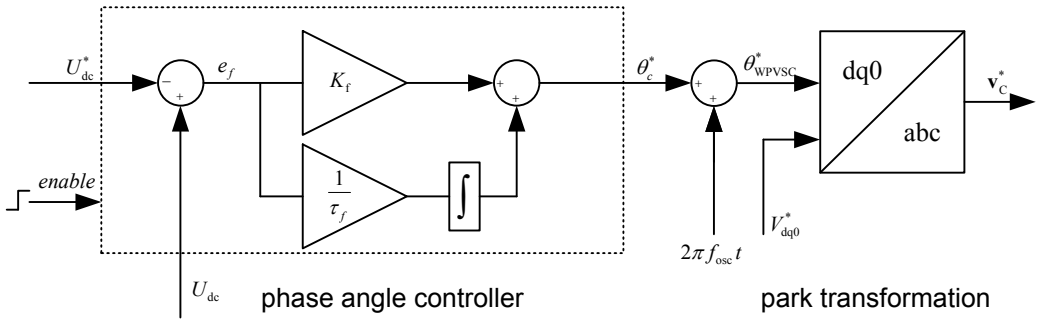


Figure 3.16: WPVSC frequency controller during FRT operating conditions.

Offshore Voltage Reduction

Reduction of the wind park voltage, or alternatively mirroring the onshore voltage to the offshore WPP, will lead to a reduced wind turbine power production by natural response. FCG (and to a limited extent DFIG) WTGs will hit their current limit at low network voltages. Consequently, less active power will be fed into the offshore AC-network. In [134], voltage reduction was successfully applied for SCIG based WPPs. As the developed electromagnetic torque of a SCIG is proportional to the square of the AC voltage magnitude, active power will be reduced quickly. Due to the sudden change in electromagnetic torque the mechanical system will react heavily to abrupt voltage changes. For DFIG based WTGs triggering of the crow bar protection should be avoided in this case. Reference [136] proposes a new voltage reduction method based on direct magnetisation of DFIGs to avoid a high DC-component in the DFIG current that normally triggers the crow bar. In this thesis it is assumed that the crow bar will eventually trigger and that advanced method was not applied. The voltage reduction has been realised by a steep decrease of the WPVSC voltage reference of the V_{PCC} controller. After direct voltage recovery, the reference signal is gradually restored to its pre-fault value.

Fast Communication

The output power of wind parks consisting of FCG and DFIG can also be reduced by establishing a fast communication link between the offshore VSC and the individual WTGs [135], [136]. Referring to figure 3.16, P^{ref} will be set to a limited value after detection of direct voltage elevation, which will consequently lead to a sudden decrease of active power production. The method is not well suited for wind parks consisting of SCIG due to the physical nature of their response. Their output power can only be reduced by pitching the blades (i.e., setting the switch in figure 3.11 to β_{ref}), which is considered too slow. Disadvantages of communication links are the latencies involved (e.g., lower reliability, inherent communication delay), which may be in the range of 10 – 100 ms. Therefore, the application of this method is not recommended [137] and should be utilised only in combination with one of the other fast power reduction methods.

Chopper Controlled Dynamic Braking Resistor

Application of a braking resistor in the DC circuit has two particular advantages. Firstly, no further power reduction method has to be applied as excess DC-link energy is dissipated in the resistors that are rated for full power. Secondly, the offshore wind park can remain in full operation during any onshore grid disturbance and the WTGs experience no mechanical stresses during chopper operation. Reference [133] distinguishes between small braking resistors that are used in combination with other fast power reduction methods and large braking resistors, which are operating at full wind park power rating. Although it has technical benefits [139, 140], it is uncommon to apply a partially-rated dynamic braking resistor from a reliability and economical viewpoint. The costs of implementing a braking resistor are largely determined by the power electronics, which must be capable of carrying the full current rating of the link.

In this thesis, the braking resistor is assumed to operating at nominal wind park power. After the FRT protection circuit is triggered, the DC-chopper controls the direct voltage to a set point slightly above its nominal value as the GSVSC is switched into current limit mode. The implementation into simulation tools can be achieved in three ways:

- by a detailed representation of the valves, their controls, and the actual resistor;
- in a quasi-stationary manner as a variable current or power source; or
- in a quasi-stationary manner as a variable resistor.

In line with the VSC and WTG model we adopt a quasi-stationary approach, mainly for computational efficiency. As the braking resistors are engaged by (PWM modulated) choppers, the overall protection system is perceived as a variable resistor. The power dissipated by the dynamic braking resistor equals

$$\begin{aligned}
 P_{\text{br}} &= \frac{U_{\text{br}}^2}{2R_{\text{br}}} = \frac{(m_{\text{br}}U_{\text{dc}})^2}{2R_{\text{br}}} \\
 &= \frac{(U_{\text{dc}})^2}{2R_{\text{br,eff}}}
 \end{aligned} \tag{3.42}$$

where P_{br} is the power dissipated by the positive and negative pole protection circuits together, U_{br} is the effective pole-to-pole voltage experienced by both resistors, m_{br} is the modulation index of each chopper, and $R_{br,eff}$ is the effective resistance as seen from one of the poles to the ground. Although $R_{br,eff}$ can be calculated from (3.42) and adjusted dynamically, this comes at a computational price. The network equations, and hence state space representation, need to be adjusted throughout the simulation. This is undesired for EMT-type simulations as these apply the trapezoidal rule for integration, an implicit algorithm that needs careful (re-)initialisation each time network elements change.

A reasonable alternative for the above difficulty is to model the dynamic braking resistor by a variable current injection based on (3.42). For the positive pole this yields

$$\begin{aligned} i_{br}^+ &= \frac{P_{br}/2}{U_{br}/2} = \frac{P_{br}}{m_{br}U_{dc}} \\ &= \frac{m_{br}U_{dc}}{2R_{br}} \end{aligned} \quad (3.43)$$

for the negative pole the relation is equal. The calculated currents are defined from the pole to ground. This must be accounted for when modelling the current sources, which are in most tools defined as branching from the reference node (ground).

The modulation index is obviously 0 when the system is in normal operation. When FRT is initiated, m_{br} is assumed to be controlled by a proportional controller. The overall block diagram is shown in figure 3.17, which also shows the limiters that are inherent to the protection scheme (i.e., the modulation index bounds and rated current of the chopper).

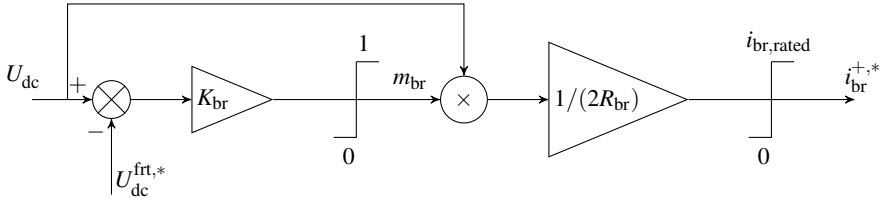


Figure 3.17: Block diagram of the chopper controlled dynamic braking resistor.

3.3.2 Implementation into Onshore and Offshore VSC Control

Except for the power-frequency droop in the WTGs, the FRT methods all act on the VSC controls on both the onshore and offshore connection points. The principal activators for FRT are overvoltages in the HVDC circuit and voltage sags in the onshore transmission system. The status of these quantities determine whether the VSC-HVDC circuit is in normal operation, needs to engage FRT mechanisms, or needs to recover to prefault operation levels. Along these dividing lines the above mentioned FRT methods have been implemented into the VSC controls.

The overall implementation of the FRT measures are modelled as a finite state machine that acts on top of the VSC controls described in section 3.1. The FRT controller implements basically 3 states (aside from the *start* state) as shown in table 3.1. The states and their possible transitions are shown in figure 3.18. $U_{dc}^{thres,+}$ and $U_{dc}^{thres,-}$ are the threshold voltages

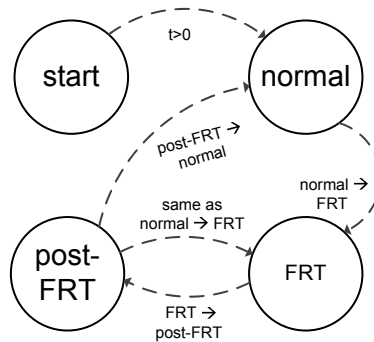
Table 3.1: *FRT regulator state machine implementation*

State	Main Duty	section
Normal	normal operation	3.1.2
FRT	ride through fault, aRCI	2.4.2 and 3.3
post-FRT	ramp-up active power to pre-fault value	2.4.2 and 3.1.6

Table 3.2: *FRT regulator state transitions and their actions (see figure 3.3 and 3.10).*

Transition	Trigger	Actions (— in figure 3.3 and 3.10)
Normal to FRT	$U_{dc} > U_{dc}^{thres,+}$ or $ V _{PCC} < V_{PCC}^{thres}$	engage braking resistor
		q-axis limiting priority (II)
FRT to post-FRT	$U_{dc} < U_{dc}^{thres,-}$ and $ V _{PCC} > V_{PCC}^{thres}$	enable aRCI (IV)
		freeze active current state (V)
		offshore FRT mode on (X)
post-FRT to normal	after $1/R_p$ second	disable braking resistor
		d-axis limiting priority (II)
		offshore FRT mode off (X)

at which FRT is triggered and disabled respectively. V_{PCC}^{thres} is picked well below nominal voltage to exclude nuisance FRT operations.

Figure 3.18: *FRT controller states and their transitions according to table 3.2.*

Chapter 4

VSC-MTDC modelling for Transient Stability Simulation

This chapter deals with the second research question stated in the Introduction (RQ2), and approaches the solution from a monolithic stability simulation point of view (RQ2-2 and RQ2-3). The VSC modelling described in chapter 3 will be put forward for quasi-stationary simulation in this chapter. This model is validated against an EMT-type two-level VSC model in Simulink. Three types of MTDC dynamic models are proposed, 1) full order state-space, 2) multi-rate improved, and 3) reduced-order. The performance (accuracy and computational complexity) is tested by a in-house developed simulation framework. This chapter describes and validates this framework against commercial power system simulators. ¹.

4.1 Introduction

Chapter 2 explained the emergence of renewable energy resources in the past decades, and the technological developments that lead to the availability of power electronics for high-voltage applications. Among other developments, this will lead to a gradual transition of the present power system from a conventional electrical machine-dominated system to a more diverse future power system. Such a network comprises a high penetration of power-electronics interfaced devices, more transnational interconnections, and advanced communication structures. As a result, the properties of the dynamic behaviour of the system as a whole will change for several time-frames of interest.

Chapter 3 introduced the modelling approach for both VSCs and offshore WPPs. Under the assumptions of balanced AC system conditions, the negligible influence of non-fundamental harmonics of voltages and currents, and a near-normal operation region of the direct voltage, both WTGs and VSCs can be modelled by time-averaged equivalent voltage sources. Particular attention was given to the inclusion of FRT requirements into the controls of VSCs, onshore and offshore alike.

Investigating the integration of VSC-HVDC connected offshore WPPs into the mainland systems requires rethinking of the simulation platform utilised. VSCs couple DC-side phe-

¹the material of this chapter is partly based on and adopted from [AA , V , M , T , C]

nomena with the AC-side phenomena through their controls. It has been shown in Chapter 2 that control actions and electromagnetic transients inside the HVDC system may interact with the electro-mechanical AC system dynamics, especially during faults. This may impair the stability of the connected AC system, particularly when the total amount of HVDC-connected power is high with respect to the total generation fleet. As the time-scale of the electromagnetic phenomena inside the HVDC system is small, the time-scale spectrum of the simulation tool to be employed should be relatively large, typically ranging from μs to 10 s. Hence, the simplifications used in, for instance, stability-type simulations cannot be one-to-one taken on for combined AC/VSC-HVDC systems. On the other hand, electromagnetic transients (EMT) simulations do offer this spectrum at the cost of a higher computational burden. Mastering these conflicting requirements is the key to answering the second main research question on how to incorporate VSC-HVDC systems into stability studies.

As will be shown in chapter 5, hybrid simulations tackle this issue by combining two domain-specific solution algorithms. The first steps towards such a platform will be given in the present chapter, which partly deals with the description and validation of the stability and EMT partitions of the in-house developed hybrid simulator.

However, one needs two distinct simulation tools: either a separate EMT-type and stability-type simulation to set up a co-simulation or a hybrid simulation that embeds the EMT-type simulation into its own stability-type simulation. Often, just one of these simulations is available, and setting up a hybrid simulation is either costly or costs a lot effort to develop. In case the application of a particular monolithic (i.e., one solver, one system) simulation environment poses no strict boundary condition to the study (i.e., only the power system domain is involved, no ICT or market), this gives rise to exploring the incorporation of the entire system into one simulation tool.

This chapter focuses on the inclusion of arbitrary VSC-HVDC structures into stability-type simulations. This approach has the merit that it relieves the need for a second EMT-type simulation. Using the stability part of the hybrid simulator several transient-stability modelling alternatives will be discussed:

- state-space modelling of VSC-MTDC;
- a multi-rate improved model of the state-space VSC-MTDC model; and
- a reduced-order model of the MTDC system.

The analysis will address the boundary conditions that allow either model simplifications or adjustments to the numerical procedures. As the state-space model will be used as a reference model, a qualitative comparison with a more detailed VSC-HVDC dynamic model will be studied.

This chapter is organised as follows. We will start with a description of the workflow and the underlying calculation mechanisms of the stability-type and EMT partitions of the simulator. Then the simplifications made to the VSC model for inclusion into a stability-type simulator are analysed. The chapter continues with the various developed MTDC network models and their respective area of application. Several case studies are performed to highlight the differences between these models and their numerical implementations.

4.2 Simulation Framework

During the course of the research conducted for this thesis the simulations have been applied in mainly four simulation environments or research frameworks:

1. PSS NETOMAC using the built-in hybrid simulation functionality;
2. Matlab using functional programming;
3. PSS[®]E version 32 and 33; and
4. Python version 2.7.

PSS Netomac offers a straightforward way to simulate parts of the system in separate partitions, and allows coupling of these during runtime. However, the black-boxed numerical solution part of the tool disallows investigation of the mutual interaction between the numerical part of the simulation and the VSC-HVDC model response. Therefore, an new simulation framework was developed containing separate stability and EMT partitions. This opens massive possibilities to study model improvements, hybrid simulations, and their interfacing techniques. This was initially done by Matlab scripting and later generalised using Python and its extensions (Numerical Python, Scientific Python, among others).

Before considering the hybrid simulation and its interfacing techniques in detail (i.e., Chapter 5), we will first describe and validate both partitions separately. Both simulations are time-stepped. The main workflow for both stability-type and EMT-type simulations are shown in figure 4.1. The details of the workflow are described next.

4.2.1 Stability-type simulation

The focus on (relatively slow) electromechanical interactions in large networks requires stability-type simulations to employ a quasi-stationary approach for the network and machine modelling. This implies that:

- electromagnetic network transients are neglected, allowing modelling of network quantities by complex phasors;
- dynamic modelling of phenomena in the 0.1 to 10 ms time frame of interest;
- time step-sizes around 1 - 10 ms.

The dynamic behaviour of equipment connected to the network nodes, such as generators and associated controls is modelled by differential equations, while their mutual coupling (the AC network) is maintained by algebraic relations only. This translates into the following set of differential-algebraic equations (DAEs):

$$\frac{dx}{dt} = \dot{x} = f(x, y) \quad (4.1)$$

$$0 = g(x, y) \quad (4.2)$$

in which x is a vector containing state variables, y is the vector of algebraic variables, and t the simulation time. Equation (4.1) represents the dynamic behavior of generators, exciters,

governors, sometimes including dynamic loads, whereas (4.2) represents the algebraic set of equations, consisting of the network solution, static load models, and algebraic controller equations. The relations in \mathbf{f} and \mathbf{g} are generally nonlinear, especially for power systems. By solving (4.1) and (4.2) each time step, the dynamic response of the system is obtained. Depending on their specifics, several methods exist to solve DEAs in the time domain, being formalised in [141].

Numerical Integration Scheme

For power system simulators there are generally two ways of solving (4.1) and (4.2). *Partitioned explicit* methods calculate the two sets of equations sequentially by solving (4.1) by any explicit numerical integration method. Subsequently, the set of algebraic equations is solved. *Simultaneous implicit* methods discretise the set of differential equations by applying implicit numerical integration methods. These equations are then solved together with the algebraic equations [142]. Partitioned explicit methods have the advantage of programming flexibility, but a relatively large *interface error* between the solutions of the differential and the algebraic part of the system. This error does not exist for simultaneous implicit methods, as (4.1) and (4.2) are solved iteratively until convergence. This allows to simulate using a larger time step size without compromising simulation accuracy.

In this thesis we apply a single-step partitioned explicit method for its particular programming merits. That is, (4.1) and (4.2) are solved separately with distinct numerical routines, and an explicit integration algorithm is used to solve (4.1). To reduce the numerical error incorporated when solving (4.1) and (4.2), the solution routine employs the predictor-corrector method for numerical integration [143].

The high-level workflow of the solution routine for the stability simulation is shown in figure 4.1a, and displays the relevant actions taken for each (fixed) time step n . First, the predictor-corrector method needs values of \mathbf{x} and \mathbf{y} to perform its numerical integration over the present time step n . For \mathbf{y} , it uses as a first estimate the values calculated by the corrector routine during the previous time step, i.e. \mathbf{y}_{n-1} .

As for the predictor step, the state variables at time t_n , $\mathbf{x}_{p,n}$, are approximated by a forward Euler predictor

$$\begin{aligned}\mathbf{x}_{p,n} &= \mathbf{x}_{n-1} + \Delta t \mathbf{f}(\mathbf{x}_{n-1}, \mathbf{y}_n^+) \\ &= \mathbf{x}_{n-1} + \Delta t \dot{\mathbf{x}}_{p,n}\end{aligned}\tag{4.3}$$

with Δt the simulation time step-size. In the event of disturbances (e.g., short-circuit, line tripping, or load (dis)connection) this approximation is invalid as some values inside \mathbf{y} or relations in \mathbf{g} may change abruptly. Hence, (4.2) must be solved first (i.e. $0 = \mathbf{g}(\mathbf{x}_{n-1}, \mathbf{y}_n^+)$) to obtain accurate starting values for (4.3). If no network changes take place at t_n however, \mathbf{y}_{n-1} can be safely used as a starting point for efficiency reasons.

The predicted value for \mathbf{x}_n is now corrected by a trapezoidal corrector according to

$$\mathbf{x}_{c,n}^{(\eta+1)} = \mathbf{x}_{n-1} + \frac{\Delta t}{2} \left[\dot{\mathbf{x}}_{p,n} + \mathbf{f}(\mathbf{x}_{c,n}^{(\eta)}, \mathbf{y}_{p,n}) \right]\tag{4.4}$$

with η the corrector iteration counter. By using $\mathbf{x}_{c,n}^{(\eta+1)}$ as a new prediction and iterating until convergence, the accuracy of (4.4) can be improved to approximate \mathbf{x}_n . Subsequently, (4.2)

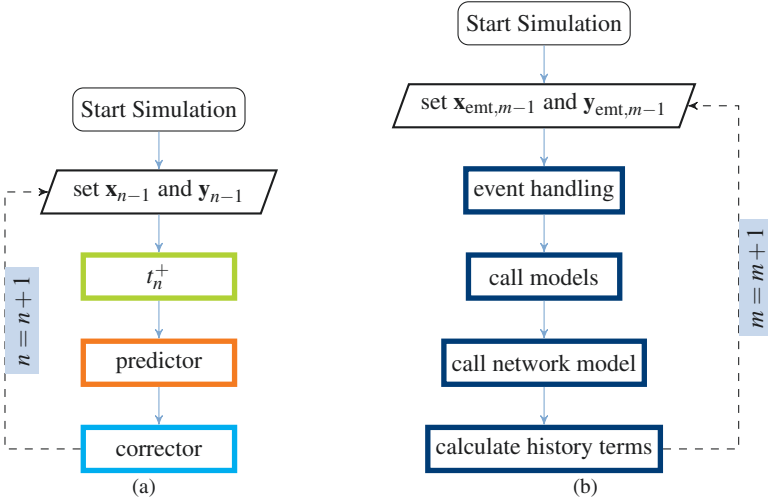


Figure 4.1: High-level work flows of the (a) stability-type simulation and (b) EMT-type simulation. In (a) the t_n^+ block solves the network after disturbances. The predictor and corrector blocks calls both the network solution and solve the set of differential equations. x and y refer to differential and algebraic variables respectively.

can be extrapolated or solved iteratively to obtain \mathbf{y}_n . The detailed solution scheme is shown in figure 4.3.

Network Modelling

The AC network is represented by quasi-stationary complex phasors according to the current injection model:

$$\mathbf{I} = \mathbf{Y} \mathbf{V} \quad (4.5)$$

in which \mathbf{I} is a column vector with nodal current injections, \mathbf{Y} the bus admittance matrix, and \mathbf{V} the nodal voltages. Currents and voltages are considered positive sequence and in per unit on network base values.

Dynamic behaviour of devices and equipment can generally be encapsulated in either \mathbf{I} or \mathbf{V} . Some of the voltages are for instance dictated by the dynamic models attached to the respective buses (e.g., slack voltage sources, models with a Thévenin-equivalent grid interface), whereas other devices such as generators and loads display current-source behaviour. In order to solve (4.5), we first expand it to

$$\begin{bmatrix} \mathbf{I}_e \\ \mathbf{I}_g \end{bmatrix} = \begin{bmatrix} \mathbf{Y}_e & \mathbf{Y}_{eg} \\ \mathbf{Y}_{ge} & \mathbf{Y}_g \end{bmatrix} \begin{bmatrix} \mathbf{E} \\ \mathbf{V}_g \end{bmatrix} \quad (4.6)$$

where \mathbf{E} are the dynamic slack voltage sources and \mathbf{I}_g are the dynamic nodal current injections from the generators, loads, and other devices. \mathbf{I}_e and \mathbf{V}_g are the nodal current injections at the dynamic slack voltage source nodes, and bus voltages in the remainder of the system respectively. Generally \mathbf{E} and \mathbf{I}_g are known whereas \mathbf{I}_e and \mathbf{V}_g are unknown. The latter

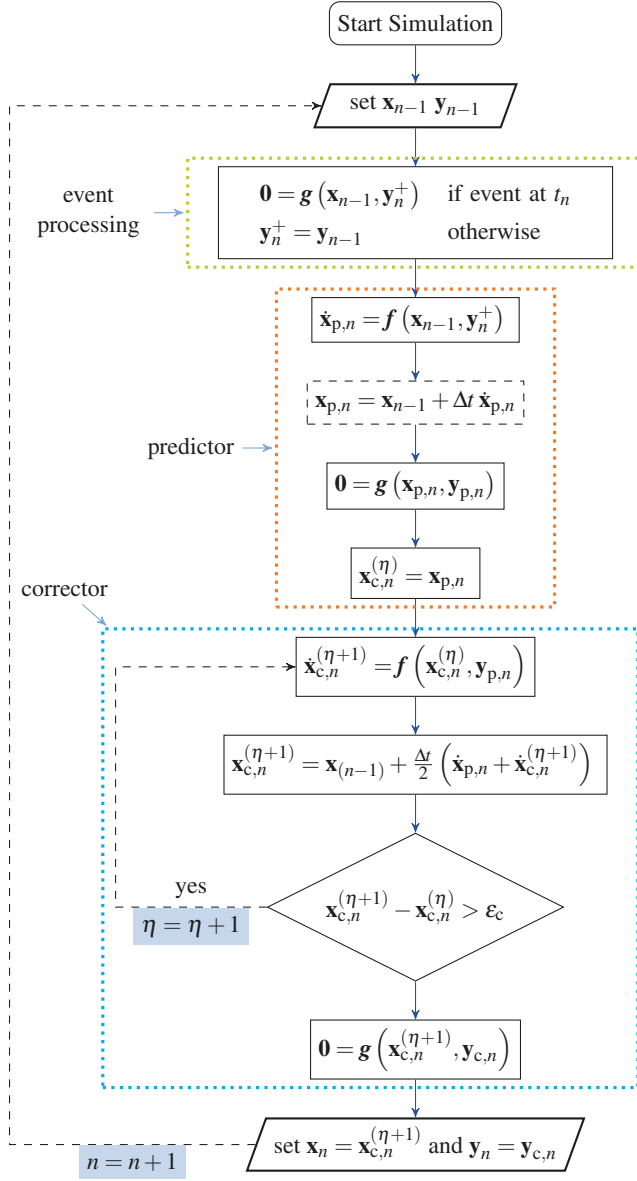


Figure 4.2

Figure 4.3: Detailed work flow of the stability-type simulation developed for this thesis.

commonly comprises the largest part of the network and can be calculated through

$$\underline{\mathbf{V}}_{\mathbf{g}} = \underline{\mathbf{Y}}_{\mathbf{gg}}^{-1} (\underline{\mathbf{I}}_{\mathbf{g}} - \underline{\mathbf{Y}}_{\mathbf{ge}} \underline{\mathbf{E}}) \quad (4.7)$$

It is significant to notice at this point that $\underline{\mathbf{V}}_{\mathbf{g}}$ and $\underline{\mathbf{I}}_{\mathbf{g}}$ are generally model inputs and outputs respectively, and hence part of \mathbf{y} . As the built-in numerical routines within Python for solving non-linear systems explicitly require real numbers, all phasors have been split into

their real and imaginary parts. Together with the relations within the dynamic models \mathbf{g} can be formulated and solved according to the iterative scheme described in Appendix A. This iterative scheme requires determination of the Jacobian (i.e., $\partial \mathbf{g} / \partial \mathbf{y}$) either at every iteration, only the first iteration (the dishonest Newton-Raphson method), or when certain accuracy thresholds are violated (the very dishonest Newton-Raphson method). The partial derivatives can either be provided analytically by the dynamic models or be determined numerically using the forward difference method [141]. In case control or current limits are hit the respective algebraic variables are 1) fixed at the limit for this particular iteration of (4.2) and 2) excluded from the Jacobian determination and Newton-Raphson solution. Table 4.1 shows how these aspects are implemented as a state machine on top of the solution routine of the stability simulator. L1 and L2 cover the situations in which one or more limiters are hit or other discontinuities occurred. Aside from the alternative treatment of algebraic variables the work flow is just like the NORMAL simulation state.

Table 4.1: *Simulation states in the stability-type simulation*

State	Use
START	Start of the simulation
NORMAL	Normal simulation, Jacobian fixed unless $\text{MODE} = 7$
L1	one or more algebraic limits violated
L2	one or more algebraic limits, being different from L1, violated

The program calls a dynamic model each time \mathbf{f} or \mathbf{g} needs to be determined. These model calls have been implemented along the lines of [144], i.e., distinct functions for the state variables and the algebraic variables. Aside from the time, \mathbf{x} , and \mathbf{y} the models also have a MODE variable as input, which carries information about solution status. An overview is shown in table 4.2. This allows a flexible way of dealing with particulars of the solution routine, such as inner integration loops of multi-rate purposes and interfacing with the EMT simulation (done in Chapter 5).

4.2.2 EMT-type simulation

Transient studies commonly concentrate on fast electromagnetic interactions between devices and their connected network elements. Like electromechanical oscillations, these interactions are commonly being induced by switching actions and short circuits. The difference however is that the transients are much faster (i.e. shorter attenuation times), and their impact is normally more local. EMT-type simulations model the network cables and lines by differential equations based on various lumped element representations, or more sophisticatedly by frequency-dependent models [145]. This requires devices to also employ electromagnetic interactions into their models (e.g. stator flux linkage for electrical machines, switching behaviour of power electronic interfaces).

Above considerations in general require EMT-simulations to apply a much smaller (fixed) time step-size for numerical integration (Δt_{emt} in the μs range). Several numerical solution methods are applied in literature, of which the commonly applied nodal analysis method is adopted for this thesis [146]. The nodal analysis method represents each branch by a one port containing a current source (i.e., I_{inj}) in parallel with a voltage source behind

MODE	Aim	Simulation state (table 4.1)
0	Normal model call	all
1	Model call during Jacobian determination	all
2	Model call of (4.1) during predictor step	all
3	First model call during trapezoidal corrector	NORMAL
4	Second or more model call during trapezoidal corrector	NORMAL
6	Model call before solving (4.2)	L2
7	Normal model call (Jacobian is determined every iteration) before solving (4.2)	all

Table 4.2: *Modes in the stability-type simulation*

an equivalent impedance (E_{br} and R_{eq} respectively). See also figure 4.4.

On network level, the branch voltages and currents are related from Kirchhoff's laws by

$$\mathbf{M}\mathbf{Y}_b\mathbf{V}_k = \mathbf{M} \left[\mathbf{Y}_b\mathbf{E}_{br} - \mathbf{I}_{inj} - \mathbf{I}_{hist} \right] \quad (4.8)$$

with \mathbf{M} the reduced adjacency matrix, \mathbf{Y}_b the branch admittance matrix containing $1/R_{eq,k}$ on the diagonal, \mathbf{V}_k the branch voltages, \mathbf{E}_{br} the external voltage sources, \mathbf{I}_{inj} the modelled current injections, and \mathbf{I}_{hist} the history currents. The determination of \mathbf{M} will be explained in section 4.3.3. The branch voltages are related to the node voltages by

$$\mathbf{V}_k = \mathbf{M}^T \mathbf{V}_n \quad (4.9)$$

where \mathbf{V}_n is the vector containing the node voltages. With substitution of (4.9) into (4.8), the nodal form is obtained, which leads us to

$$\mathbf{Y}_n \mathbf{V}_n = \mathbf{I}_n \quad (4.10)$$

in which \mathbf{Y}_n is the nodal admittance matrix given by

$$\mathbf{Y}_n = \mathbf{M}\mathbf{Y}_b\mathbf{M}^T \quad (4.11)$$

and \mathbf{I}_n the vector of nodal current injections, i.e.,

$$\mathbf{I}_n = \mathbf{M} \left[\mathbf{Y}_b\mathbf{E}_{br} - \mathbf{I}_{inj} - \mathbf{I}_{hist} \right] \quad (4.12)$$

The differential equations that describe the behaviour of each branch are then discretized according to an implicit numerical integration algorithm, and moulded into this branch representation (by means of R_{eq} and I_{hist}) for a particular time step-size. This process is called *numerical integrator substitution*, and allows a non-iterative solution of the network currents

and voltages [147]. For any passive branch element this gives the following relation for the branch current

$$\begin{aligned} I_{k,m+1} &= I_{\text{hist},m} + \frac{1}{R_{\text{eq}}} (V_{f,m+1} - V_{t,m+1}) \\ &= I_{\text{hist},m} + \frac{1}{R_{\text{eq}}} V_{k,m+1} \end{aligned} \quad (4.13)$$

of branch k spanning from node f to node t . We apply the trapezoidal rule of integration for normal operating conditions, and switch to the backward Euler method in case interpolation is needed. An overview of the respective history current terms and equivalent branch resistances is given in table 4.3 for the trapezoidal method and in table 4.4 for the backward Euler method.

element	$1/R_{\text{eq}}$	$I_{\text{hist},m}$
R	$1/R$	0
L	$\frac{\Delta t_{\text{emt}}}{2L}$	$I_{k,m} + \frac{\Delta t_{\text{emt}}}{2L} V_{k,m}$
C	$\frac{2C}{\Delta t_{\text{emt}}}$	$-I_{k,m} - \frac{2C}{\Delta t_{\text{emt}}} V_{k,m}$
RL	$\frac{\Delta t_{\text{emt}}/2L}{1 + \Delta t_{\text{emt}}R/2L}$	$\frac{1 - \Delta t_{\text{emt}}R/2L}{1 + \Delta t_{\text{emt}}R/2L} I_{k,m} + \frac{\Delta t_{\text{emt}}/2L}{1 + \Delta t_{\text{emt}}R/2L} V_{k,m}$
RC	$\frac{1}{R + \Delta t/2C}$	$\frac{1 - \Delta t_{\text{emt}}R/2C}{1 + \Delta t_{\text{emt}}R/2C} I_{k,m} - \frac{1}{R + \Delta t_{\text{emt}}/2C} V_{k,m}$

Table 4.3: *Equivalent branch admittance and history terms per branch type applied to the trapezoidal rule for numerical integration.*

element	$1/R_{\text{eq}}$	$I_{\text{hist},m}$
R	$1/R$	0
L	$\frac{\Delta t_{\text{emt}}}{L}$	$I_{k,m}$
C	$\frac{C}{\Delta t_{\text{emt}}}$	$-\frac{C}{\Delta t_{\text{emt}}} V_{k,m}$
RL	$\frac{1}{R + L/\Delta t_{\text{emt}}}$	$\frac{L/\Delta t_{\text{emt}}}{R + L/\Delta t_{\text{emt}}} V_{k,m}$
RC	$\frac{1}{R + \Delta t/C}$	$\frac{R}{R + \Delta t_{\text{emt}}/C} I_{k,m} - \frac{1}{R + \Delta t_{\text{emt}}/C} V_{k,m}$

Table 4.4: *Equivalent branch admittance and history terms per branch type applied to the backward Euler numerical integration method.*

The device models are generally non-linear and are being solved separately from the network, using a delay of one time step Δt_{emt} . Controllers and devices use the same integration routine (i.e. the trapezoidal rule) and are discretized by the bilinear transform. Subsequently, the models interface to the network by setting their current or voltage source output for the present time step.

The workflow for the EMT simulation environment is shown in figure 4.1b. First, the state and algebraic variables (control variables, $\mathbf{V}_{k,m}$, etc.) from the previous time step ($m -$

1) as well as the *history terms* of the branch currents (i.e., $\mathbf{I}_{\text{hist},m}$) are used as an input to the devices and control modules of the present time step m . These history terms are basically the known parts of the implicit integration algorithm (e.g. voltages and currents from the previous time-step), being modelled as a current source for the network model. In case of an event inside the network, the implicit integration algorithm requires recalculation of the history terms in order to succeed. The procedure continues with calling all models to do numerical integration and to set the respective branch output currents and voltages (i.e., $\mathbf{I}_{\text{inj},m}$ and $\mathbf{E}_{\text{br},m}$). Then, the network nodal voltages (i.e., \mathbf{V}_n) are calculated by the nodal analysis method (i.e., using (4.12) and solving (4.10) for \mathbf{V}_n), which are subsequently used for recalculating the history terms before the simulation advances to the next time step.

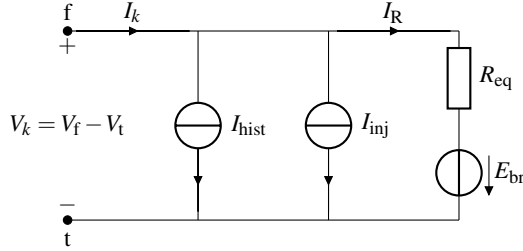


Figure 4.4: Branch model used for the EMT-type simulation.

4.3 Quasi-stationary VSC-MTDC model

4.3.1 AC-side Grid Interface and Controls

The VSC model introduced in Chapter 3 is dedicated to averaged behaviour in EMT-type simulations and can to a large extent be applied for stability simulators too. There are a couple of boundary conditions that need to be taken into account when modelling VSCs:

- the AC grid interface of the VSC
- the synchronisation of the VSC reference frame
- the applicability for extensive grid studies

The positive-sequence modelling of the AC grid implies balanced and undistorted conditions; only the fundamental frequency is of relevance. The grid interface at the AC side of the VSC thus consists of complex impedances and can now be expressed as

$$\underline{V}_c = \underline{V}_{\text{PCC}} + \underline{I}_c \underline{Z}_c \quad (4.14)$$

which yields for the terminal current

$$\underline{I}_c = \frac{\underline{V}_c - \underline{V}_{\text{PCC}}}{R_c + jX_c} \quad (4.15)$$

In line with output of the EMT model the AC terminal of the VSC is represented by a positive-sequence voltage source as

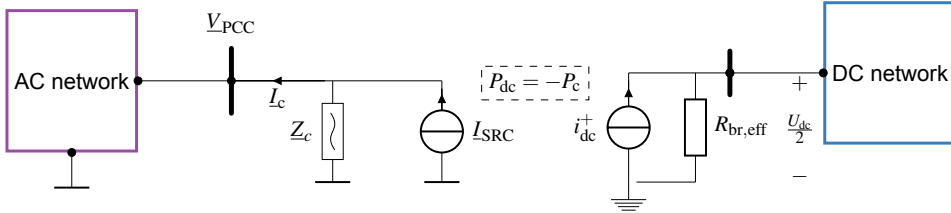


Figure 4.5: Averaged transient stability VSC model. AC side: positive sequence representation, DC side: symmetrical monopole with only the positive pole represented.

$$\underline{V}_c = (v_d^* + jv_q^*) e^{j\phi_{PLL}} \quad (4.16)$$

where v_d^* and v_q^* are the d and q axis voltage reference values respectively, and ϕ_{PLL} the rotation angle of the d - q reference frame. Because dL_c/dt terms are disregarded—the relations are purely algebraic—no cross coupling occurs between the d and q axis when transforming from the synchronous (i.e., x - y) reference frame to the d - q reference frame of the VSC. Alongside the fast rise time of the current controller (i.e., in the ms range) this argues for neglecting this control mode assuming current set points to be tracked instantaneously. Using (4.16) and (4.14) the terminal voltage of the VSC can be calculated by

$$\underline{V}_c = \underline{V}_{PCC} + \underline{Z}_c (i_{c,d}^* + ji_{c,q}^*) e^{j\phi_{PLL}} \quad (4.17)$$

in which $i_{c,d}^*$ and $i_{c,q}^*$ are the d and q axis current reference values. For stability simulators it is common (for PSS[®]E a strict requisite) to commence a node elimination on the VSC terminal node and represent the Thévenin voltage source of (4.17) by a Norton current injection instead. Such a grid interface is shown in figure 4.5. Using (4.17) the current source value equals

$$\begin{aligned} I_{SRC} &= \frac{\underline{V}_{PCC}}{\underline{Z}_c} + I_c^{\text{ref}} \\ &= \frac{\underline{V}_{PCC}}{\underline{Z}_c} + (i_{c,d}^* + ji_{c,q}^*) e^{j\phi_{PLL}} \end{aligned} \quad (4.18)$$

where I_{SRC} is the Norton current injection and \underline{Z}_{SRC} is the Norton impedance, being the converter series impedance. The complex phasor diagram of this setup is depicted in figure 4.6. For direct control the VSC acts as a pure voltage source and the Norton current injection is described by

$$I_{SRC} = \frac{\underline{V}_c^{\text{ref}}}{\underline{Z}_{SRC}} = \frac{(v_{c,d}^* + jv_{c,q}^*)}{\underline{Z}_c} e^{j\phi_c^*} \quad (4.19)$$

The implementation of the synchronisation loops cannot be a simple reproduction of the d - q - z PLL introduced in Chapter 3. δ_{PLL} is a result of tracking both varying frequency and voltage angle. The frequency of the network is assumed fixed (i.e., ω_s) for stability-type

simulations. The PLL can hence react on variations of ϕ_{PCC} only. The issue here is that variations in ϕ_{PCC} are a result from variations in the network reference frame position and angle variations caused by machine and device dynamics, i.e.,

$$\phi_v = \int_0^t (\omega_K - \omega_s) dt + \theta_K(0) + \phi_{v,\text{dyn}} \quad (4.20)$$

where ω_K is the frequency of the network reference frame, $\theta_K(0)$ the initial angular displacement of the network reference frame, and $\phi_{v,\text{dyn}}$ the angle variation caused by machine and device dynamics. The latter is the one we are interested in but cannot be calculated by also using ω_K as an input, which is often not available. PLL dynamics would hence massively depend on the reference frame dynamics. Using ω_K as an input is problematic to implement in a generalised way, as various network reference frame realisations exist, often based on (multi-) machine dynamics. These reference frame models are often part of the solution core of the simulation tool, and are usually black-boxed hence not accessible by default.

As a trade-off between model complexity and the need for accurate VSC dynamics we assume the d - q reference frame to align with V_{PCC} using a first-order delay function having the same bandwidth as the PLL. For 25 rad/s this implies synchronisation within 2 cycles.

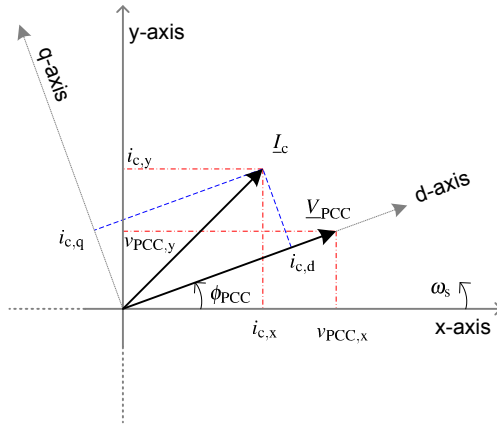


Figure 4.6: Phasor diagram of the VSC terminal voltage and current.

The outer controllers of the VSC as well as the FRT controllers are largely similar to the vector and direct controllers shown in figure 3.3 and 3.10. As mentioned in section 4.2 stability models have multiple model calls per time-step to facilitate the iterative solution scheme for solving (4.2). Especially with discontinuities this may lead to numerical issues. The modes shown in table 4.2 provide a way to work around these. The FRT controller for instance, a finite state machine, is only invoked when MODE equals 2 or 3 to prevent the corrector to diverge during events. PSS[®]E offers similar variables that allow the same behaviour as achieved with MODE.

4.3.2 DC grid interface and Power Balance Model

The HVDC side is assumed to be of the symmetrical monopole type, with the additional assumption that the voltage and power are equally distributed across the positive and negative poles. This will be treated in more detail in the following section, but for the grid interface

at the HVDC side this implies single-pole equivalent modelling (see right side of figure 4.5).

As point on wave values are unavailable and the terminal voltage is eliminated from the network model the power balance model is slightly different from (3.32). First P_c needs to be calculated. This can be done using the network quantities available at a particular iteration of (4.2) by

$$\begin{aligned} P_c &= \text{Re}\{\underline{V}_c \underline{I}_c^*\} \\ &= \text{Re}\left\{\underline{V}_c \left(\underline{I}_{\text{SRC}} - \frac{\underline{V}_{\text{PCC}}}{\underline{Z}_c}\right)^*\right\} \end{aligned} \quad (4.21)$$

or by using the reference values of the outer controllers instead, which leads to

$$\begin{aligned} P_c &= P_{\text{PCC}} - |\underline{I}_c|^2 R_c \\ &= P_{\text{PCC}} - \left(i_{c,d}^{*2} + i_{c,q}^{*2}\right) R_c \end{aligned} \quad (4.22)$$

Once P_c is known the positive pole current injection equals $i_{dc}^+ = -P_c/U_{dc}$, which is passed on to the MTDC model discussed next.

4.3.3 State-Space Model of VSC-MTDC for Stability Studies

Since stability-type simulations are designed particularly to study AC systems by quasi-stationary complex phasors, HVDC transmission must be incorporated by user-written dynamic models. As a first approach this is achieved by developing a general state-space representation of HVDC transmission, for which we will use [148, 149] as a starting point for the HVDC model development and tool-specific implementation. The approach uses the DC nodal current injections (i.e., $I_{dc,j}^+$) of the VSC power balance models as inputs, and provides the DC nodal voltages (i.e., $U_{dc,j}/2$) as input quantities for the VSC models. Figure 4.7 shows the branch models that are used for this model. Submarine cables are modelled by their π -equivalent (figure 4.7a), whereas the VSCs' DC-side capacitors and braking resistors are modelled by an RC shunt branch according to figure 4.7b.

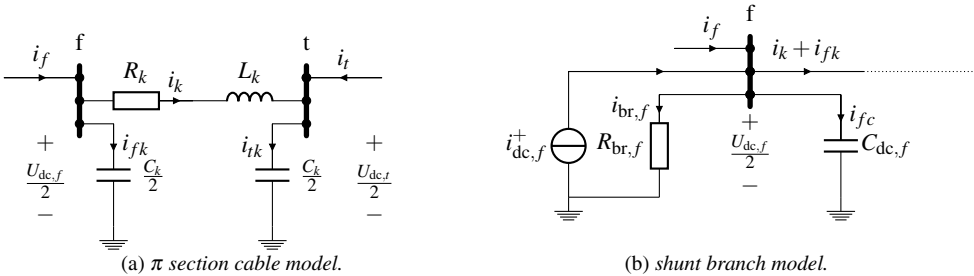


Figure 4.7: Branch models for cables and VSC shunts.

Assuming the general case of having a VSC—and hence shunt branches—at both sides of the submarine cable, the electro-magnetic interactions can be described by

$$\frac{dU_{dc,f}}{dt} = \frac{2}{C_{dc,f} + \frac{C_k}{2}} \left(i_f + i_{dc,f} - i_k - \frac{U_{dc,f}}{2R_{br,eff,f}} \right) \quad (4.23)$$

$$\frac{dU_{dc,t}}{dt} = \frac{2}{C_{dc,t} + \frac{C_k}{2}} \left(i_t + i_{dc,t} + i_k - \frac{U_{dc,t}}{2R_{br,eff,t}} \right) \quad (4.24)$$

$$\frac{di_k}{dt} = \frac{1}{L_k} \left(\frac{U_{dc,f} - U_{dc,t}}{2} - i_k R_k \right) \quad (4.25)$$

where $U_{dc,f}/2$ and $U_{dc,t}/2$ are the *from* and *to* node voltages respectively, i_k the branch current, i_{dc}^+ the nodal current injections provided by the VSC power balance, i_f and i_t the sum of the branch currents connected to *f* and *t*, and $R_{br,eff}$ the effective value of the braking resistors. This system of three first-order differential equations can be cast into state-space formulation, where i_{dc}^+ are the system inputs.

This concept is generalised to arbitrary topologies by considering the MTDC grid as a directed graph using the current direction as a reference, and subsequently determining the adjacency matrix with

$$M_{a,k,j} = \begin{cases} 1 & \text{if branch } k \text{ connects from node } j \\ -1 & \text{if branch } k \text{ connects to node } j \\ 0 & \text{otherwise} \end{cases} \quad (4.26)$$

where \mathbf{M}_a is the $K \times J$ unreduced adjacency matrix, with K and J the total number of branches and nodes respectively. Shunt branches always connect *to* the ground, which is taken as the reference node. The column corresponding to the reference node is removed from \mathbf{M}_a to obtain the adjacency matrix \mathbf{M} , which contains no linearly dependent columns. Using \mathbf{M} , the system of equations of an arbitrarily structured MTDC schemes can be generalised as

$$\begin{aligned} \dot{\mathbf{x}}_{DC} &= \mathbf{f}_{DC}(\mathbf{x}_{DC}, \mathbf{y}_{DC}) = \mathbf{A}\mathbf{x}_{DC} + \mathbf{B}\mathbf{y}_{DC} \\ &= \left[\begin{array}{c|c} -\mathbf{R}_{ch}\mathbf{C}_{aux} & -\mathbf{C}_{aux}\mathbf{M}^T \\ \hline \mathbf{L}_{aux}\mathbf{M} & -\mathbf{R}_{aux}\mathbf{L}_{aux} \end{array} \right] \left[\begin{array}{c} \mathbf{u}_{DC} \\ \mathbf{i}_{br} \end{array} \right] \\ &+ \left[\begin{array}{c|c} \mathbf{C}_{aux} & \mathbf{0}_{J \times K} \\ \hline \mathbf{0}_{K \times J} & \mathbf{0}_{K \times K} \end{array} \right] \left[\begin{array}{c} \mathbf{i}_{DC} \\ \mathbf{0}_{K \times 1} \end{array} \right] \end{aligned} \quad (4.27)$$

where \mathbf{x}_{DC} and \mathbf{y}_{DC} are the state and algebraic input vectors, \mathbf{A} and \mathbf{B} the state and input matrices respectively, \mathbf{u}_{DC} the vector with DC node voltages, \mathbf{i}_{br} the shunt and cable currents, and \mathbf{i}_{DC} the input nodal current injections. The model contains no pure voltage sources, which is assumed plausible for VSC-HVDC transmission.

\mathbf{R}_{ch} is the $K \times K$ diagonal matrix containing the effective dynamic braking resistances in case these are modelled as variable resistances instead of variations in the active power balance. Its elements are given by

$$R_{ch,kk} = \begin{cases} \frac{1}{2R_{br,eff,k}} & \text{if } R_{br,eff,k} \neq 0 \text{ and } k \leq K_{sh} \\ 0 & \text{otherwise} \end{cases} \quad (4.28)$$

The first K_{sh} branches are assumed shunt branches. \mathbf{C}_{aux} is an $J \times J$ diagonal matrix defined by

$$C_{\text{aux},j,j} = \begin{cases} \frac{2}{C_{\text{bus},j}} & \text{if } C_{\text{bus},j} \neq 0 \\ 0 & \text{otherwise} \end{cases} \quad (4.29)$$

where

$$C_{\text{bus},j} = \sum_{k=1}^{K_{\text{sh}}} C_k M_{kj} + \sum_{k=K_{\text{sh}}+1}^K \frac{C_k}{2} |M_{kj}| \quad (4.30)$$

\mathbf{L}_{aux} is a $K \times K$ diagonal matrix containing the cable inductances as

$$L_{\text{aux},kk} = \begin{cases} \frac{1}{2L_k} & \text{if } L_k \neq 0 \\ 0 & \text{otherwise} \end{cases} \quad (4.31)$$

and $\mathbf{R}_{\text{aux}} = \text{diag}[R_1 \ R_2 \ \dots \ R_K]$ the $K \times K$ diagonal matrix containing the cable resistances.

4.3.4 Inclusion of VSC-HVDC into Power Flow Analysis

The state variables in (4.27) need to be initialised correctly. As common with stability type simulations all dynamic model variables are initialised after first executing a single-phase equivalent power flow. Then the models are initialised according to a merit order, depending on the position of the model inside a larger composite model. For PSS[®]E for instance the VSC models are cast into the built-in synchronous generator composite frame, in which the VSC and its outer controls take the generator slot, and the MTDC model takes the governor slot. As a governor allows connection to multiple machines, this enables an interface of variables through the inner arrays of PSS[®]E. A similar approach has been taken for the in-house developed simulation environment.

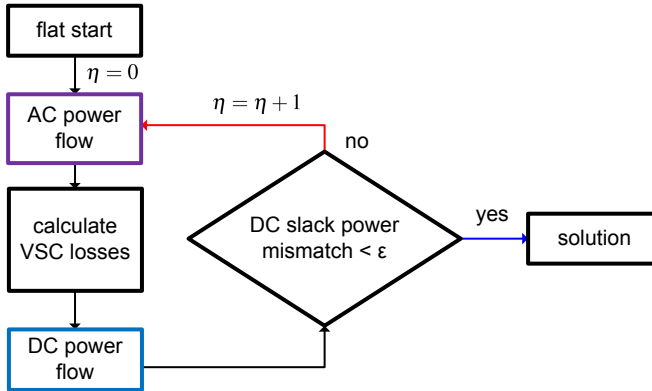


Figure 4.8: Sequential AC/DC power flow algorithm.

Contrary to governing systems, however, the issue here is that the MTDC model must be taken into consideration during the power flow stage of the simulation. This is needed to calculate the initial nodal voltages and branch currents accordingly. To acquire these we implemented the sequential AC/DC power flow algorithm introduced in [150, 151]. Figure

4.8 shows the workflow of this method. The first step is a normal AC power flow calculation that encompasses all synchronous areas. This model represents onshore VSCs as PV or PQ nodes and offshore VSCs as slack nodes. In case a loss model is used for the VSC—we neglect these operational losses—these need to be calculated after convergence of the AC power flow. The third step is a dedicated DC power flow. In general there exist three types of DC nodes: stiff direct voltage, fixed power injection, and voltage dependent power injection. The latter is applied for droop control. As offshore VSCs act as slack sources at the AC side, these must behave as fixed power injections at the DC side. Onshore VSCs can take any type of DC node for power flow analysis. After convergence, the AC-side power injections of the onshore VSCs (PQ and PV) are updated, a new power flow is executed and so on.

The DC power flow generally uses its power injections as a mismatch vector, which implies that VSCs behaving as a AC slack source may new mismatches in the DC grid. Similarly DC slack nodes and droop-controlled converters may introduce new mismatches in the AC side power. Hence, the power flows are executed sequentially until the direct voltages remain nearly constant. For the networks used throughout this thesis there were typically 2 or 3 power flow iterations needed between the AC and DC side.

4.4 Improved State-Space Modelling by Multi-Rate Techniques

The state-space model described in section 4.3.3 allows a generalised way of including MTDC grids into stability-type simulations. This comes at a computational price, however, because the time step size of the entire simulation needs to be reduced significantly. This is unworkable for large-scale systems. The first improvement is to separate the solution of (4.1) of the MTDC system and the VSCs' FRT controls from the rest of the dynamic models, and to simulate these models at a smaller time step-size Δt_{mr} . Moreover, the DC side protection mechanism is now modelled as a variable current source instead of a time-varying resistor. This multi-rate technique is applied through the inner integration loop shown in figure 4.9. A similar approach has been taken in [152], albeit dedicated to LCC-HVDC.

It starts with a forward-Euler integration step of the multi-rate improved model. Then the obtained DC state variables are used to invoke the FRT model, which determines the DC nodal current injections for the next time step of the inner integration loop (i.e., \mathbf{g}_{FRT}). The DC current injection is now given by

$$i_{dc,j,m}^+ = \frac{P_{j,m}}{U_{dc,j,m}} = \frac{(-P_c|_{m=0} - P_{br,j,m})}{U_{dc,j,m}} \quad (4.32)$$

which makes the current injection calculated in \mathbf{g}_{dc} dependent on both the AC-side power available at $m = 0$ and the power drawn by the FRT model. It turned out that including this model into the inner integration loop notably improved the numerical stability of the simulation.

At the end of the inner integration loop, the vectors of the main solution algorithm must be updated to be compliant with both the predictor and the trapezoidal corrector of the stability-type simulation. This is done by calculating the slope based on the first (i.e. $x_{dc,m-\frac{\Delta t}{\Delta t_{mr}}}$), and the last calculated state (i.e., $x_{dc,m}$).

In case numerous corrector iterations are necessary, it is redundant and too time-

consuming to execute the inner-integration loop continually. Therefore, it is assumed that the model is accurate enough to be invoked only during the first corrector step, when $\text{MODE}=3$. The solver of the stability-type simulation then continues with the trapezoidal corrector (i.e., $\text{MODE}=4$).

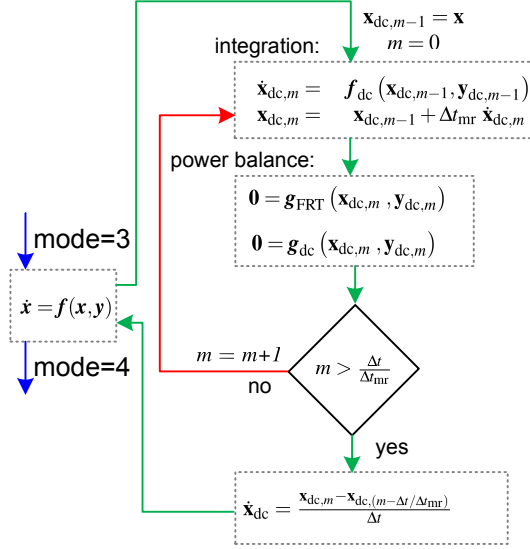


Figure 4.9: Calculation sequence for the inner integration loop of the multi-rate improved model. The inner integration loop is invoked like an ordinary dynamic model, but only between $\text{MODE}=3$ and $\text{MODE}=4$ (see table 4.2).

4.5 Reduced-order State-Space MTDC Model

Another option to enable the stability-type simulation to use a larger time step-size is to reduce the state space model to a one-node equivalent DC hub. An adjusted form of this approach has also been taken in [117]. This copper plate assumption lumps all the pole-to-ground capacitance of both the DC cables and the VSC shunts, and neglects all inductive elements present in the MTDC system. The DC dynamics are then given by

$$\frac{dU_{dc}}{dt} = \frac{1}{C_{dc}} \left(\sum_{j=1}^J i_{DC,j}^+ - i_{br,j}^+ - \frac{P_{loss}(0)}{U_{dc}} \right) \quad (4.33)$$

where U_{dc} is the system-wide direct voltage, $C_{dc} = \sum_{j=1}^J C_{bus,j}$, $i_{DC,j}^+$ the nodal current injections for all J DC nodes, $i_{br,j}^+$ the currents drawn by braking resistors, and $P_{loss}(0)$ the total HVDC cable losses calculated from the AC/DC power flow at $t = 0$.

The merit of using this lumped capacitance is that the introduced time-constant allows simulation at a time-step size of around half a cycle without introducing numerical instabilities. It is also assumed that not the actual value of the direct voltage is significant to the AC/DC interaction, but rather its dynamics. As a matter of fact, the fictitious single DC node does not have an actual location and a choice should be made on the initial value of

this voltage. In this case, the average of all DC nodal voltages at $t = 0$ is assumed as an initial value for U_{dc} . Consequently, the droop characteristics of all VSC models should be shifted to obtain $u_{dc,j}^* = u_{dc}$ for correct initialisation. Note that the reduced-order state-space model precludes the application of more advanced control methods that highly rely on the local direct voltage, like the voltage margin method.

4.6 Simulation Studies

The VSC-MTDC models developed in section 4.3 and their improvements proposed in section 4.4 and 4.5 will now be tested using the transient stability framework described in section 4.2. Before we can draw plausible conclusions about their applicability, however, we first have to assess the validity of the tools we apply for that: the in-house developed simulation framework and the quasi-stationary VSC-HVDC model.

Ideally speaking all these simulations must be performed under similar circumstances, notably control parameters and network topology, AC and DC alike. Unfortunately, the validation and operational simulations have been performed at different stages of this research. As a result, the AC test systems could not be aligned perfectly. Notwithstanding this small inconsistency, all the control parameters, DC-side dimensioning, and WPP models are aligned between the simulation cases conducted in this section. In Appendix C it is shown how these example networks relate to each other.

4.6.1 Simulator Validation Against PSS[®]E and PSS[®]NETOMAC

For validating the in-house developed simulation framework a qualitative approach is used by first creating numerical and operational conditions that are equal or similar across the simulation tools and secondly comparing the time-domain results after invoking a severe disturbance. For the stability part of the simulation it was possible to compare the results with both PSS[®]NETOMAC and PSS[®]E. For the EMT partition of the simulator PSS[®]NETOMAC was the only available tool.

The validity of the simulation framework as such does not strictly need the inclusion of VSC models or otherwise sophisticated devices. As a matter of fact, it is considered desirable to apply the simplest use case possible that still meet the following requirements:

- the network setup is plausible from a power system domain viewpoint;
- the network contains at least one dynamic, non-linear model to trigger the iterative scheme to solve (4.2); and
- the disturbance applied triggers (rotor) angle displacements; these are significant for transient stability assessment.

Although this can have several interpretations, we chose to apply a single-machine infinite bus system, the single-line diagram of which is depicted in figure 4.10. From left to right it contains an external system behind an impedance, a load, a double line circuit to the coupling point, a machine transformer, and a synchronous generator.

The external system is represented as a fixed source behind impedance. In the stability simulation this can be done by setting \underline{E} , PSS[®]NETOMAC natively supports this too, and in PSS[®]E this can be achieved by the GENCLS (i.e., the 2nd-order classical generator model,

which contains the swing equation only) dynamic model setting the inertia to infinite. The source impedance is calculated according to a short circuit power of 5000 MVA at nominal voltage of 230 kV, and an R/X ratio of 0.1.

In each simulation the load is modelled as entirely voltage dependent as a shunt impedance based on the voltage resulting from the power flow. No ZIP load is used here as the system would then contain multiple dynamic models, which does not contribute to the validation as such.

The double line circuit and the machine transformer have been modelled by series impedances. The lines are 50 km long and common line parameters have been selected from [153]. The machine transformer is rated at 192 MVA and has a short circuit voltage of 10% (reactive).

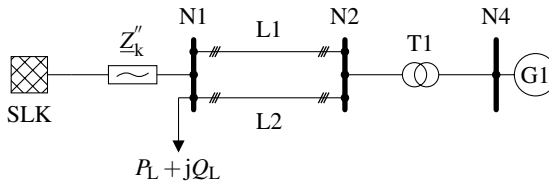


Figure 4.10: *Single-machine infinite bus system used for validating the in-house developed simulation framework.*

The local generator is a round rotor synchronous machine, the parameters of which have been adopted from G2 of the IEEE 9-bus system (see Appendix C). For the sake of simplicity no excitation and governing systems have been applied. The excitation voltage and mechanical power are hence assumed fixed. In PSS[®]NETOMAC and the in-house developed simulator the synchronous generator is modelled by the common Parkian representation: the 6th and 8th order models for the stability and EMT partitions respectively. In PSS[®]E the GENROU model is applied, which is mathematically identical but uses operational parameters instead. As the generator model of PSS[®]NETOMAC is grey-boxed (i.e., block diagram available but numerical implementation not) we also implemented a user-written machine model that replicates the equations from the program manual, and hence [153], and uses the grid interface proposed in [147] to sustain the network solution. For the stability part our synchronous generator model is implemented as in [147]. For the EMT partition we apply a grid interface similar to [154], though the compensation current needed meticulous fine-tuning and exact reproduction of the results from [154] was not attained.

Figure 4.11 shows the time domain response of the system after a 180 ms fault at N1. It compares the various simulation platforms used throughout this thesis. The stability simulation is shown in all plots whereas the EMT simulation results are limited to the rotor angle response of G1. We can make the following observations concerning the response:

- The clearing time is high, which can be observed by the back swing in the generator voltage response (i.e., figure 4.11a). From a comparison angle this is desirable as it highlights the differences between the simulations.

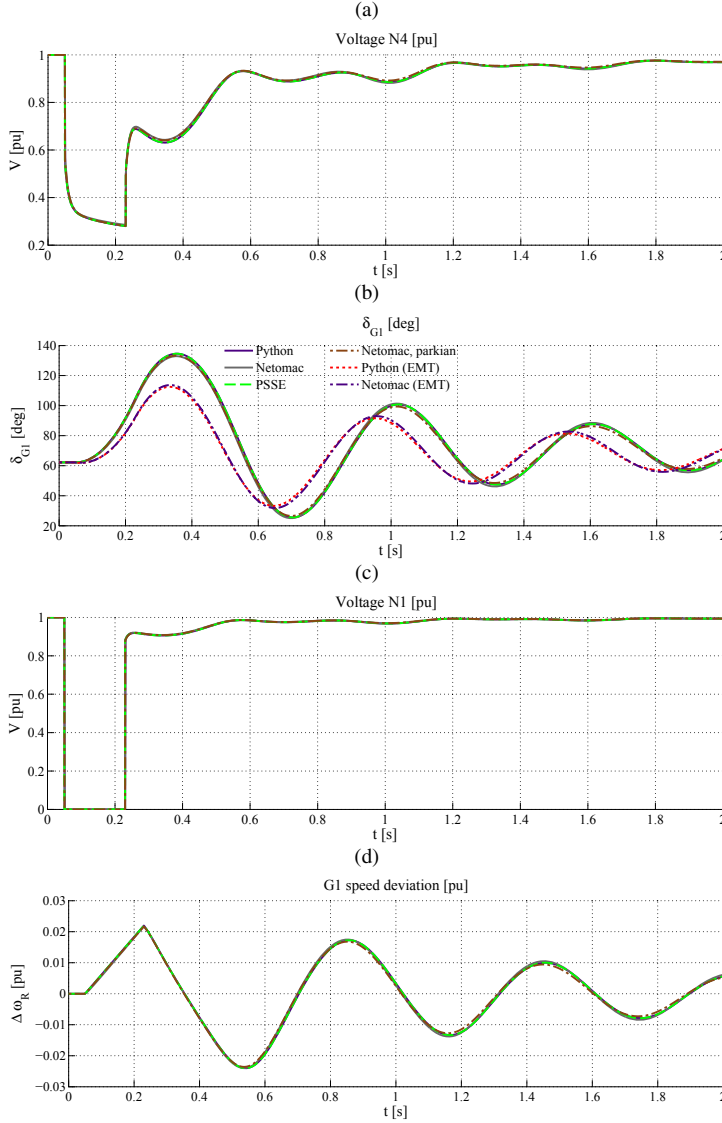


Figure 4.11: *Dynamic response of G1 after a 180 ms three phase fault at N1, (a) terminal voltage G1, (b) rotor angle δ_{G1} , (c) voltage magnitude N1, (d) per unit rotor speed deviation of G1. The rotor angle response is shown for both stability and EMT simulations.*

- All stability generator models show similar damping time constants and oscillation frequencies.
- The stability part of the hybrid simulation exactly coincides with the time domain response of PSS[®]E.
- PSS[®]NETOMAC differs at most around 5 % from PSS[®]E and the in-house developed stability simulation. This difference is most prominent in the voltage magnitude im-

mediately after fault clearance, and the maximum rotor angle excursion.

- The Parkian 6th order generator model implemented into PSS[®]NETOMAC as a custom generator model behaves similar to the built-in generator model. It also shows noticeable differences with PSS[®]E and the in-house developed stability simulation.
- The EMT rotor angle response appreciably differs from the ones obtained by the stability simulations, which is plausible considering the differences in network and modelling accuracy. Although not exactly equal to the reference, our EMT simulation tracks the response of PSS[®]NETOMAC within a few %. This is considered sufficient as 1) no widely accepted open-source EMT tools could be employed and 2) the generator model and its network interface algorithm are grey-boxed.

We can gather from the simulation results that the built-in dynamic model of PSS[®]NETOMAC is mathematically equivalent to the Parkian model and the observable differences with PSS[®]E can be attributed to either differences in numerical solution algorithms, or the machine-network coupling. The investigation of the observed discrepancies are beyond the scope of this thesis and we hence consider the stability simulation developed for this thesis successfully validated against PSS[®]E, and the EMT part validated against PSS[®]NETOMAC.

4.6.2 Validity of the Quasi-Stationary Model

While the models introduced in section 4.3 are a common approach for normal operating conditions (e.g. AC voltage and frequency variations, wind fluctuations) [148], the applicability during FRT conditions requires also a proper inclusion of the device's protection discussed in Chapter 3. In practice, their operating region depends among others on the bandwidth of the inner current controller, the IGBT switching scheme, the harmonic regime, and the power electronic topology. This gives rise to the need for a comparison between the discussed model and a detailed EMT-type model that does not neglect these aspects.

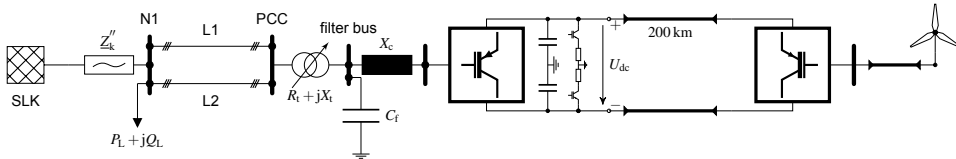


Figure 4.12: Test circuit for validation of the quasi-stationary VSC model.

The single line diagram of the test system that we apply for this purpose is shown in figure 4.12. From left to right it consists of a transmission system equivalent akin to that in figure 4.10, and a 200 km point-to-point VSC-HVDC link that connects a WPP to the shore (right). The AC system properties are equal to the system used in section 4.6.1, except for the rated voltage, which is 380 kV. The generator and the machine transformer have been replaced by a 600 MW VSC that is grid connected by a transformer, filter, and phase reactor configuration. The short circuit voltage of the grid interface equals 10%, and Z_c was equally split into a phase reactor and a step-up transformer. The VSC applies a switching frequency of 1950 Hz, the harmonics of which are filtered accordingly by a 45 MVar filter. The AC system contains no generator as it is desirable to exclude machine dynamics hence making the comparison of the individual VSC models more accurate. The nominal pole-to-neutral direct voltage equals 320 kV and cable parameters have been applied from [155].

The offshore WPP is aggregatedly represented as a single full converter generator model. The offshore VSC applies direct control and hence acts as a slack to the rest of the WPP. FRT is achieved by a dynamic braking resistor installed at the onshore substation.

The EMT simulation was done in Matlab/Simulink by employing a two-level, PWM modulated VSC using the standard blocks of the SimPowerSystems toolbox. The inner current controller of this model is based on [156]. The quasi-stationary model was implemented as a user-written model in PSS[®]E version 33. All outer control parameters as well as the FRT thresholds and state transitions were harmonised between the two simulations. The Simulink model employs a fixed time-step size of $50 \mu\text{s}$, while in PSS[®]E Δt had to be selected as small as $100 \mu\text{s}$.

Figure 4.13 shows the response of the VSC models to a 1 pu symmetrical voltage sag in the external system (SLK). After clearance, the VSC recovers its active power with a recovery rate of 5 pu/s. The peaks in V_{PCC} and $i_{\text{c,d}}$ at fault ignition and clearance can be mainly attributed to

1. the power electronic characteristics and the PWM response of the device, which for a very short instant causes a large voltage difference between the DC-side and the PCC, and
2. the response of the inner current controller, which has to quickly reduce this current but has bandwidth limitations (e.g. measurement delays). For the quasi-stationary model these transitions are algebraic and hence instantaneous.

The direct voltage response shows that for both models the dynamic braking resistor is able to restrict the voltage to at most 5% above nominal. After the onshore active power has been fully recovered the voltage returns to its nominal value.

In general the discrepancy between the two models is relatively small, notably at the onshore power system side of the VSC-HVDC link. The response of the variable that mainly determines the interaction between VSCs offshore—the direct voltage—compares well to the detailed EMT model even during the fault. This allows using the quasi-stationary model for the FRT and post-FRT actions in the transient-stability time frame, which is our main focus after all.

4.6.3 Comparison between Transient Stability Models

The MTDC models discussed in this chapter will now be tested for computational performance and modelling accuracy. The former is measured by tracking execution times. The latter is measured by comparing time-domain responses to each other while considering the full-order state-space model as a reference. This model is considered the most detailed of the discussed stability models and is hence taken as a reference simulation.

The benchmark system is shown in Figure 4.14. It contains 2 identical Western System Coordinating Council (WSCC) 3-generator, 9-bus systems [157]. The generator parameters of this system can be found in Appendix C. These two systems are connected by a 3-terminal VSC-HVDC scheme that interlinks a 600 MW offshore WPP (VSC2). In order to effortlessly absorb all wind power, the active parts of all loads have been doubled. Furthermore, all generators have been equipped with standard TGOV1 governing and SEXS excitation systems. VSC1 and VSC2 are in vector control mode, using continuous AC voltage magnitude control by (3.31) and a direct-voltage droop regulation to control the power exchange with the

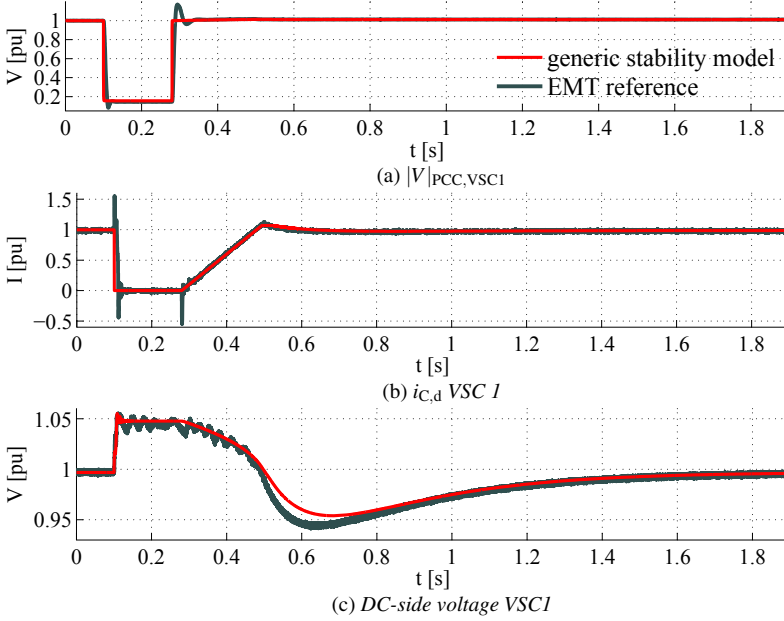


Figure 4.13: Response of the VSC-HVDC link after an onshore fault for both the quasi-stationary VSC model described in section 4.3 and a detailed EMT-type model.

AC-side (i.e., figure 3.9). In case the VSCs' current limits are hit, the current references are curtailed proportionally across $i_{c,d}^*$ and $i_{c,q}^*$.

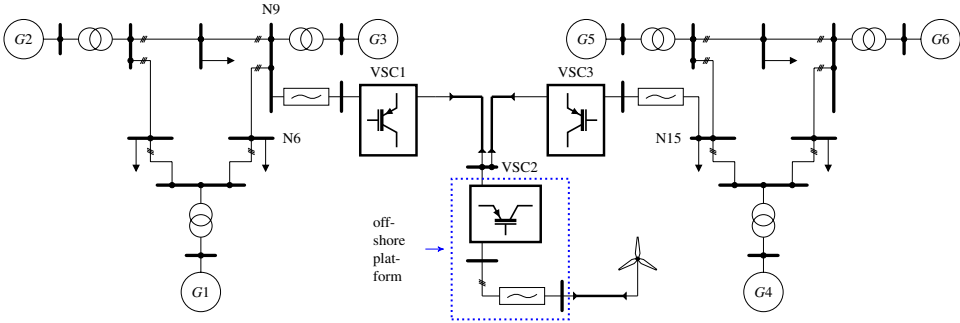


Figure 4.14: Test system used for comparing the proposed VSC-HVDC dynamic models for transient stability analysis.

Disconnection of the offshore WPP

First, the system will be subject to a load rejection by VSC2, which in practice amounts to disconnection of the entire WPP. From a system viewpoint this disturbance is quite significant: around 300 MW needs to be balanced in each onshore system. Figure 4.15 shows the system reaction and compares the three discussed MTDC dynamic models.

It can be seen that the power imbalance caused by VSC2 causes the direct voltage to drop quickly. The direct voltage droop controllers of VSC1 and VSC2 react to this by practically stopping their active power output. This results in a situation where the governing systems in both AC systems have to re-establish the power balance.

Despite the severity of this disturbance—half of all generation in the system is lost—its influence on the response of the individual MTDC models is not clearly perceptible. The trace of the rotor angle of G1 closely follows the reference simulation for both the multi-rate improved model and the reduced-order HVDC model. From a transient-stability viewpoint, it can hence be concluded that all three dynamic models suffice for the given disturbance.

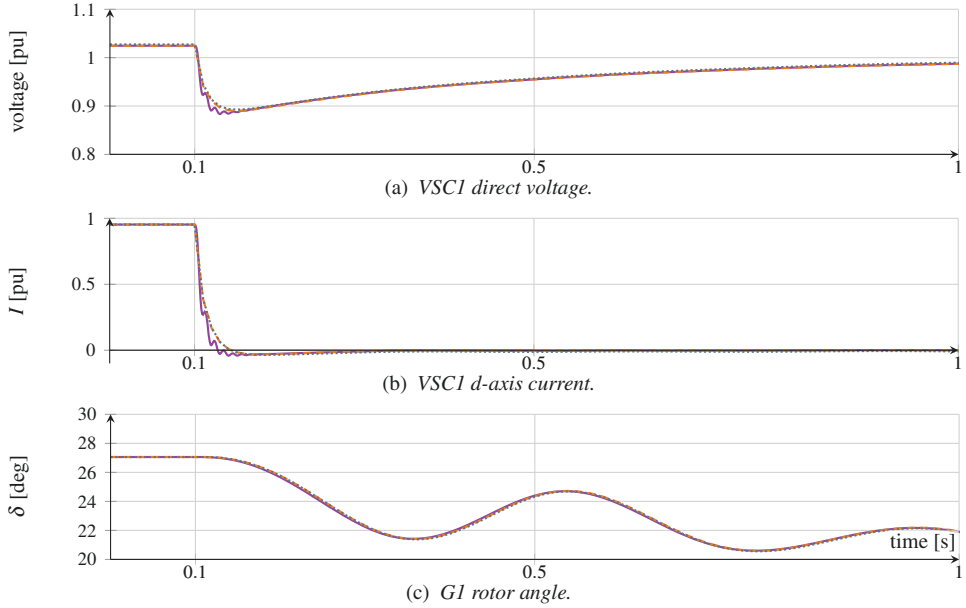


Figure 4.15: Time-domain results after a 600 MW load rejection by VSC3 for 3 types of HVDC modelling: state-space (solid, purple), multi-rate (dashed, orange), and reduced-order (dotted, grey).

Short circuit in the transmission system

Next, the models will be compared for the system response following a bus fault at N6, which self-clears after 180 ms. For this situation the HVDC system is operated asymmetrically. That is, the output of the offshore WPP was changed to 180 MW while VSC3 injects 125 MW into the DC scheme. To achieve this unit commitment, the loads in the right WSCC system were restored to their original values. Figure 4.16 compares the respective MTDC models for a 2 s simulation run.

The short-circuit at N6 induces a voltage drop at N9, which causes VSC1 to violate its current limit thus limiting the power infeed to the AC side. As a result, the direct voltage starts to rise without causing VSC1 to enter the FRT state. However, U_{dc} at VSC3 passes its 1.1 pu threshold value too (figure 4.16c) and as a result, its braking resistors are also activated, dissipating all excess energy in the DC system. After fault clearance, the VSCs

swiftly recover their power infeed to the AC system and switch to the normal operating state. Hence, the FRT of the MTDC system was achieved successfully.

The differences between the reduced-order HVDC model, the state-space, and the multi-rate improved dynamic models are now more prominently visible. In particular, $i_{c,d}$ of VSC1 and the resulting deviation of the rotor angle dynamics. The discrepancy between the reduced-order HVDC model and the reference simulation is caused by the fact that by design just one direct voltage is available to the VSC models. U_{dc} initialises at the system's average. For the reduced-order HVDC model, the FRT system of VSC3 does not trigger on the elevated direct voltage, as is the case with the other MTDC dynamic models. This is an immediate consequence of the model reduction – the FRT models use the local direct voltage as an input – and hence leads to the shown inaccuracy.

Computational Performance

Table 4.5 shows the execution times of all simulations, which were performed on a Microsoft Windows 7 workstation containing an i7-2630QM CPU and 4GB RAM. The entire simulation environment was implemented by Python scripting without further optimising the computational functions. Therefore, the shown execution times are much higher compared to (commercial) compiled software. PSS[®]E for instance, was able to simulate the first case faster than wall clock time using the multi-rate improved model and $\Delta t = 5$ ms.

Case 1 (figure 4.15) had a simulation time of 1 s whereas the simulation time of case 2 (figure 4.16) was 2 s. It can be observed that the case in which a short-circuit was simulated took much longer compared to the first case. This difference can be attributed to the amount of re-calculations of the Jacobian matrix, which much way higher in case of simulating the short-circuit.

Nevertheless the differences between the MTDC models in computational performance are plainly observable. Due to the small time constants in the DC system, the state-space MTDC model had to be simulated at a smaller time-step size for the entire network, which strongly reduces the efficacy of the stability-type simulation as an instrument to assess the transient stability of large power systems. The multi-rate improved MTDC model turns out to be an excellent alternative, also from an execution time point of view.

Model	Δt	Δt_{mr}	figure 4.15	figure 4.16
state space	1 ms	n/a	50 s	500 s
multi-rate	10 ms	100 μ s	17.6 s	111 s
reduced-order	10 ms	n/a	10.7 s	82 s

Table 4.5: *Simulation time step-size and absolute execution times.*

4.7 Summary and Conclusions

This chapter dealt with the inclusion of averaged VSC-HVDC models into transient stability simulations, and hence aimed at answering the second research question stated in the Introduction. Although some commercial simulation packages offer vendor-specific VSC-HVDC link models, they mostly do not contain relevant electromagnetic transient phenomena. This

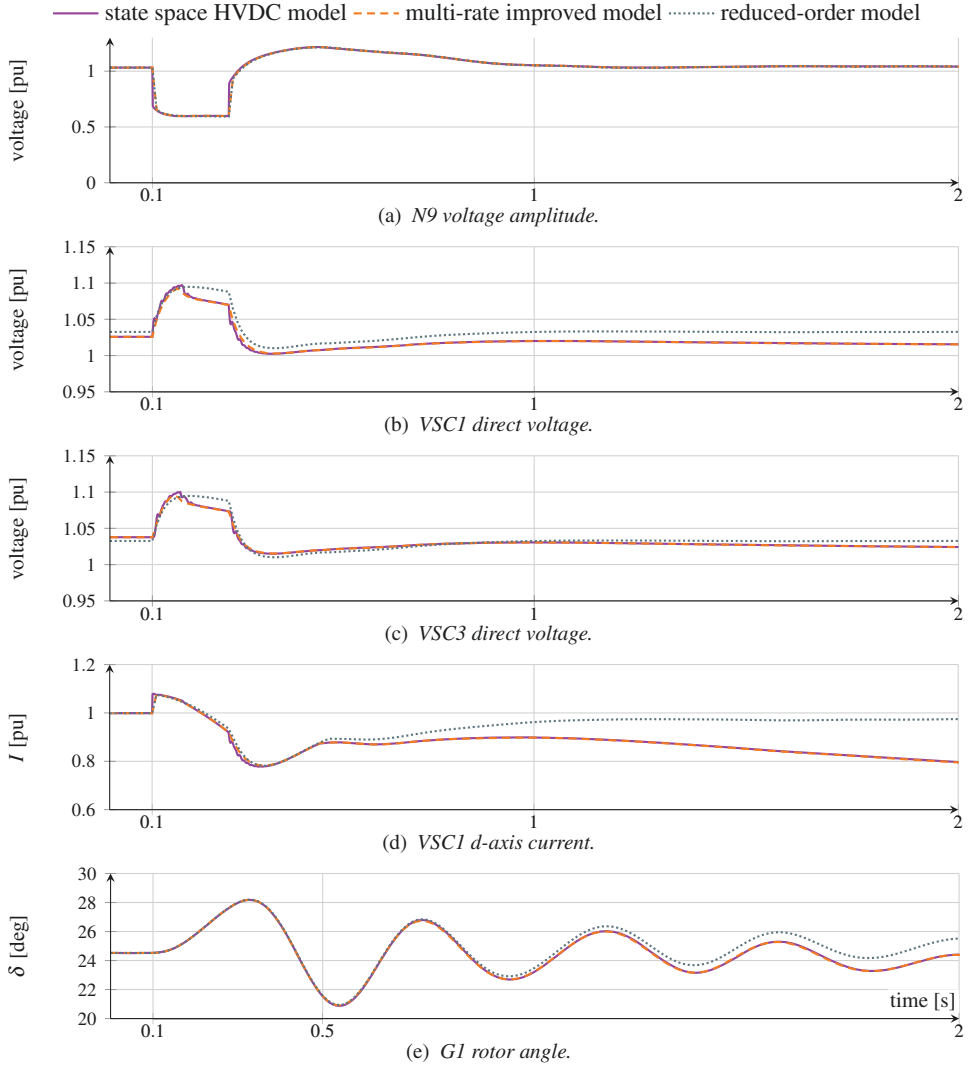


Figure 4.16: System response after a 180 ms bus fault at N6 for 3 types of HVDC modelling: state-space (solid, purple), multi-rate (dashed, orange), and reduced-order (dotted, grey).

makes these models only valid for point-to-point connections and can in general not be extended to multi-terminal VSC-HVDC networks.

It was shown in which way the VSC model discussed in chapter 3 can be simplified for stability-type simulations. Both onshore and offshore VSCs are assumed to be modelled as Norton current injections. Considering the bandwidth needed for the respective controllers, and the electromagnetic transients that might interact with some of these VSC controls, it was shown that the inner current controller can be safely disregarded. The response of the phase locked loop model depends on the reference frame adopted for the AC network model. If the designed bandwidth of the PLL is high compared to the time step size of the stability-type simulation, the VSC can be assumed to be continually aligned with the PCC voltage,

and the PLL dynamics can be simplified to a first-order delay.

Using the above simplifications, the VSC model was extended with a state-space model of a VSC-MTDC system. This model allows a systematic coupling of onshore and off-shore VSCs through any desirable grid topology. The VSC-MTDC model was successfully validated against a two-level VSC model in Simulink. The small time constants inside the combined VSC-HVDC state-space model force the entire simulation to be executed using a small time step-size for numerical integration. This results in unacceptably long simulation times.

One of the available alternatives is to simplify the HVDC dynamic model in such a fashion that only those phenomena that significantly influence the AC system-level behaviour are contained in the dynamic model, and that irrelevant dynamics are excluded. In this case, all DC-side inductances and resistances have been neglected, while all pole-to-ground capacitances were lumped together at one central node. This copper plate assumption results in just one eigenvalue (and equivalent time constant) for the entire HVDC system, and allows simulating the combined power system at workable simulation speeds. However, the gain in execution speed comes at the expense of modelling accuracy. The copper-plate assumed VSC-HVDC system was tested on a hybrid AC/DC topology. Since only one lumped DC node is present, those device models that require the local direct voltage as an input will show inaccurate behaviour, also on AC system level.

Another alternative is to employ multi-rate methods. This chapter showed that the HVDC model can be wrapped by an internal integration loop, which applies a smaller time step-size than the main stability-type simulation. Together these comprise the dynamic model of the DC-side of the system, using the VSC as an interface model. Several aspects of this construction have been analysed in detail. It was shown that the VSCs fault-ride through equipment should be included into the inner integration loop as well to improve numerical stability. The applied predictor-corrector method forces multiple dynamic model calls per integration step. In this respect, it was shown that disregarding the HVDC model in the trapezoidal corrector did not lead to significant impairment of numerical stability or loss of system-level simulation accuracy. This gives rise to a simplified numerical solution and thereby alleviating the computational burden.

This chapter also detailed the in-house simulation framework that is used as a test bed for this and the next chapter. The stability-type simulation was validated against the dynamic layer of PSS[®]E. This was done by using a SMIB network with and without electric machinery in order to distinguish between the solution of the differential system and algebraic system of equations. It was shown that although strictly speaking mathematically not identical, the network solutions of the developed stability-type simulation and the PSS[®]E reference case are in concordance with each other. Therefore, the described stability-type simulation can be considered sufficiently well validated.

The EMT-type simulation was compared against the EMT partition of PSS[®]NETOMAC. The synchronous machine models are based on the 8th-order Parkian model and using equivalent circuits for the direct and quadrature axes. The SMIB system response showed slight differences between the investigated simulations. This difference was most prominently visible in the synchronous machine rotor angle and speed excursions. The differences became relatively smaller when reducing the time step sizes for numerical integration. Notwithstanding this small issue, the EMT-type simulation is considered adequately validated to act as a testbed for the new modelling approaches developed for this thesis.

Chapter 5

Simulation of VSC-MTDC by Hybrid Methods

This chapter is about the development of hybrid simulation methods to study the dynamic interaction between AC and VSC-HVDC grids, thereby addressing RQ2 from a different angle. ¹. Hybrid EMT/stability simulations allows integrated AC/DC systems to be studied accurately without compromising on the simulation speed merit of transient stability simulations.

Existing methods that have been previously considered and applied in literature are taken as a starting point for the application to VSC-HVDC. It will be shown that existing interfacing techniques exhibit undesired dynamic behaviour. Therefore, several adjustments are implemented to improve the accuracy of the VSC-HVDC model response. Simulations on a variety of test systems under several sensitivities demonstrate a generalised applicability of these improvements.

5.1 Introduction

Chapter 2 and 3 addressed the deployment of renewable energy sources and power electronics at high-voltage level in the past decades, and their respective modelling and control as assumed in this thesis. Subsequently, chapter 4 put forward the need for advanced modelling and simulation methods, which is chiefly induced by the increased stiffness of the entire system. Several ways of modelling MTDC grids in stability simulations have been treated, validated, and compared. Moreover, a hybrid simulation environment that enables detailed study of such models as well as their underlying solution mechanisms was described and validated, for stability and EMT alike.

Combining several types of simulations can resolve many of the aforementioned challenges, notably accuracy versus speed. This approach stems from the perception that only those parts of the system that need sophisticated and (highly) detailed modelling are simulated by electromagnetic transients simulations. The lion's share not needing this level of detail is incorporated by stability-type simulations. The two simulations are coupled or *interfaced* by placing equivalents of both systems into each other. These equivalents are

¹the material of this chapter is based on [D , U , V , W , AA]

updated at predefined instants according to an *interaction protocol*.

Hybrid simulations offer noteworthy flexibility with respect to separate stability-type and EMT-type simulations. For instance when the study needs models available in distinct simulation tools. Combining these models would require either considerable model simplifications, or (re-)developing simplified models inside detailed simulation environments. A more practical situation is when one vendor-specific model is only available in a particular simulation package as a closed source model. In these cases, coupling several simulation tools through their respective application program interface can alleviate the effort needed to build the entire case study.

The interfacing techniques involved with such combined or hybrid EMT-type and stability-type simulations have been developed over the past decades. This chapter investigates to what extent the existing methods suffice for studying the VSC-HVDC models developed for this thesis, and proposes improvements for the concerned interfacing techniques. These include

- an improved procedure to update the equivalent sources in the EMT-type simulation after disturbances in the stability-type simulation;
- an advanced interaction protocol that enables causal first-order hold filtering of quasi-stationary voltage and current phasors; and
- a special interaction protocol for determining the voltage and current quasi-stationary phasors from the AC waveforms present in the EMT-type simulation.

This chapter is organised as follows. Firstly, the need for an advanced simulation approach will be elaborated upon, which is followed by a survey of the current state-of-the-art in terms of hybrid simulations and interfacing techniques. Secondly, the implementation of the hybrid simulation in this thesis is explained. This chapter continues by investigating the applicability of various existing interfacing techniques to multi-terminal VSC-HVDC. Subsequently, various improvements are introduced to include VSC-HVDC systems into hybrid simulations more accurately. These methods will be tested on a single-VSC and a multi-terminal VSC-HVDC test system respectively. The chapter concludes with an overview of the main findings.

5.2 Literature Overview and Contribution of this Chapter

5.2.1 Literature Overview on Co-Simulations

Combined simulations, or *co-simulations*, couple two or more simulations to each other, investigating the integral behaviour of a system. Apart from power engineering [158–160], co-simulation find its application in a multitude of engineering areas, such as control engineering [161], mixed communication/physical systems [162, 163], building performance systems [164], and embedded systems [165]. Co-simulations are being applied for mainly two reasons:

- to overcome significant modelling differences between the concerned (sub)systems;
- to resolve the differences in (numerical) solution routines; and

- for computational merits such as parallelisation and distributed computing;

First, the *multi-physics* system of interest may consist of several subsystems, each of which exhibits a unique physical behaviour. As a matter of fact, these subsystems are commonly investigated separately using sophisticated modelling and simulation paradigms, being based on a profound set of assumptions which have evolved over sometimes even decades. Including such subsystems into one particular monolithic approach is generally impracticable, and the exchange of model outputs between separate simulation at (pre)defined instances is therefore a promising alternative.

Second, the computational aspects of a monolithic procedure (i.e. representing different physical models and or systems into one solution routine) can be prohibitive. This especially holds for the occasions in which the numerical solution methods of the respective subsystems differ in design and complexity. These aspects include for instance event-driven systems such as state-machines and communication networks, which are commonly implemented as discrete simulations [166]. For physical systems on the other hand, it is customary to represent the behaviour by continuous differential equations, which are usually being solved discretely by numerical integration.

Third, even if the numerical solution routines were compatible with each other, allowing a monolithic approach, the entire simulation could lead to disproportionately long computing times. One example in the scope of this thesis is the difference in time step-sizes between the numerical solution routines of EMT and stability-type simulations. The system itself can be represented in either simulation environment relatively easily. However, the stiffness of the resulting models will lead to unworkably long simulation times. This gives rise to executing such simulations separately while synchronising their outputs at predefined instances or specific events in either system.

For time-domain studies, mainly two simulation workflows exist: serial and parallel. Figure 5.1 shows such a workflow for a co-simulation of two simulations. Irrespective of the physical systems being simulated and their solution algorithms, the two simulations exchange outputs at predefined instances during runtime following an *interaction protocol*. Either simulation shall contain an *interface model* that processes outputs from the other simulation to create an input for its own system, and vice versa. The series or *sequential* approach shown in figure 5.1a generally has two such interfacing instances per overall simulation step, which corresponds to one discrete time step here. The sequential workflow makes it necessary to execute both simulations in succession and thereby introducing an additional waiting constraint. The parallel simulation approach shown in figure 5.1b bears the advantage to be more flexible in terms of interfacing instances and parallelisation of the numerical solutions, amongst others. Several implementations and numerical issues of co-simulations have been elaborated and formalised in [167, 168].

We focus in this thesis on time-domain simulations of power system electromagnetic transients and electromechanical interactions. In spite of demonstrating noticeable resemblances to each other—both phenomena occur in the same system and their numerical solution methods are strictly speaking compatible—the stiff nature of the resulting monolithic approach inhibits workable simulation speeds. Consequently, our motivation to adopt a combined simulation approach stems from the computational merits involved.

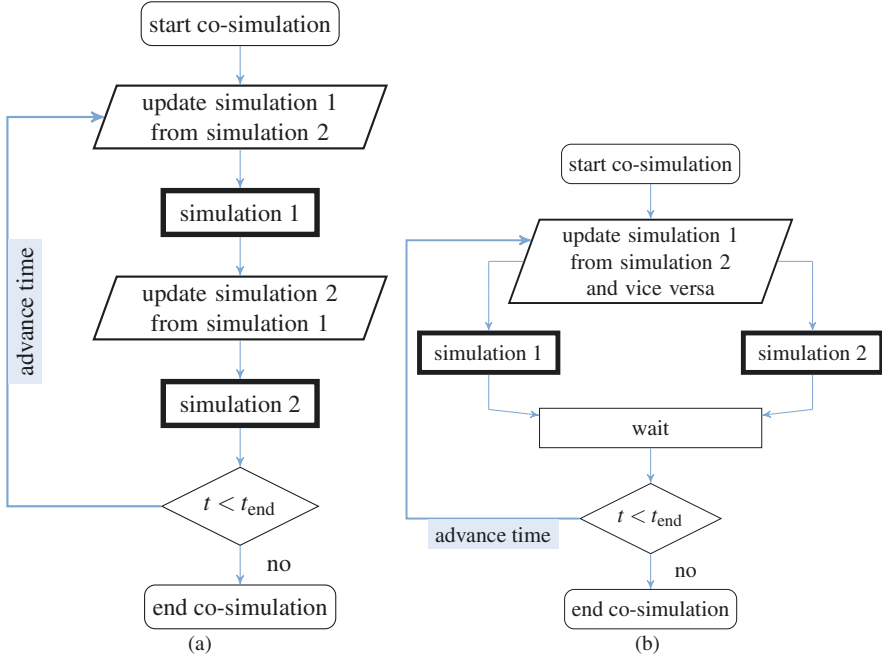


Figure 5.1: Co-simulation synchronisation workflows. a) serial, b) parallel.

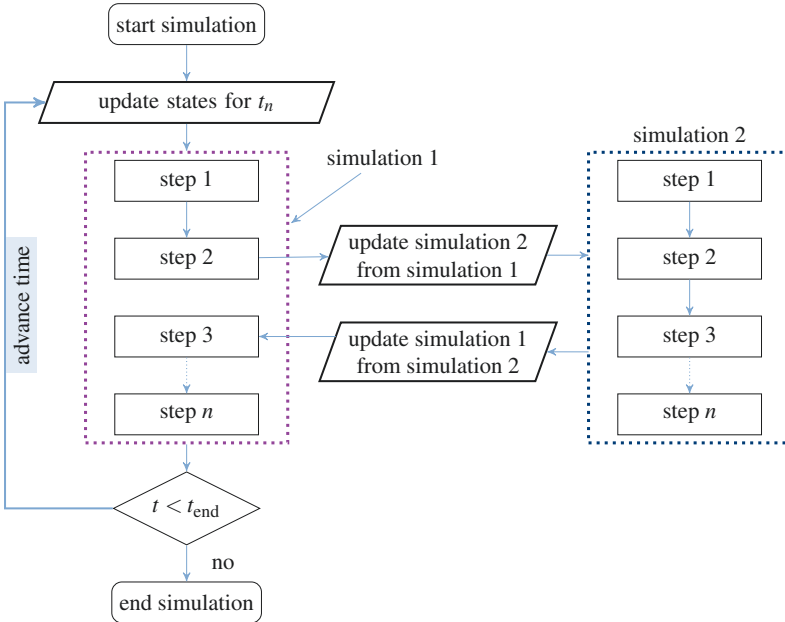


Figure 5.2: Hybrid simulation workflow. Simulation 1 acts as a master simulator, which dictates the interfacing steps of simulation 2.

Hybrid Simulations

A special case of combining two simulations is the hybrid simulation approach, the workflow of which is shown in figure 5.2. It can be seen that contrary to purely co-simulation in which both simulations are practically separated, hybrid simulations embed a secondary simulation into the main simulation environment, and thereby acting as a master. Although both hybrid and co-simulations have no formal definition in the restricted sense, this is their main difference. Assuming that all partitions of a hybrid simulation consist of a number of consecutive steps, the main simulation invokes the embedded simulation and uses the interfaced output of this simulation as an input for the main numerical routine. Figure 5.2 shows a sequential hybrid simulation but basically a parallel approach could be applied as well: the interfacing instances would in such cases be different, and should not necessarily be the next consecutive step of the main simulation.

On the one hand, hybrid simulations allow more flexibility from the application viewpoint as interfacing instances should not strictly be at the start or end of each calculation step (i.e. time step) of the main simulation. On the other hand, solution routines are usually not the parts of simulations that are easily accessible, or the end user desires to adjust anyway. Notwithstanding these issues, the nature of the numerical solution schemes and interfacing techniques are largely similar for co-simulations and hybrid simulations. We therefore assume the results of this research, applying a hybrid power system simulation, to be applicable to both.

5.2.2 Literature Overview of Hybrid Stability and EMT simulations

The wide variety of devices and equipment comprising the power system entails a broad spectrum of physical phenomena. These range from local and device-specific electromagnetic transients to the electromechanical swings of electric machinery and even inter-area oscillations. The prohibitive computation power during the emergence of digital simulation of power system phenomena in the time-domain converged in mainly two simulation approaches:

- electromagnetic transients (EMT-) type simulations [169]; and
- Stability-type simulations [170, 171];

EMT-type simulations aim to focus on fast interactions between the installed equipment and their interface to the grid, the geographical impact of which is commonly limited. They require a detailed representation of the physical behaviour of the devices involved and their surrounding network, which needs the time step-size for numerical integration in the μ s range.

Stability-type simulations, sometimes also referred to as quasi-stationary simulations (QSS) or transient stability simulations, aim to study phenomena with a bandwidth between 0.1 Hz and 10 Hz. This comprises rotor angle stability, voltage stability, and frequency stability, amongst others. The quasi-stationary modelling of some devices and network connections of stability-type simulations permit a larger time step-size, in the ms range, yet allowing simulation of large networks.

Both types of simulations investigated separate aspects of the grid integration of new plants and other devices, which fit well into the computational restrictions at the time. The increased penetration of power electronic devices at high-voltage level, mainly bulk HVDC

transmission, gave rise to the development of time-domain models for grid integration studies. These models were either purely static [172] or included elementary DC-link and control dynamics for EMT-type simulations [173] and for transient stability simulations respectively [174]. It was reckoned that HVDC links, especially during discontinuous events such as commutation failures, would affect the transient stability [175, 176]. A more detailed representation of the entire HVDC link and its surrounding AC network was therefore indispensable.

As a first approach to more accurately assess the transient stability aspects of HVDC links was to couple the quasi-stationary AC machine and network modelling and the wave-shape transient modelling of the HVDC link and its AC mains circuit. This has been outlined in three now classic papers on combining EMT-type and transient stability-type simulations [177]. The approach was to simulate the combined AC/DC system using the stability type simulation until a disturbance occurred at the AC side of the HVDC connection terminal. The network was then split into an AC part and an HVDC part, using the AC sides of the coupling transformers as the *interface node*. The AC part was included into the stability-type simulation and contained a Thévenin representation of the HVDC link at its connection terminals. In the same fashion, the HVDC part was implemented into the EMT-type simulation, and contained a Thévenin equivalent of the connected AC system. By sequentially executing the stability-type and the EMT-type simulation during the fault, both system equivalents were adjusted accordingly, based on their mutual apparent power exchange, and the accuracy mismatch between both equivalents.

This simulation concept has been improved over the past decades [178]. In [179], the interface between both types of simulation was generalised to not merely contain LCC-HVDC links, but also larger network segments or even multiple interface nodes. Moreover, the analysis showed that the optimal location of the interface bus depends on the harmonic distortion as well as the unbalances observed around the interface node. The authors also proposed a list of modifications for EMTP to implement such a hybrid simulation. Later publications showed numerous accuracy improvements from a physical modelling viewpoint [180, 181], from a numerical perspective [182–187], and in terms of the inclusion into existing simulation tools [188].

The existing research focuses mainly on the representation of the stability part of the hybrid simulation into the EMT-part. This is mainly brought about by the desire to study device design and their compatibility with the network. Such studies needed a correct AC system representation inside the EMT-type simulation across a wide frequency spectrum. This gave rise to the development of comprehensive frequency dependent network equivalents to facilitate highly detailed device modelling [189, 190].

The current challenge of assessing the transient stability effects of the massive integration of VSC-HVDC connections requires the phenomena and controls causing such fundamental-frequency effects to be sufficiently implemented into the corresponding models. The design of VSCs allows practically reduced AC-side modelling, whereas detailed controls and DC-side representation is a strict requisite. The emphasis on the large-scale AC system aspects makes our focus different from the existing body of work; the hybrid simulation approach is in this case rather a substitution of the relatively slow state-space model discussed in chapter 4 and an alternative to its multi-rate implementation.

5.2.3 Contribution of this Chapter

Generalised modelling of (multi-terminal) VSC-HVDC in stability-type simulations by hybrid methods has not yet been reported in literature, while it is key for assessing future combined AC/DC transmission expansions. This chapter contributes knowledge on the implementation of the VSC-HVDC models discussed in chapter 3 into such hybrid simulations, and specifically addresses the sub-question of RQ2:

Given the modelling assumptions, fault ride-through implementation, and control strategies of VSC-HVDC, how can averaged EMT models be interfaced universally with transient-stability simulation tools?

During the analysis, it is studied how the existing interfacing techniques and numerical methods comply to the behaviour of VSC-HVDC. Based on the findings obtained, we propose improvements and adjustments to the current state-of-the-art. More specifically, this chapter contributes on the following subjects:

1. Testing the response of the hybrid simulation with a VSC-HVDC link in the EMT partition and compare the behaviour of the interface variables to a co-simulation implementation of such a system under test;
2. The development of an improved procedure to update the Thévenin equivalent sources in the EMT part of the simulation;
3. An advanced interaction protocol allowing causal first-order hold processing of the Thévenin source value sequences;
4. A special interaction protocol to determine the voltage and current quasi-stationary phasors from the AC waveshapes present in the EMT part of the simulation.

Firstly, a comparison will be made between two specific implementations of a conventional interaction protocol. This provides insight in the merits a hybrid simulation could have compared to a pure co-simulation. In order to assess the challenges VSC systems yield for these existing interfacing techniques while retaining the same physical modelling, the same methods are applied to a purely passive system (i.e., no dynamic models involved in the entire system under test). These simulations will show us that the current interfacing techniques are deficient for the suggested VSC modelling, nourishing the need for extensions to the existing state-of-art.

Subsequently, we will focus on the specifics of the performance of the developed averaged VSC models in the proposed hybrid simulation framework. To make the mutual interaction between the EMT part and the stability part of the simulation more accurate, several interfacing techniques and numerical procedure improvements as well as their implementation into the simulation environment are suggested.

To verify the obtained findings on simulation speed and accuracy, we compare the results to both a pure EMT-type implementation of the applied cases, and an implementation into a stability-type simulation using the state-space model developed in chapter 4. This is conducted under several sensitivities, such as alternating the time step-size of both simulations, and the phasor determination window lengths.

5.3 Hybrid EMT-type and Stability-type Simulation

5.3.1 Overview of Interfacing Techniques

Over the past decades, the terminology with regard to hybrid EMT-type and stability-type simulations has been to some extent harmonised. This thesis follows the definitions and workflow related in [178] as closely as possible. Figure 5.3 shows an overview of the building blocks of a typical hybrid power system simulation.

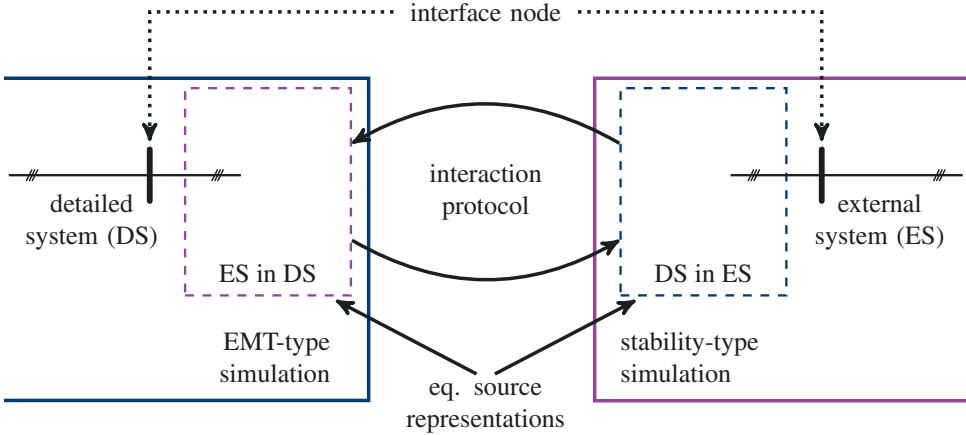


Figure 5.3: Terminology overview of hybrid simulations.

First, the system must be split into two or more partitions, each of which the physical modelling complies to either EMT-type or stability-type simulations. The part that needs a more detailed modelling and simulation approach is the *detailed system* (DS), and is shown left. It commonly comprehends:

1. LCC-HVDC links [177, 191];
2. parts of the system that contains imbalances or waveform distortion [179, 181];
3. FACTS devices in general [180, 192], or systems with FACTS devices [193];
4. synchronous generators that need sophisticated device-level modelling [181, 184]; and
5. distribution networks requiring greater detail [194].

the behaviour of which needs to be studied by EMT-type simulations. The *external system* (ES) is referred to as remainder of the network, and can be addressed in less detail by the stability-type simulation (shown right). The location inside the network at which the split is realised is usually a three phase *interface node*, but a special interface network is also an option [177, 179]. The size of the detailed system, and hence the location of the interface node, depends strongly on 1) the EMT phenomena of interest, 2) the level of modelling, and 3) the available computational resources.

As the network modeling of stability-type and EMT-type simulations differ significantly, network quantities and control variables must be transformed from one simulation paradigm

to the other. Moreover, the dynamics of the external system should be reflected into the detailed system correctly and vice versa. Both the ES and the DS fetch information about the network quantities from the boundaries of the neighbouring system, and use this information to establish run-time interaction between these partitions. This is achieved as follows:

1. at the interface node, the neighbouring system is represented by an *equivalent source*, either Norton or Thévenin based, forming a composite *interface model*;
2. inside the DS, this is typically a three-phase point-on-wave variable source in conjunction with an impedance that reflects the ES' system impedance for a particular frequency;
3. inside the ES, this equivalent source is a fundamental-frequency, positive-sequence projection of the DS;
4. the equivalent has several adjustable parameters, the values of which are determined by the network quantity acquisition method and the source transformations involved. Relevant source values, i.e. impedance, amplitude, frequency, and phase angle can be updated each time step or network iteration of the stability-type simulation;

The implementation of these steps into the overall simulation is covered by the *interaction protocol* (IP). It defines at which instances in the simulation workflow shown in figure 4.1 the equivalent sources are updated, in which order, and how the interface model transforms the network values from one system to the second. The methods used for IPs, equivalent source representations, and interface models are in this thesis referred to as *interfacing techniques*.

5.3.2 Implementation of Existing Interfacing Techniques in this Thesis

Existing interfacing techniques are taken as a reference. From this starting point, we will incorporate the physical modelling of VSC-HVDC discussed in chapter 3, and ascertain if present methods suffice and which adjustments will cause any effect. We will therefore start with the description of the interface dynamic model and its design into the hybrid simulation.

As mentioned in the previous section, the interface model is a composite dynamic model that resides in both simulations. It hence comprises two equivalent source presentations: one in the detailed system representing the external system, and one the other way around. These sources are being accompanied by two dynamic models. One model is contained within the iterative part of the stability simulation, i.e. inside $g(\mathbf{x}, \mathbf{y})$. The second part of the dynamic interface model is implemented as a discrete model inside the EMT-type simulation.

Representation of the external system into the detailed system

Mainly two methods to incorporate the external system into the detailed system have been proposed:

- a time-varying three-phase voltage source (i.e. Thévenin equivalent) [177];
- a time-varying three-phase current source (i.e. Norton equivalent), possibly complemented with a frequency-dependent network equivalent impedance [181, 189, 190];

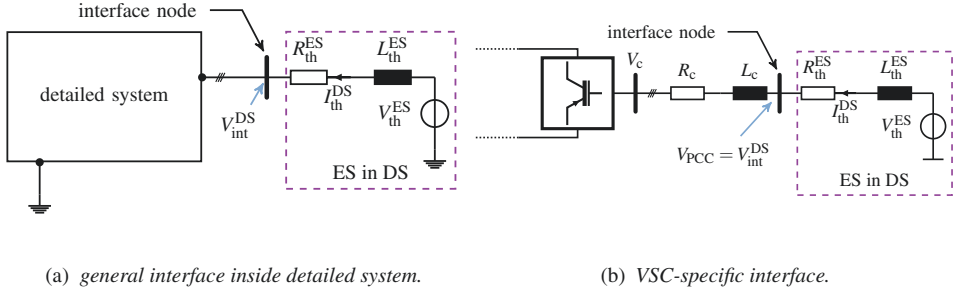


Figure 5.4: Thévenin equivalent representation of the external system.

The former is shown in figure 5.4a. The choice of which source and network model to apply very much depends on the approach taken and goal of the study. Most references focus on the response of a highly detailed model, usually of a FACTS device. This necessitates a comprehensive inclusion of the external system into the detailed system for a wide range of frequencies. This thesis does not implement this approach for several reasons. First, the averaged VSC model does not contain any power electronic switching: the modulation index is directly transformed to the voltage projection in the d-q reference frame of the VSC, neglecting the pulse width modulator. As a result, no switching harmonics occur and the higher frequencies are hence of a lesser concern. Second, the external system models used for this research are based on positive sequence, quasi-stationary behaviour. Apart from the fundamental frequency no accurate harmonic data can hence be established as the data is unavailable. Third, a considerable amount of network branches would be added to the EMT-network, increasing the number of states without adding insight into the phenomena of interest, which would make the hybrid approach computationally less competitive.

Above considerations inhibit the application of a frequency-dependent network equivalent. Hence, our focus is to implement a Thévenin equivalent source at fundamental frequency and optimise its interfacing techniques for VSCs. A single-line diagram of the network arrangement around the interface node is shown in figure 5.4b. It contains the converter bus connected to the point of common coupling through the VSC reactor and interface transformer, being modelled by a lumped impedance $\underline{Z}_c = R_c + jX_c$. We assume the interface node to be at the PCC of the VSCs in order to limit the network size of the detailed system.

The Thévenin impedance $\underline{Z}_{th}^{ES} = R_{th}^{ES} + j\omega_s L_{th}^{ES}$ is the fundamental-frequency projection of the external system impedance as seen from the interface node. The linearity of the AC network equations allow a relatively straightforward determination of \underline{Z}_{th}^{ES} by the superposition principle. The traditional way is to conduct an open and short-circuit test inside the external system [195]. In normal operation, the Thévenin voltage is given by

$$\underline{V}_{th}^{ES} = \underline{V}_{int}^{ES} + I_{th}^{DS} \underline{Z}_{th}^{ES} \quad (5.1)$$

Then, the VSC is disconnected and a three phase fault is induced at the interface node, having a fault impedance \underline{Z}_{flt} . The Thévenin impedance of the ES now mainly determines the corresponding fault current that flows out of the external system as

$$\underline{V}_{th}^{ES} = I_{flt}^{DS} \underline{Z}_{flt} + I_{flt} \underline{Z}_{th}^{ES} \quad (5.2)$$

By eliminating \underline{V}_{th}^{ES} from (5.2) and then re-arranging, the Thévenin impedance can be obtained:

$$\underline{Z}_{th}^{ES} = \frac{\underline{V}_{int}^{ES} - \underline{I}_{flt} \underline{Z}_{flt}}{\underline{I}_{flt}^{DS} - \underline{I}_{th}^{DS}} \quad (5.3)$$

An alternative method to calculate \underline{Z}_{th}^{ES} is by using the bus impedance matrix of the external system [196]. This is done by calculating the voltage change resulting from a known current injection at the interface node, while keeping all other nodal current injections unaltered, i.e. $\Delta \underline{V}_n = \underline{Z}_{nn}^{GG} \Delta \underline{I}_n$. In fact, any deviation from a certain initial voltage is determined by the driving point impedance, which allows the system to be reduced to a voltage behind impedance, a Thévenin source,

$$\underline{V}_{th}^{ES} = \underline{V}_{int}^{ES} + \underline{Z}_{th}^{ES} \underline{I}_{int}$$

where $\underline{Z}_{th}^{ES} = \underline{Z}_{nn}^{GG}$ and $\underline{V}_{th}^{ES} = \underline{V}_{int}^{ES} |_{\underline{I}_{int}=0}$. This alternative method has been applied for this research because 1) the numerical influence of the (low) fault impedance appeared to be large in case \underline{Z}_{th}^{ES} was determined by an open and short circuit test, and 2) the network solution of the stability-type simulation tears the network into a current-source driven part and a voltage-source driven part, permitting the bus impedance matrix to be used directly without any additional calculations.

Each time step t_n , \underline{V}_{th}^{ES} is calculated from the stability-type simulation according to

$$\underline{V}_{th}^{ES} = \underline{V}_{int}^{ES} - \underline{I}_{int}^{ES} \underline{Z}_{th}^{ES} = |\underline{V}_{th}^{ES}| e^{j\phi_{th}} \quad (5.4)$$

where \underline{V}_{th}^{ES} is the ES Thévenin voltage phasor projection inside the detailed system. \underline{V}_{int}^{ES} and \underline{I}_{int}^{ES} are the interface voltage and interface branch currents, as being interfaced from the external system. Next, \underline{V}_{th}^{ES} is used to set the three-phase Thévenin equivalent inside the detailed system by

$$V_{th,a}^{ES}[m] = \hat{V}_{th}^{ES} \cos(\theta_K[m] + \phi_{th}[m]) \quad (5.5)$$

$$V_{th,b}^{ES}[m] = \hat{V}_{th}^{ES} \cos(\theta_K[m] + \phi_{th}[m] - \frac{2\pi}{3}) \quad (5.6)$$

$$V_{th,c}^{ES}[m] = \hat{V}_{th}^{ES} \cos(\theta_K[m] + \phi_{th}[m] + \frac{2\pi}{3}) \quad (5.7)$$

in which \hat{V}_{th} is the peak value of \underline{V}_{th}^{ES} , m is the m^{th} sample of the EMT partition, $\theta_K[m] = \int_0^{t_{emt}[m]} \omega_K[n] dt_{emt}$, and $\phi_{th}[m]$ is the (filtered) angle of \underline{V}_{th}^{ES} . $\omega_K[n]$ is the frequency of the external system reference frame in rad s^{-1} . The voltages of (5.7) are displaced symmetrically among the voltage triangle. This balance is assumed plausible owing to the positive sequence based modelling inside the external system.

The combination of values to be updated each time step n of the stability-type simulation and their respective filtering determine the interaction between the external and the detailed system. Several implementations for updating \hat{V}_{th}^{ES} and ϕ_{th} are examined in this thesis. The simplest approach is to update it through zero-order hold (ZOH) filtering by

$$\hat{V}_{th}^{ES}[m] = |V|_{th}^{ES}[k] \quad (5.8)$$

$$\phi_{th}[m] = \phi_{th}[k] \quad (5.9)$$

with the exact update instance k defined by the interaction protocols discussed in section 5.3.2. A more sophisticated first-order hold method, the applicability of which depends on the interaction protocol used is proposed in section 5.4.3.

To summarise, the general sequence for interfacing *from* the external system *to* the detailed system is done as follows:

1. at t_k , fetch the interface node voltage \underline{V}_{int}^{ES} and branch current I_{int}^{ES} from the ES network model.
2. calculate \underline{V}_{th}^{ES} according to (5.4);
3. set the amplitude, frequency, and phase angle of time-varying three phase voltage source (i.e. (5.7))
4. run the discrete interface model according to the interaction protocol, thereby using filtering methods for $\hat{V}_{th}^{ES}[m]$ and $\phi_{th}[m]$ such as (5.9);

Representation of the detailed system into the external system

The representation of the detailed system inside the external system revolves around projecting the detailed system's behaviour to the positive-sequence, fundamental-frequency based modelling approach of the external system. The interfacing techniques involved focus on the grid interface inside the external system and on fetching the positive-sequence phasors from the EMT waveforms.

The representation of the grid interface around the interface node depends on the network model used for the external system, which can be either power injection based or current injection based. As the tools used for this thesis (PSSE, PSS Netomac) use the current injection method, our hybrid modelling framework adopts this approach too. Hence, the detailed system itself can be represented by a time-varying Thévenin equivalent or a Norton equivalent. Although early references model this by a time-varying Thévenin equivalent [177, 179], we model the detailed system into the external system by a time-varying Norton current injection. A Norton source appeared to give slightly better iterative behaviour and requires no additional Thévenin node in the external system.

This time-varying Norton equivalent is shown in figure 5.5. The network arrangement consists of

- a Norton impedance connected to the reference node \underline{Z}_{th}^{DS} , which equals the Thévenin impedance of the detailed system;
- a Norton current source I_{int}^{DS} which dictates the interaction between the detailed and the external system.

During initialisation of the EMT-type simulation, \underline{Z}_{th}^{DS} is calculated from the positive-sequence bus impedance matrix of the detailed system in a similar fashion as was done with \underline{Z}_{th}^{ES} in section 5.3.2. That is, $\underline{Z}_{th}^{DS} = \underline{Z}_{emt,nn}^{GG}$, with n being the interface node index. The

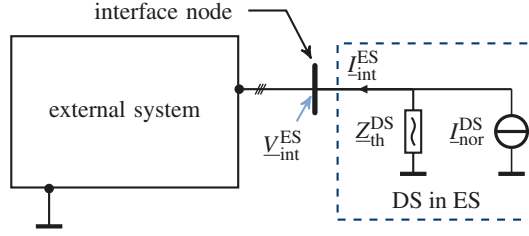


Figure 5.5: *Equivalent representation of the detailed system in the external system through a dynamic Norton current source.*

Norton current injection is based on the waveform-to-phasor transformation of the interface branch currents and nodal voltages, and can be determined in several ways. The simplest method is to only calculate I_{int}^{DS} , and use this as a substitution for I_{int}^{ES} to determine I_{nor}^{DS} :

$$I_{nor}^{DS} = \frac{V_{int}^{ES} - I_{int}^{DS} Z_{th}^{DS}}{Z_{th}^{DS}} \quad (5.10)$$

See also figure 5.5. In spite of neglecting the interface voltage dynamics of the detailed system, just 3 waveform-to-phasor transformations have to be carried out, thereby providing some potential computational benefits for the interface method. An alternative approach is to use both the interface nodal voltage and branch current, i.e.

$$I_{nor}^{DS} = \frac{V_{int}^{DS} - I_{int}^{DS} Z_{th}^{DS}}{Z_{th}^{DS}} \quad (5.11)$$

which has a notable benefit compared to (5.10) because the current injection is independent of V_{int}^{ES} . This facilitates the convergence of the network iterations in $\mathbf{g}(\mathbf{x}, \mathbf{y}) = 0$ at the cost of a more computationally expensive phasor determination. A third way of setting the Norton equivalent source is to use the apparent power flowing through the interface branch:

$$I_{nor}^{DS} = \frac{V_{int}^{ES} - \left(\frac{S_{int}^{DS}}{V_{int}^{ES}} \right)^* Z_{th}^{DS}}{Z_{th}^{DS}} \quad (5.12)$$

with $S_{int}^{DS} = V_{int}^{DS} I_{int}^{DS*}$. At first sight this seems to combine both computational downsides of the interfacing techniques: a total of 6 phasors have to be calculated per interface, and the network iterations are more complex. An immense advantage of using S_{int}^{DS} however is its independence on the reference frame, and thereby overcoming one of the major modelling differences between the external and the detailed system. Especially for multi-machine systems or non-coupled asynchronous areas this can be an issue, as phasors may start to rotate after disturbances. For that reason we implement (5.12) for this thesis.

Phasor determination of the detailed system network quantities Network quantities in the detailed system are point-on-wave, and equivalent source projection at the interface node in the external system involves transformations to fundamental-frequency positive-sequence voltage and current phasors, or derived quantities (e.g. active and reactive power). Well-

established Fourier or curve-fitting methods can be applied to calculate these [197–200]. Their respective implementation (e.g. window length W , applied filtering, discontinuity handling) determines the interaction between the detailed and the external system.

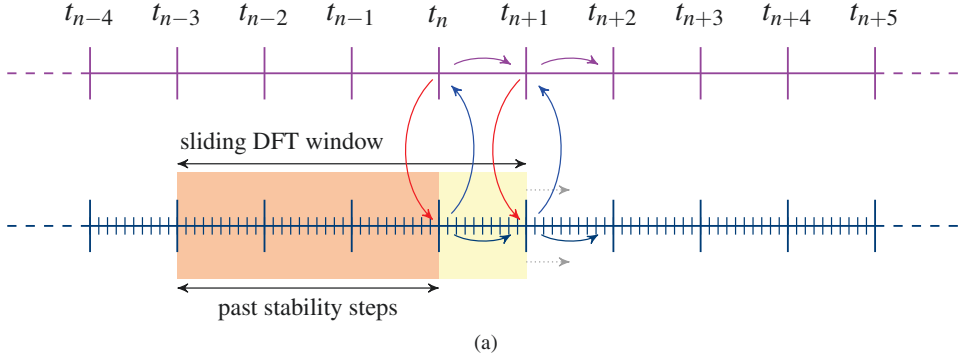


Figure 5.6: *Phasor determination window in the detailed system. Above: stability-type simulation timeline. Below: EMT-type simulation timeline.*

The requirements for the phasor determination are illustrated by figure 5.6. It contains two time lines. The upper one shows the calculation steps of the stability-type simulation, which are indicated by the small vertical bars and have an index n . The EMT-type simulation has a much smaller time step size—the vertical bars on the bottom time line are much closer to each other. The calculation steps of the EMT-type simulation have index m , and each stability time step is assumed to enclose M EMT-time steps (i.e. $M = \frac{\Delta t}{\Delta t_{\text{emt}}}$). The red and blue arrows show the interfacing instances, which will be described in the next section. Whenever the stability-type simulation needs to set $I_{\text{not}}^{\text{DS}}$, the interface model uses the causally available waveforms at the interface location in the detailed system. This *sampling window* is depicted in orange and yellow, and slides rightwards as the simulation goes on. The amount of samples—the window size—must be sufficient for the algorithm to accurately determine the fundamental frequency component of the waveforms. In case of electrical circuit simulations it is customary that such a window spans multiple time steps of the stability simulation, i.e. $W > M$.

In this thesis we apply an interpolating, least-mean-square curve fitting method to determine the positive-sequence component of the interface network quantities. Such methods rely on minimising the mean square error between a sampled signal and a predefined polynomial equation. For the voltage of phase a at the interface node, $V_{\text{int},a}$, this polynomial is for instance

$$v_{\text{cf},a}(t) = \hat{v}_{\text{cf}} \cos(2\pi f_s t + \phi_v) = c_1 \cos(2\pi f_s t) + c_2 \sin(2\pi f_s t) \quad (5.13)$$

where f_s is the (estimated) fundamental frequency. Using the Euler relations for complex exponentials, its space vector projection on the α - β reference frame is defined as

$$\hat{v}_{\text{cf},a}^F = \hat{v}_{\text{cf}} \cos(\phi_v) + j\hat{v}_{\text{cf}} \sin(\phi_v) = c_1 - jc_2 \quad (5.14)$$

The space vector of $V_{\text{int},a}$ itself, $\hat{v}_{\text{int},a}^F$, rotates clockwise at rate f_{DS} . We assume this frequency to equal f_K of the external system reference frame. Although this is not true in general and EMT-type simulations do not rely on reference frames, this assumption holds

for the particular interface shown in figure 5.4. Being defined in the α - β reference frame, the space vector of the fitted polynomial $v_{cf,a}(t)$ will also rotate clockwise. As a result the projection on the reference frame of the external system must hence be accounted for by

$$\hat{v}_{cf,a}^K = \hat{v}_{cf,a}^F \underline{T}^{F \rightarrow K} = (c_1 - jc_2) e^{-j\theta_K} \quad (5.15)$$

Where \underline{T} is reference frame transformation, and $\theta_K = \int_{t_{emt}=0}^{m-W} \omega_K dt$. Next, the quasi-stationary phasor can be deduced from (5.15):

$$V_{int,a} = \frac{\hat{v}_{cf,a}^K}{\sqrt{2}} = \frac{e^{-j\theta_K}}{\sqrt{2}} (c_1 - jc_2) \quad (5.16)$$

c_1 and c_2 are calculated as follows [198]. For a rectangular sampling window of length W the mean square error between $V_{int,a}$ and $v_{cf,a}(t)$ equals

$$\varepsilon_{cf} = \sum_{k=0}^{W-1} (V_{int,a}[m-W+k] - c_1 \cos[2\pi f_s k \Delta t_{emt}] - c_2 \sin[2\pi f_s k \Delta t_{emt}])^2 \quad (5.17)$$

where the k is the sampling index. To minimise this error, the partial derivatives of ε_{cf} with respect to c_1 and c_2 must equal 0. What follows are two equations with two unknowns:

$$\begin{aligned} c_1 A + c_2 B &= \sum_{k=0}^{W-1} V_{int,a}[m-W+k] \cos[2\pi f_s k \Delta t_{emt}] \\ c_1 B + c_2 C &= \sum_{k=0}^{W-1} V_{int,a}[m-W+k] \sin[2\pi f_s k \Delta t_{emt}] \end{aligned} \quad (5.18)$$

with

$$\begin{aligned} A &= \sum_{k=0}^{W-1} \cos^2[2k\pi f_s \Delta t_{emt}] \\ B &= \sum_{k=0}^{W-1} \sin[2k\pi f_s \Delta t_{emt}] \cos[2k\pi f_s \Delta t_{emt}] \\ C &= \sum_{k=0}^{W-1} \sin^2[2k\pi f_s \Delta t_{emt}] \end{aligned} \quad (5.19)$$

c_1 and c_2 can now be obtained by backwards substitution

$$\begin{aligned} c_1 &= \sum_{k=0}^{W-1} K_{1k} V_{int,a}[m-W+k] \\ c_2 &= \sum_{k=0}^{W-1} K_{2k} V_{int,a}[m-W+k] \end{aligned} \quad (5.20)$$

in which K_{1k} and K_{2k} are independent of the waveforms and solely related to the fitting polynomial and window length:

$$\begin{aligned} K_{1k} &= \frac{1}{AC - B^2} (C \cos [2\pi f_s k \Delta t_{\text{emt}}] - B \sin [2\pi f_s k \Delta t_{\text{emt}}]) \\ K_{2k} &= \frac{1}{AC - B^2} (A \sin [2\pi f_s k \Delta t_{\text{emt}}] - B \cos [2\pi f_s k \Delta t_{\text{emt}}]) \end{aligned} \quad (5.21)$$

$I_{\text{nor}}^{\text{DS}}$ is the de facto positive sequence projection of the interface flow for which $\underline{v}_{\text{int},012}^{\text{DS}}$ and $\underline{i}_{\text{int},012}^{\text{DS}}$ must be determined. At $t_{\text{emt}}[m]$, $\underline{V}_{\text{int}}^{\text{DS}}$ is defined as the positive sequence value of

$$\underline{v}_{\text{int},012}^{\text{DS}} = \mathbf{S}^{-1} \underline{v}_{\text{int},abc} \quad (5.22)$$

for W sampled values of $V_{\text{int},abc}$, where

$$\mathbf{S}^{-1} = \frac{1}{3} \begin{bmatrix} 1 & 1 & 1 \\ 1 & e^{\frac{2j\pi}{3}} & e^{\frac{4j\pi}{3}} \\ 1 & e^{\frac{4j\pi}{3}} & e^{\frac{2j\pi}{3}} \end{bmatrix} \quad (5.23)$$

and $\underline{v}_{\text{int},abc}^{\text{DS}} = \left[\underline{V}_{\text{int},a}^{\text{DS}} \ \underline{V}_{\text{int},b}^{\text{DS}} \ \underline{V}_{\text{int},c}^{\text{DS}} \right]^T$. Using (5.16), the phase voltage phasors can be calculated:

$$\underline{v}_{\text{int},abc}^{\text{DS}} = \frac{e^{-j\theta_K}}{\sqrt{2}} \left(\sum_{k=0}^{W-1} K_{1k} \underline{v}_{\text{int},abc}[m - W + k] - jK_{2k} \underline{v}_{\text{int},abc}[m - W + k] \right) \quad (5.24)$$

in which $\underline{v}_{\text{int},abc} = [V_{\text{int},a} \ V_{\text{int},b} \ V_{\text{int},c}]^T$. The same procedure goes for the interface currents. As soon as the quasi-stationary phasors of the individual interface currents and voltages are computed, normally after each $M = \Delta t / \Delta t_{\text{emt}}$ calculation steps, their positive-sequence values can be calculated by (5.22) as

$$\underline{I}_{\text{int}}^{\text{DS}} = \frac{1}{3} \left(\underline{I}_{\text{int},a}^{\text{DS}} + \underline{I}_{\text{int},b}^{\text{DS}} e^{-j\frac{2\pi}{3}} + \underline{I}_{\text{int},c}^{\text{DS}} e^{j\frac{2\pi}{3}} \right) \quad (5.25)$$

$$\underline{V}_{\text{int}}^{\text{DS}} = \frac{1}{3} \left(\underline{V}_{\text{int},a}^{\text{DS}} + \underline{V}_{\text{int},b}^{\text{DS}} e^{-j\frac{2\pi}{3}} + \underline{V}_{\text{int},c}^{\text{DS}} e^{j\frac{2\pi}{3}} \right) \quad (5.26)$$

For each interface location, the Norton current injection in the external system is now defined by (5.10) - (5.12).

Implementation and computation considerations The sampled values for the interface voltages and currents are stored during the discrete model call of the interface model. The curve fitting algorithm is executed each first iteration of the solution procedure for (4.2). As (5.12) is part of \mathbf{g} , the obtained values for $\underline{V}_{\text{int}}^{\text{DS}}$ and $\underline{I}_{\text{int}}^{\text{DS}}$ are then used as quantities to iterate against. For a fixed window length, A, B, C remain unaltered during the simulation. Moreover, K_{1k} and K_{2k} are fixed sequences that do not have to be recomputed each time the interface model requests a Norton current injection. Reusing these variables gave computational and implementation benefits for the recursive algorithm against its more elegant non-recursive counterpart [199].

One particular issue that commonly occurs with Fourier algorithms is spectral leakage.

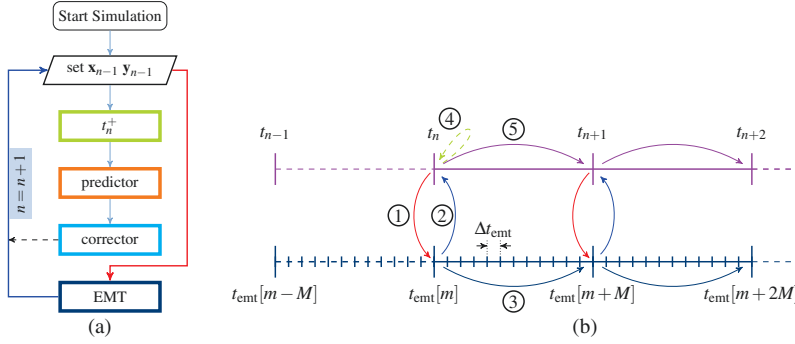


Figure 5.7: (a) conventional interaction protocol, (b) two stability time steps of the conventional IP

This occurs in case the frequency of the sampled signal differs from the fundamental frequency *estimated* for the Fourier series components. This manifests itself in the presence of side harmonics of the DFT spectral components, and entails a mismatch in the quasi-stationary phasor determination. This issue is more prominent for the angle than for the magnitude of the phasor [201]. This phenomenon was also experienced with the curve-fitting algorithm, which assumes the power frequency to fit the curve on. Using the apparent power as an interface variable resolved this issue.

Numerical Implementation

The interfacing techniques (interface model, equivalent representations, variable transformations) must be performed in a particular order, some of which make more sense than others. The corresponding interaction protocol (IP) defines such order. It dictates the interfacing actions either from an external process that runs both simulations (co-simulation) or inside a master-slave configuration (i.e. hybrid simulation). The scope of this research is limited to serial IPs using fixed time step-sizes for both simulations. The serial approach was chosen because the most prominent offline dynamic power system simulations do not employ parallel processing yet.

As discussed in section 4.2, the stability-type and EMT-type simulations have their own specific workflow for a typical calculation time step. Somewhere inside this workflow the interface model is being called. Co-simulations run the concerned simulations as separate processes, and the access to their numerical integration schemes is restricted to the application program interfaces. Several commercially available tools fall into this category. For this research it is assumed that co-simulations can purely access their child processes at the start and end of each calculation step of the numerical integration routine.

Conversely, this limitation is absent for hybrid simulations as it is assumed that the API is more flexible. Thus, numerical integration, network iterations, and initialisation routines can theoretically be invoked at arbitrary instants. For the workflows shown in figure 4.1 this yields 3 possible interfacing moments for the stability-type simulation and 4 for the EMT-type simulation. We will fix on those interface interrupts valuable for the accuracy of transient stability assessment, such as interfacing in the event of network changes.

co-simulation interaction protocols A common way of showing the IP of an interfacing method is through the diagrams of figure 5.7. Figure 5.7a contains the workflow of a stability

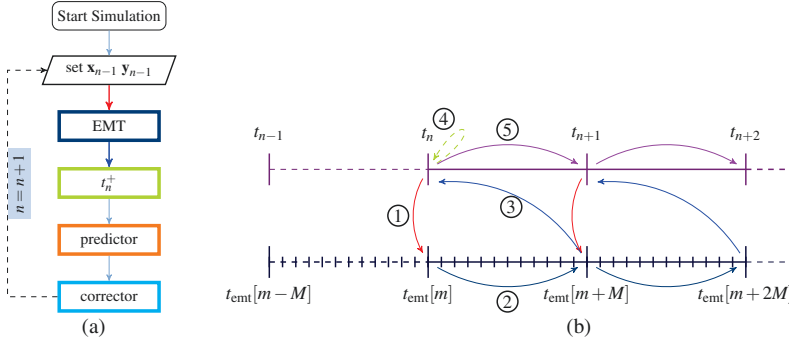


Figure 5.8: (a) EMT priority interaction protocol, (b) two stability time steps of the EMT priority IP.

and EMT-type co-simulation from t_n to t_{n+1} . The stability simulation is depicted by its three main calculation steps (i.e. event handling, and the predictor-corrector steps). The EMT simulation is aggregatedly displayed by a single block. As can be seen, the various steps inside the respective simulations are run sequentially without being interrupted along their integration routines. The red arrow indicates interfacing between the stability and the EMT simulation, the blue arrow interfacing between the EMT and the stability-type simulation. Figure 5.7b shows two time lines, the upper of which contains the time steps of the stability-type simulation shown by small vertical bars. The bottom time line does the same for the EMT-type simulation, which naturally contains more calculation steps as $\Delta t_{emt} \ll \Delta t$. Numerous arrows are projected on these time lines, accompanied by encircled numbers. They define the sequence in which the calculation steps are performed. In this case, each time step starts with updating V_{th}^{ES} based on historically available network quantities in y_{n-1} (step ①). Subsequently, the same is done for the Norton current injection into the external system (step ②). Then, the EMT-type simulation is run until $t_{emt}[m+M]$ (step ③). The same is done for the stability simulation (steps ④ and ⑤). Step ④ is solely carried out in case of events. As this IP interfaces between the detailed and the external system simultaneously on the time line (i.e. at t_n and $t_{emt}[m]$), merely causally available results can be used for updating the equivalent source representations. Occurrences in one system are hence always delayed by Δt before their effects on the other system is manifested. This IP was among the first implemented in combined EMT and stability simulations, and we therefore refer to it as the *conventional IP*.

An alternative to the conventional IP is the *EMT priority IP* shown in figure 5.8. The main difference compared to the previous IP is the interface instant from the EMT-type to the stability-type simulation (step ③), which occurs at $t_{emt}[m+M]$. This allows the external system to represent the detailed system response more accurately because steps ① and ② include the interaction of both simulations of the present time step as well. This is specially applicable to VSCs, which are modelled inside the detailed system.

hybrid simulation interaction protocols In order to interlace both simulations more thoroughly, we tear the stability-type simulation into a part that handles events at t_n^+ , and a part that calculates the dynamic response. For the conventional and EMT priority IPs, this is shown in figure 5.9. The main concept is that simulation as a whole would benefit from including the system changes into both the external and the detailed system as soon as they

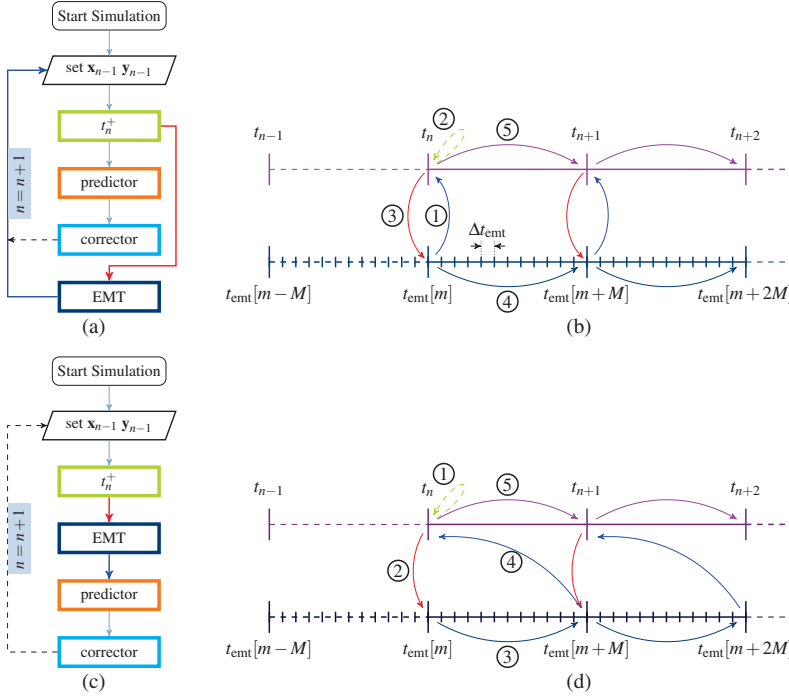


Figure 5.9: Interaction protocols using hybrid methods. *a & b: conventional IP, c & d: EMT priority IP.*

occur. For the conventional IP of figures 5.9a and 5.9b this implies that the external system first sets its Norton equivalent of the detailed system based on the known simulation data (step ①). Subsequently the event, essentially a short circuit, is engaged and the nodal voltages must be calculated according to (4.2) (i.e. step ②). The equivalent source inside the detailed system can now be set according to these new nodal voltages and currents (step ③), after which both simulations can continue to the next interfacing interrupt at t_{n+1} . In the same way, the EMT Priority IP can be adjusted to make use of hybrid methods, as shown in figure 5.9c and 5.9d.

5.4 Interface Technique Improvements in this Thesis

5.4.1 Thévenin Impedance recalculation during faults

As discussed in section 5.3.2 the Thévenin impedance $\underline{Z}_{\text{th}}^{\text{ES}} = R_{\text{th}}^{\text{ES}} + j\omega_s L_{\text{th}}^{\text{ES}}$ can be either calculated through open and short-circuit tests in the external system, or obtained from the bus impedance matrix. The latter method has been applied for this thesis.

Traditional interfacing techniques focus on the alteration of the detailed system's Thévenin source values (magnitude and angle) and leave the adjustment of $\underline{Z}_{\text{th}}^{\text{ES}}$ out of consideration. Altering this impedance in the EMT-type simulation requires a (partial) re-factorization of the network model solution matrices, and re-initialisation of corresponding

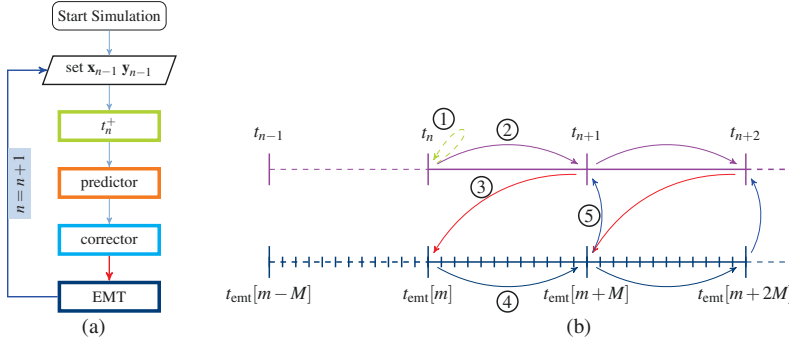


Figure 5.10: *The external system priority interaction protocol.*

network elements, which is not provided by every EMT-simulation program by default. Especially co-simulation requires availability of this functionality by the respective API [202]. Therefore, we compare the interface behaviour with and without re-factorization to establish the advantage of using a hybrid simulation over a co-simulation.

As the network model of the external system is considered linear its input impedance as seen from the interface node will remain constant throughout the simulation, unless its physical layout changes. The ignition and clearance of a fault is such an event. The procedure to adjust $\underline{Z}_{\text{th}}^{\text{ES}}$ and resume the hybrid simulation is as follows:

1. invoke event at t_n^+ inside the external system and solve (4.2);
2. calculate $\underline{Z}_{\text{th}}^{\text{ES}}$ from $\underline{Z}_{\text{in}}^{\text{GG}}$;
3. adjust RL -branch parameters of each phase of $\underline{Z}_{\text{th}}^{\text{ES}}$, while keeping all other branches untouched;
4. recalculate Y_{eq} of the adjusted branches;
5. calculate historical terms $I_{\text{hist,th}}$ assuming continuous branch current constraint;
6. refactorise EMT network matrices (i.e., $\mathbf{Y}_{\text{br,eq}}^{\text{EMT}}$);
7. determine $\underline{V}_{\text{th}}^{\text{ES}}$ and resume simulation at $t_{\text{emt}}[m]$.

Steps 3–6 act on the EMT network model and the branch history current sources. For the RL -branches of the grid interface shown in figure 5.4b, the history currents depend on the nodal voltages at $t_{\text{emt}}[m]$. This causes the trapezoidal integration rule to carry on the voltage terms of the previous time step into the solution. For branch current discontinuities (i.e., steps) this is an issue and causes numerical oscillations. For steps in branch voltages, as is the case here, the trapezoidal method provides sufficient damping [203]. Hence, no additional measures have to be taken except for changing Y_{eq} of $I_{\text{hist,th}}[m]$.

5.4.2 The External System Priority Interaction Protocol

An alternative option to implement the sequential hybrid simulation is to give the external system priority during each time step. Such an IP is shown in figure 5.10. The external

system runs first (steps ① and ②), interfaces its response with the detailed system (step ③), which is then run until the next interface interrupt (steps ④ and ⑤). At first sight, this IP looks unnatural, especially in light of the VSC response being considered here. The effect of the detailed system on the external system, and hence VSC response, would be delayed by δt just as with the conventional IP. This approach bears a great advantage however in terms of the representation of the external system into the detailed system: any method that filters angular magnitudes becomes interpolating, which potentially benefits the VSC response. Application of the external system priority IP has to our best knowledge not been reported in literature yet and this thesis will study the differences with respect to the more common IPs in section 5.5.

5.4.3 Improved Angular Magnitude filtering

The downside of the zero-order hold approach to update the Thévenin equivalent inside the detailed system is that the stepwise changes in ϕ_{th} at $t[k]$ influence the performance of the applied interfacing technique, and cause unrealistic VSC model responses, which also propagate into the HVDC system. A smoother yet accurate tracking of ϕ_{th} is hence invaluable.

We propose to apply a first-order hold (FOH) approach to approximate the course of ϕ_{th} during the EMT run between two updating instances:

$$\phi_{th}[m] = \frac{\phi_{th}[k] - \phi_{th}[k-1]}{\Delta t} \Delta t_{emt}(m - m_u) + \phi_{th}[n] \quad (5.27)$$

with m_u the value of m at the start of the EMT-type calculation loop each time (5.5)-(5.7) are updated from the stability-type simulation. Eq. (5.27) is based either on extrapolation or interpolation, depending on the values available from the stability-type simulation at $t_{emt}[m_u]$.

5.4.4 Improved External System Priority IP during ac-side events

While the external system priority IP discussed in section 5.4.2 features the convenience of causal filtering techniques for EMT quantities, it potentially also introduces a delayed interaction between the detailed system and the external system. Especially for low short circuit ratios of the subsystem of interest this can impact the external system accuracy.

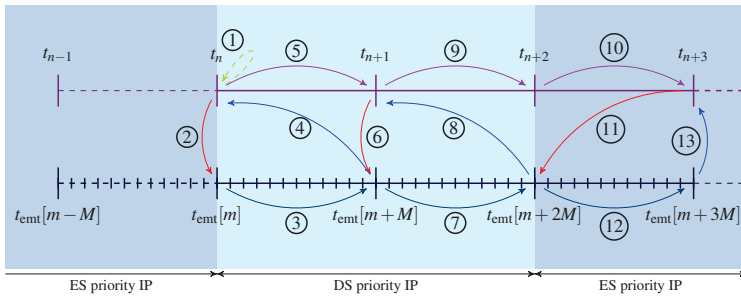


Figure 5.11: *Improvement to external system priority IP for more accurate interfacing during events in the external system.*

In order to resolve this potential issue the IP shown in figure 5.10 is combined with the IP prioritising the detailed system (i.e., figure 5.9c and 5.9d). This composite IP is shown in figure 5.11. Essentially this IP follows the workflow that runs the external system first, interfaces to the detailed system, and then runs the detailed system. At disturbances (t_n) however, the IP swaps this priority towards the detailed system. After event handling at t_n^+ (i.e., step ①) the algorithm continues until sufficient samples are available from the external system to afford a causal implementation of (5.27), viz. steps ② to ⑨. Then, the IP returns to its original calculation order by first simulating the external system (step ⑩), interfacing with the detailed system (step ⑪), running the detailed system (step ⑫), interfacing with the external system (step ⑬), and so forth.

First-order hold filtering needs to use values from the previous calculation step of the external system, or predict them. As the external system itself is non-causal at t_n , filtering for ϕ_{th} will show unrealistic values. Therefore, steps ① – ⑨ use the zero-order hold approach given by (5.9), whereas the remainder of the simulation applies first-order hold filtering for ϕ_{th} as given by (5.27).

5.4.5 Interaction Protocol Improvements Under Small Time Step-Size Conditions

During normal operating conditions or small-signal disturbances, the causality conditions for transforming waveforms to phasors in the detailed network are favourable due to relatively small changes in amplitude and angle. Therefore, the interaction protocols of figure 5.9d or 5.10b will suffice, even in case $W > M$. However, in the event of disturbances, the sliding window needs to be reset and accurate voltage and current phasors cannot be obtained for $W > M$. This requires either the moving window to be shortened or the calculation order to be changed, which is shown in figure 5.12, in which W_f is the moving DFT window after events in the external system.

In this thesis we developed a new IP, the calculation sequence of which is shown in figure 5.13. This interaction protocol employs the same steps as in figure 5.9d until a disturbance inside the external system occurs at t_n . After the solution of the algebraic equations (i.e. step ①) and updating all equivalent sources in the detailed system (step ②), the EMT-type simulation is run until $t_{emt} = t_{emt}[m + M + W]$ (step ③), after which the required phasor calculations can be performed (step ④) and used for the iterative procedure of the stability-type simulation (step ⑤). Depending on M , this jump-over procedure shall be repeated until the discontinuity instance is out of range of the moving window (steps ⑥ - ⑮). Subsequently the program returns to the prefault interaction protocol using the default sliding window length W .

An alternative option for the phasor determination during faults is to change W_f , as with the improved interaction protocol shown in figure 5.14. Here, the jump-over time and W_f are variable and decrease from the initial value of W to M . This is shown for four stability simulation time steps (steps ⑥ - ⑮). This alternative interaction protocol offers a substantial speed advantage compared to the one shown in figure 5.13. As a matter of fact, this IP still satisfies the main purpose of correct phasor determination after faults, i.e., fast transients are smoothed while those applicable to transient stability are still covered.

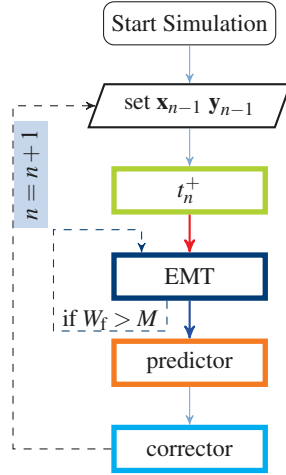


Figure 5.12: Improved work flow of the stability-type simulation for restarting DFT after events in the external system.

5.5 Simulation Studies

5.5.1 Simulation Setup

Simulation Parameters

The simulations performed in this chapter are conducted using three test systems (see also figure 5.15):

1. a three-phase slack source connecting a passive load through a parallel connection;
2. a three-phase slack source connecting a local generator and a VSC through a parallel line;
3. a three-terminal VSC-HVDC system, which interconnects an offshore wind power plant and two identical equivalent power systems.

The former two are used to examine the accuracy of existing interfacing techniques and the proposed improvements. The simulations performed using these systems hence address the accuracy aspect of the sub-question of research question 2 (also stated in section 5.2.3). The three terminal HVDC network aims at assessing the computational performance of the algorithm compared to conventional monolithic simulation approaches, and hence treats the simulation speed-up aspect of the same sub-question.

We will start with the performance of conventional IPs in case the detailed system consists of a passive load. As the entire detailed system is passive, any observable difference in response can be attributed to the interfacing technique applied. Subsequently, the load is replaced by a VSC to reveal any interactions between its dynamics and the IP adopted. Then, the influence of alternative IPs is studied as well as the various methods to improve to the overall interface behaviour.

Various implementations of the interfacing technique improvements are subsequently tested on the third system, the three-terminal VSC-HVDC system, aiming at extrapolating

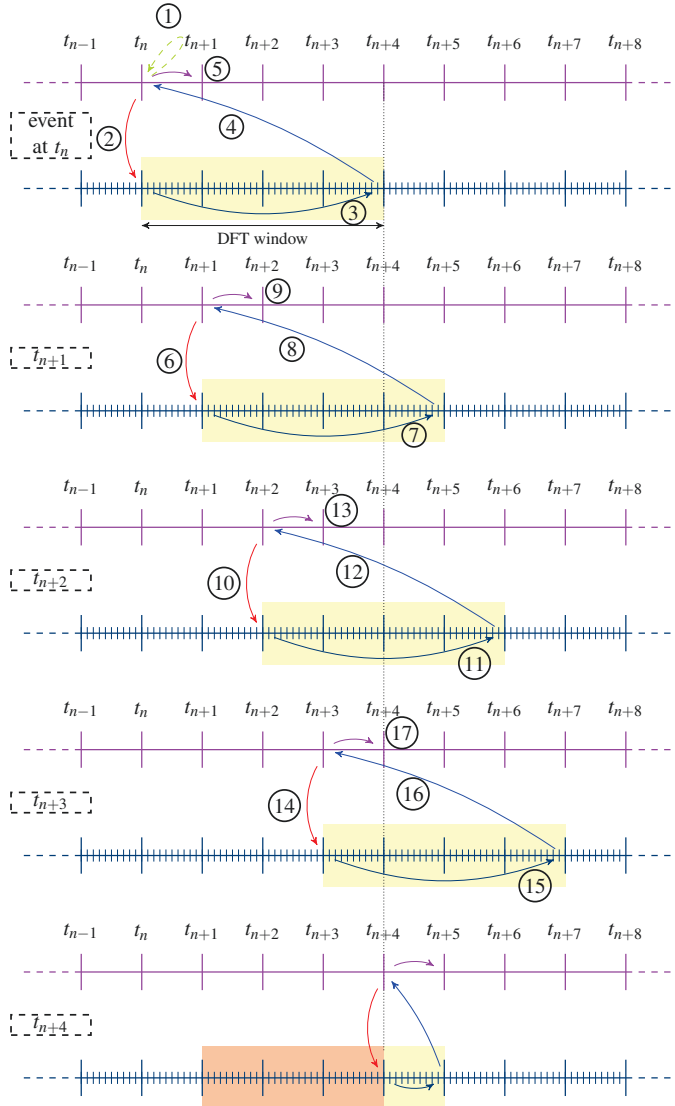


Figure 5.13: Interaction protocol (IP3 in table 5.1) during faults.

the findings from the former two systems towards more complex grids. Aside from the modelling flexibility the potential merit of hybrid simulations above traditional simulations is their increased overall simulation speed. This will be studied by comparing the relative computation times of the hybrid simulation, an EMT reference simulation, and a transient stability reference simulation, while taking the AC system size as a parameter to vary.

Table 5.1 summarises the various interaction protocols used for the hybrid simulations, either taken from literature or developed for this thesis based on the needs for VSC-HVDC modelling. Table 5.2 summarises the applied variations per case.

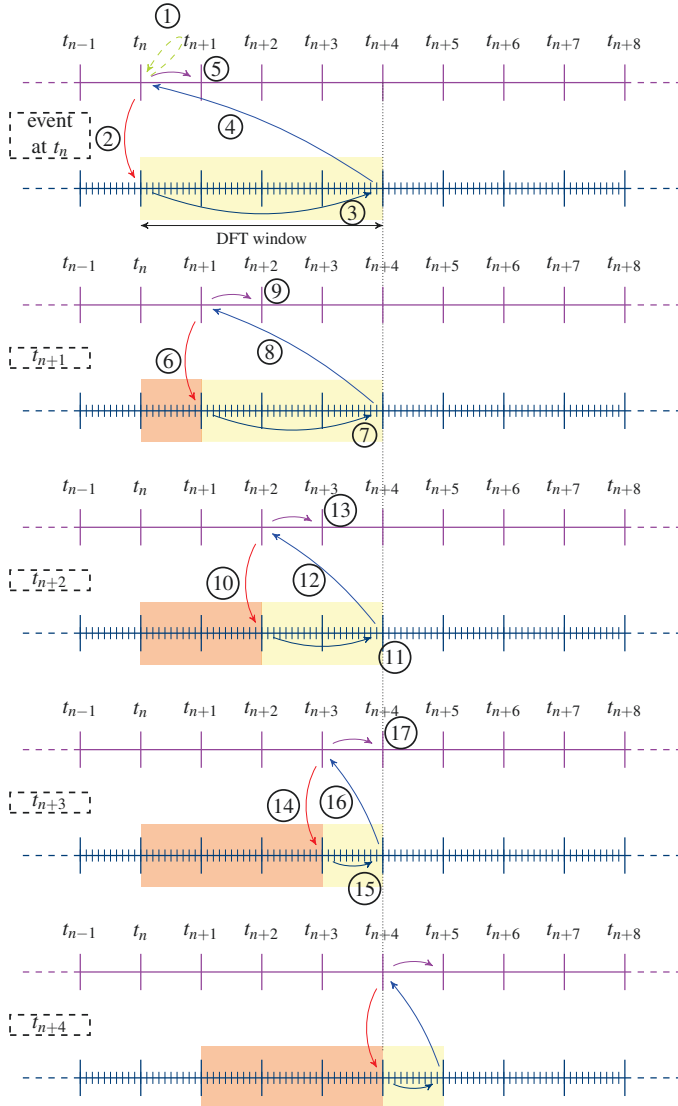


Figure 5.14: Improved interaction protocol (IP4 in table 5.1) during faults.

Test Network Description

The applied test networks are shown in figure 5.15. In each network, the detailed system is contained within the dashed areas and simulated by EMT, while the remainder of the system is included in the stability-type simulation. As the systems are related to other test systems applied across this thesis, their common parameters are discussed in Appendix C while the parameters special to this chapter are shown in table 5.3.

Figure 5.15a is the plainest of the three test systems. The external system comprises a 1000 MVA, 230 kV three-phase system equivalent using an R over X ratio of 0.1 (between nodes N1 and SLK), and two 100 km parallel overhead lines (L1, L2). The detailed system

name	shorthand	properties	Figure
conventional IPs	IP0		5.7 & 5.8
improved conventional IP	IP0+		5.9b
DS Priority IP	IP1		5.9d
ES Priority IP	IP2		5.10b
Improved ES Priority IP	IP2(+1)		5.11
IP for small Δt	IP3		5.13
improved IP for small Δt	IP4		5.14

Table 5.1: *overview of interaction protocols (IP) applied in this chapter*

results Fig.	5.16	5.17	5.18	5.19	5.20	5.21	5.22	5.23
network Fig.	5.15a	5.15b	5.15b	5.15b	5.15b	5.15b	5.15b	5.15c
SW1	closed	closed	closed	open	closed	closed	open	closed
contribution	base case	improved ES event handling	IP comparison for VSC	Z_{th}^{ES} after events	ZOH & FOH, prio IP	causal FOH, ES prio IP	small Δt conditions	MTDC application

Table 5.2: *Overview of the investigated interfacing techniques for VSC-HVDC and their individual contribution to the state-of-the-art. SW1 refers to the position of the switch connecting the local generator in Figure 5.15c.*

consists of an inductive load (i.e., Load1) connected by a 10 km overhead line (L3). Dynamically, the load is modelled by a neutrally grounded, symmetrical series RL branch. SW1 is opened to exclude machine dynamics.

parameter	value
line length	100km
S_k''	1000 MV A
R_{L3}	$0.05\Omega/\text{km}$
X_{L3}	$0.407\Omega/\text{km}$
length L3	10km
P_{vsc}	234MW
Q_{vsc}	15MVar
P_{Load1}	160MW
Q_{Load1}	70MVar
Z_c	$0.15 + j15 \Omega$
E_{dc}	300kV
C_{VSC}	$30\mu\text{F}$

Table 5.3

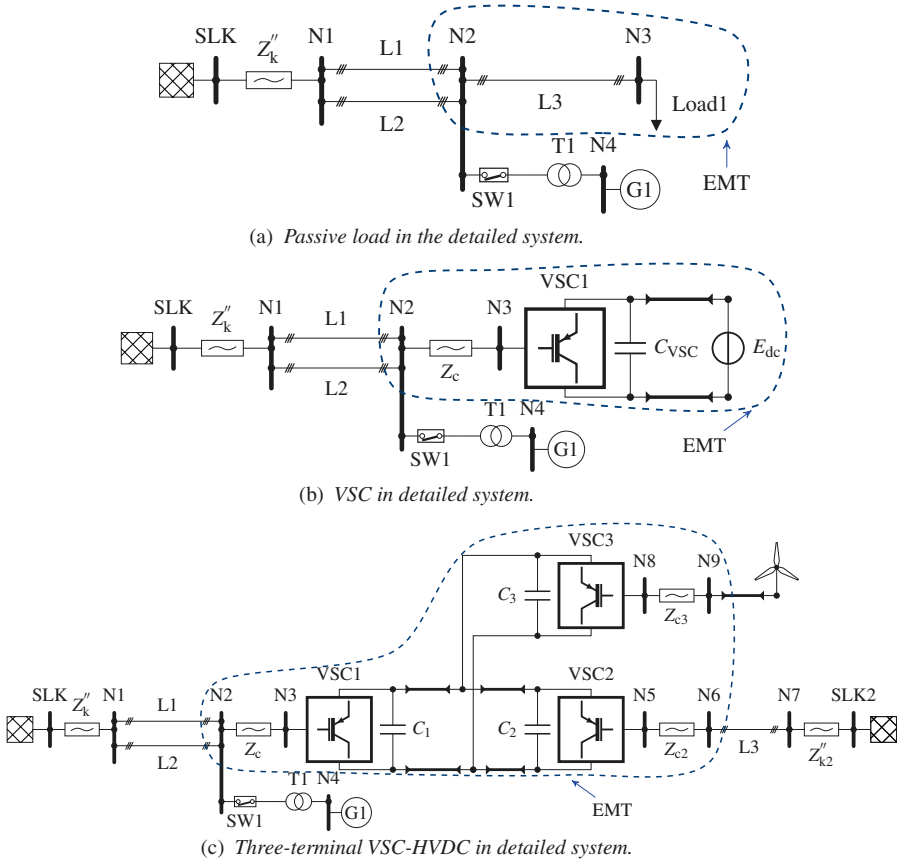


Figure 5.15: Test networks used for examining the proposed improvements to the interfacing techniques.

The network shown in figure 5.15b is an alteration of this network. The external system remains identical to figure 5.15a, except for G1 which can be included by switching SW1. Inside the detailed system, the load is replaced by a 300 MVA-rated VSC terminal that is connected to a 300 kV DC-slack source (i.e., E_{dc}) by a 100 km bipolar sub-marine cable. In spite of the downside of showing unrealistic dynamic behaviour at the DC-side of the VSC, we take advantage of the application of a stiff dc source since differences between interfacing techniques can be clearly distinguished. The same holds for using SW1, which can exclude machine dynamics if desired, attributing differences in dynamics fully to the variations applied to the interfacing techniques.

The three-terminal VSC-HVDC scheme shown in figure 5.15c consists of two onshore AC equivalents. The left onshore network is identical to figure 5.15b with SW1 closed; the right network is symmetrical to it, except for the absent local generator. VSC1 and VSC2 are connected through a 200 km bipolar sub-marine cable, which is branched off right in the centre to VSC3, connecting a 600 MW rated offshore WPP. The collection grid is represented by an aggregated type 4 WTG according to the model developed in Chapter 3. The generated power distributes equally among VSC1 and VSC3 by direct-voltage droop control. N2, N6,

and N9 are interface nodes and hence included in both parts of the hybrid simulation. The system comprises formally 3 external systems and 1 detailed system. The external systems are included in a single network model however, and hence forming one monolithic entity.

Quantitative Analysis

Aside from the visual inspection of the time-domain results, we will also examine the accuracy of the interfacing techniques by calculating their maximum and mean absolute deviation with respect to the EMT and stability reference simulations. The maximum deviation is determined by

$$\hat{\epsilon} = \max (||x_i - x_{\text{ref},i}||) \quad (5.28)$$

where $\hat{\epsilon}$ is the maximum deviation, and x_i the i^{th} sample of the observed variable x . The mean absolute deviation is calculated by

$$\tilde{\epsilon} = \frac{1}{N_s} \sum_{i=1}^{i=N_s} ||x_i - x_{\text{ref},i}|| \quad (5.29)$$

where $\tilde{\epsilon}$ is the mean absolute deviation of x , and N_s is the number of steps of the compared time-domain variable. In case one simulation has more samples than the other, down-sampling is applied for harmonisation purposes. System-level quantities (e.g., δ_{G1} and $|V|_{N2}^{\text{ES}}$) are compared to the QSS reference model, whereas device-level variables (e.g., V_{dc} and $\Delta\gamma$) are compared to the EMT reference. We regard this distinction plausible because

1. the difference in network and generator modelling between EMT-type simulations and stability-type simulations makes the latter more attractive for system-level studies (i.e., large network size);
2. the main scope of the hybrid simulation dealt with in this chapter is to include averaged VSC-MTDC modelling fast and accurately into stability-type simulations; and
3. on device-level, the accuracy with respect to the EMT reference simulation is already known to be relevant, and therefore not subject to investigation here.

5.5.2 Application of existing interfacing techniques

Passive Circuit in Detailed System

As was discussed in section 5.5.1 we start with a fairly trivial implementation of a hybrid simulation in which the external system comprises a slack source and two parallel lines. These lines connect to a static load which is contained inside the detailed system (figure 5.15a). A separate EMT simulation acts as a reference. The considered interaction protocols are the conventional IP of figure 5.7 and a variation of this IP featuring improved external system event handling (i.e., figure 5.8).

At $t = 0.05$ s we inflict a three-phase short circuit at N1 with a 180 ms clearing time. The time-domain response of the hybrid simulation is shown in figure 5.16, displaying the interface node voltage and current magnitudes (external system) and waveforms (detailed system) respectively. Notwithstanding the visual differences at fault ignition and clearance, we can generally gather from the results that both IPs perform adequately for the given test system.

At fault ignition we can observe an apparent difference between the two IPs: the conventional IP shows a delay of Δt , being half a cycle here, for the voltage dip before it exerts any effect on the detailed system quantities (i.e., figure 5.16a and 5.16c). The interface node voltage magnitude $|V|_{\text{int},N2}^{\text{ES}}$ does not show this effect because the detailed system is passive and thereby not causing dynamic interactions with the external system. The IP does hence not show any effect here. The current magnitude of line L3 shown in figure 5.16d on the other hand does show a subtle distinction between the IPs adopted and the EMT reference simulation. As the current is calculated by (5.25), essentially using detailed system waveforms. The delay present in figure 5.16c we hence also observe in figure 5.16d.

During the disturbance both hybrid simulations align well with the reference simulation – no visible differences can be seen. At fault clearance however, the delayed behaviour of the conventional IP is again clearly perceptible in the current and voltage waveforms. The improved conventional IP immediately processes the fault clearing event in the detailed system interface model, hence the immediate voltage recovery. There is another notable difference is visible between the hybrid simulations and the EMT reference simulation: owing to the inherent per-phase fault clearance in the EMT simulation, the current and voltage waveforms do not coincide. This is also reflected in the phasor magnitudes of the interface quantities.

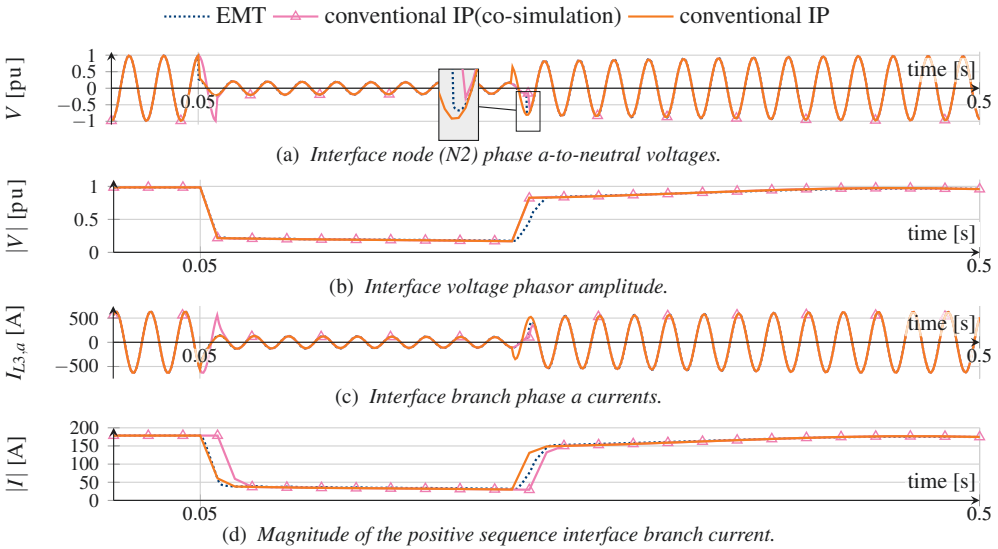


Figure 5.16: EMT versus hybrid simulation comparison for a passive load in the detailed system.

VSC in Detailed System

The previous case showed that in spite of the minor differences in dynamic response, the particular interaction protocols do not have a significant influence on the system behaviour. With the following case, which replaces the passive load with a VSC interface, we assess the implications VSC-HVDC has for the conventional IPs. The grid configuration is shown in figure 5.15b, and the VSC controls are configured according to vector control setup related in Chapter 3. The considered IPs are consistent with the preceding case.

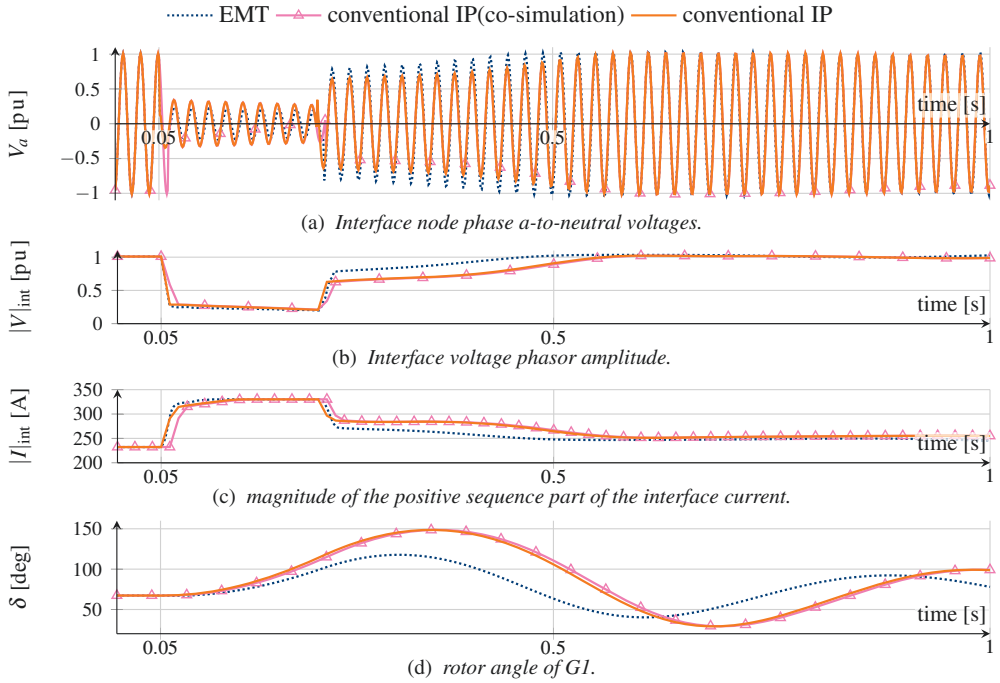


Figure 5.17: *Simulation results after a fault in the external system, having a VSC-HVDC link in the detailed system*

In accordance with the passive load case figure 5.17 shows the response of the system after a 180 ms three-phase fault at N1. In general, the response of the VSC to the voltage sag is as expected: the VSC runs into its current limit during the fault (figure 5.17c) and aims to restore its prefault operating condition after fault interruption as quickly as technically feasible. Aside from the IP-specific differences at fault ignition and clearance, there is a clear difference between the EMT reference simulation and the two hybrid simulations after fault clearance as well. These can be explained by the basic implementation of the interfacing techniques rather than by the differences between EMT and stability modelling of the external system.

On account of the different synchronous generator models — the EMT and the stability simulations employ 8th and 6th order models respectively — we could attribute these differences to the level of detail applied for the external system devices (e.g., figure 5.17d). However, the previous case also contained this modelling difference and apart from the event handling, no observable deviations between the EMT and hybrid simulations were present. Hence, the cause is rather the mere fact that the detailed system is now active and the VSC model interacts with the interface model.

In order to assess to which extent the interfacing techniques affect the VSC-HVDC system response, we now compare the improved conventional IP (figure 5.9b), the DS priority IP (figure 5.9d), and the ES priority IP (figure 5.10b), and thereby also centering on one of the detailed system quantities, the PLL angle $\Delta\gamma_{PLL}$ of the VSC. The EMT simulation is being shown for reference purposes. Figure 5.18 shows a 1 s simulation response under equal system and disturbance criteria.

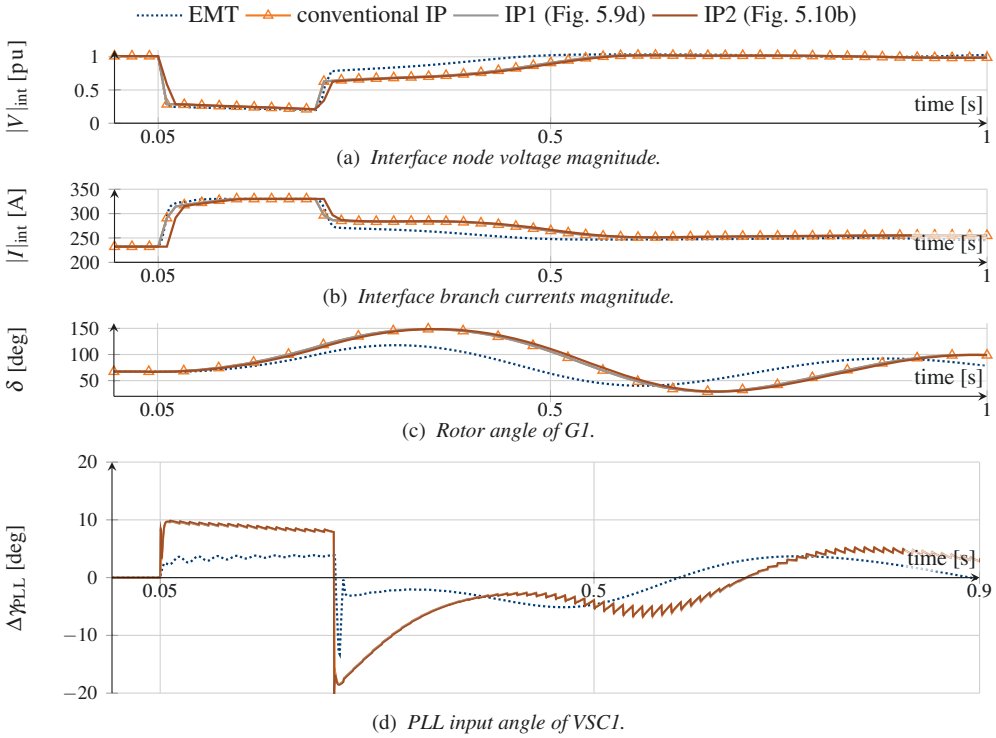


Figure 5.18: EMT versus hybrid simulation comparison for a VSC in detailed system; comparison between conventional interaction protocols.

From the results we can observe a number of differences among the hybrid simulations themselves and between the hybrid simulations and the EMT reference:

1. The ES priority IP shows a delayed response at fault ignition and clearance. This is similar behaviour as the conventional IPs showed in figure 5.17; in this case, however, the delay is not caused by the event handling algorithm but by the inherent delay between the external and detailed systems. Interactions coming from the detailed system are hence typically delayed by Δt . This phenomenon is also visible in δ_{G1} : although the maximum rotor angle deviations of the hybrid simulations as such are equal, the ES Priority IP shows a Δt delay in when the maximum value is reached.
2. As for the interface voltages and currents: the differences between the hybrid simulations and the EMT reference manifest themselves especially during the fault (i.e., the voltage waveforms of figure 5.18a), and this error propagates after fault clearance (i.e., figure 5.18b and 5.18c – the mismatch in the interface phasor magnitudes);
3. For the hybrid simulation the PLL input angle differs significantly from the EMT reference (see figure 5.18d). As a matter of fact, $\Delta\gamma_{PLL}$ also displays discontinuous jumps around 0.5 s. Aside from the observations under 2, which also account for the discrepancies of $\Delta\gamma_{PLL}$ during and promptly after the fault, the IPs appear to cause numerical issues inside the detailed system model. These discontinuous jumps also propagate into the DC-side of the VSC.

4. the maximum rotor angle of the hybrid simulation deviates around 30° from the EMT reference simulations. As has been noted before this (significant) difference is brought about by the generator model level of detail.

Based on the simulation results, which show the consequences of assessing a VSC inside the detailed system through conventional hybrid simulations, it is evident that the currently applied interfacing techniques possess a couple of shortcomings that need to be addressed. The IPs discussed so far focus on the simulation sequence per time step of the stability simulation (Δt) and the fault handling inside the external system, but do not explicitly take the equivalent source representations into account. The following cases will show how the interface technique improvements discussed in section 5.4 can facilitate the applicability of hybrid simulations for VSCs.

5.5.3 Interface Technique Improvements for VSC-HVDC

This section studies the interface technique improvements introduced in section 5.4 and necessitated by the results of preceding case studies. We will show the implications of a variable Thévenin source impedance Z_{th}^{ES} inside the detailed system, addressing observation 2 of the previous case. Then, the extrapolative filtering of angular magnitudes (i.e., ϕ_{th}) will be investigated, and thereby dealing with observation 3 of the preceding case. We continue with studying an improved ES-priority based IP that resolves the Δt delay issues being noticed in figure 5.17. Finally, the phasor capturing issues for small Δt will be discussed.

Factorisation of the EMT-type Simulation After Events

A variable implementation of Z_{th}^{ES} as outlined in section 5.4.1 potentially improves the representation of the external system as seen from the detailed system, in this case the VSC terminals. To study this, the same test network is applied as the preceding cases (figure 5.15b), now with SW1 opened to exclude the influence of G1. Though this compromises on the compatibility with a realistic external system, observable differences can now be better accredited to the applied variations in interface modelling. To emulate more realistic FRT behaviour of the VSC, the active power control scheme is equipped with post-fault active power recovery rate of 5 pu/s.

As discussed in section 5.5.1 two reference simulations are applied: an EMT-type simulation that simulates the VSC according to the model introduced in chapter 3, and a stability-type simulation employing the quasi-stationary model developed in chapter 4. The former focuses on detailed system quantities whereas the latter is used to compare external-system level behaviour.

Figure 5.19 shows the combined system response after a 180 ms three-phase fault at N1, both for a hybrid simulation in which Z_{th}^{ES} is updated at events inside the external system (i.e., at $t = 0.05$ s and $t = 0.23$ s), and for a hybrid simulation in which Z_{th}^{ES} remains fixed. It can be seen that the response of the case in which re-factorisation in the EMT simulation is implemented, is barely distinguishable from the EMT reference simulation, except during fault clearing. The EMT-type simulation is subject to phase-by-phase fault clearing while the stability-type simulation clears the three phases simultaneously due to the applied positive-sequence network representation (i.e., figure 5.19a). This introduces a slight but acceptable discrepancy between the hybrid and the EMT reference simulation, which is also visible in the interface voltage magnitudes (i.e., figure 5.19b). In the QSS model, the inner current

controller of the VSC is neglected, making $i_{C,d}$ and $i_{C,q}$ algebraic variables that can change instantaneously according to (4.2). This is primarily visible in $i_{C,q}$ at fault ignition (i.e., figure 5.19d) and in $i_{C,d}$ at fault clearance. From the results we can infer that updating Z_{th}^{ES} is effective at the expense of the necessary re-factorisation in the EMT-type simulation.

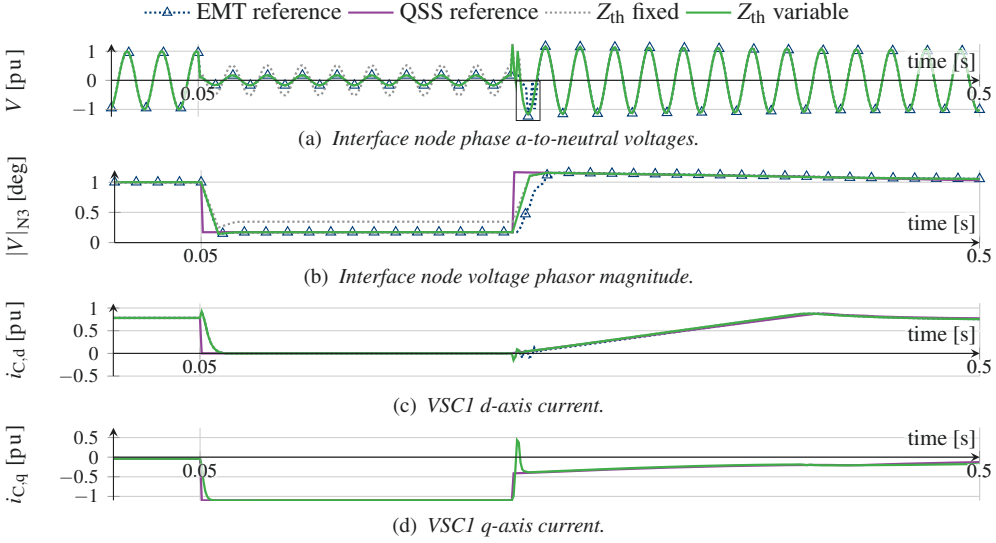


Figure 5.19: Difference between updating Z_{th} at events and keeping it constant throughout the simulation

Improved EMT Thevenin Source Update Method

As was shown during the previous case study the equivalent source representation of the external system inside the detailed system has a significant effect on the VSC response. We will now study the influence of the update method of V_{th}^{ES} method on the device and system level accuracy of the hybrid simulation, and thereby mainly addressing the recurring discontinuous jumps in the VSC's quantities that appeared in figure 5.18. As phasor angle dynamics must be present to assess this, the generator dynamics are now included again by closing SW1. The operating conditions (i.e., initial power flow, VSC post-FRT ramping rate) remain unchanged. The simulation parameters are slightly altered: $\Delta t = 10$ ms in order to enhance the visibility of the source updating algorithms, the re-factorization improvement presented in figure 5.19 is applied, and all cases use the detailed system priority interaction protocol of figure 5.9d.

We consider the following implementations for updating $|V|_{th}^{ES}$ and ϕ_{th}^{ES} :

1. according to the zero-order hold filter of (5.9).
2. according to first order hold filtering of (5.27), using interpolation through t_n and t_{n-1} ; and
3. according to extrapolative first order hold filtering of (5.27), and using a zero order hold approach promptly after the event to create favourable causality conditions.

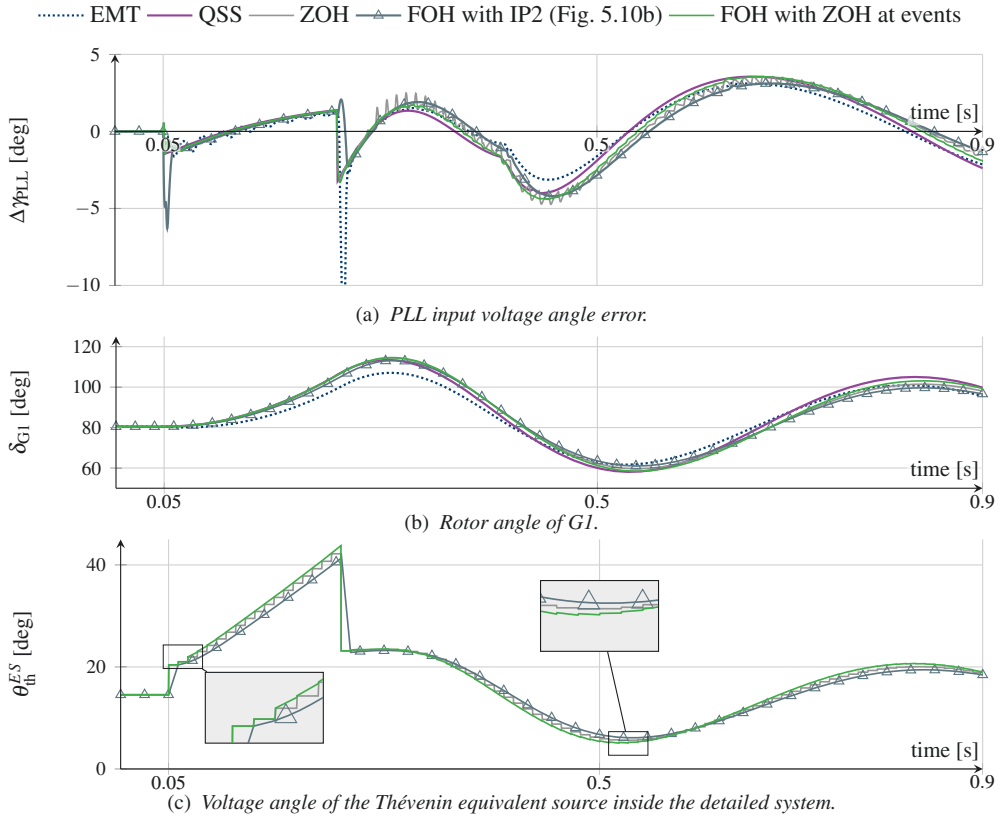


Figure 5.20: Effect of zero-order hold and first order hold filtering of interface nodal voltage angles input for updating E_{th} .

Figure 5.20 shows the simulation results after applying the same disturbance as before. The differences between the EMT reference and the hybrid simulations are now clearly perceptible, especially in δ_{G1} . This is to a great extent caused by the higher-order machine modelling for EMT-type simulations (e.g. rotor back-swing). This modelling difference is not present in the stability-type reference simulation; hence the external system response matches better with the quasi-stationary implementation of the system.

Among the implementations of the hybrid simulations we can discern a couple of differences, mainly in the detailed system: the recurring steps in $\Delta\gamma_{PLL}$ for the zero order hold filtering, the substantially smoother responses of the first-order hold implementations, and the responses of $\Delta\gamma_{PLL}$ at t_n^+ .

First, the results show a clear difference between the zero-order hold filtered source and both first-order hold implementations, especially visible after fault clearance. The inferior PLL response to the zero-order hold is inadmissible as the recurring discontinuous jumps propagate across the HVDC side. Both first-order hold approaches mostly resolve this issue although the extrapolative character is still visible.

The interpolative first-order hold filter interfaces output variables from the external system with a Δt delay, which causes difficulties for the algorithm at t_n^+ . That is, (5.27) uses for

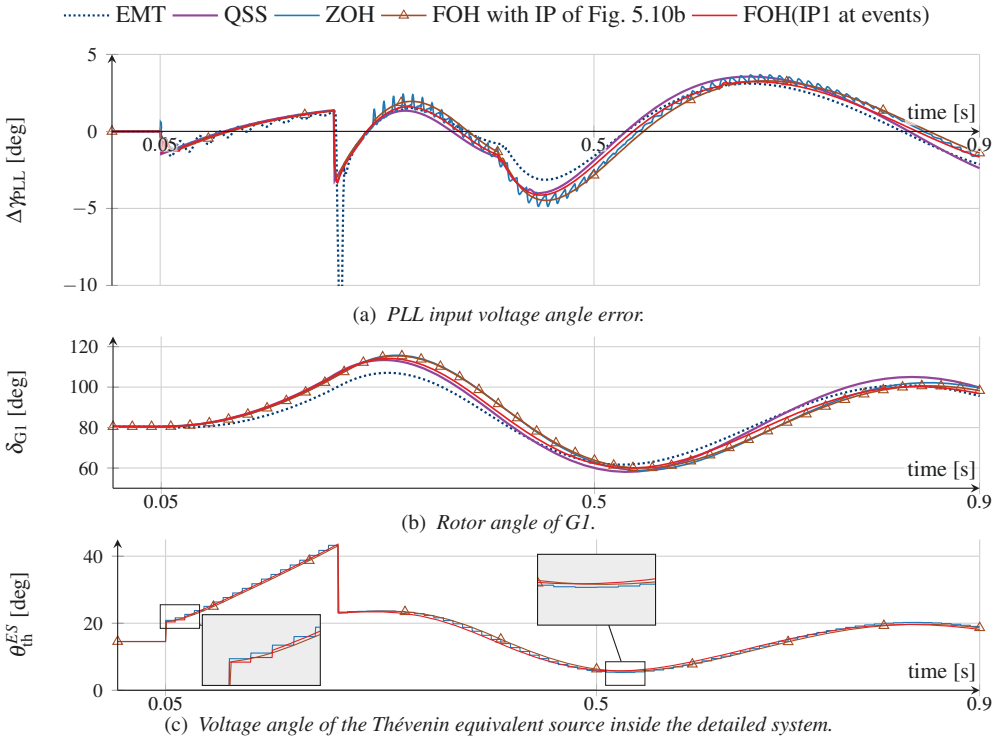


Figure 5.21: Zero-order hold and (causal) first order hold filtering of interface nodal voltage angles input for updating E_{th} , using a novel IP that prioritises the external system in the calculation order (Fig. 5.11).

$\phi_{th}[k-1]$ and $|V_{th}^{ES}[k-1]$ the values at t_{n-1} and for $\phi_{th}[k]$ and $|V_{th}^{ES}[k]$ the values at t_n^+ . As short circuits typically causes steps in these algebraic quantities, this is perceived by (5.27) as a substantial gradient to which ϕ_{th} and \hat{V}_{th}^{ES} interpolate (see also figure 5.20c). Aside from the linear change of the source values, \underline{z}_{th}^{ES} is updated promptly at t^+ . A combination of these factors lead to a rather jumpy (and unrealistic) response of the PLL at events in the external system.

The extrapolating first order hold potentially bears the same difficulty at t_n^+ , as the gradients of ϕ_{th} and \hat{V}_{th}^{ES} are undefined. This is overcome by changing the filtering method to zero-order hold at t_n^+ for at least one time step of the external system (figure 5.20c implements two to visualise the difference). After sound causality conditions have been reached the algorithm changes back to the extrapolative first-order hold. This improved implementation also acts positively on the external system response, as the Δt delay is not present any longer.

Advanced Interaction Protocol for Causal First-Order Hold Filtering

The previous case is now repeated using the interaction protocol of figure 5.10b, which changes the order in which the external and detailed system are synchronised sequentially, while using the following implementations for updating ϕ_{th} and $|V_{th}^{ES}|$:

1. using the zero order hold filtering given by (5.9);
2. according to the first order hold filtering given by (5.27), which is interpolating between t_n and t_{n+1} of figure 5.10;
3. according to first order hold interpolation, with special treatment at events in the external system (see figure 5.11).

Figure 5.21 shows the system response. The detailed system behaviour of the VSC matches qualitatively with both the EMT and QSS references, the slight differences are on account of the network and generator modelling detail in both simulations. $\Delta\gamma_{\text{PLL}}$ of the EMT reference (figure 5.21a) shows a considerable discrepancy with the other simulations at fault clearing (peaks at -15°). This behaviour is caused by the fault clearing, which must be done per phase at the current zero crossing.

Between the implementations of the hybrid simulations we can discern two main differences: 1) the recurring steps in $\Delta\gamma_{\text{PLL}}$ for the zero order hold synchronisation and 2) the first order hold interpolations, which see to an unperturbed response in the detailed system. In contrast to the implementations shown in figure 5.20, both first order hold approaches are interpolative. The main differences, favouring the implementation of figure 5.11, are during fault ignition (see figure 5.21c). At events the algorithm switches temporarily to the detailed system priority interaction protocol with first order hold filtering. The benefit of this tighter coupling between the detailed and the external system is evident from figure 5.21b: the rotor angle response lies closer to the QSS reference, and the maximum rotor swing shows little delay.

Table 5.4: Accuracy of Thévenin source update methods

	QSS		EMT		Hybrid	
Figure	5.20 & 5.21	5.20 & 5.21	5.20	5.20	5.21	5.21
Plot	—	—	—	—	—
Δt	1	n/a	10	10	10	10
IP(at event)	n/a	n/a	1	1	2	2(+1)
$\mathbf{V}_{\text{th}}^{\text{ES}}$	n/a	n/a	ZOH	FOH	FOH	FOH
$\hat{\epsilon}(\delta_{\text{G1}})$	0	0.085	0.0529	0.0469	0.1081	0.0476
$\tilde{\epsilon}(\delta_{\text{G1}})$	0	0.0508	0.0191	0.0178	0.0400	0.0168
$\hat{\epsilon}(\Delta\gamma)$	0.0073	0	0.0081	0.0078	0.0088	0.0063
$\tilde{\epsilon}(\Delta\gamma)$	0.2639	0	0.2635	0.2605	0.2624	0.2599

Aside for the qualitative assessment of the simulation results outlined before, the results are also quantitatively compared according to section 5.5.1. Table 5.4 shows the maximum and mean absolute errors of the rotor angle and PLL input angle. It can be seen that the application of first order hold filtering reduces both system-level and device-level errors, and that switching from the external system priority IP to the detailed system priority IP at events combines the merits of causal (i.e., interpolative) first order hold filtering and undelayed interaction between the subsystems at events in the external system.

The implementations for updating $|V|_{th}^{ES}$ and ϕ_{th} have also been assessed for different time step sizes. For zero order hold filtering, decreasing Δt to 5 ms leads to a 41 % and 10 % reduction in the system-level and device-level errors respectively. For first order hold filtering, the system-level errors show a 30 % reduction with respect to $\Delta t = 10$ ms, while device-level errors do not change significantly. Reducing Δt further to 1 ms does not lead to significant accuracy improvements.

Advanced Interaction Protocol During AC System Faults

We will now address the behavior of the interface in case $\Delta t < W \cdot \Delta t_{emt}$, which makes the curve fitting method inaccurate directly after the disturbance. All cases use $\Delta t = 1$ ms, and SW1 is open to exclude machine dynamics. The default window length is 10 ms. Four possible methods to deal with the phasor determination during events in the external system:

1. Do nothing special, i.e., keep $W = W_f = 10$ ms and accept potential errors. This is the base case.
2. Decrease the window length to W_f for n stability time steps for a predefined amount of time;
3. Keep the same W , but use the run-back interaction protocol of figure 5.13; or
4. Keep the same W , but use the improved run-back interaction protocol of figure 5.14.

The post-event period in which the methods are applied is one cycle (i.e. 20 ms) here to visualise the differences, but should in theory have a minimum duration of $W \cdot \Delta t_{emt}$. The EMT phasor magnitudes are calculated post-runtime based on the discrete Fourier transform using a 20 ms sliding window. Figure 5.22 shows the interface voltage waveforms and the calculated phasor magnitudes respectively.

The simulations show that method 1 and 2 show a significant discrepancy with the QSS reference case (i.e., $\Delta t = 1$ ms). Though the visible peaks for method 2 in the voltage and current phasors follow from the waveforms, figure 5.22a also shows that this is the only moment where the EMT and hybrid simulations differ. These peaks cause an unrealistic phasor determination for method 2, which is inadmissible from an accuracy and a numerical stability standpoint alike. Yet it would be more realistic to apply a longer window length, which is done for method 3 and 4.

Both show acceptable performance, with a 91% and a 79% accuracy improvement respectively, based on $\bar{\epsilon}$ of the quantitative analysis shown in table 5.5. Method 4 is preferred due to the reduced amount of EMT calculation steps that shall be done during the application of the interaction protocol of figure 5.14 compared to the interaction protocol of figure 5.13. In case of $\Delta t = 5$ ms, the maximum error between method 2 and method 3 and 4 reduces by 20% whereas the mean absolute error decreases by 36%. This is due to the reduced amount of simulation steps within the interaction protocols of figure 5.13 and 5.14.

5.5.4 Application of the Advanced Interfacing Techniques to VSC-MTDC

Various interfacing techniques that proved their advantages (but also challenges) in the previous sections are now implemented for the mulit-terminal VSC-HVDC system of figure

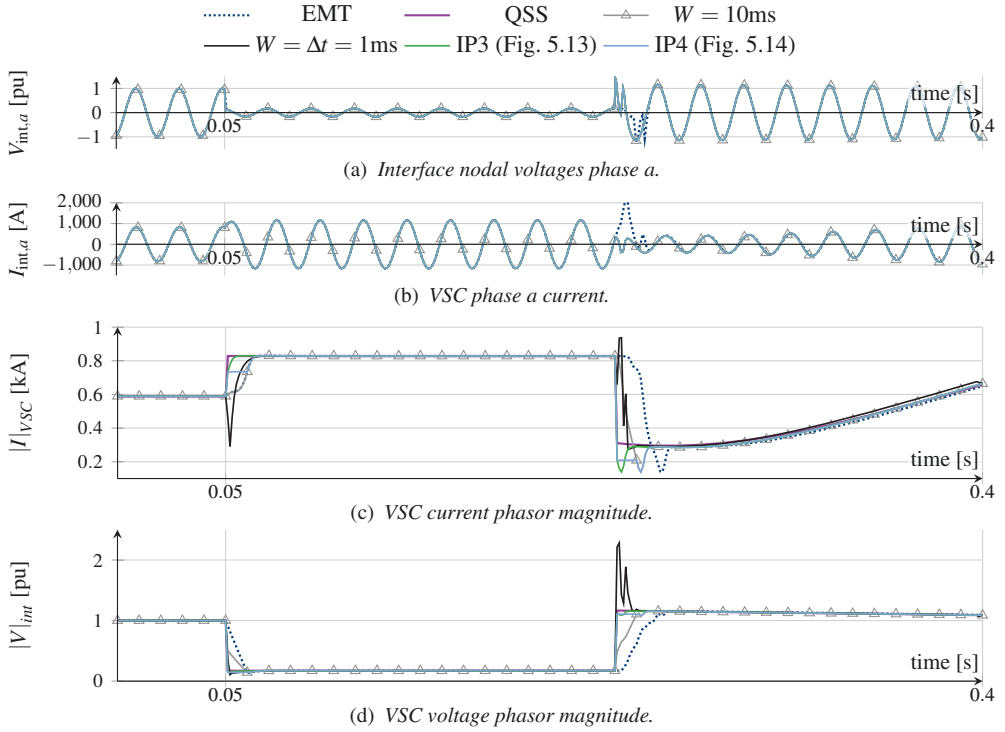


Figure 5.22: Simulation results showing the effect of applying a different IP during faults in the external system under small Δt conditions.

Table 5.5: Accuracy of the interface model at external system events

	QSS	W=10 ms	W= Δt =1 ms	IP3 (Fig. 5.13)	IP4 (Fig. 5.14)
$\hat{\epsilon}(V _{N2})$	0	0.6882	1.1171	0.0779	0.0727
$\tilde{\epsilon}(V _{N2})$	0	0.0159	0.0124	0.0015	0.0034

5.15c. The detailed system contains now multiple interface nodes (N2, N6, N9) to the external system. Per sub-case, all corresponding interfacing models use the same interfacing technique.

Four interfacing technique variations are applied. These are subdivided into variations

Table 5.6: Investigated interfacing techniques for VSC-MTDC, see Fig. 5.23

subcase (SC)	SC1 (—)	SC2 (—)	SC3 (—)	SC4 (—)
Z_{th}^{ES}	fixed	variable	variable	variable
V_{th}^{ES}	ZOH	FOH	FOH	FOH
IP	IP1 (Fig. 5.9d)	IP1(Fig. 5.9d)	IP2 (Fig. 5.10b)	IP 2(+1) (Fig. 5.11)

that need the EMT-type simulation integrated into the stability simulation, and variations that cannot touch the solvers directly. The sub-cases are

1. the detailed system priority interaction protocol of figure 5.9d using zero-order hold filtering for updating $|V|_{th}^{ES}$ and ϕ_{th} .
2. the same interaction protocol as sub case 1, now using predictive first-order hold filtering for the Thevenin source quantities.
3. the external system interaction protocol of figure 5.10b using causal first-order hold filtering.
4. the improved external system interaction protocol of figure 5.11

Table 5.6 gives an overview of the selected interface model parameters per sub case. The more basic interaction protocols of figure 5.7a caused numerical instabilities for $\Delta t = 10$ ms and are hence left out of the analysis.

Figure 5.23 shows for a 1.5 s simulation run several relevant network quantities. We can observe that U_{dc} rises rapidly during the onshore fault at N1, and VSC1 and VSC3 switch to FRT mode by engaging their chopper-controlled resistors. These continue to operate after voltage recovery until the onshore VSCs finish active-power ramping.

In general, it can be concluded that all sub-cases show plausible interaction between the detailed system and the external systems, with the most prominent differences visible between sub-case 1 and 2–4, which is on account of the updating method for Z_{th}^{ES} and the less accurate zero-order hold filtering applied for sub-case 1.

Table 5.7 shows the system and device level errors. The device-level error is relatively small (i.e., 1 % for sub-case 1), whereas the system-level accuracy is notably improved when using the advanced interaction protocol (i.e., sub-case 4). Variation on Δt showed an error reduction of $\tilde{\epsilon}(\delta_{G1})$ of 25 % for $\Delta t = 5$ ms and 52 % for $\Delta t = 1$ ms, whereas no significant accuracy improvements could be observed on device-level variables. For the used averaged VSC model, this implies that a higher Δt does not lead to decreased accuracy inside the detailed system.

Table 5.7: *Accuracy of the interface implementations for the VSC-MTDC system, see also Table 5.6*

	QSS	EMT	SC1	SC2	SC3	SC4
$\hat{\epsilon}(\delta_{G1}) \times 10^{-2}$	0	12	20.95	5.93	11.29	5.64
$\tilde{\epsilon}(\delta_{G1}) \times 10^{-2}$	0	5.11	8.67	1.91	1.92	0.92
$\tilde{\epsilon}(U_{dc}) \times 10^{-4}$	10	0	10	5.78	5.93	6.82

5.6 Summary and Conclusions

VSC-HVDC systems introduce interactions between DC-side electromagnetic transients and electro-mechanical oscillations inside the connected AC systems. The part of the grid integration studies that concentrate on stability impacts commonly employ time-domain simulations. The specifications of the respective simulation tool should include this wide range

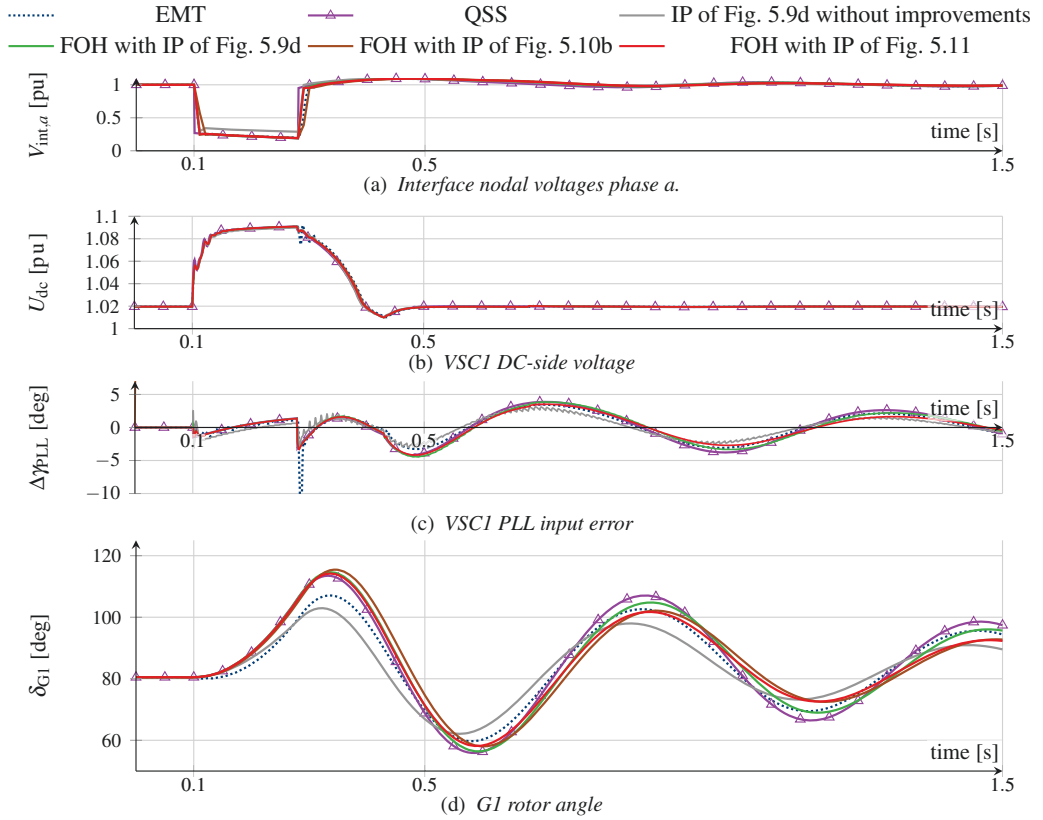


Figure 5.23: Multi-terminal simulation results for EMT, QSS, and variants of the hybrid simulation methods as per table 5.6.

of transient phenomena. This chapter extended the discussion that began in chapter 4 and elaborated on the most flexible of the available alternatives: hybrid simulations.

In order to study the simulation accuracy in detail, a separate simulation environment, written in Python, was developed for this thesis. This platform consists of a stability-type simulation and an EMT-type simulation, the numerical integration routine and solution parameters of which can be freely adjusted. This flexibility was needed in order to study several interaction protocols and interfacing techniques.

It was first investigated to what degree the available interfacing techniques from the literature were adequate for the VSC-HVDC models developed for this thesis. It was shown that existing interfacing techniques as commonly applied within co-simulation environments showed to be too inaccurate for studying transient stability based AC/VSC-HVDC interactions. The incompatibility between the two types of simulations manifested itself predominantly in cases where the difference in time-step sizes between the detailed and external system was large and during severe voltage and current angle excursions in the external system.

Next, it was shown that a significant accuracy gain can be achieved by improving the fashion in which the equivalent sources are updated, especially the external system equival-

ent inside the detailed system. This equivalent source is represented by a dynamically changing Thevenin equivalent. During faults inside the external system, this impedance must be adjusted and the corresponding EMT-part of the hybrid simulation must be re-initialised.

Another notable improvement proposed in this chapter is the way in which the angular magnitudes of the external system (i.e., the stability-type simulation) are filtered and processed into its Thevenin equivalent inside the detailed system. Conventional interfacing techniques use either zero-order hold filtering or no filtering at all. This chapter implemented a first-order hold filter procedure and developed a novel interaction protocol which allows causal angular magnitude filtering. This improvement showed a favourable (accurate) response in the external system, and smoother dynamic behaviour of the concerned VSC model in the detailed system.

Apart from improving the representation of the external system inside the detailed system, this chapter also dealt with the quasi-stationary phasor determination of the positive-sequence Norton current injection inside the external system. In the event of faults, the corresponding DFT or curve-fitting method must restart. Especially for cases in which the time-step size of the stability-type simulation is small, i.e. in the order of ms, this procedure can be inaccurate and eventually lead to incorrect interfacing between the respective simulations. This chapter introduced an iterative interaction protocol which accounts for this challenge by stepping over the originally intended interfacing instance until a quasi-stationary phasor can be determined correctly.

As a proof of concept, the improved interfacing techniques have been applied to a small example system containing only one VSC terminal. A combination of the proposed improvements were subsequently implemented on a multi-terminal VSC-HVDC system. The system-level and device-level accuracy of the simulation have been investigated quantitatively by comparing the developed improvements to a full EMT-type simulation and hybrid simulations which employ conventional interfacing methods. Variation of the external system (i.e. the stability-part of the simulation) time step-size showed marginal device-level accuracy improvements whereas system-level accuracy improved. This allows the application of the largest time step-size that is numerically allowed, yet enabling favourable execution speeds for the integral simulation.

Chapter 6

Stability Assessment of Hybrid AC/VSC-HVDC Networks

This chapter deals with the first research question stated in the Introduction. The impacts and support of VSC-HVDC on the transient stability of the onshore power system are addressed by first identifying the parameters that are expected to cause system-level interactions. Then these interactions are studied in three stages. First the impact is studied on an example system and then verified using a dynamic model of the Northwestern European power system. Finally it is shown how supplementary controls during and after onshore faults can support transient stability.¹

6.1 Introduction

Chapter 2 and 3 have been addressing the modelling, operation, and control of VSC-HVDC and offshore wind power. Chapter 4 and 5 addressed advanced modelling and simulation methods for combined AC and VSC-HVDC systems. This chapter will use the modelling and simulation approach devised previously to assess the (technological) impact of an offshore VSC-MTDC grid on the AC system stability of the Northwestern European power system, answering research question 1 stated in the Introduction accordingly.

In the past years, the view on the development of offshore wind power and multi-terminal VSC-HVDC interconnections has been crystallised thanks to

- several Europe-wide research and policy initiatives to explore the possibilities for realising an electrical infrastructure offshore;
- technological developments in VSC-HVDC transmission, which foster the protection of such a network during faults;
- realisation of national targets for deploying offshore wind power plants;

The deployment of offshore wind power plants in the German part of the North Sea, partly grid connected by VSC-HVDC, are the most striking example of these manifestations. On

¹the material of this chapter is partly based on and adopted from [s , C , AC , N , Q]

the other hand, the currently installed VSC-HVDC structures pose boundary conditions to the emergence of a grid offshore from a legal, economic, and technological perspective. Such uncertainties have to be taken into account as assumptions for the investigated scenarios.

Another notable point of interest can be found in the technological differences between the existing devices inside the AC power system and the VSC-HVDC connected offshore WPPs. The latter must be compatible with the behaviour of electrical machinery, specially during faults. Investigating the FRT of these schemes is hence vital for assessing the impact of this change in generation fleet on issues such as stability and security of supply.

In this chapter, the above mentioned considerations will be combined by first analysing the *impact* of the FRT and post-FRT actions of VSC-HVDC connected offshore wind power plants on an example AC-system equivalent, the dynamic properties of which can be altered accordingly. This analysis uses the FRT methods introduced in Chapter 3 and the multi-rate improved VSC-HVDC model developed in Chapter 5.

Subsequently, the findings from this example system will be extrapolated to a more realistic Northwestern European power system. This case study integrates more than 36 GW offshore wind through VSC-HVDC. The influence of several parameters such as FRT implementation, offshore grid topology, and the offshore active power management strategy on the dynamics and operation of the power system will be shown, and whether these can ultimately support transient stability. The analysis is conducted in the time-domain both quantitatively (i.e., CCTs, maximum deviations, etc.) and qualitatively by assessing the trajectories of response variables.

The remainder of this chapter is organised as follows. Firstly we will discuss the simulation approach, assumptions, boundary conditions, parameters, and implementation. Secondly, the simulation studies on a small-scale power system will be performed. This is followed by the impact and support assessment on the representative Northwestern European power system.

6.2 Study Approach and Simulation Setup

6.2.1 Approach

It is our goal to answer the first research question stated in the introduction. We will thus study the impact of the operation and control of an offshore grid based on VSC-HVDC transmission on the transient stability of the mainland transmission system. The terms *operation and control* and *transient stability* implicate a cause-and-effect relationship, which is not necessarily causal. We thus need to quantify the following:

- the *response variable* that we associate with transient stability, and is assumed to be caused by a change in operation and control of VSC-HVDC.
- which *parameters* of the *functions under test* in the operation and control of VSC-HVDC do we expect to be relevant to the interaction with the power system in terms of transient stability.
- how the functions under test relate to each other and the components of the entire system configuration.

Subsequently we will deterministically choose a set of parameters to vary, deduce what their

individual influence on transient stability is, and eventually assess how offshore VSC-HVDC can support stability.

Transient Stability Assessment

Looking to transient stability as a black boxed "function" of the power system, as stated in the introduction, we need to basically assess what response variable tells us the level of transient stability. The ability of the system to remain synchronised is mostly determined by the magnetic coupling inside the connected electric machines, which is commonly put to the test during voltage dips experienced at the machine terminals. Voltage dips are commonly caused by short circuits in the external system, the duration, configuration, and location of which can be considered as a parameter.

Corresponding rotors will accelerate during the fault and decelerate after fault clearance. If the clearing time was short enough, the rotor magnetic field keeps coupled with the rotating stator field and corresponding oscillations superposed to the nominal rotation speed are damped out by the rotor and stator electric and magnetic circuits accordingly. If during this deceleration after fault clearance the magnetic pole of rotor circuit slips away from the rotating stator field it is coupled to, the rotor either slips to the next magnetic pole or drifts away. Machine models generally output this level of magnetic coupling by their rotor speed ω_r and electrical angle δ_r , which can hence be used as a performance indicator.

Critical clearing times (CCT) are associated with the (in)ability of the (a)synchronous generators in a particular system to maintain the magnetic coupling between the stator and rotor field after events, most importantly short circuits. For a given system and operating point the CCT is specific to a node: it is the fault clearing time that precisely allows all generators to retain synchronism. For a given generator however, the acceleration is most severe in case there is zero retained voltage at its terminals. We can hence safely reduce this *design space* to the set of generator coupling points, making a CCT specific to a generator instead. The system-wide CCT is in our context the minimum value of all CCTs of the individual generators.

In elementary systems this first swing stability can best be quantified by the equal-area criterion in the δ_r - P plane, and CCTs can even be calculated analytically under some assumptions [196]. For multi-machine systems, which are considered in this thesis, this is more complex, not in the least owing to the non-linear load models and VSCs close to the considered generator locations. Hence, CCTs will be calculated by considering the time-domain response.

For time-domain simulations various other options exist to assess the transient stability performance. Prony analysis is for instance an alternative way of quantitatively studying the response variables. In the case studies of this chapter we mainly assess the system response qualitatively by looking at the time domain response of synchronous generators.

System Functions and Study Parameters

The main functions and controls that are expected to influence the transient stability have been discussed in section 2.4. For each of these functions it is essential to examine how they exert their impact on other functions or components contained within the system, and eventually on the transient stability. Subsequently the parameters that cause this interaction need to be defined. For hybrid AC/VSC-HVDC networks with large scale offshore WPPs (both point-to-point and MTDC) these functions are, amongst others:

- the direct voltage control of the HVDC network
- the FRT controls, both onshore and offshore
- the current limiting scheme in the VSC
- the additional reactive current injection in the onshore VSC
- the reactive current controller of the onshore VSC
- the post-fault active power recovery
- voltage controls and FRT measures of AC connected WPPs
- the dynamic performance of the AC transmission system itself

In the context of this thesis we earlier focused on direct voltage control, FRT, additional reactive current injection during faults, and post-fault active power recovery. Along these lines we aim at selecting parameters inside these functions.

Direct voltage control is commonly implemented in a cascaded fashion. In light of figure 3.9, the operation along the droop line of figure 2.13 is realised by the VSC internally, whereas the reference values (i.e., U_{dc}^* , P_{dc}^*) and droop constant are set by a supervisory HVDC controller. By altering the droop constant (i.e., $1/D = 0$) a pure power controller can be achieved. Likewise we can equip the VSC with pure direct voltage controller by disabling the power input (i.e., $P_{dc}^* = 0$ and $1/D = 1$). With these parameters the way how variations in the direct voltage influence the active power output of the VSC can be altered, and so the rotor angle response. Varying just one of the direct voltage control parameters is expected to show only effect under normal operating conditions. Instead, changing the entire operating characteristic is expected to inflict propagation of dynamics over the HVDC system.

The FRT supervisory controller operates on various parameters of the VSC controls (see table 3.2), and engages FRT measures such as the dynamic breaking resistor or offshore voltage amplitude reduction. These measures themselves act on the active power balance between AC and HVDC, and thereby on the direct voltage and hence transient stability. In the context of this study we will focus on:

- the *type* of WTG installed offshore. The applicability of a particular FRT concept depends on this [133].
- K_V and K_{aRCI} , higher values are expected to support transient stability.
- the active power recovery rate R_p , as some FRT methods are expected to not be compatible with slow recovery rates, impairing transient stability.

the latter two will now be discussed in more detail.

The additional reactive current injection is engaged by the FRT supervisory controller and operates according to (3.31) and thereby supports the voltage at the coupling point. This potentially facilitates other converters to not disconnect or run into their current limit. It is expected that aRCI in this manner supports in maintaining transient stability. The only parameters here is K_{aRCI} . The voltage controller for normal operation behaves similarly, and its influence is expected chiefly during post-fault recovery.

Recovering the active power of the VSC towards its pre-fault value shall be achieved as quickly as technically feasible. For obvious reasons the recovery rate of this restoration (i.e., R_p) is a parameter to consider for transient stability assessment. Yet, the feasibility of a particular ramping rate goes hand in hand with the type of FRT hence type of offshore WTGs.

Aside from the parameters that shall be considered for the control functionality, the power system itself to a large extent determines the ability to maintain transient stability. Potential parameters to consider here include the overall unit commitment and loading of the generators, the amount of wind-fuelled generators, the penetration of converter-interfaced generation not implementing any of the above functionality, the location of the coupling point of the VSC hence the grid strength.

An overview of the potential set of parameters and the functional interactions inside the system configuration is given in figure 6.1; their foreseen impacts on transient stability are summarised in table 6.1.

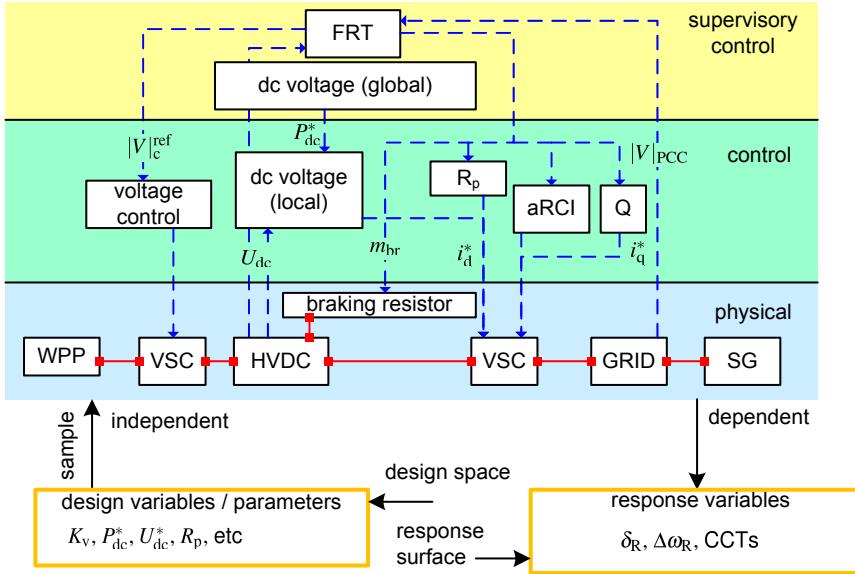


Figure 6.1: System-level interactions between the various components and control functionality. Q : reactive power and voltage controller; $aRCI$: additional reactive current injection, R_p : active power recovery, SG : synchronous generator.

control function	parameter(s), see section 3.1	expected effect on stability support
DC voltage	D, P_{dc}^*, U_{dc}^*	rejection of disturbance dynamics
voltage/reactive power	K_v, K_{aRCI}	voltage control supports stability
active power recovery	R_p	higher ramping rates support stability
FRT	type (e.g., voltage reduction)	voltage reduction limits R_p

Table 6.1: Control functions, parameters, and foreseen impact on power system dynamics

General Study Outline

Now the VSC-HVDC functional interactions with the transient stability problem have been discussed we need to define an approach to cast these parameters and interactions into concrete case studies. It would be most straightforward to define a time horizon, model the transmission system, and then test the hybrid AC/HVDC system under various circumstances. Unfortunately, this workflow makes it hard to study the expected strong relation between transmission grid parameters and transient stability. Therefore, this study takes the following approach:

1. Investigate the impact of FRT and post-FRT control methods and parameters on the stability of onshore transmission system using a *small* test system. This system enables the opportunity to easily take AC system properties as parameters to vary. This provides valuable insight into the foreseen interactions.
2. Deploy a representative dynamic model of a realistic version of the future transmission system, ensure that the grid parameters are projectable on the test system used in step 1, and check the validity of the findings obtained using the example system under 1.
3. Using the transmission model of step 2, assess how offshore VSC-HVDC transmission can support the transient stability.

which is also summarised by table 6.2. Step 1 allows easy modifications in the AC-side of the system. The follow-up steps enable easy alterations in the HVDC part of the system. However, modifying the unit commitment or the network characteristics are less straightforward and the linked assumptions need to be considered carefully. This is tackled by selecting scenarios, which set high-level system and operation boundaries that cannot be modified easily.

Step	Network	Parameters	Goal
1	small, see Fig. 6.3	type of FRT, R_p , S_k'' , γ_{conv}	Effect of grid and control parameters on transient stability during FRT and post-FRT
2	large, see Fig. 6.4	type of FRT, R_p , MTDC topology	Validity of step 1 for fixed AC grid parameters
3	large, see Fig. 6.4	U_{dc} , K_{aRCI} , scenario	Assess stability support of control functions for several scenarios

Table 6.2: Overview of the approach taken for the case studied in this chapter.

6.2.2 Scenario Selection

The scenarios selected for this study serve the following goals:

1. to assess the impact of the offshore wind penetration on the stability support by VSC-HVDC

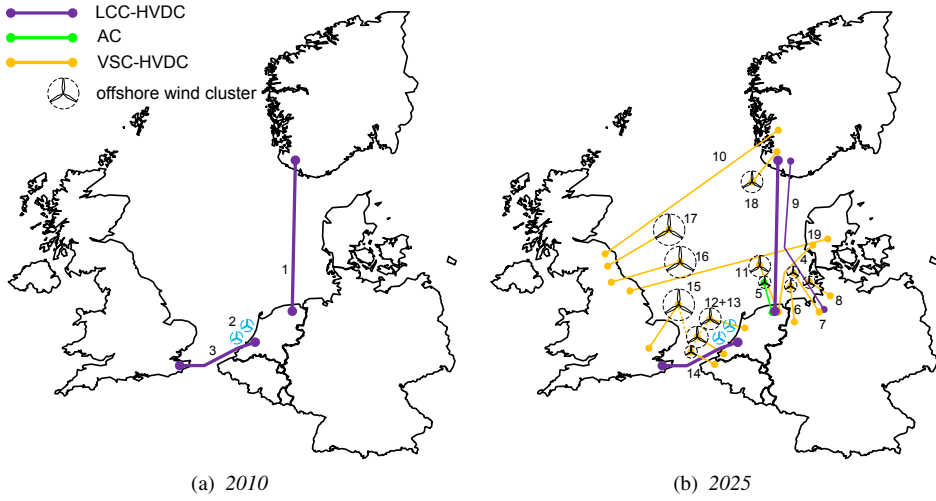


Figure 6.2: Offshore WPP locations and trans-national interconnections for the 2014 and 2025 scenarios in the North Sea. Locations and trajectories are approximated and merely for indicative purposes. Dashed yellow lines: cross-WPP connections that will be considered in this study.

2. to study how the CCTs of the future transmission system will change.

The first goal calls for a high-wind and a low-wind scenario in which the power is conveyed ashore by VSC-HVDC. The topology is expected to play a crucial role here as MTDC expands the interconnection capacity in the event of low utilisation by wind. In contrast to a high-wind scenario, for low-wind the unit commitment and loading of conventional generation is expected to vary with the HVDC network topology.

The second goal specifically calls for a reference scenario to compare against. As we study a *future* transmission system it is eminent to check the transient stability against the present network, which must be largely equal to one of the scenarios that contains an offshore HVDC network in terms of unit commitment and demand-side behaviour.

As a boundary condition we take the offshore infrastructure as already constructed, currently under construction, predicted by various outlook reports, or planned by TSOs in, for instance, network development plans [204, 205]. Figure 6.2 shows a non-exhaustive overview of the existing and projected offshore network infrastructure and offshore WPP clusters for 2014 and 2025 respectively. The annotations and estimated transmission capacities are shown in table 6.3. Which of these offshore WPPs and interconnectors will actually be implemented into the test system and under what assumptions will be discussed in section 6.2.3.

The main parameters on scenario level are the total load, conventional generator commitment, amount of wind-fuelled generation, and transnational flows, AC and DC alike. The focus of this research is mainly on the dynamic behaviour of the Dutch transmission system. For devising the scenario we hence emphasise on carefully selecting the Dutch parameters, and will, apart from some exceptions, leave parameters of (electrically) remote countries out of consideration. Table 6.4 gives a general overview of the scenario objectives. A general

no	infra	capacity [MW]	ref
1	NorNed	700	[206]
2	Dutch offshore WPPs	228	[207, 208]
3	BritNed	1200	[209]
4	COBRACable	700	[99]
5	Gemini offshore WPP	600	[210]
6-8	German offshore WPPs	10800	[211]
9	NORD Link	1400	[212]
10	NSN Link	1400	[213]
11	Eemshaven offshore area	1000	[214, 215]
12-13	Beverwijck and Borssele areas	4500	[214, 215]
14	Belgian offshore wind sites	2000	[216]
15	East Anglia	7400	[211]
16	Hornsea	5400	[211]
17	Dogger Bank	4800	[211]
18	Norwegian offshore wind site	1000	[217, 218]
19	Viking Link	1400	[219]

Table 6.3: *Electrical infrastructure and capacities of VSC-HVDC and WPPs in the North Sea.*

set of parameters on scenario level and their values can be found in table 6.5.

Scenario	Goal
Base	Reference for effect of the offshore grid on stability
High-wind	Effect of high wind penetration on stability
Low-wind, PtP	Effect of low wind penetration on stability
Low-wind, MTDC	Influence of offshore network topology on FRT and stability

Table 6.4: *Assessment goals of the selected scenarios.*

6.2.3 System Description

Example system with point-to-point VSC-HVDC link

The interactions of the FRT and post-FRT mechanisms discussed in section 6.2.1 with the onshore system as well as with each other will be analysed using the test power system shown in figure 6.3. It contains one synchronous area representing a simplified dynamic equivalent model of a power system. It comprises

- an external system (G_{ext}), the size, inertia, and loading of which can be altered ac-

property	base	high-wind	low wind, PtP	low-wind, MTDC
time horizon	2014	2025	2025	2025
total load	13390	13390	13390	13390
wind onshore	350	4234	590	590
wind offshore	40	5708	650	650
conventional generation	12707	4058	11093	10045
cross-border import from Germany (AC)	1187	5779	1328	781
cross-border import from Belgium (AC)	-2519	-3445	-2555	-2709
cross-border import (NorNed+BritNed)	2100	-2100	2100	2100
cross-border import COBRACable	n/a	-700	683	683
cross-border import (offshore VSC-MTDC)	n/a	0	n/a	1762

Table 6.5: *Selected scenarios and main loading figures for the Dutch transmission system. Values are given in MW.*

cordingly,

- an offshore WPP consisting of either type 3 (DFIG) or type 4 (FCG) wind turbine equivalents
- a 200 km ± 320 kV VSC-HVDC link. Onshore, the VSC is connected to the external system by a 30 km, 380 kV double line circuit.
- a synchronous generator (G1), which represents the local power system dynamics. Its rating is kept fixed at 192 MW,
- a load $\underline{Z}_L = R_L + jQ_L$ modeled by a fixed impedance, and
- a current source, which represents the remaining, converter-interfaced generation inside the AC system (i.e., P_{conv}). This includes for instance solar and onshore wind that do not participate in any controls shown in figure 6.1.

Except for the VSC-HVDC model, all devices and generators use PSS[®]E standard models. G_{ext} is represented by the classical model (i.e., GENCLS), G1 by the 6th-order model using the parameters from the IEEE 9-bus system [157], and all WTGs employ the standard type 3 or 4 grid-interface, electrical, mechanical, and pitch control models. The WTG model parameters have been selected such that the behaviour of the WTG model in section 3.2 is replicated. To achieve this, the current limiting scheme was set to q -axis priority and the shaft needed to be represented by a single-mass model.

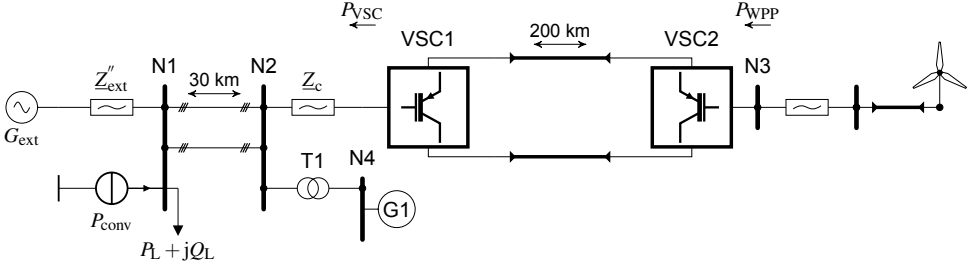


Figure 6.3: Test system containing a point-to-point VSC-HVDC connection of an offshore WPP.

Table 6.6: AC line and VSC-HVDC cable parameters

$U_{ac,nom}$	380 kV	$U_{dc,nom}$	± 320 kV
$R_c + jX_c$	$0.0015 + j0.15$ pu	C_{VSC}	$60 \mu F$
R_{line}	0.0367 km^{-1}	R_{dc}	0.0087 km^{-1}
X_{line}	0.367 km^{-1}	L_{dc}	0.127 mH km^{-1}
		C_{dc}	280 nF km^{-1}

The VSC-HVDC link is represented by the multi-rate improved dynamic model that was developed in section 4.4. The VSCs have a current limit of 1.1 pu, giving precedence to $i_{c,q}$ during and after faults. By default the additional reactive current injection is enabled during FRT using $K_{aRCI} = 2$. The DC threshold voltage for FRT of the VSC-HVDC link is assumed 1.05 pu, allowing $\pm 5\%$ for the direct voltage droop control. The electrical parameters of figure 6.3 are given in table 6.6. The HVDC submarine cable parameters are based on a 1000 MW, ± 320 kV symmetrical monopole configuration [155], being modelled as π -equivalent sections of 100 km each. In order to achieve equal time constants when analyzing different power ratings, these parameters are scaled proportionally. The same holds for C_{VSC} , which is based on a $\tau_{dc} = 20$ ms charging time-constant for a 300 MW rated VSC according to (2.19) [108]. HVDC connections exceeding 1 GW are assumed to be composed of multiple parallel cables each rated 1 GW. Ratings will be scaled similarly to the cables and VSCs of the example system in figure 6.3.

Western European Power System with offshore VSC-HVDC network

General System Properties: To test whether the findings from the analysis on the single-area system of figure 6.3 also hold for a more realistic situation, notably a more representative network, parts of the cases simulated on this system are subsequently implemented on an interconnected AC and VSC-HVDC power system based on the scenarios developed earlier. To obtain a representative network for the 2025 time horizon, this research utilised an existing dynamic model of the Dutch power system and its neighbouring transmission systems, by courtesy of TenneT TSO B.V. This model took 2010 as a reference year and consisted of:

- the Dutch transmission system (from 50 to 380 kV) with its main conventional power plants, existing onshore and offshore WPPs, and conventional HVDC connections to Norway and the UK,

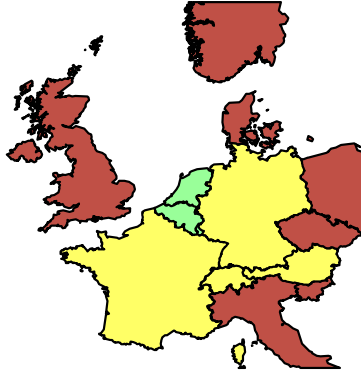


Figure 6.4: . *Level of detail in the power flow and dynamic layers of the transmission system model. Green: all nodes above 50 kV, all generators with $S_{\text{rated}} > 50$ MVA. Yellow: all nodes above 220 kV, all machines with $S_{\text{rated}} > 100$ MVA. Red: aggregated transmission network and machines, no governing and excitation systems modelled.*

- the 380 kV transmission system of the surrounding countries (i.e. Germany, Belgium, France) and their main conventional generation units, and
- simplified dynamic equivalents of the remaining Western European power system, modelled at boundary buses.

Reference scenario (2014): Taking this system as a starting point the scenarios of table 6.5 have been implemented. Figure 6.4 shows the included countries and the general level of detail of the power system model. To make the model representative for 2014 it was first extended with the Randstad 380 kV South ring and 1000 MW of installed offshore WPPs in Germany, all connected through VSC-HVDC. Additionally, the model was extended with a dynamic equivalent of the British system, as proposed in [220].

Trans-national interconnectors across the North-Sea: The reduced level of detail for the neighbouring power systems also poses boundaries on which of the offshore infrastructure to represent and which not. As the Western Danish and Nordic power systems are represented by dynamic equivalents rather than realistic networks, the NSN interconnector as well as the Viking link will be left out of consideration. This is assumed plausible, especially because of the rather large electrical distance between the Dutch power system and the landing points of these interconnectors. COBRACable was implemented as a 700 MW rated VSC-HVDC link. NORDLink, NorNed, and BritNed are based on LCC technology and obtaining connection-specific dynamic data was unfeasible. Assessing their dynamic behaviour was hence left outside the scope of this work and their operation is represented by constant loads (positive load for exporting, negative for importing).

Installed wind power: All grid models for the reference year 2025 contain an equal amount of installed wind power plants. Offshore WPPs that are known to be connected through AC submarine cables have been grid connected accordingly (i.e., the Gemini and Luchterduinen wind parks). For Belgium the total amount of predicted offshore wind power, 2000 MW is split into 50% HVDC and 50% AC connection. The German and the remote UK round 3 offshore WPPs are all assumed to be connected by VSC-HVDC. Offshore, the wind

parks are represented as clusters according to table 6.3. These clusters are then connected to the shore by parallel VSCs with a maximum rating of 1200 MW, which was the maximum rating on the market at the moment of conducting the study.

As per [221], the 2025 scenarios assume 6000 MW of installed wind power in the Netherlands, which is assumed to be dispersed across the country and therefore connected as clusters at transmission level. WindEurope (formerly EWEA) predicts 62.5 GW of installed onshore wind in Germany for the year 2030 [35]. Because the currently installed capacity is 45.5 GW [222], we assume the wind generation fleet to grow linearly and have a size of 55 GW by 2025. The WPPs are assumed to be concentrated in Northern Germany and are represented by 11 clusters of 5 GW. A similar approach is taken for Belgium, which has a capacity scenario of 3 GW for 2020 and 3.3 GW for 2030 [35].

Conventional Generation: The Energiewende in Germany has led to phasing out nuclear-fuelled power plants, among others. This is accounted for in the 2025 scenarios. For Borssele, Doel, and Tihange we assume that their operation continues to at least 2025, although this is close to the scheduled end-of-life for Tihange. The present coal price has led to widespread mothballing of gas-fired power plants. We assume, however, that these power stations can still be dispatched by the 2025 time horizon.

Offshore HVDC network topology: The design of a future trans-national grid on the North-Sea has been subject of various research projects over the past years, covering different abstraction levels (e.g., policy, economic feasibility, transmission technology). It would be naive to just assume a top-down designed meshed HVDC grid connecting all offshore WPPs without considering the economic feasibility. The physical (i.e., technology) and control (i.e., ancillary services, trade, protection) layers of the grid are expected to play a significant role on policy level, however, and we hence aim for qualitatively assessing the differences between various network topologies. Keeping this as an objective we will therefore alter the network topology of the offshore HVDC transmission from pure radial to multi-terminal, as shown by the dashed connections between East Anglia (15) via (14) to the Borssele and Beverwijck areas (i.e., 12+13).

A more detailed diagram of the MTDC part of the system is shown in figure 6.5. The MTDC link integrates in total 12.9 GW of offshore wind power into the UK and Continental European systems, distributed as follows: 7.4 GW in the UK, 1 GW in Belgium, and 4.5 GW in the Netherlands. The offshore VSC-MTDC topology of the area of interest can be varied by removing the interconnecting WPP links (i.e., the dashed lines between the offshore VSCs), resulting in purely radial VSC-HVDC connections. The trans-national offshore links (dotted, yellow) are assumed to have a rated capacity of 2 GW. All shown WPPs contain full-converter interfaced generators (i.e. type 4) wind turbine equivalent models. Apart from the VSC-MTDC scheme shown in figure 6.5, 21 GW of offshore wind power is integrated through separate radial VSC-HVDC links in Northern England and Germany (not shown).

Unit Commitment and VSC Loading: Aside from implementing the North ring of the Randstad 380 kV grid extension, the German grid also needed to be reinforced to facilitate the large amounts of wind power infeed in Northern Germany [223]. These are mainly expansions inside the AC transmission system of Northern Germany; the Suedlink expansion is considered outside the scope of this study.

All 2025 scenarios bear the same AC grid configuration, have the same installed wind power capacity, and have equal load demand. The scenarios diverge for the amount of instantaneous wind power, which calls for different VSC and conventional generator loading.

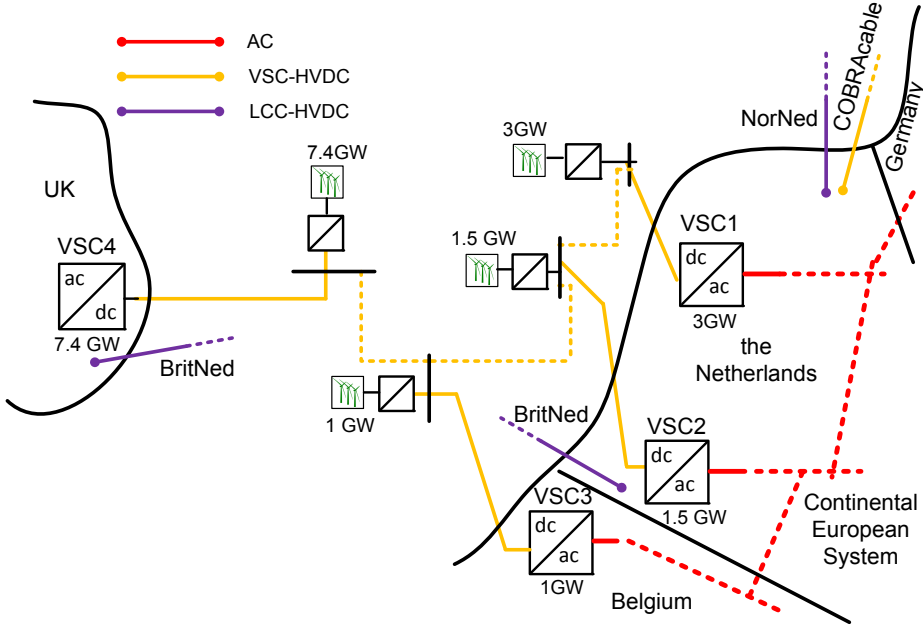


Figure 6.5: Northwestern European power system with VSC-MTDC connected offshore wind.

The high wind scenario assumes all WPPs to be operating at 90% of rated power (this assumption has been discussed in section 2.2.3), hence very little transmission capacity is left for trade and marginal transnational power flows take place over the MTDC grid. Reconfiguring from a radially connected to a multi-terminal HVDC network does not significantly change the conventional generator loading.

For the low-wind case things are different. Here, we assume the wind power plants shown in figure 6.5 to be loaded 10%, and utilise 100% (i.e., 2 GW) of the transnational connection capacity between the UK and the Netherlands. The onshore VSCs are hence only partly loaded. Similar loading is assumed for the Dutch onshore WPPs. The other offshore WPPs are loaded 10%. As the demand is equal to the high wind scenario, the remaining power has to be covered by conventional units and international trade. We have to keep in mind that for an offshore HVDC network that consists of point-to-point connected WPPs, no additional trading can be achieved during low-wind conditions. This automatically implies a different unit commitment leading to slightly difference load flow conditions compared to the MTDC option. We assume this issue to be resolvable by international trade through the AC transmission system or existing HVDC links. From the dynamic behaviour viewpoint it needs to be investigated whether this has any consequences for supporting stability.

6.2.4 Parameter Selection and Case Study Setup

FRT and active power recovery impacts

The first step in the overall approach is to show how and under which circumstances FRT schemes of VSC-HVDC connected offshore WPPs influence the AC system stability. This is done using the elementary test system discussed in the previous section and shown in figure 6.3. All cases are studied in the time domain and take a bus fault at N1 as a disturbance to trigger the functional interactions.

1. Stability effect of FRT of the VSC-HVDC link: As discussed in section 6.2.1, FRT by engaging a dynamic braking resistor, and FRT by offshore WPP voltage amplitude reduction are both implemented. The efficacy will be tested for WPPs consisting of either type 3 or type 4 WTGs. The compatibility of these methods with post-FRT control will also be shown by observing their combined influence on the onshore generator response. The onshore transmission system parameters remain constant.

2. Influence of post-fault active power recovery: This is realised by ramping up the VSCs AC power at rates in between $R_p = 5 \text{ pu/s}$ and 0.5 pu/s , based on the VSC rated power. It is expected that this affects the availability of the active power in both the DC (FRT control) and the AC systems (rotor angle stability). The offshore WPP consists of a type 4 equivalent WTG and the VSC-HVDC link uses a dynamic braking resistor to ride through the onshore fault. Immediate (i.e., $R_p = \infty$) active power recovery after fault clearance is taken as a reference situation.

3. The effect of offshore wind penetration: the instantaneous amount of offshore wind integrated into the power system by VSC-HVDC relative to the instantaneous load served pre-fault, i.e., $\gamma_{\text{vsc}} = \frac{P_{\text{vsc}}}{P_L}$. P_L is fixed and the rating of G_{ext} is for that reason scaled accordingly. We achieve this by changing both its rated power and its equivalent impedance Z_{ext}'' . A higher γ_{vsc} is anticipated to negatively impact transient stability. Yet, additional support by VSCs is supposed to sort more effect for higher γ_{vsc} .

4. The impact of AC system inertia and short-circuit power: Future power systems will contain more converter-interfaced generation, at the cost of de-commitment of conventional power plants. Among other things, this transition will lead to a power system containing fewer rotating machines directly coupled to the grid. The corresponding reduction in the system's total rotating inertia and short circuit power (S_k'') will make the future power system inherently less transiently stable. Under these circumstances it is shown what additional effects the FRT functionalities may have. The decreasing rotating inertia is modeled by adjusting the ratio $\gamma_{\text{conv}} = \frac{P_{\text{conv}}}{P_L}$, while keeping γ_{vsc} constant and decreasing the rating of the external grid equivalent. P_{conv} is modeled by a constant current source and is assumed not to contribute to grid support during faults.

Projection on the Northwestern European Power System, high-wind Scenario

The case studies discussed on section 6.2.4 are performed on the single area system. Despite the flexibility to use the AC system properties as a parameter, the system does not allow to modify the HVDC network topology and study its influence on the onshore electromechanical dynamics. As a matter of fact, the impacts found in the more elementary cases shall also be tested on a more realistic power system. Both aspects will be treated in this case study.

To realise the above we will use the grid configuration of figure 6.5 and will apply the high-wind scenario. This implies a worst-case disturbance scenario. This scenario has a total offshore wind penetration with respect to the load of 20%, while 15% is provided by onshore renewables. That is, $\gamma_{\text{VSC}} = 0.2$ and $\gamma_{\text{conv}} = 0.15$. The grid strength on transmission level varies per location, but is in the order of $S_k'' = 20 \text{ GVA}$. The fault location is chosen deterministically at the MAASBRACHT substation because the voltage dip endured at the terminals of VSC1-3 triggers all of them to enter the FRT state. All offshore WPPs are assumed to be of type 4 and their VSC-HVDC links utilise the dynamic braking resistor to achieve FRT.

As the grid-side properties are fixed, the remaining parameters to be varied are predominantly on the HVDC side of the grid configuration. First, it will be studied whether active power recovery rates impact the stability of the onshore system in the same fashion as in the single area system. All WPPs are connected radially to the shore. As all HVDC links have to attain FRT, it makes sense to see how much energy is being drained away into the braking resistors. As this is dissipated it cannot be used for the active power balance in the AC systems, eventually impairing transient stability. Therefore, the total amount of dissipated power over the 4 VSCs (i.e., $P_{\text{ftr}} = \sum_{k=1}^4 P_{\text{ftr},k}$) is used as a response variable in addition to the $\Delta\omega_{\text{NL}}$ and δ_{NL} .

Aside from taking VSC-HVDC functionality as parameters, we take advantage of changing the offshore HVDC network topology as well. Hence the impact of the ramping rates on the dynamics of both the Continental European grid and the UK equivalent (i.e., $\Delta\omega_{\text{UK}}$) can be assessed. As the duty of restoring the energy balance inside the HVDC grid is now shared among all interconnected VSCs, also the unaffected ones, it is anticipated that the presence of MTDC connections as such has a positive influence on the stability. To what degree will be assessed by also taking the active power recovery rate (i.e., R_p) as a parameter.

Transient Stability Support by an Offshore VSC-HVDC grid

The cases discussed previously revolve around quantifying the parameters that impact transient stability. The final stage of the grid studies in this chapter takes also the system loading (i.e., the scenarios) and various control parameters into account, and with it the ability to *support* transient stability. From this stage, we will also take CCTs into account to quantify the effect of a certain parameter on transient stability. The approach for examining the stability support is along the lines of the main HVDC system functions during normal operation, FRT, and active power recovery (i.e., post-FRT). This also tallies with the states within the FRT controller (see figure 3.18).

type of DC voltage control	foreseen effect
droop control	dynamics propagated
UK power mode, others droop control	mainland disturbances rejected
one droop controlled VSC	partial propagation, still benefits

Table 6.7: *Direct voltage control variations and foreseen effect on power system dynamics.*

Robust control of DC voltage during and after faults in the AC system During normal operating conditions the dominant function of the HVDC system that interacts with the AC

transmission system is the direct voltage control. The main duties of this control system are to maintain the direct voltage within its operating limits and to regulate the active power flows across the HVDC grid. Its behaviour during faults is treated as a secondary effect. In the context of this research however, it is important to study the influence of voltage control on the AC-side dynamics during onshore short-circuits, abiding by its primary functional requirements.

Taking the high wind scenario as a starting point, the HVDC network is equipped with droop control. This essentially implies that all VSCs share the duty of maintaining the voltage thus power balance in the HVDC grid. Events such as load rejection, current limit violation, and active power recovery will be perceived by all connected onshore VSCs and their coupled AC transmission systems. Alternative approaches, which are the parameters here, are pure power control by a particular area, and a mixture of droop controlled VSCs and terminals that operate in fixed power mode. This is summarised in table 6.7. The rotor speed deviations in both the Continental and UK power systems, the direct voltage, and the CCTs in the Dutch power system are taken as response variables.

The simulations are repeated for the low wind scenario employing the MTDC option. Reduced utilisation of the WPPs yields reduced VSC loading and higher trans-national flows through the HVDC grid. The suspicion is that the loading has no significant impact on the conclusions already drawn with the high wind scenario.

type of voltage support	effect on stability
fixed reactive power mode	lowest CCTs
voltage control	marginal
aRCI	notable support

Table 6.8: *Foreseen voltage support capabilities by VSCs*

Transient stability support of large scale VSC-MTDC connected offshore wind power

For scrutinising the support of VSC-HVDC during FRT we will aim for reactive power control, voltage control, and additional reactive current injection during faults. The high-wind scenario is used here adopting direct voltage droop control in the MTDC part of the offshore network.

Reactive power control will be taken as a reference by maintaining a near-unity power factor at the PCC. We expect voltage control and aRCI to support the transient stability (see table 6.8). This will be studied quantitatively by taking CCTs and qualitatively by taking the machine speed variations as response variables.

Effect of voltage support on transient stability under scenario variation For the high-wind scenario the hypothesis will be tested whether voltage control and aRCI will support transient stability (qualitatively) and to what extent (quantitatively). This is, however, just for one particular wind condition, recovery rate, VSC loading, and unit commitment. Therefore, the level of support will be tested under parameter variation of 1) scenario and hence generator loading and HVDC network topology, and 2) active power recovery rates.

By also including the 2014 reference scenario we can gain a valuable insight into how the CCTs will change for the Dutch system when large amounts of offshore wind power will be integrated through VSC-HVDC transmission. By comparing the reference with the low-wind scenario the effect of the pure presence of an offshore grid can be studied. A

comparison between the low-wind with the high-wind scenarios unveils the effect of wind power itself on stability, under the assumptions drawn in section 6.2.2.

6.2.5 Response Variable Treatment

CCT determination

CCTs are considered one of the key performance indicators for assessing the level of transient stability, especially first swing stability. In section 6.2.1 we discussed under which assumptions we determine the CCTs of the Dutch transmission system. The algorithm for determining the system's CCT is not defined yet. As mentioned, it is very hard if not impossible to calculate a CCT analytically for multi-machine systems, so it is determined by time-domain simulations. Ideally speaking a short circuit shall be inflicted at the terminals of the machine of interest, and vary its duration iteratively until the CCT is determined within predefined accuracy boundaries. Unfortunately, PSS[®]E does not offer any fully automated function or interface to determine a CCT. Hence, the binary search algorithm (i.e., algorithm 6.1) was implemented into the dynamic layer of the program.

As many iterative approaches, this binary search algorithm relies on picking sensible starting values for t_{ft}^+ and t_{ft}^- . ε shall be higher than the simulation time step-size Δt . For $\varepsilon = 5$ ms, the algorithm commonly finds the CCT in around 5 iterations per machine bus.

Quantitative Analysis

Inspection of generator rotor angle excursions and speed deviations, AC and DC voltage magnitudes, and VSC active power exchanges will be performed to qualitatively determine the effects of the simulation parameters on the power system dynamics. The effect of the grid strength parameter will be investigated quantitatively by estimating the minimum and maximum generator speed excursions as well as their maximum and absolute mean average deviation with respect to the reference simulation, which differs per case. The maximum deviation is determined by

$$D_{\text{max}} = \max(|y_i - y_{\text{ref},i}|) \quad (6.1)$$

in which D_{max} is the maximum deviation, and y_i the i^{th} response sample of the observed dependent variable y . The mean absolute deviation is calculated by

$$D_{\text{abs}} = \frac{1}{N_s} \sum_{i=1}^{i=N_s} |y_i - y_{\text{ref},i}| \quad (6.2)$$

where D_{abs} is the mean absolute deviation of y , and N_s is the length of the compared time-domain response variable.

Algorithm 6.1 Calculate CCTs using PSS[®]E**Require:** load flow converged and dynamic models initialised

```

1:  $t_{\text{flt}}^- \leftarrow 0.1$ 
2:  $t_{\text{flt}}^+ \leftarrow 0.4$ 
3:  $t_{\text{flt}} \leftarrow \frac{t_{\text{flt}}^- + t_{\text{flt}}^+}{2}$ 
4: Load dynamic snapshot
5: Set initial rotor angle vector  $\delta_0$ 
6: for all Dutch synchronous generator buses  $b$  do
7:   reset  $t_{\text{flt}}, t_{\text{flt}}^+, t_{\text{flt}}^-$ 
8:   while CCT not found do
9:     invoke short circuit at  $b$ 
10:    run until  $t_{\text{flt}}$ 
11:    remove short circuit at  $b$ 
12:    run until  $2 \times t_{\text{flt}}$ 
13:     $\Delta\delta \leftarrow \delta(t) - \delta_0$ 
14:    if any element of  $\Delta\delta > 180^\circ$  then
15:       $t_{\text{flt}}^+ \leftarrow t_{\text{flt}} \{t_{\text{CCT}} < t_{\text{flt}}\}$ 
16:    else {no element of  $\Delta\delta > 180^\circ$ }
17:       $t_{\text{flt}}^- \leftarrow t_{\text{flt}} \{t_{\text{CCT}} > t_{\text{flt}}\}$ 
18:    end if
19:     $t_{\text{flt}} \leftarrow \frac{t_{\text{flt}}^- + t_{\text{flt}}^+}{2}$ 
20:    if  $|t_{\text{flt}}^+ - t_{\text{flt}}^-| < \varepsilon$  then
21:       $t_{\text{CCT}}[b] \leftarrow t_{\text{flt}}$ 
22:      CCT found
23:    else {CCT not found}
24:      reload snapshot file, load network, initialise dynamic models
25:    end if
26:  end while
27: end for
28:  $t_{\text{CCT},\text{sys}} = \text{average}(t_{\text{CCT}})$ 

```

6.3 Case Study 1: Stability Impacts of FRT and Post-FRT of VSC-HVDC links

6.3.1 Stability impacts of VSC-HVDC FRT

First, the system of figure 6.3 is used to show the effect of the FRT method and WTG technology on the onshore power system dynamics. The rating of the VSC-HVDC link is assumed 300 MW and $S_k'' = 2.5$ GVA, all provided by synchronous generation, i.e., $\gamma_{\text{conv}} = 0$. All but one cases use $R_p = 5$ pu/s.

Figure 6.6 demonstrates the response of the system after a 180 ms fault at N1 for several combinations of FRT and WTG types. It can be seen that all FRT strategies yield different maximum DC voltages and post-fault dynamics. In case offshore WPP voltage reduction is applied as FRT strategy, the offshore WTGs enter their FRT states and cause their dynamics to propagate into the DC system (figure 6.6b). Notably for DFIG WTGs this leads to a

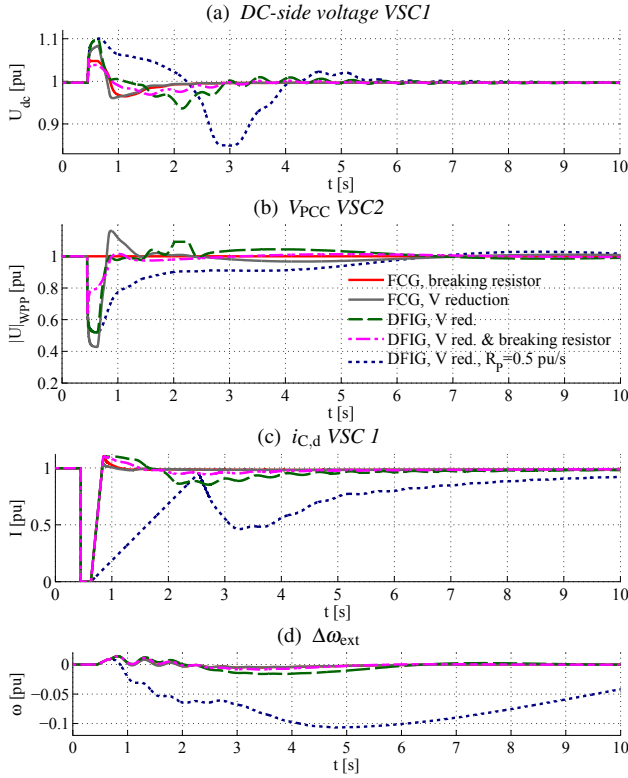


Figure 6.6: Dynamic response of the VSC-HVDC link after a fault at N1 for several fault ride-through implementations and 2 WTG technologies.

different AC system response as well (figure 6.6d). On the other hand, when a dynamic braking resistor is applied for FRT, hardly any additional electromechanical dynamics from the WPP are propagated through the DC system. This is beneficial, since these dynamics may compound the onshore rotor angle stability problem.

Grid connection requirements of the offshore collection grid could restrict the capabilities for reducing the WPP voltage amplitude for FRT purposes (i.e., it must stay compliant to the FRT voltage curve). For the relatively fast R_p chosen here this is strictly speaking not an issue, but for a slower R_p , it becomes relevant. This is illustrated by the case where $R_p = 0.5$ pu/s: due to the slower recovery rate, the FRT controls interact with the rotor blade pitch controller of the offshore WTGs. As a result, the direct voltage returns to its nominal value more slowly after the fault. This impacts V_{PCC} by a retained voltage dip, and induces more severe onshore rotor speed deviations. Hence, the recovery rate of the WTGs and the onshore VSC may limit the applicability of offshore voltage reduction.

The application of a dynamic braking resistor complementary to offshore voltage reduction is a good alternative and leads to faster draining of the excess energy inside the HVDC link. This can be seen in figure 6.6a where the combination of the two FRT methods gives the lowest maximum direct voltage during the onshore fault. Eventually, this also allows more flexibility to stay within the operating limits offshore.

The simulations have been repeated for a stronger AC system with $S_k'' = 20$ GVA. Figure

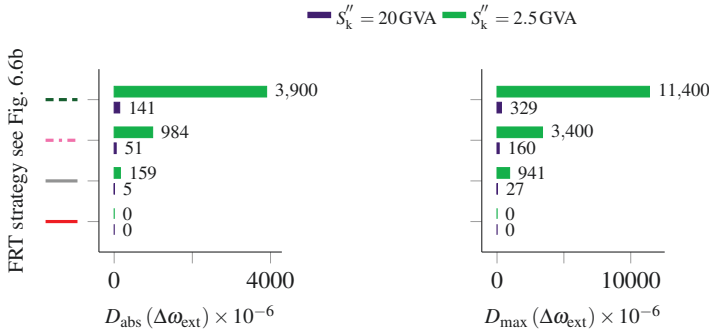


Figure 6.7: The mean absolute difference of $\Delta\omega_{\text{ext}}$ and its maximum difference with respect to the FRT by a dynamic braking resistor, for $S_k'' = 20 \text{ GVA}$ and $S_k'' = 2.5 \text{ GVA}$.

6.7 shows the mean absolute difference and maximum average difference of the external system angular speed (ω_{ext}) for $S_k'' = 20 \text{ GVA}$ and $S_k'' = 2.5 \text{ GVA}$ respectively. Both variations in S_k'' take the situation in which no offshore voltage reduction is applied as a reference. The chart shows that the difference between the FRT methods applied reduces considerably with increasing grid strength, which implies that the AC system dynamics become less sensitive to the FRT method applied.

6.3.2 Stability impacts of active power recovery

The previous case showed the effect of the FRT strategy on the AC system dynamics, keeping the active power recovery rate at $R_p = 5 \text{ pu/s}$. We will continue with keeping the AC side parameters fixed (i.e. $S_k'' = 2.5 \text{ GVA}$, $\gamma_{\text{conv}} = 0$), restricting the FRT method to a dynamic braking resistor, and varying R_p from $0.5 - 5 \text{ pu/s}$. These cases take immediate active power recovery after the fault as a reference. Figure 6.8 shows the system response.

It can be seen that depending on R_p , the DC side power balance needs more time to restore, which is reflected into the direct voltage behavior (Figure 6.8a). At the AC side, the active power balance is also distorted longer with decreasing ramp rates R_p . This leads to a speed (and hence frequency) drop up to several percent points with respect to nominal. In this fashion, the VSC operates in the time-range of the generator governing systems, which is only desirable in case it actively participates in frequency control.

In order to study the influence of a larger (and hence stronger) power system, the variations in R_p are repeated for $S_k'' = 20 \text{ GVA}$. Figure 6.9 shows for several active power recovery rates the maximum negative excursion and the mean absolute deviation of the rotor speed deviation of the external system, $\Delta\omega_{\text{ext}}$. Immediate power recovery (i.e., $R_p = \infty$) is taken as a reference. It can be seen that for a high short-circuit power (large power system, dominated by synchronously-connected generation), the ramping rate has negligible impact on the rotor speed deviations as compared to the case in which the amount of conventional generation is relatively low.

6.3.3 Effect of VSC-HVDC connected offshore wind power penetration

Figure 6.9 shows that the VSC active power recovery rate has less influence on the power system dynamics in case the connected power system is stronger. In order to study in which

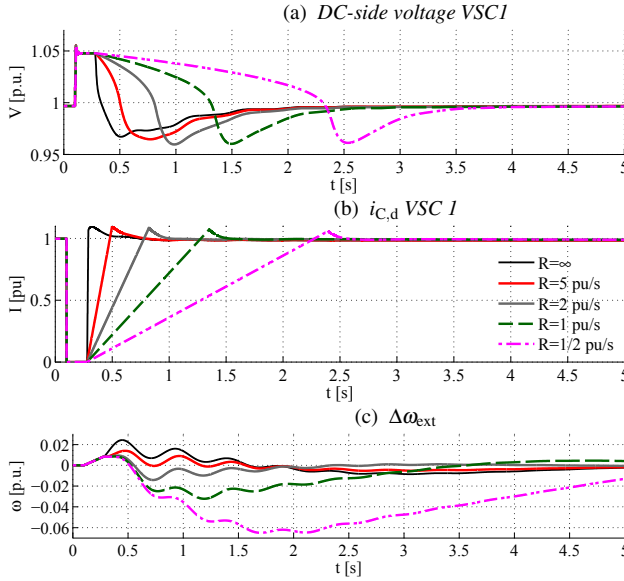


Figure 6.8: Dynamic response of the VSC-HVDC link after a fault at N1 for active power recovery rates ranging from 0.5 pu/s to 5 pu/s.

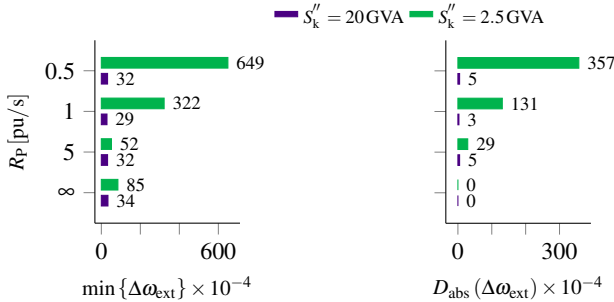


Figure 6.9: The maximum negative excursion of $\Delta\omega_{ext}$ and its mean absolute deviation with respect to immediate active power recovery for $S_k'' = 20 \text{ GVA}$ and $S_k'' = 2.5 \text{ GVA}$.

way the VSC-HVDC connected wind power penetration influences this, we will now vary P_{VSC} and the HVDC cable ratings from the 300 MW of the previous case up to 5000 MW. The load P_L is assumed constant at 20 GW. As a result, the conventional generation infeed is reduced from 19.7 GW to 15 GW, and hence the rating of the external system is reduced. The active power recovery rate of the VSC is assumed 1 pu/s.

Figure 6.10 shows the speed deviation of the external system equivalent generator. It can be seen that for higher values of γ_{VSC} , the generator response has a higher frequency deviation due to the reduced amount of rotating inertia. Moreover, the amount of active power that is to be recovered after the fault increases considerably, and this interaction constitutes an additional burden for the remaining conventional generation.

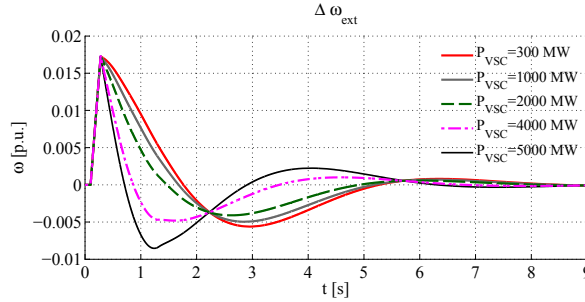


Figure 6.10: AC system response for various VSC-HVDC connected offshore wind power penetrations.

6.3.4 Influence of Converter-Interfaced Onshore Generation

The preceding cases showed that the active power recovery rate of the connected VSCs has a considerable influence on the AC system dynamics. It was also shown that this post-FRT action influences the onshore dynamics more prominently with increasing offshore wind power penetration. As discussed in section 6.2.2 the future power system will not just contain offshore VSCs and conventional generators, but also other (onshore) converter-interfaced generation. The next case varies the relative amount of converter based generation from $\gamma_{\text{conv}} = 0$ to 0.5 while assuming the offshore wind penetration and total load 5000 MW and 20 GW respectively. As a result, the total conventional generation is reduced from 15 GW to 5 GW.

Figure 6.11 shows the corresponding time-domain response of the external system after a 180 ms fault at N1. It can be seen that the maximum negative speed deviation increases substantially in case the relative amount of conventional generation decreases. Compared to $\gamma_{\text{conv}} = 0$, which is also assumed in Figure 6.10, the amplitude of the negative speed deviation increases by a factor 5. This puts severe stress on the short-circuit capability of the remaining conventional generation, their governing systems, and the transient stability of the power system in general.

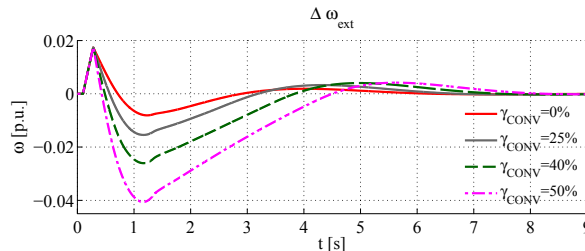


Figure 6.11: AC system response for 5 GW VSC-HVDC connected offshore wind power combined with increasing onshore converter based generation.

6.4 Case Study 2: Stability Impacts of a Future Offshore VSC-HVDC Grid

6.4.1 Effect of post-fault active power recovery on onshore dynamics

The simulation studies performed on the test system of figure 6.3 showed that FRT and post-FRT schemes impact the transient stability of the power system, especially when the relative amount of conventional generation decreases, the amount of VSC-HVDC integrated wind power increases, and their active power recovery rates are relatively slow. As discussed the next step is to verify the findings using a Northwestern European dynamic transmission system model (see figure 6.5) invoking a 180 ms bus fault at the MAASBRACHT substation.

The total power drained off by the chopper-controlled braking resistors of VSC1–3 is shown in figure 6.12a. It can be seen that at fault clearance, 3850 MW of VSC infeed is temporarily unavailable due to the FRT actions. Figure 6.12b shows the speed deviation of a local synchronous generator. Due to the delayed availability of the VSC active power infeed, the amplitude of the speed deviation increases up to 66 % for $R_p = 0.5$ pu/s.

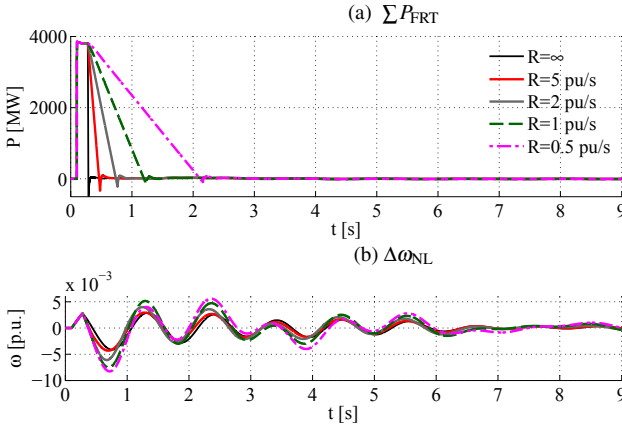


Figure 6.12: Response of the VSC-HVDC links and the speed of a local generator after a fault inside the Dutch system for several active power recovery rates.

6.4.2 Radial versus meshed HVDC topology

Next, the influence of the offshore VSC-HVDC structure will be studied. For that, all offshore WPPs of figure 6.5 are linked to each other by 2000 MW-rated connections. The resulting VSC-MTDC structure is controlled according to a common droop line, making onshore active power infeed deviations proportional to direct voltage variations. The fault location and FRT implementation are assumed equal to the previous case.

Figure 6.13 compares the system response of the VSC-MTDC interconnected UK-Continental European system to the situation in which only radial connections exist. Both situations apply $R_p = 1$ pu/s. It can be seen that the average power dissipated by all dynamic braking resistors (including VSC4) during the fault is 3400 MW, which is 12 % less compared to merely radial WPP connections. Moreover, the total amount of energy dissipated is reduced by 26%. The VSCs that are connected to adjacent synchronous areas do not exper-

ience a voltage sag (here VSC4). Figure 6.13 shows that in meshed HVDC structures, such VSCs can participate in restoring the power balance inside the HVDC system through their droop control, fostering the FRT of the entire MTDC scheme.

Figure 6.13b shows the rotational speed deviation of a large synchronous generator inside the Dutch transmission system. It can be seen that for this scenario and fault location the offshore topology has negligible influence on the speed deviations observed in the faulted AC system. It does however affect the power system dynamics of interconnected systems where the VSCs share in the FRT duty of the entire VSC-MTDC. Figure 6.14 shows this effect for different active power recovery rates. For lower values of R_p the UK-side VSC participates longer in restoring the DC side active power balance, which would put a higher burden on the respective governing systems, which act in both the rotor angle and frequency stability time-range of the UK system dynamics. Hence, the improved FRT that VSC-MTDC structures offer comes at the price of disrupting the active power balance in healthy synchronous areas that were otherwise isolated from faults in adjacent synchronous areas. The next simulation study deals with this issue in more detail.

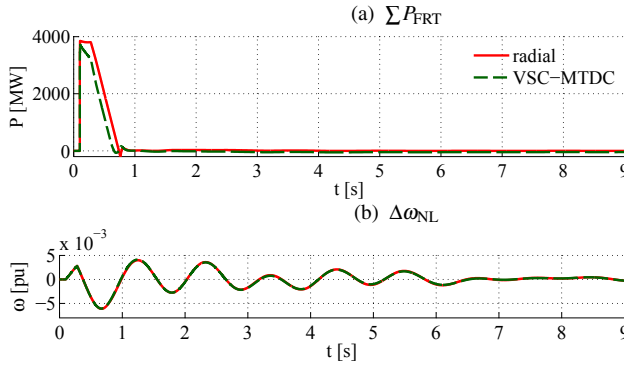


Figure 6.13: Comparison of radial versus multi-terminal VSC-HVDC connections on the North Sea, for an active power recovery rate of 1 pu/s.

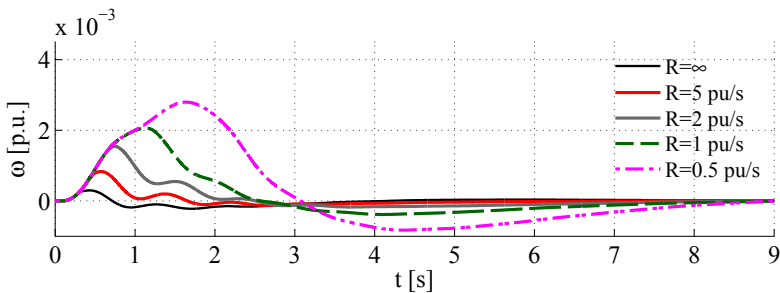


Figure 6.14: Response of the UK system equivalent after a fault in the Continental system for active power recovery rates ranging from 0.5 pu/s to 5 pu/s.

6.5 Case Study 3: Stability Support by VSC-MTDC

The final step in stability assessment of hybrid AC-VSC-MTDC networks is to examine the effects of direct voltage control, voltage support, and post fault recovery rates, as discussed in section 6.2.4.

6.5.1 Robust direct voltage control of MTDC transmission

The effect of the MTDC control strategy on the AC transmission system dynamics is studied by keeping all other control parameters fixed, i.e.,

- all VSCs apply a recovery rate of $R_p = 5 \text{ pu/s}$;
- additional reactive current injection during faults is disabled for all VSCs;
- all VSCs apply reactive power control;
- the fault location is fixed at the GEERTRUIDENBERG 380 kV substation; and
- all onshore VSCs apply a 1.075 pu direct voltage threshold for FRT.

The cross-WPP links in figure 6.5 (i.e., the dashed lines) are in service and, depending on the scenario, power can be exchanged trans-nationally. The system response for three different direct voltage control strategies after a 180 ms fault is shown in figure 6.15 . Firstly, it can be seen that for each control strategy the MTDC scheme successfully rides through the onshore fault. The differences in direct voltage behaviour are small and only distinguishable during FRT operation. The same goes for the Dutch transmission system response (only one generator shown). Adjacent synchronous areas that are coupled through VSC-MTDC, however, do perceive this short circuit as power output variations of the connected VSCs. As can be seen in figure 6.15c this behaviour depends on the control strategy adopted, and peak of the rotor speed variations are roughly 10% of the ones observed in the mainland transmission system. The propagation of these disturbances is undesirable because of the interaction with devices using the frequency as a control input, among others. This issue can be resolved by switching the VSC in the UK power system to power control mode, which is VSC4 in figure 6.5. This dynamically separates the two synchronous areas without violating the direct voltage control requirements. An alternative approach is to have one droop controlled VSC per country or per synchronous area while equipping the remaining VSCs in the MTDC network with fixed power control. This bears the potential merit of knowing beforehand where power variations can be expected in case of contingencies (short circuits, load rejections). For this particular case this gives a slightly higher peak value of $\Delta\omega_{UK}$, but aside from that no significant differences can be observed compared to the droop-oriented control. An alternative study using a different MTDC network strategy showed direct voltage and rotor angle responses in between those obtained with the droop and fixed power control modes [221].

For the high-wind scenario, the WPP to shore cables are fully utilised so hardly any power is transferred between the synchronous areas. For the low-wind scenario things are different: the Dutch part of the transmission system imports over 1700 MW from the UK, thereby highly utilising the cross-border MTDC transmission capacity. Under these circumstances, the simulations were repeated, yielding highly similar results with the main difference that

the maximum frequency excursion in the UK system is 38% of the one shown for the high-wind scenario.

As can be seen in figure 6.15 for the high-wind scenario, the direct control method itself does not have major impact on the rotor speed (and implicitly frequency) of the affected power system. The CCT analysis for all three control methods on both scenarios affirms this: for the high-wind scenario the average CCT of all generators is 0.336 s whereas for the low-wind scenario this is 0.311 s. The impact of the direct voltage control strategy was not observable in these quantitative figures. We can hence infer that under the set of assumptions taken for this chapter the control method adopted does not affect the transient stability of the faulted system, but nonetheless may trigger dynamics in the interconnected synchronous areas.

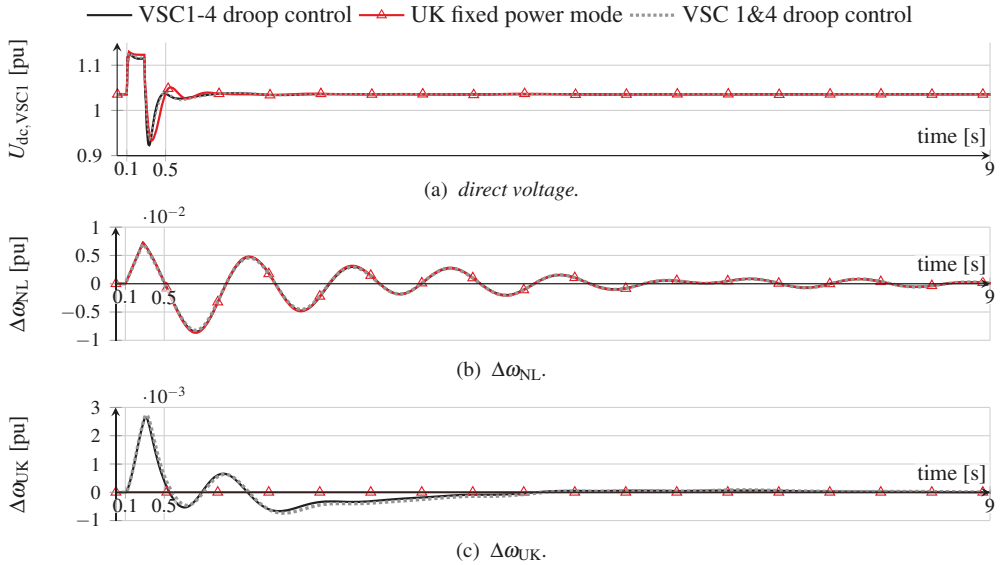


Figure 6.15: *Continental European and UK system response after a 180 ms bus fault in the Dutch transmission system (high-wind scenario).*

6.5.2 Stability support assessment

The previous case showed that the direct voltage control itself does not impact the transient stability of the onshore transmission system, despite the propagation of disturbances from one synchronous area to the second. As indicated, supporting the AC terminal voltage in order to limit the geographical impact of a fault is expected to support the transient stability. We approach this by taking the high-wind scenario using reactive power control as a base case (none of the VSCs actively support the voltage). Subsequently all VSCs except the COBRACable terminals are equipped with voltage control using a $K_v = 2$ and a large integrating time constant. The final two case variations add also the aRCI controller on top of the voltage controller.

Figure 6.16 shows the AC terminal voltage of VSC1 and the rotor speed perturbations for a large generator in the Dutch power system. From the voltage response it can be clearly

seen that the network as such is strong—the voltage recovers almost immediately after fault clearance. Applying voltage magnitude control boosts the voltage but as it is predominantly intended for control during normal operating conditions the time constants are relatively slow. The effects on the rotor dynamics hence remain essentially small. For aRCI this is different. As this proportional controller is only engaged during FRT and post-FRT mode, it does not interact with the other critical transmission system functions such as primary control. During the fault, the rotor acceleration is reduced by 32% and also after fault clearance the amplitude is reduced as compared to reactive power control.

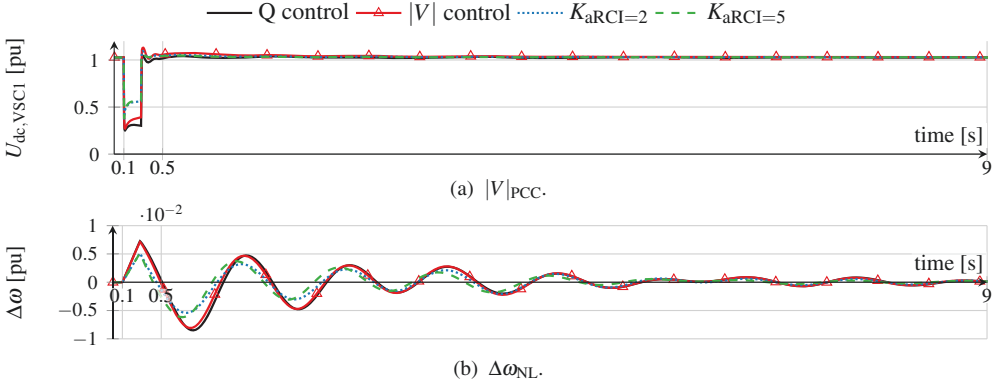


Figure 6.16: VSC voltage and frequency response for various reactive current control strategies.

From the above it is manifest that aRCI improves the system dynamics, even in transmission systems with a high short circuit power. The CCTs of each case variation, however, remain unaltered just like the previous cases in which we varied the direct voltage control method (i.e., the average CCT equals 336 ms). This can be accounted for by the relatively small effect of voltage control after fault clearance due to the electrically strong system. Besides, CCTs are calculated by applying a short circuit at the machine terminals. The machine loading and local controls are then the dominant factors for first swing stability, and the effect of VSC controls is marginal.

In order to better quantify the differences between the parameter variations adopted here we instead calculated the CCT for the employed fault location. For reactive power and voltage control the CCTs are 367 ms and 401 ms respectively. When applying $K_{aRCI} = 2$ and $K_{aRCI} = 5$ these CCTs increase to 455 ms and 490 ms, which is a 33% improvement compared to applying solely reactive power control (see figure 6.16b).

The above simulations have been conducted while keeping the scenario (high wind) and active power recovery rates ($R_p = 5$) fixed. The CCT analysis has been repeated by also varying the ramping rates and the applied scenario. The results are shown in figure 6.17. First, we can conclude that the effect of aRCI is independent of the maximum active power recovery rate applied—for each ramping rate near equal CCTs are acquired. Second, the effect of aRCI is most prominently observable in the high-wind scenario. This is in line with the expectations as the VSC-based infeed is 142% of the conventional generation. For the low wind scenarios the effect of aRCI is marginal and within the accuracy margin of the stability simulation. Although the VSCs are still connected to the AC system in these scenarios, and can hence provide extensive voltage support, the behaviour of the connected electrical

machines appears to be dominant. Moreover, the CCTs for both low-wind scenarios are equal, which implies that the MTDC network topology does not have any significant effect on the first swing stability of the mainland system.

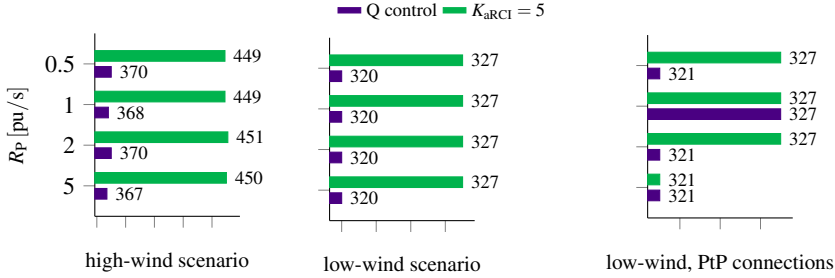


Figure 6.17: CCTs (in ms) for fault location Geertruidenberg 380 kV.

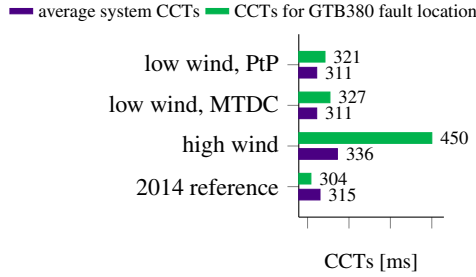


Figure 6.18: Comparison of CCTs for all applied scenarios.

The above case studies have been carried out by assuming a 2025 time horizon, in which a substantial proportion of the conventional generation has been substituted largely by wind power. The applied parameter variations answered to a large extent how VSC-MTDC will impact the onshore dynamics, especially transient stability. However, a comparison with the present situation has not been made yet. Figure 6.18 compares the average and location-specific CCTs for all scenarios against the 2014 reference scenario. Especially for the high-wind case we can see the benefit of the large-scale integration of VSCs: the transient stability of the remaining dispatched synchronous generators is boosted. The reference scenario has no VSC-HVDC except for the first HVDC connected offshore WPPs in Germany. The CCTs in this scenario are slightly lower than the 2025 scenarios, even without any voltage support enabled. We can infer from this that under the present set of study assumptions the presence of a VSC-HVDC offshore grid itself does not negatively affect the transient stability. On the contrary: the stability slightly improves.

6.5.3 Computational considerations

All case studies of this chapter have been executed on a Windows 7 workstation with an Intel i7-5600U CPU and 8 GB RAM. The PSS[®]E dynamic simulations are single-threaded. The time step-sizes were $\Delta t = 1$ ms for the stability simulation and $\Delta t_{mr} = 100 \mu s$ for the internal integration loop of the multi-rate improved HVDC model.

The network has 1755 buses in total and 200 dynamics plant models, 34 of which VSCs. The simulation of each parameter variation took 62 s and the execution of the CCT algorithm took 854 s for the high-wind scenario. For one specific bus the CCT calculation takes 110 s. The low-wind scenario has more synchronous generators committed, and the CCT calculations take 80 % longer.

The dynamic HVDC model that does not employ multi-rate techniques takes 612 s per parameter variation. The multi-rate improved model hence boasts a factor 10 execution speed gain. For the CCT analysis conducted in this chapter the simulations would have taken more than 4 days without this speed improvement.

6.6 Summary

This chapter answered the first research question and its background questions as stated in the introduction. We analysed in detail the impact of FRT and post-FRT on the dynamic behaviour of the future power system, and investigated under which circumstances the functions revolving around FRT and post-FRT can sustain transient stability. Several case studies have been performed using the modelling, control, and simulation methods developed earlier in this thesis. This was first done on an example system to explore which sensitivities affect the dynamics of the power system, and subsequently on a more realistic European power system to corroborate these findings and to explore support options.

The first part of the analysis was performed on an example system containing a VSC-HVDC connected WPP. This enabled us to take grid properties as parameters to vary, AC and DC alike. It was shown that the relation between the post-FRT active power recovery rate and the onshore rotor angle excursions was significant, especially in case the amount of offshore wind generation was large with respect to the conventional generation. These case studies also exposed the relation between the active power ramping rates applied in the onshore system and the combination of wind turbine technology and FRT methods applied.

Subsequently, parts of the findings obtained from the example system have been verified on a more realistic case study with a 2025 time-horizon. The grid configuration allowed to distinguish between radial VSC-HVDC connections and a MTDC offshore grid, which interconnected in total 12.9 GW of installed offshore WPPs. It was shown that the influence of the active power recovery rate on the system dynamics corresponded to those obtained earlier. The FRT duty of VSC-MTDC is less challenging compared to the point-to-point option because 1) the perceived load rejection is small compared to the power in-feed by the offshore WPPs, and 2) the options to balance the power are more extensive.

The geographical impact of the fault is larger for VSC-MTDC: the FRT dynamics propagate through the HVDC system to the connected VSCs, and may hence affect the operation of healthy synchronous areas. The corresponding dynamics should fit within the local requirements. Therefore, the gain of improved FRT capability comes at the price of propagated and possibly challenging to control dynamics. It has been highlighted that combining various direct voltage control options can block such dynamics.

Besides highlighting the interactions between various control functions that are usually strictly separated from each other, we also assessed the stability support options of a VSC-MTDC network. This was achieved by drawing up three scenarios: high-wind, low-wind with point-to-point links, and low-wind with VSC-MTDC. It was shown that notably additional reactive current injection boosts the critical clearing times (33% for the high-wind

scenario). The additional influence of the MTDC network topology on stability support was marginal. As compared to the 2014 reference scenario, the system average CCTs do not change significantly whereas location-specific CCTs slightly increase, for high-wind and low-wind scenarios alike.

Chapter 7

Conclusions and Recommendations

7.1 Conclusions

The grid integration of renewable energy sources at all voltage levels in the power system is politically, economically, and technically challenging. The emergence of HVDC transmission based on VSC technology allows for massive connection of large wind power plants connected far offshore. It is foreseen that in the coming decades such DC connected power park modules will substitute a significant proportion of the present day fossil-fuelled conventional power plants. This thesis has been focused on the technical aspects of integrating VSC-HVDC based offshore wind power plants into the onshore transmission system.

The emphasis of these technical aspects was on the rotor angle stability impacts of a (possibly multi-terminal) VSC-HVDC network. The accompanied studies are commonly performed with transient stability analysers, which allow simulation of large power systems with reasonable execution speeds. This comes at the expense of network and device model simplifications while precisely including those functions that affect the generators' response variables (i.e., rotor speed, angles).

Stability-type simulation are lacking standard VSC-MTDC models. The VSC-HVDC functions that are foreseen to impact transient stability hence needed to be modelled accurately and computationally efficiently. The fault ride-through of VSC-HVDC links has been taken as a typical example to showcase the fact that these modelling and simulation requirements clash. This has lead to two main research questions that needed to be addressed, stated in section 1.2. In short: first, what are the transient stability impacts of VSC-MTDC? Second, how can these impacts be modelled and simulated accurately and efficiently? Answering these questions led us to the detailed conclusions listed in the coming subsections.

7.1.1 Development of VSC-HVDC models for FRT analysis

Onshore fault ride-through is one of the main requirements the plant owner has to fulfil and constitutes as major technical challenge especially for VSC-HVDC connected wind power plants. VSC and wind turbine models from the existing body of work have been taken as a starting point and have subsequently been adjusted for FRT analysis. This study applied the

averaged model of the VSC employing vector control onshore and direct control offshore. For electromagnetic transients (EMT) simulations the grid interface is assumed a balanced three-phase voltage source while for stability-type simulations this grid interface is modelled by a complex Norton current injection.

An FRT controller was proposed, which is a state machine acting on top of the controls for normal operation and can detect AC and DC voltage violations, switch VSCs to various operating states, and eventually contribute to maintaining synchronism with the grid during faults. This thesis then qualitatively investigated the applicability of several concepts to ride through an onshore fault for the two main types of wind turbine generators (DFIG and FCG). Employing a dynamic braking resistor located at one of the VSC terminals showed the most beneficial direct voltage behaviour: during faults the direct voltage can be easily maintained around the normal operating region and post-fault recovery proved to bear no significant issues, in the onshore and HVDC system alike. Offshore voltage amplitude reduction, or mirroring the voltage perceived onshore to the offshore VSC, basically transfers the FRT duty from the VSC terminal ashore to the individual wind turbine generators. Here we observed issues especially for slow active power recovery rates. The maximum recovery rate is determined by the 'weakest link' inside the VSC-HVDC connected offshore WPP. For offshore voltage amplitude reduction this turned out to be the DFIG-based wind turbines, the individual FRT of which caused an endured voltage dip in the offshore collection grid, thereby violating local connection requirements.

7.1.2 Combined EMT and stability-type Simulation Framework

To scrutinise the simulation aspects of mixed AC/VSC-HVDC systems, a simulation framework was developed and validated. Compared to using commercial alternatives this allowed 1) accessing and adjusting numerical solution routines of the individual simulators, 2) dynamic modelling of components free from simulation framework boundaries, 3) studying in detail the coupling issues that arise when synchronising between the simulators.

The individual power system simulation concepts are well developed, numerically optimised, and well documented over the past 4 decades. The *stability-type partition* of the framework was qualitatively validated against both PSS[®]E and PSS[®]NETOMAC. Keeping network, power flow, and dynamic models as similar as possible, unaccountable (minor) differences have been observed between the in-house developed simulation and PSS[®]NETOMAC, whereas the results largely coincided with PSS[®]E. As for the *EMT-type partition*, the simulation framework is considered validated against PSS[®]NETOMAC, in spite of negligible discrepancies that can be mainly attributed to the generator-network interface models, which differ between the simulators.

7.1.3 Improved Monolithic Modelling and Simulation Techniques for Transient Stability Studies

A state-space model suitable for analysing generalised HVDC networks based on VSC technology was developed and refined throughout this research. It consists of an HVDC dynamic model that allows an arbitrary connection of π -branches and shunt circuits. At each bus an associated VSC dynamic model can be defined. The inputs of the HVDC model are the AC-side active power injections of the VSCs, whereas its outputs to the VSCs are the nodal voltages.

Especially the HVDC part of the model contains small time constants that cause instabilities in the numerical solution routine, hence requiring reduction of the time step-size for numerical integration. Two alternatives have been investigated: 1) a reduced-order version of the MTDC system, and 2) a multi-rate improved version of the state-space VSC-MTDC system.

The first alternative disregarded all submarine cable electrical elements except the pole-to-ground capacitance. These capacitances were then lumped to one imaginary central DC node. For small perturbations (load rejection) this showed adequate results but for FRT the simplification was too crude because the controls for achieving FRT rely on accurate measurements of the local direct voltages.

The second alternative wraps the HVDC grid with its associated short time-constants into an inner integration loop. Its transients are then simulated at an appropriate, small time step-size whereas the remainder of the system employs the default time step-size. This model showed accurate results also for FRT behaviour. For simulations on an elementary test system boasted a factor 5 speed improvement.

7.1.4 Advanced Hybrid EMT and Stability Simulation of VSC-HVDC

The behaviour of power electronic systems and large transmission networks are commonly examined separately using either EMT or stability-type simulations. The electromagnetic transients of large-scale VSC-HVDC systems need, however, to be taken into account when assessing power system stability. It was shown that combining EMT and stability-type simulations provide the required accuracy while the execution speed of the simulation is notably faster than conducting a full EMT simulation for the entire system under test.

The application of such hybrid simulations for generalised VSC-HVDC networks has been the main scientific contribution of this thesis. Several aspects have been addressed in detail and lead to corresponding scientific innovations:

- How existing interaction protocols and interface techniques function specifically for VSC-HVDC. It turned out that existing protocols were too inaccurate, especially during faults, during angle excursions in the external system, and when the difference in integration time step-sizes between the stability and EMT partitions were large;
- How the representation of one system into the other must be adjusted to improve the accuracy with respect to a full EMT simulation. The largest gain was reaped by adjusting the equivalent source impedances at events in the external system. This comes at the cost of a full reinitialising of the EMT partition of the hybrid simulation.
- Filtering of network quantities, especially voltage and current angles. A novel interaction protocol with first-order hold filtering demonstrated a smooth and rigid coupling between both partitions, including during faults
- The phasor determination in the detailed system. In case the time step-size of the stability partition is small the phasor determination algorithm fails during faults. For such occasions, this thesis has developed an iterative interaction protocol for the EMT partition. It jumps over the intentional synchronisation interval and iterates with the stability partition until a reasonable sampling window has been obtained.

Both hybrid simulation and multi-rate transient stability simulation provided the desired accuracy and computational performance. The application of hybrid simulations, multi-

rate modelling, or reduced-order representation of combined AC/VSC-HVDC systems very much depends on other boundary conditions, such as data and dynamic model availability and accessibility (grey boxed vs black boxed), and the readiness of the software tool for connecting it to another tool. For this reason the stability assessment in chapter 6, has been carried out in PSS[®]E using the multi-rate improved VSC-MTDC model.

7.1.5 Stability impacts of multi-terminal VSC-HVDC transmission

The excellent controllability of VSC-HVDC potentially offers a wide variety of stability support measures. Yet, the behaviour of VSC-HVDC during faults is highly non-linear. This gives rise to the necessity of comprehensively studying the transient stability impacts. Studies on a small test system showed that the relation between post-FRT recovery rates and onshore frequency deviations is powerful, especially for: 1) electrically weak systems, 2) systems with a high offshore wind penetration, and 3) power systems with a large proportion of converter interfaced generation.

To assess the impact and support capabilities of a future offshore MTDC grid at the North Sea, a dynamic model of the Northwestern European power system was employed and adjusted for the approximate 2025 time horizon. High and low wind scenarios were devised which in total integrate up to 36 GW offshore and 24 GW onshore wind power respectively. 13 GW of the aforementioned offshore wind was integrated through VSC-HVDC. The HVDC network was distributed over 3 countries and its topology could be altered from point-to-point to MTDC.

First, the findings obtained from the elementary test system have been verified on this much larger and more realistic power system. Second, it was found that the propagation of dynamics from one synchronous area to the second is inherent to droop control and causes nuisance interactions in the primary control time-frame of interest. This is considered undesirable and can be mitigated by a combination of fixed power and direct voltage droop control. Third, it was studied how VSC can positively impact (i.e., support) stability, support that is. Additional reactive current injection during faults improved the transient stability of the Dutch transmission system, i.e., 33% higher CCTs for the high-wind scenario.

7.2 Recommendations for Further Research

7.2.1 Quasi-stationary Modelling of VSC-HVDC

The developed models have been derived based on the two-level VSC topology, which limits the applicability of the model for events (faults) at the HVDC side of the VSC. MMC technology has more sophisticated techniques to block the reverse current. It is advised to check the readiness of the present model for the controls and functionality that MMCs offer, and if needed modify parts of the dynamic VSC model accordingly.

The phase-locked loop of the VSC stability model has been left out of consideration since synchronisation was assumed to be instantaneous. This assumption should be tested in follow-up research. It is recommended to take the speed deviation of the network reference frame into account for the angle tracking mechanism.

For the reduced order HVDC model it is recommended to take the HVDC topology into account by also including the submarine cable resistances or by letting the corresponding VSC sub-models act on the direct voltage changes (i.e. dU/dt) instead. It is expected that

the desired level of accuracy is achieved whereas simulation at a near-normal (i.e., ms range) time step-size is feasible.

To reduce computational effort, the multi-rate improved HVDC model was only called during the first iterations of the predictor-corrector method. An exact numerical stability analysis of this simplification was outside the scope of this thesis. As a follow-up it is recommended to transcribe the solution routine in the z-domain and conduct a detailed eigenvalue analysis. It is foreseen that this will eventually lead to a more optimal implementation of the model into the overall solution routine, also for PSS[®]E.

7.2.2 Hybrid Simulations

In this thesis we assumed *fixed* time step-sized for all simulators. An assessment of the applicability and numerical stability impacts of the proposed interfacing techniques for *adaptive* time step-size simulations is strongly advised.

The application of the proposed hybrid simulation strongly revolved around averaged VSC models under balanced circumstances, both for the AC and DC sides. Testing the interfacing techniques under other conditions such as 1) single-phase faults, 2) faults in the detailed system (i.e., the EMT partition), 3) applicability for embedded VSC-HVDC links, and 4) applicability for highly detailed EMT models are recommended to be conducted to further refine the coupling methods for VSC-HVDC.

The research was done in a testing environment that used simple memory sharing between the various partitions. For generalisation purposes this definitely needs further development, preferably allowing seemingly effortless connection of various industry grade EMT and stability-type simulators. The functional mock-up interface specification and high-level architecture standards are considered essential building blocks to achieve this.

The validation of the EMT partition of the inhouse developed simulation showed slight differences with the PSS[®]NETOMAC reference simulation. The cause of this behaviour could not be determined with full certainty, and can depend on

- the implementation of the network solution algorithm
- the procedure by which disturbances (mainly faults) are implemented into the solution scheme.
- the method to couple the device dynamic models with the network model

Especially the latter is generally considered challenging and the cause of many slight discrepancies between EMT-type simulators. It is hence recommended to, just like the stability partition, check the validity of the EMT model against a third tool.

7.2.3 Stability Support of VSC-HVDC

The assumption that the wind speed varies little during the transient stability analysis seems plausible but has not been extensively tested in this thesis. Under certain conditions, especially in the non-linear region of the rotor speed-mechanical power relationship, post-fault active power recovery may not be fulfilled accordingly. It is recommended to assess this by also varying wind conditions during FRT studies.

We have taken 90% of the rated WPP power as a reasonable operating point for high-wind conditions: using offshore re-analysis data from 2007 it was shown that this accounts for at

least 24% of the time. This was assumed a plausible trade-off between taking a (for stability) worst case condition (100% utilisation, which happens only around 20% of the time) and a more realistic operating conditions. It has not been studied how the FRT controls affect the stability for low wind speed conditions. A follow-up analysis taking partial utilisation into account is thus advised.

Grid parameters like the WPP loading, the fault locations and generator loadings have been taken deterministically. The natural behaviour of these aspects are, however, stochastic. That is, some faults are more likely to occur than others and the same goes for their locations. Taking such a stochastic approach is considered vital to strengthen the transient stability impact conclusions.

It became apparent from the case studies that system-wide CCTs provide insufficient insight into the impact of VSC-HVDC based parameters on the dynamics—qualitative differences were plainly observable after all. The dominant factors for CCTs appear to be the generator-specific loading and control. CCTs for locations further down the transmission system do show explicable differences in CCTs. It is as follow-up research recommended to reassess the applicability of CCTs for the purpose of studying VSC-HVDC impacts on stability.

The simulation studies conducted for this thesis showed a significant improvement of the transient stability for the high-wind scenario, whereas the support was less manifest for the low-wind scenarios. This fosters the conjecture that underlaying assumptions of the scenarios have a major influence on the eventual outcomes. The scope in this research project was too narrow to assess this in detail. The essential recommendations for refining these assumptions in follow-up research are as follows:

- ensure geographic harmonisation of the level of modelling detail, both static and dynamic;
- properly account for power system stabilisers of all mainland generators;
- consider German North-South embedded HVDC links;
- model the electrical vicinity of the VSC coupling points in more detail; and
- include plausible and validated dynamic models of the COBRACable, NorNed, and BritNed HVDC links.

Appendix A

Iterative Procedure for Systems of Non-Linear Equations

A.1 Fixed-point iteration

In general, the problem containing a system of m equations and m unknowns takes the following standard form for a fixed-point iterative algorithm

$$\mathbf{y}^{(\eta+1)} = \mathbf{F}(\mathbf{y}^{(\eta)}) = \begin{bmatrix} F_1(y_1, y_2, \dots, y_m) \\ F_2(y_1, y_2, \dots, y_m) \\ \vdots \\ F_m(y_1, y_2, \dots, y_m) \end{bmatrix} \quad (\text{A.1})$$

where η is the iteration number. Under proper starting conditions and favourable system sensitivities, this algorithm converges to the *fixed-point* \mathbf{y}^{sol}

$$\lim_{\eta \rightarrow \infty} \mathbf{y}^{(\eta)} = \mathbf{y}^{sol} \quad (\text{A.2})$$

A.2 Newton-Raphson Algorithm

For the Newton-Raphson iterative procedure, the problem should be formulated in the following form

$$\mathbf{r}(\mathbf{y}) = \begin{bmatrix} r_1(y_1, y_2, \dots, y_m) \\ r_2(y_1, y_2, \dots, y_m) \\ \vdots \\ r_m(y_1, y_2, \dots, y_m) \end{bmatrix} = \mathbf{0} \quad (\text{A.3})$$

which only holds at the solution \mathbf{y}^{sol} . Later on, (A.3) shall be moulded in a form suitable for fixed point iteration. Suppose $\mathbf{y}^{(\eta)}$ is the η^{th} guess for \mathbf{y} , the first-order Taylor expansion

around \mathbf{y}^η is given by

$$\mathbf{r}(\mathbf{y}) = \mathbf{r}(\mathbf{y}^{(\eta)}) + \left. \frac{\partial \mathbf{r}}{\partial \mathbf{y}} \right|_{\mathbf{y}=\mathbf{y}^{(\eta)}} (\mathbf{y} - \mathbf{y}^{(\eta)}) + \text{error} \quad (\text{A.4})$$

where ∂ is the partial derivative operator. Now, $\mathbf{y} = \mathbf{y}^{(\eta+1)}$ is the next value of interest as it is *assumed* to lie closer to \mathbf{y}^{sol} than $\mathbf{y}^{(\eta)}$. For $\mathbf{y}^{(\eta+1)}$ approximately holds

$$\mathbf{r}(\mathbf{y}^{(\eta+1)}) \approx \mathbf{r}(\mathbf{y}^{(\eta)}) + \left. \frac{\partial \mathbf{r}}{\partial \mathbf{y}} \right|_{\mathbf{y}=\mathbf{y}^{(\eta)}} (\mathbf{y}^{(\eta+1)} - \mathbf{y}^{(\eta)}) \quad (\text{A.5})$$

Assuming $\mathbf{r}(\mathbf{y}^{(\eta+1)}) \ll \mathbf{r}(\mathbf{y}^{(\eta)})$ and rearranging gives

$$\mathbf{y}^{(\eta+1)} = \mathbf{y}^{(\eta)} - \left[\left. \frac{\partial \mathbf{r}}{\partial \mathbf{y}} \right|_{\mathbf{y}=\mathbf{y}^{(\eta)}} \right]^{-1} \mathbf{r}(\mathbf{y}^{(\eta)}) \quad (\text{A.6})$$

which is in the form suitable for inclusion into the fixed point iteration procedure given by (A.1), with

$$\mathbf{y}^{(\eta+1)} = \mathbf{F}(\mathbf{y}^{(\eta)}) = \mathbf{y}^{(\eta)} - \mathbf{J}^{-1} \left|_{\mathbf{y}=\mathbf{y}^{(\eta)}} \mathbf{r}(\mathbf{y}^{(\eta)}) \right. \quad (\text{A.7})$$

where

$$\mathbf{J} = \begin{bmatrix} \frac{\partial r_1(\mathbf{y}^{(\eta)})}{\partial y_1} & \cdots & \frac{\partial r_1(\mathbf{y}^{(\eta)})}{\partial y_m} \\ \vdots & \ddots & \vdots \\ \frac{\partial r_m(\mathbf{y}^{(\eta)})}{\partial y_1} & \cdots & \frac{\partial r_m(\mathbf{y}^{(\eta)})}{\partial y_m} \end{bmatrix} \quad (\text{A.8})$$

is the $m \times m$ Jacobian matrix. The newly obtained value of \mathbf{y} is then used as a starting value for the next iteration, until the absolute difference between two subsequent calculations of \mathbf{y} is smaller than the defined absolute tolerance ε , i.e.

$$\left\| \mathbf{y}^{(\eta+1)} - \mathbf{y}^{(\eta)} \right\| < \varepsilon \quad \forall \mathbf{y} \in \mathbf{y} \quad (\text{A.9})$$

The error check and stop criterion can also be performed on the mismatch vector $\mathbf{r}(\mathbf{y}^{(\eta)})$. In short, the calculation sequence for a full Newton-Raphson iteration is given by

1. Define $\mathbf{r}(\mathbf{y})$;
2. Choose reasonable starting values for \mathbf{y} , $\mathbf{y}^{(0)}$;
3. Calculate $\mathbf{r}(\mathbf{y}^{(\eta)})$;
4. Calculate $\mathbf{y}^{(\eta)}$ by (A.6);
5. if (A.9) holds, stop; else
6. $\mathbf{y}^{(\eta)} = \mathbf{y}^{(\eta+1)}$, $\eta = \eta + 1$, and go to step 3.

Appendix B

Reference Frames, Space Vectors, Phasors

B.1 Sinusoidal quantities

Periodic function

$$x(t) = (t + T_0) \quad (\text{B.1})$$

where t is the time in s, $T_0 = \frac{1}{f}$ the fundamental period in s, and f the frequency in Hz.

Sinusoidal quantity with fundamental period T_0

$$x(t) = \hat{x} \cos(\theta + \phi_x) \quad (\text{B.2})$$

where $\theta = \int_0^t \omega dt$, $\omega = 2\pi f$ the rotational frequency in rads^{-1} , \hat{x} the peak value of the sinusoidal quantity, and ϕ_x the angle of $x(t)$ for $x(0)$ in rad.

set of three-phase sinusoidal voltages

$$\begin{aligned} \mathbf{v} = \mathbf{v}_{abc} &= \begin{bmatrix} V_a & V_b & V_c \end{bmatrix}^T \\ &= \begin{bmatrix} \hat{V}_a \cos(\theta + \phi_a) \\ \hat{V}_b \cos(\theta + \phi_b) \\ \hat{V}_c \cos(\theta + \phi_c) \end{bmatrix} = \begin{bmatrix} \sqrt{2} |V_a| \cos(\theta + \phi_a) \\ \sqrt{2} |V_b| \cos(\theta + \phi_b) \\ \sqrt{2} |V_c| \cos(\theta + \phi_c) \end{bmatrix} \end{aligned} \quad (\text{B.3})$$

B.2 Common Transformations for Three-Phase Systems

B.2.1 Clarke transformation

$$\mathbf{v}_{\alpha\beta\gamma} = \mathbf{T}^{\text{abc} \rightarrow \alpha\beta\gamma} \mathbf{v}_{\text{abc}} \quad (\text{B.4})$$

where

$$\mathbf{T}^{abc \rightarrow \alpha\beta\gamma} = \frac{2}{3} \begin{bmatrix} 1 & \cos \frac{2}{3}\pi & \cos \frac{4}{3}\pi \\ 0 & \sin \frac{2}{3}\pi & \sin \frac{4}{3}\pi \\ \frac{1}{2} & \frac{1}{2} & \frac{1}{2} \end{bmatrix} = \frac{2}{3} \begin{bmatrix} 1 & -\frac{1}{2} & -\frac{1}{2} \\ 0 & \frac{1}{2}\sqrt{3} & -\frac{1}{2}\sqrt{3} \\ \frac{1}{2} & \frac{1}{2} & \frac{1}{2} \end{bmatrix} = \begin{bmatrix} \frac{2}{3} & -\frac{1}{3} & -\frac{1}{3} \\ 0 & \frac{1}{\sqrt{3}} & -\frac{1}{\sqrt{3}} \\ \frac{1}{3} & \frac{1}{3} & \frac{1}{3} \end{bmatrix} \quad (\text{B.5})$$

The Clarke transformation is purely mathematical and it has no physical meaning. Yet, it is important for reference frame transformations. Note that at $t = 0$ s, U_α has the same angle as U_a . The inverse transformation is given by

$$\mathbf{v}_{abc} = \mathbf{T}^{\alpha\beta\gamma \rightarrow abc} \mathbf{v}_{\alpha\beta\gamma} \quad (\text{B.6})$$

with

$$\mathbf{T}^{\alpha\beta\gamma \rightarrow abc} = \mathbf{T}^{abc \rightarrow \alpha\beta\gamma}{}^{-1} = \begin{bmatrix} 1 & 0 & 1 \\ -\frac{1}{2} & \frac{1}{2}\sqrt{3} & 1 \\ -\frac{1}{2} & -\frac{1}{2}\sqrt{3} & 1 \end{bmatrix} \quad (\text{B.7})$$

B.2.2 Park transformation

In many subjects, a change of variables hugely supports model calculation. In that respect the Park transformation is relevant to power system calculations by its particular (rotor oriented) reference frame modelling for machines. When using the Park transformation, sinusoidal quantities which have approximately the rotor rotating frequency become stationary, and vice versa. It is given by

$$\begin{aligned} \mathbf{v}_{dq0} &= \mathbf{T}^{\alpha\beta\gamma \rightarrow dq0} \mathbf{v}_{\alpha\beta\gamma} \\ &= \mathbf{T}^{\alpha\beta\gamma \rightarrow dq0} \mathbf{T}^{abc \rightarrow \alpha\beta\gamma} \mathbf{v}_{abc} \\ &= \mathbf{T}^{abc \rightarrow dq0} \mathbf{v}_{abc} \end{aligned} \quad (\text{B.8})$$

where

$$\mathbf{T}^{\alpha\beta\gamma \rightarrow dq0} = \begin{bmatrix} \cos \theta_R & \sin \theta_R & 0 \\ -\sin \theta_R & \cos \theta_R & 0 \\ 0 & 0 & 1 \end{bmatrix} \quad (\text{B.9})$$

and

$$\begin{aligned}\mathbf{T}^{abc \rightarrow dq0} &= \frac{2}{3} \begin{bmatrix} \cos \theta_R & \sin \theta_R & 0 \\ -\sin \theta_R & \cos \theta_R & 0 \\ 0 & 0 & 1 \end{bmatrix} \begin{bmatrix} 1 & \cos \frac{2}{3}\pi & \cos \frac{4}{3}\pi \\ 0 & \sin \frac{2}{3}\pi & \sin \frac{4}{3}\pi \\ \frac{1}{2} & \frac{1}{2} & \frac{1}{2} \end{bmatrix} \\ &= \frac{2}{3} \begin{bmatrix} \cos \theta_R & \cos(\theta_R - \frac{2}{3}\pi) & \cos(\theta_R - \frac{4}{3}\pi) \\ -\sin \theta_R & -\sin(\theta_R - \frac{2}{3}\pi) & -\sin(\theta_R - \frac{4}{3}\pi) \\ \frac{1}{2} & \frac{1}{2} & \frac{1}{2} \end{bmatrix}\end{aligned}\quad (\text{B.10})$$

θ_R Is the angular displacement of a machine rotor. It is given by

$$\theta_R = \int_0^t \omega_R d\tau + \theta_R(0) \quad (\text{B.11})$$

with $\theta_R(0)$ is the initial position of the rotor. The inverse Park transformation transforms the $d-q-0$ quantities back to the three-phase waveforms by

$$\begin{aligned}\mathbf{v}_{abc} &= \mathbf{T}^{abc \rightarrow dq0^{-1}} \mathbf{v}_{dq0} \\ &= \mathbf{T}^{dq0 \rightarrow abc} \mathbf{v}_{dq0} \\ &= \mathbf{T}^{\alpha\beta\gamma \rightarrow abc} \mathbf{T}^{dq0 \rightarrow \alpha\beta\gamma} \mathbf{v}_{dq0}\end{aligned}\quad (\text{B.12})$$

with

$$\mathbf{T}^{dq0 \rightarrow \alpha\beta\gamma} = \mathbf{T}^{\alpha\beta\gamma \rightarrow dq0}(-\theta_R) = \begin{bmatrix} \cos \theta_R & -\sin \theta_R & 0 \\ \sin \theta_R & \cos \theta_R & 0 \\ 0 & 0 & 1 \end{bmatrix} \quad (\text{B.13})$$

and

$$\begin{aligned}\mathbf{T}^{dq0 \rightarrow abc} &= \begin{bmatrix} 1 & 0 & 1 \\ -\frac{1}{2} & \frac{1}{2}\sqrt{3} & 1 \\ -\frac{1}{2} & -\frac{1}{2}\sqrt{3} & 1 \end{bmatrix} \begin{bmatrix} \cos \theta_R & -\sin \theta_R & 0 \\ \sin \theta_R & \cos \theta_R & 0 \\ 0 & 0 & 1 \end{bmatrix} \\ &= \begin{bmatrix} \cos \theta_R & -\sin \theta_R & 1 \\ \cos(\theta_R - \frac{2}{3}\pi) & -\sin(\theta_R - \frac{2}{3}\pi) & 1 \\ \cos(\theta_R - \frac{4}{3}\pi) & -\sin(\theta_R - \frac{4}{3}\pi) & 1 \end{bmatrix}\end{aligned}\quad (\text{B.14})$$

B.2.3 Space Vectors

A space vector is a mathematical representation of a sinusoidal waveform $x(t)$ projected on the complex plane by

$$\begin{aligned}
\underline{\hat{x}} &= \hat{x} e^{j\phi_x} e^{j\theta} \\
&= \hat{x} e^{j(\theta + \phi_x)} \\
&= \text{Re}\{\underline{\hat{x}}\} + j\text{Im}\{\underline{\hat{x}}\} \\
&= \hat{x} [\cos(\theta + \phi_x) + j \sin(\theta + \phi_x)] \\
&\stackrel{d\omega/dt=0}{=} \hat{x} \cos(\omega t + \phi_x) + j \hat{x} \sin(\omega t + \phi_x)
\end{aligned} \tag{B.15}$$

$\underline{\hat{x}}$ can be graphically interpreted as a vector having the length of the amplitude of $x(t)$, which rotates counterclockwise with respect to the reference real axis at a rate of ω rad s⁻¹. For $t = 0$ s holds

$$\underline{\hat{x}}(0) = \hat{x} (\cos \phi_x + j \sin \phi_x) \tag{B.16}$$

B.2.4 Space Vector Representation of Reference Frame Transformations

If the set of sinusoidal voltages given by (B.3) is assumed balanced, i.e.

- all voltages have equal amplitudes, i.e. $\hat{V}_a = \hat{V}_b = \hat{V}_c = \hat{V}$;
- all voltages have an equal fundamental frequency;
- The voltages contain no harmonics higher than fundamental; and
- The voltages are distributed 120 from each other.

the Clark transform of (B.4) reduces to

$$\mathbf{v}_{\alpha\beta\gamma} = \frac{2}{3} \begin{bmatrix} 1 & -\frac{1}{2} & -\frac{1}{2} \\ 0 & \frac{1}{2}\sqrt{3} & -\frac{1}{2}\sqrt{3} \\ \frac{1}{2} & \frac{1}{2} & \frac{1}{2} \end{bmatrix} \begin{bmatrix} \hat{V} \cos(\theta + \phi_v) \\ \hat{V} \cos(\theta + \phi_v - \frac{2}{3}\pi) \\ \hat{V} \cos(\theta + \phi_v + \frac{2}{3}\pi) \end{bmatrix} = \begin{bmatrix} \hat{V} \cos(\theta + \phi_v) \\ \hat{V} \sin(\theta + \phi_v) \\ 0 \end{bmatrix} \tag{B.17}$$

which can be cast into a space vector by projecting V_α and V_β on the real and imaginary axis respectively by

$$\underline{\hat{V}}^F = V_\alpha + jV_\beta = \hat{V} e^{j(\theta + \phi_v)} \tag{B.18}$$

where F implies the stationary or *fixed* reference frame. That is, the complex axes in which the space vector is defined have no inherent rotational speed. As a result, a balanced set of three phase voltages can be respresented in the stationary reference frame without losing information.

Another benefit of assuming a balanced set of three phase voltages includes the simplification of the Park transformation of (B.9). It reduces to a clockwise Cartesian rotation for a balanced set of voltages and can be represented by a complex transformation as

$$\underline{\hat{V}}^R = \underline{T}^{F \rightarrow R} \underline{\hat{V}}^F = V_d^R + jV_q^R = \hat{V} e^{j(\phi_v + \theta - \theta_R)} \quad (\text{B.19})$$

where $\underline{\hat{V}}^R$ is the d - q projection on the rotor-oriented reference frame and

$$\underline{T}^{F \rightarrow R} = e^{-j\theta_R} \quad (\text{B.20})$$

B.2.5 The Arbitrary Reference Frame

The reference frame of interest can, in fact, rotate at any arbitrary speed, or don't rotate at all. Therefore, the transformations described in the previous sections will be generalised to one moving at an arbitrary rotational speed ω_K , yielding the angle displacement

$$\theta_K = \int_0^t \omega_K d\tau + \theta_K(0) \quad (\text{B.21})$$

In the arbitrary reference frame, the space vector of a balanced set of three-phase voltages is given by

$$\underline{\hat{V}}^K = V_d^K + jV_q^K = \hat{V} e^{j(\phi_v + \theta - \theta_K)} \quad (\text{B.22})$$

Like the Park transformation, this is a change of variables transformation from the stationary reference frame to the arbitrary reference frame

$$\begin{aligned} \underline{\hat{V}}^{\omega_K} &= \underline{T}^{F \rightarrow K} \underline{\hat{V}}^F \\ &= e^{-j\theta_K} \underline{\hat{V}}^F \end{aligned} \quad (\text{B.23})$$

Suppose the space vector in the rotor-oriented reference frame, $\underline{\hat{V}}^{\omega_R}$, is to be represented in an arbitrary reference frame. That is, the space vector shall be transformed back to the stationary reference frame and subsequently to an arbitrary reference frame. This is relevant to DFIG wind turbines where the rotor voltages have the slip frequency $\omega_K = \omega_R - \omega_S$. This transformation is given by

$$\begin{aligned} \underline{\hat{V}}^{\omega_K} &= \underline{T}^{R \rightarrow K} \underline{\hat{V}}^{\omega_R} \\ &= \underline{T}^{F \rightarrow K} \underline{\hat{V}}^F \\ &= \underline{T}^{F \rightarrow K} \underline{T}^{R \rightarrow F} \underline{\hat{V}}^{\omega_R} \\ &= e^{-j\theta_K} e^{j\theta_R} \underline{\hat{V}}^{\omega_R} \end{aligned} \quad (\text{B.24})$$

Hence

$$\begin{aligned} \underline{T}^{R \rightarrow K} &= e^{j(\theta_R - \theta_K)} \\ &= e^{j\Delta\theta} \underline{T}^{R \rightarrow F} \end{aligned} \quad (\text{B.25})$$

Table B.1: *commonly used reference frames*

ID	ω	Name	Description
F	$\omega_F = 0$	Fixed (stationary) α - β reference frame	Voltage and current waveform representation
R	ω_R	Rotor-oriented d - q reference frame	Parkian machine models, multi-machine systems
S	ω_S	Synchronous x - y reference frame	(quasi-)stationary phasors, stability simulations, commonly equals $2\pi 50 \text{ rad s}^{-1}$
K	ω_K	Arbitrary d - q reference frame	PLLs (wind turbine generators, power electronic converters)

This relation holds for any pair of reference frames, and simplifies to (B.23) in case the reference frame to be transformed from is fixed, i.e. $\omega_F = 0$. Similarly, the inverse transform is given by

$$\begin{aligned}
 \underline{T}^{K \rightarrow R} &= e^{j(-(\theta_R - \theta_K))} \\
 &= e^{-j\Delta\theta^{R \rightarrow K}} \\
 &= e^{j\Delta\theta^{K \rightarrow R}}
 \end{aligned} \tag{B.26}$$

Table B.1 shows commonly used reference frames. figure B.1 shows an exemplary space vector diagram for $\underline{\hat{V}}^F = \hat{V} e^{j(\omega t + \phi_v)}$, with $\phi_v = 20^\circ$, and $\hat{V} = 311.12 \text{ V}$.

B.3 Complex Phasors

Power system analysis to a great extent relies on a network representation by complex phasors. These can be either completely stationary or quasi stationary. It will be shown that stationary complex phasors are non-time varying by definition whereas quasi-stationary phasors may and are defined within a reference frame or relative to a reference vector. Both variants will be linked by the definition of space vectors.

Suppose the frequency of $V(t)$ is assumed constant in time, i.e., $d\omega/dt = 0$. The voltage of phase a is given by

$$V_a(t) = \hat{V} \cos(\omega t + \phi_v) \tag{B.27}$$

For a balanced set of three phase voltages, the space vector is defined in the stationary reference frame as

$$\underline{\hat{V}}^F = \hat{V} e^{j(\omega t + \phi_v)} \tag{B.28}$$

The stationary complex phasor is defined as [224]:

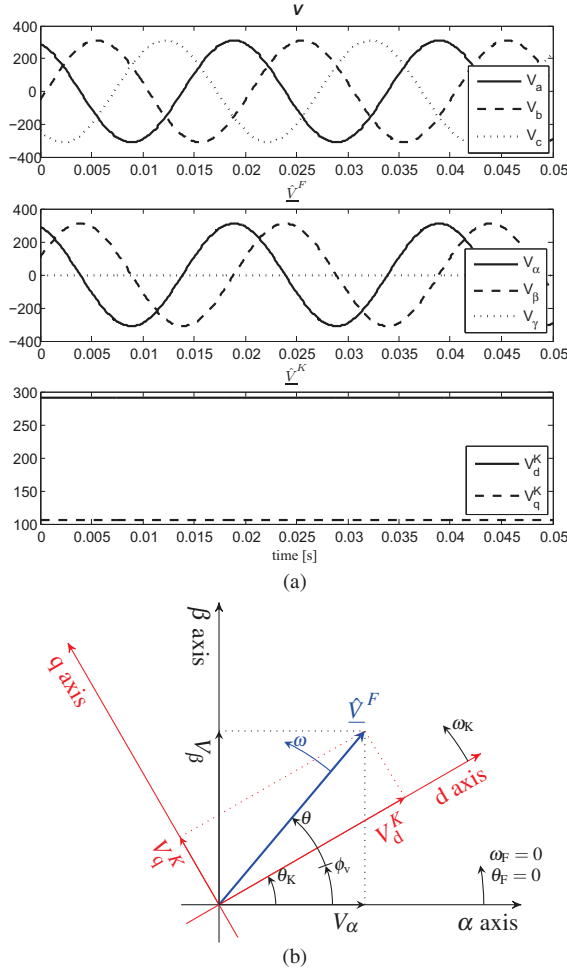


Figure B.1: Exemplary reference frame projection of a voltage space vector. (a) Individual phase voltages and transformed quantities, (b) Reference frames position of transformed voltages

$$\begin{aligned}\underline{V} &= \frac{\hat{V}}{\sqrt{2}} e^{-j\omega t} = \frac{\hat{V}(0)}{\sqrt{2}} \\ &= |V| e^{j\phi_v}\end{aligned}\tag{B.29}$$

where $|V|$ the complex magnitude of \underline{V} . $|V|$ is also commonly used for indicating the *RMS-value* of $V(t)$, i.e.

$$|x|_{\text{RMS}} = \sqrt{\frac{1}{T_0} \int_t^{t+T_0} x^2(\tau) d\tau}\tag{B.30}$$

Which equals $|x|$ in case \hat{x} and ω remain constant and no harmonic distortion is present. This distinction should be made when describing time domain simulations, in which quasi-stationary phasors are employed.

The above definition of stationary complex phasors is commonly used for steady-state analysis of power systems, notably power flow calculations. For real-time measurements and dynamic simulation of power systems, the system frequency may vary and is determined by the connected electric machinery. The rotational speed of the reference frame in which the network and dynamic models are represented may change dynamically too. Depending in the type of simulation adopted, the network may or may not be represented by complex quantities. If so, its impedance values are mapped on a particular frequency, usually the nominal system frequency, which is unaltered during simulation. As a result, the angles of voltages and currents change algebraically after network changes, and hence the value of $|V|$ and ϕ_V in (B.29).

These elements necessitate a more sophisticated definition of \underline{V} in the time domain by reference frames. In the arbitrary reference frame, $\hat{\underline{V}}$ is defined as

$$\hat{\underline{V}}^K = \underline{\hat{V}}^F e^{-j(\omega_K t + \theta_K(0))} \quad (\text{B.31})$$

Over time, \hat{V} , ϕ_V , ω_K may vary, while ω is assumed equal to ω_S .

$$\underline{\hat{V}}^K = \hat{V}(\mathbf{x}, \mathbf{y}, t) e^{j(\phi_V^K(\mathbf{x}, \mathbf{y}, t))} \quad (\text{B.32})$$

where

$$\phi_V^K(\mathbf{x}, \mathbf{y}, t) = - \int \Delta\omega_K(\mathbf{x}, \mathbf{y}, t) dt + \phi_V(\mathbf{x}, \mathbf{y}, t) - \theta_K(0) \quad (\text{B.33})$$

and $\Delta\omega_K = \omega_K(\mathbf{x}, \mathbf{y}, t) - \omega_S$. The quasi-stationary complex phasor is now given by

$$\underline{V} = \frac{\hat{\underline{V}}^K(t)}{\sqrt{2}} = |V|(t) e^{j\phi_V^K(t)} \quad (\text{B.34})$$

The definition from (B.34) shows that the phasor angle depends on mainly three parts:

1. a part that is determined by the angle displacement of the reference frame with respect to the synchronous reference frame, i.e. $-\int \Delta\omega_K(\mathbf{x}, \mathbf{y}, t) dt$;
2. a part that is determined by either network disturbances or machine and device control actions, i.e. $\phi_V(\mathbf{x}, \mathbf{y}, t)$; and
3. a fixed part, which is the initial position of the reference frame of interest with respect to the stationary reference frame, i.e. $\theta_K(0)$.

If apparent from the context, the t, \mathbf{x} , and \mathbf{y} dependency as well as the reference frame superscript (here K) will not be explicitly shown. To summarise, the following can be observed with regard to complex phasors and space vectors

1. The complex phasor \underline{V} is stationary in case 1) a relation to a particular reference frame is irrelevant or 2) the analysis concerns steady-state quantities only (such as power flow analysis).
2. The complex phasor equals the RMS value of the space vector in the arbitrary reference frame rotating at an angular speed equal to the frequency of the concerned sinusoidal quantity. In this context, phasors are often referred to as quasi-stationary, as 1)

the speed of the reference frame may change or 2) the analysis concerns dynamically changing quantities within the system.

3. In all other reference frames, $\hat{\underline{V}}^K$ would rotate clockwise at a rate of $\omega - \omega_K$, where ω is the angular speed of the reference frame of interest. In other words, the space vector becomes periodic.
4. It is common to assume nominal system frequency (ω_s) for the respective sinusoidal quantity. Hence, the space vector in the synchronous reference frame is stationary and is given by $\hat{\underline{V}}^{\omega_s} = \sqrt{2}\underline{V}$.

Appendix C

Test Network Data

As the various chapters contribute differently to answering the research questions, the applied test systems are not necessarily equal. We have essentially conducted the various aspects of the scientific contributions in an order that inhibited us to equalise benchmark system criteria and parameters. However, the general structure of the systems and their underlying assumptions are harmonised as properly as feasible. For reproduction purposes, this appendix gives an overview of the elementary single machine infinite bus system and the IEEE 9-bus 3 generator system, for parameters and derived quantities alike. These benchmark systems are subsequently used as AC representations of the various HVDC configurations used for the analysis.

C.1 Extended Single Machine Infinite Bus System

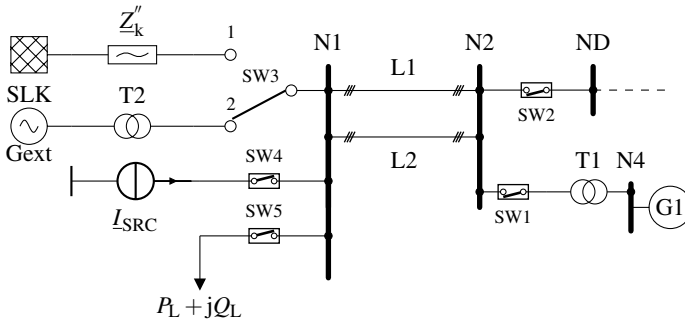


Figure C.1: *Extended Single Machine Infinite Bus System.*

Figure C.1 shows the elementary test network used throughout this thesis. Table C.1 shows how the various switches in this generalised SMIB system are configured. The parameters are shown in table C.2.

Table C.1: AC test network configurations throughout the cases conducted for this thesis.

Sections	SW1	SW2	SW3	SW4	SW5
CH4 (validation)	closed	open	1	open	closed
CH4 (multi-rate)	open	closed	1	open	open
CH5 (hybrid)	closed	closed	1	open	open
CH6 (stability impacts)	closed	closed	2	closed	closed

Table C.2: SMIB network parameters

R_{L1}	0.05	Ω/km
L_{L1}	12.9	mHkm^{-1}
S_k''	1000	MVA
R/X	0.1	pu
$S_{\text{rated},G1}$	128	MVA
$S_{\text{rated},T1}$	150	MVA
R/X_{T1}	0.01	pu
length L1 and L2	50	km

C.2 IEEE 9-Bus System

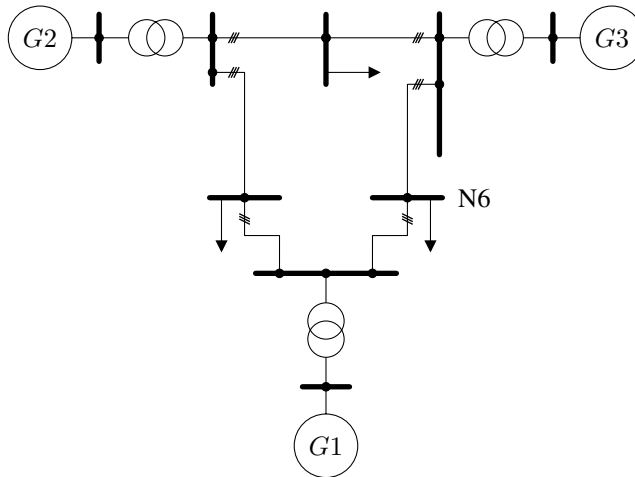


Figure C.2: Single-line diagram of the IEEE 9-bus test system.

- steady state and transient parameters have been taken from [157] and are converted to machine base MVA, i.e., $S_{\text{base}} = S_{\text{rated}}$.
- sub-transient parameters and open circuit time constants have been added as standard values for salient pole (G1) and round-rotor (G2, G3) machines [153].

Table C.3: *Generator parameters of the IEEE 9 bus system. Nomenclature adopted from [153]*

parameter	unit	G1	G2	G3
S_{rated}	MVA	247.5	192	128
U_{rated}	kV	16.5	18.0	13.8
H	s	9.55	3.33	2.35
R_s	pu	1.0×10^{-4}	1.0×10^{-4}	1.0×10^{-4}
x_a	pu	0.083	0.1	0.095
x_d	pu	0.3614	1.72	1.68
τ'_{do}	s	8.96	6.0	5.89
x'_d	pu	0.15	0.23	0.232
τ''_{do}	s	0.02	0.02	0.02
x''_d	pu	0.15	0.12	0.12
x_q	pu	0.24	1.66	1.61
τ'_{qo}	s	0.02	0.535	0.6
x'_q	pu	0.24	0.378	0.32
τ''_{qo}	s	0.02	0.02	0.02
x''_q	pu	0.24	0.12	0.12

- line parameters, transformer short circuit voltages, and initial power flow data are not displayed here but can nonetheless be found in [157].

Nomenclature

Symbols having multiple subscripts or superscripts use commas to separate these, while obeying the following precedence order

1. symbol-specific (e.g. ϕ_x for sinusoidal quantity x);
2. system-specific (e.g. node indication);
3. device-specific (e.g. terminal indication, name);
4. model-specific (e.g. d -axis decomposition); and
5. time-specific (e.g. $0, N$).

Lower case quantities are always in the per-unit system of either the device or system they represent. Uppercase variables represent per unit quantities in the system (network) base or quantities expressed in international system of units (SI). Voltages in the network base may be lowercase if not confusing. Table C.4 gives an overview of the per unit notation for various parts in the electrical system.

Table C.4: *per unit notation*

	DC	device	AC network	SI
voltage	u	v	V or v	V
current	I_{dc}	i	I	I
power	P_{dc}	p	P	P
impedance	R	z	\underline{Z}	\underline{Z}

Abbreviations

AC	Alternating Current
API	Application Program Interface
aRCI	additional Reactive Current Injection
CCT	Critical Clearing Time
CONV	Converter

DC	Direct Current
DFIG	Doubly-Fed Induction Generator
DS	Detailed System
EMT	Electro-Magnetic Transient
ES	External System
FCG	Full Converter Generator
FRT	Fault Ride-Through
GSVSC	Grid Side VSC
HVDC	High Voltage DC
IGBT	Insulated Gate Bi-polar Transistor
IP	Interaction Protocol
LCC	Line-Commutated Converter
MMC	Modular Multi-level Converter
MPPT	Maximum Power Point Tracking
MTDC	Multi-Terminal HVDC
PCC	Point of Common Coupling
PLL	Phase Locked Loop
PWM	Pulse Width Modulation
QSS	Quasi-Stationary Simulations
SCIG	Squirrel-Caged Induction Generator
SM	Sub-Module
VSC	Voltage Sourced Converter
WPP	Wind Power Plant
WPVSC	Wind Park VSC
WTG	Wind Turbine Generator

General Notation

x	Scalar variable
$x(t)$	Continuous time-dependent variable
x_n	Discrete variable

$\mathbf{x}_{m \times 1}$	Column vector with m rows containing scalar variables x
$\mathbf{X}_{m \times n}$	Matrix with m rows and n columns containing scalar variables x (pu) or X (SI)
$f(x)$	Scalar function (1 variable)
f_n	Discrete function
$F(\mathbf{x})$	Scalar function (m variables)
$\mathbf{f}(\mathbf{x})$	Vector with scalar functions (vector function)
$\ x\ $	Absolute value of x
\hat{x}	Peak value of sinusoidal quantity
$\underline{x} = \text{Re}\{\underline{x}\} + j\text{Im}\{\underline{x}\}$	Complex quantity
$\text{Re}\{\underline{x}\}$	Real part of \underline{x}
$\text{Im}\{\underline{x}\}$	Imaginary part of \underline{x}
$ x $	Magnitude of \underline{x}
$\underline{\mathbf{X}}$	Matrix containing complex elements \underline{x}
$\hat{\underline{x}}^S$	Space vector of sinusoidal waveform $x(t)$ in the reference frame rotating with $\omega_S = d\theta_S/dt$

General Symbols

\mathbf{J}	Jacobian matrix
$\mathbf{r}(\mathbf{y})$	mismatch function for the Newton-Raphson algorithm
\mathbf{M}	Adjacency matrix
$\underline{T}^{A \rightarrow B}$	Space vector transformation from reference frame A to B
\hat{w}	Internal tracking space vector of a PLL
A	Surface area
C	Electric Capacitance
C_p	Wind power coefficient
D	Droop constant, damping constant, deviation
E	Energy, voltage source
f	Frequency
$G(s)$	Controller transfer function
H	Inertia constant

$H(s)$	Filter transfer function
I	Current
k	Proportional gain
m	Modulation index
n	Rotation speed
P	Active power
Q	Reactive power
R	Electric Resistance
R_p	Active power recovery rate
S	Complex or appearent power
s	Generator slip, Laplace operator
T	Torque
t	Time
U	DC voltage
V	AC voltage
v_w	Wind speed
W	Sample window
X	Reactance
x	State variable
Y	Admittance
j	Imaginary unit, where $j^2 = -1$
$\Delta\gamma$	PLL input angle deviation
Δt	Time step-size
δ	Rotor angle, voltage angle difference
γ	Torsional angular displacement of the shaft, ratio of committed type of generation
ω	Angular frequency
ϕ	Voltage phasor angle
τ	Time constant

θ	Space vector rotation angle
φ	Current angle
α	Delay angle, bandwidth
β	Pitch angle
ε	Deviation, convergence threshold
λ	Tip speed ratio
ρ	Volumetric mass density

Subscripts

ag	Air gap
base	Base value for per unit calculations
br	Related to dynamic braking resistor, branch
ch	Related to dynamic braking resistor
c	Converter side, related to corrector part of integration routine
dc	Related to DC side
eff	Effective
eq	Equivalent
ext	Related to external system
f	Filter bus
hist	Related to historic terms of current injections
inj	Related to current injection
i	Integration
LL	Line-to-line
Ln	Line-to-neutral
lp	Low-pass
L	Load
m	Modulation, mechanic
opt	Optimum
p	Proportional, related to predictor

rec	Related to recovery voltage
ret	Related to retained voltage
shaft	Rotor shaft
t	Transformer-side
w	Wind
<i>e</i>	Related to slack sources, electric
<i>g</i>	Related to current injection sources
<i>m</i>	Time step of EMT simulation
<i>n</i>	Time step of stability simulation
<i>f</i>	<i>from</i> node index
<i>j</i>	DC node index
<i>k</i>	Branch index
<i>t</i>	<i>to</i> node index
flt	Fault
int	Interface
mr	Multi-rate
R	Related to the rotor
α	Real-axis decomposition of a space vector in the stationary reference frame
β	Imaginary-axis decomposition of a space vector in the stationary reference frame
d	d-axis decomposition of a (space) vector
q	q-axis decomposition of a (space) vector
x	x-axis decomposition of a (space) vector in the synchronous reference frame
y	y-axis decomposition of a (space) vector in the synchronous reference frame
s	Related to machine stator and synchronous quantities
th	Thévenin

Superscripts

sol	Solution of a fixed point iteration process
ϵ	Absolute tolerance
*	Complex conjugate, set-point value
+	Related to + pole of the HVDC circuit, related to after event
—	Related to — pole of the HVDC circuit, related to before event
(η)	Iteration index
C	Converter d – q reference frame
F	Fixed or α – β – γ reference frame
$k \rightarrow n$	From node k to node n
in	Related to input
thres	Threshold value

Definitions

<i>Assumption</i>	Uncertain or variable parameter that must be specified inside a scenario.
<i>Boundary condition</i>	Parameter that are laid down or are considered fixed.
<i>Case</i>	Variations that can be studied within the framework of the particular scenario.
<i>Configuration</i>	An arrangement of the parts of the system under investigation and the form or shape that this arrangement produces
<i>Intermittent power generation</i>	Power being generated irregularly by either the fully rated power or no infeed at all
<i>Nominal value</i>	Value of a quantity used to designate and identify a component, device, equipment, or system Note: the nominal value is generally a rounded value.
<i>Quasi-stationary phasor</i>	A complex quantity which length equals the RMS value of a space vector and which angle is defined relative to the reference angle
<i>Rated value</i>	Value of a quantity used for specification purposes, established for a specified set of operating conditions of a component, device, equipment, or system.
<i>Renewable energy sources</i>	Energy mined from non-fossil sources.

<i>Scenario</i>	Combination of transmission network, policy, technology, and social developments which constitute the boundary conditions for case studies.
<i>Stationary phasor</i>	Complex quantity that represents the RMS value of a space vector at $t = 0$ s.
<i>Sustainable</i>	Meet present needs and do not impede future needs.
<i>System Configuration</i>	An assembly of (sub-)systems, components, connections, domains, and attributes relevant to a particular test case.
<i>System</i>	Set of interrelated elements considered in a defined context as a whole and separated from their environment.
<i>Topology</i>	The way the parts of the system under investigation are arranged or related

List of Publications

Journal Publications

- [A] P. Palensky, A. A. van der Meer, C. D. López, A. Jozeph, and K. Pan, “Co-simulation of intelligent power systems - fundamentals, software architecture, numerics, and coupling,” *IEEE Ind. Electron. Mag.*, vol. 11, no. 1, pp. 34–50, Mar. 2017.
- [B] P. Palensky, A. A. van der Meer, C. D. López, A. Jozeph, and K. Pan, “Applied cosimulation of intelligent power systems: Implementing hybrid simulators for complex power systems,” *IEEE Ind. Electron. Mag.*, vol. 11, no. 2, pp. 6–21, Jun. 2017.
- [C] A. A. van der Meer, M. Ndreko, M. Gibescu, and M. A. M. M. van der Meijden, “The effect of FRT behavior of VSC-HVDC connected offshore wind power plants on AC/DC system dynamics,” *IEEE Trans. Power Del.*, vol. 31, no. 2, pp. 878–887, Apr. 2016.
- [D] A. A. van der Meer, M. Gibescu, M. A. M. M. van der Meijden, W. L. Kling, and J. A. Ferreira, “Advanced hybrid transient stability and EMT simulation for VSC-HVDC systems,” *IEEE Trans. Power Del.*, vol. 30, no. 3, pp. 1057–1066, Jun. 2015, .

Conference Publications

- [E] A. A. van der Meer, P. Palensky, K. Heussen, D. E. Morales Bondy, O. Gehrke, C. Steinbrink, M. Blank, S. Lehnhoff, E. Widl, C. Moyo, T. I. Strasser, V. H. Nguyen, N. Akroud, M. H. Syed, E. A., S. Rohjans, R. Brandl, and A. M. Rohjans, “Cyber-physical energy systems modeling, test specification, and co-simulation based testing,” in *Workshop on Modeling and Simulation of Cyber-Physical Energy Systems*, Pittsburgh, PA, Apr., 21, 2017.
- [F] P. Kotsampopoulos, N. Hatziargyriou, T. I. Strasser, C. Moyo, S. Rohjans, C. Steinbrink, S. Lehnhoff, P. Palensky, A. A. van der Meer, D. E. Morales Bondy, K. Heussen, M. Calin, A. Khavari, S. M., J. E. Rodriguez, and G. M. Burt, “Validating intelligent power and energy systems – a discussion of educational needs,” in *proc. 8th int. conf. on Industrial Applications of Holonic and Multi-Agent Systems*, Lyon, France, Aug., 28–30, 2017.
- [G] C. D. López, A. A. van der Meer, M. Cvetkovic, and P. Palensky, “A variable-rate co-simulation environment for the dynamic analysis of multi-area power systems,” in *proc. IEEE PowerTech*, Manchester, UK, Jun., 18–22, 2017.
- [H] A. D. Perilla, A. A. van der Meer, J. L. Rueda, A. Alefragkis, and M. A. M. M. van der Meijden, “Influence of active power gradient control of an MMC-HVDC link on long-

- term frequency stability,” in *proc. IEEE PES General Meeting*, Chicago, IL, Jul., 16–20, 2017.
- [I] C. Steinbrink, S. Lehnhoff, S. Rohjans, T. I. Strasser, E. Widl, C. Moyo, G. Lauss, F. Lehfuss, M. Faschang, P. Palensky, A. A. van der Meer, K. Heussen, O. Gehrke, E. Guillo-Sansano, M. H. Syed, A. Emhemed, R. Brandl, V. H. Nguyen, A. Khavari, Q. T. Tran, P. Kotsampopoulos, N. Hatziargyriou, N. Akroud, E. Rikos, and M. Z. Degefa, “Simulation-based validation of smart grids – status quo and future research trends,” in *proc. 8th int. conf. on Industrial Applications of Holonic and Multi-Agent Systems*, Lyon, France, Aug., 28–30, 2017.
 - [J] C. Steinbrink, A. A. van der Meer, M. Cvetkovic, D. Babazadeh, S. Rohjans, P. Palensky, and S. Lehnhoff, “Smart grid co-simulation with MOSAIK and HLA: A comparison study,” in *6th D-A-CH+ conference on Energy Informatics*, Lugano, Switzerland, Oct., 5–6, 2017, accepted for presentation.
 - [K] T. I. Strasser, C. Moyo, R. Bründlinger, S. Lehnhoff, M. Blank, P. Palensky, A. A. van der Meer, K. Heussen, O. Gehrke, J. E. Rodriguez, J. Merino, S. C., M. Verga, M. Calin, K. A., S. M., E. de Jong, S. Rohjans, A. Kulmana, K. Mäki, R. Brandl, F. Coffele, G. M. Burt, P. Kotsampopoulos, and N. Hatziargyriou, “An integrated research infrastructure for validating cyber-physical energy systems,” in *proc. 8th int. conf. on Industrial Applications of Holonic and Multi-Agent Systems*, Lyon, France, Aug., 28–30, 2017.
 - [L] M. Ndreko, M. Popov, A. A. van der Meer, and M. A. M. M. van der Meijden, “The effect of the offshore vsc-hvdc connected wind power plants on the unbalanced faulted behavior of ac transmission systems,” in *proc. ENERGYCON 2016*, Leuven, Belgium, Apr., 4–8, 2016.
 - [M] A. A. van der Meer, J. L. Rueda, F. Faria da Silva, M. Gibescu, and M. A. M. M. van der Meijden, “Computationally efficient transient stability modeling of multi-terminal vsc-hvdc,” in *proc. IEEE PES general meeting*, Boston, MA, Jul., 17–21, 2016.
 - [N] A. A. van der Meer, M. Ndreko, M. Gibescu, M. A. M. M. van der Meijden, and W. L. Kling, “Stability assessment of VSC-HVDC connected large-scale offshore wind power: a north-sea region case study,” in *Proc. IEEE PowerTech*, Eindhoven, the Netherlands, Jun., 29 – Jul., 2, 2015.
 - [O] M. Ndreko, A. A. van der Meer, M. Gibescu, and M. A. M. M. van der Meijden, “Impact of DC voltage control parameters on AC/DC system dynamics under faulted conditions,” in *proc. IEEE Power and Energy Society General Meeting*, Washington DC, Jul., 27–31, 2014.
 - [P] J. Beerten, O. Gomis-Bellmunt, X. Guillaud, J. Rimez, A. A. van der Meer, and D. van Hertem, “Modelling and control of HVDC grids: a key challenge for the future power system,” in *18th Power System Computation Conference*, Wroclaw, Poland, Aug., 18–22, 2014.
 - [Q] M. Ndreko, A. A. van der Meer, M. Gibescu, M. A. M. M. van der Meijden, J. A. Bos, and K. P. J. Jansen, “Transient stability analysis of an onshore power system with multi-terminal offshore VSC-HVDC transmission: A case study for the netherlands,” in *Power and Energy Society General Meeting*, Vancouver, Canada, Jul., 21–25, 2013.
 - [R] M. Ndreko, A. A. van der Meer, B. G. Rawn, M. Gibescu, and M. A. M. M. van der Meijden, “Damping power system oscillations by VSC-based HVDC networks: A north sea grid case study,” in *International workshop on Large Scale Integration of Wind Power into Power Systems as well as on Transmission Networks for Offshore*

Wind Power Plants, London, UK, Oct., 22–24, 2013.

- [S] L. Bergfjord, A. van der Meer, A. R. Ciupuliga, and M. Gibescu, “Effects of offshore grid design on multi-area power system operation,” in *6th IEEE Young Researchers Symposium in Electrical Power Engineering*, Delft, the Netherlands, Apr., 16–17, 2012.
- [T] P. J. D. Chainho, A. A. van der Meer, R. L. Hendriks, M. Gibescu, and M. A. M. M. van der Meijden, “General modeling of multi-terminal VSC-HVDC systems for transient stability studies,” in *6th IEEE Young Researchers Symposium in Electrical Power Engineering*, Delft, the Netherlands, Apr., 16–17, 2012.
- [U] A. A. van der Meer, R. L. Hendriks, M. Gibescu, J. A. Ferreira, and W. L. Kling, “Hybrid simulation methods to perform grid integration studies for large scale offshore wind power connected through VSC-HVDC,” in *Proc. EPE Joint Wind Energy and T & D Chapters Seminar*, Trondheim, Norway, May, 9–11, 2011.
- [V] A. A. van der Meer, R. Hendriks, M. Gibescu, and W. L. Kling, “Interfacing methods for combined stability and electro-magnetic transient simulations applied to VSC-HVDC,” in *International Conf. on Power System Transients*, Delft, the Netherlands, Jun., 14–17, 2011.
- [W] A. A. van der Meer, R. L. Hendriks, M. Gibescu, J. A. Ferreira, M. A. M. M. van der Meijden, and W. L. Kling, “Combined simulation method for improved performance in grid integration studies including multi-terminal VSC-HVDC,” in *Proc. Renewable Power Generation conference*, Edinburgh, United Kingdom, Sep., 6–8, 2011.
- [X] J. C. Boemer, A. A. van der Meer, B. G. Rawn, R. L. Hendriks, M. Gibescu, M. A. M. M. van der Meijden, W. L. Kling, and J. A. Ferreira, “Network fault response of transmission systems with active distribution systems during reverse power flows,” in *International workshop on Large Scale Integration of Wind Power into Power Systems as well as on Transmission Networks for Offshore Wind Power Plants*, Aarhus, Denmark, Oct., 25–26, 2011.
- [Y] J. C. Boemer, A. A. van der Meer, R. L. Rawn, B. G. and Hendriks, A. R. Ciupuliga, M. Gibescu, W. L. Kling, and J. A. Ferreira, “Fault ride-through requirements for on-shore wind power plants in europe: the needs of the power system,” in *IEEE Power and Energy General Meeting*, Detroit, MI, Jul., 24–28, 2011.
- [Z] C. Ismunandar, A. A. van der Meer, R. L. Hendriks, M. Gibescu, and W. L. Kling, “Control of multi-terminal VSC-HVDC for wind power integration using the voltage-margin method,” in *Proc. 9th International workshop on Large Scale Integration of Wind Power into Power Systems as well as on Transmission Networks for Offshore Wind Power Plants*, Québec City, Canada, Oct., 18–19, 2010, pp. 427–434.
- [AA] A. A. van der Meer, R. L. Hendriks, and W. L. Kling, “Combined stability and electro-magnetic transients simulation of offshore wind power connected through multi-terminal VSC-HVDC,” in *Proc. PES General Meeting*, Minneapolis, MN, Jul., 24–29, 2010.
- [AB] A. A. van der Meer, R. Teixeira Pinto, M. Gibescu, P. Bauer, J. T. G. Pierik, F. D. J. Nieuwenhout, R. L. Hendriks, W. L. Kling, and G. A. M. van Kuik, “Offshore transnational grids in europe: The north sea transnational grid research project in relation to other research initiatives,” in *Proc. 9th International workshop on Large Scale Integration of Wind Power into Power Systems as well as on Transmission Networks for Offshore Wind Power Plants*, Québec City, Canada, Oct. 18–19, 2010, pp. 521–528.
- [AC] A. A. van der Meer, R. L. Hendriks, and W. L. Kling, “A survey of fast power reduction

- methods for VSC connected wind power plants consisting of different turbine types,” in *EPE wind energy chapter 2nd seminar*, Stockholm, Sweden, Apr., 23–24, 2009.
- [AD] A. A. van der Meer and M. Popov, “Directional relay co-ordination in ungrounded MV radial distribution networks using a RTDS,” in *International Conf. on Power System Transients*, Kyoto, Japan, Jun., 2–6, 2009.
- [AE] R. L. Hendriks, A. A. van der Meer, and W. L. Kling, “Impact on system stability of different voltage control schemes of wind power plants connected through AC and VSC-HVDC transmission,” in *Nordic Wind Power Conference*, Rønne, Denmark, Sep., 10–11, 2009.

Other Publications

- [AF] A. A. van der Meer, “Cyber-physical energy systems modeling, test specification, and co-simulation based testing,” Apr. 2017, keynote talk at MSCPES 2017.
- [AG] E. Widl *et al.*, “Simulator coupling and smart grid libraries,” Austrian Institute of Technology, Tech. Rep., Apr. 2017, deliverable D-JRA2.1. [Online]. Available: <https://erigrid.eu/dissemination/>
- [AH] A. A. van der Meer, M. Ndreko, B. R. Rawn, and M. Gibescu, “Dynamic behaviour and transient stability assessment of a North-Sea region case containing VSC-HVDC transmission,” Delft University of Technology, Tech. Rep., Apr. 2013, WP 6.2. NSTG Project Technical Report Part II. [Online]. Available: <http://www.nstg-project.nl/project/publications/>
- [AI] A. A. van der Meer, “Directional relay co-ordination in ungrounded medium voltage radial distribution networks using a real-time digital simulator,” Master’s thesis, Delft University of Technology, Delft, the Netherlands, Sep. 2008.

Bibliography

- [1] M. A. M. van der Meijden, "A sustainable and reliable electricity system; inevitable and challenging: Een duurzaam en betrouwbaar elektriciteitssysteem; onontkoombaar en uitdagend," Inaugural speech, Feb., 10, 2012. Available online at: <https://repository.tudelft.nl/islandora/object/uuid%3A3d04f70f-38a1-47f4-898e-0330f528ad47>
- [2] J. M. Kroon, "Hoge spanning – leveringszekerheid in een veranderende wereld," 12e Hidde Nijland rede, Nov., 16, 2012.
- [3] International Energy Agency, "Key world energy statistics," <http://www.iea.org/publications/freepublications/publication/keyworld2014.pdf>, 2014, accessed: 2015-02-18.
- [4] Consultatiedocument KCD 2015. (2015, Feb.) TenneT TSO B.V. Arnhem, the Netherlands. Available online at: http://www.tennet.eu/fileadmin/user_upload/Company/News/English/2015/20150220_TenneT_Consultatiedocument_KCD.pdf Last accessed: Aug. 2016.
- [5] GPD long-term forecast. (2016, Jun.) The Organisation for Economic Co-operation and Development (OECD). Paris, France. Available online at: <https://data.oecd.org/gdp/gdp-long-term-forecast.htm> Last accessed: Aug. 2016.
- [6] World Energy Outlook 2016. (2016) International Energy Agency. Paris, France. Available online at: <http://www.worldenergyoutlook.org>
- [7] World bank open data. (2016, Jun.) the World Bank Group. Available online at: <http://data.worldbank.org/> Last accessed Aug. 2016.
- [8] International Energy Agency. Key electricity trends: Excerpt from: Electricity information. (2015, Jul.). Available online at: <http://www.iea.org/publications/freepublications/publication/Electricitytrends.pdf> Last accessed: Aug. 2016.
- [9] Core Writing Team, R.K. Pachauri and L.A. Meyer (eds.), "Climate change 2014: Synthesis report. contribution of working groups i, ii and iii to the fifth assessment report of the intergovernmental panel on climate change," IPCC, Geneva, Switzerland, synthesis report, 2014. Available online at: <http://www.ipcc.ch/report/ar5/syr/>
- [10] UN Climate Change Conference (COP21), "Paris agreement," Dec. 2015. Available online at: <http://www.cop21.gouv.fr/>
- [11] S. Teske, "Energy [R]evolution - a sustainable world energy outlook 2015," Greenpeace, GWEC, SolarPower Europe, Tech. Rep., Sep. 2015. Available online at: <http://www.greenpeace.org/international/en/campaigns/climate-change/energyrevolution/>
- [12] Sociaal Economische Raad, "Energieakkoord voor duurzame groei," Sep. 2013. Available online at: <http://www.energieakkoordser.nl/> Last accessed: Aug. 2016.
- [13] B. Ummels, "Wind integration - power system operation with large-scale wind power in liberalised environments," Ph.D. dissertation, Delft University of Technology, 2009.
- [14] A. R. Ciupuliga, "Transmission expansion planning under increased uncertainties - towards efficient and sustainable power systems," Ph.D. dissertation, Delft University of Technology, Nov. 2013.
- [15] Twenties - transmitting wind, "TWENTIES project - final report," Oct. 2013. Available online at: http://www.twenties-project.eu/system/files/Twenties%20final%20report_web_v2.pdf
- [16] N. Mohan, T. M. Undeland, and W. P. Robbins, *Power Electronics - Converters, Applications, and Design*, 2nd ed. New York, NY: John Wiley & Sons, 1995.
- [17] COBRACable Nederland - Denemarken. (2016, Apr.) Rijksdienst voor Ondernemend Nederland (RVO). Available online at: <http://www.rvo.nl/subsidies-regelingen/cobracable-nederland-denemarken> Last accessed: Aug. 2016.
- [18] J. A. Overbeeke, P. Antenbrink, J. Chhatta RA, M. E. van den Dongen, J. Doornbos, J. M. ten Kate, and A. M. Pothof, "Investerings TenneT in Nederlands hoogspanningsnet; toezicht van het Rijk op het publieke belang," Algemene Rekenkamer, Den Haag, the Netherlands, Tech. Rep., Feb. 2015. Available online at: http://www.rekenkamer.nl/Publicaties/Onderzoeksrapporten/Introductions/2015/02/Investerings_TenneT_in_Nederlands_hoogspanningsnet
- [19] BorWin1 - one of the most remote offshore wind farm clusters in the world is connected to the German grid by a 400 MW +/-150 kV HVDC Light transmission system from ABB. (2015) ABB. Available online at: <http://new.abb.com/systems/hvdc/references/borwin1> Last accessed Aug. 2016.
- [20] G. W. Adamowitsch, "Connection to offshore wind power in Northern Europe (North Sea – Baltic Sea)," European Commission, Brussels, Belgium, Tech. Rep., 2009. Available online at: http://ec.europa.eu/energy/infrastructure/tent_e/coordinators_en.htm
- [21] A. Woyte, J. De Decker, and V. Van Thong, "A North Sea electricity grid [R]evolution," Greenpeace – 3E, Brussels, Belgium, Tech. Rep., 2008.
- [22] N. Fichaux, J. Wilkes, F. Van Hulle, and A. Cronin, "Oceans of opportunity," EWEA, Tech. Rep., 2009. Available online at: <http://www.ewea.org>
- [23] The OffshoreGrid project. Available online at: <http://www.offshoregrid.eu/> Last accessed Aug. 2017.
- [24] North seas countries' offshore grid initiative (NSCOGI). ENTSO/e. Available online at: <http://www.benelux.int/nl/kernthemas/energie/nscogi-2012-report/> Last accessed Aug. 2017.
- [25] M. van der Meijden, "Future north sea infrastructure based on dogger bank modular island," in *proc. 15th Wind Integration*

- Workshop, Vienna, Austria, Nov., 15–17, 2016.
- [26] F. Van Hulle, "Integrating Wind - Developing Europe's power market for the large-scale integration of wind power," European Wind Energy Association, Brussels, Belgium, Tech. Rep., 2009, tradewind.
 - [27] IEA wind task 25: Power systems with large amounts of wind power. IEA. Available online at: https://www.ieawind.org/task_25.html Last accessed: Aug. 2017.
 - [28] P. Kundur, J. Paserba, V. Ajjarapu, G. Andersson, A. Bose, C. Canizares, N. Hatziargyriou, D. Hill, A. Stankovic, C. Taylor, T. Van Cutsem, and V. Vittal, "Definition and classification of power system stability," *IEEE Trans. Power Syst.*, vol. 19, no. 3, pp. 1387–1401, 2004.
 - [29] J. Beerten, "Modeling and control of dc grids," Ph.D. dissertation, KU Leuven, 2013.
 - [30] S. Shariat Torbaghan, "Transmission expansion planning of transnational offshore grids: A techno-economic and legal approach case study of the north sea offshore grid," Ph.D. dissertation, Delft University of Technology, Feb. 2016.
 - [31] V. Akhmatov, M. Callavik, C. Franck, S. Rye, T. Ahndorf, M. Bucher, H. Muller, F. Schettler, and R. Wiget, "Technical guidelines and prestandardization work for first HVDC grids," *IEEE Trans. Power Del.*, vol. 29, no. 1, pp. 327–335, Feb. 2014.
 - [32] M. Hajian, D. Jovicic, and B. Wu, "Evaluation of semiconductor based methods for fault isolation on high voltage dc grids," *Smart Grid, IEEE Transactions on*, vol. 4, no. 2, pp. 1171–1179, Jun. 2013.
 - [33] *Wind turbines - Part 27-1: Electrical simulation models - Wind turbines*, IEC 61400-27-1:2015, International Electrotechnical Commission Std., Nov. 2015.
 - [34] J. Fortmann, N. Miller, Y. Kazachkov, J. Bech, B. Andersen, P. Pourbeik, and P. E. Sørensen, "Wind plant models in IEC 61400-27-2 and WECC - latest developments in international standards on wind turbine and wind plant modeling," in *14th International Workshop on Large-Scale Integration of Wind Power into Power Systems as well as on Transmission Networks for Offshore Wind Power Plants*, Brussels, Belgium, Oct., 20–22, 2015.
 - [35] G. Corbetta, A. Ho, and I. Pineda, "Wind energy scenarios for 2030," EWEA, Tech. Rep., Aug. 2015. Available online at: <https://windeurope.org/about-wind/reports/>
 - [36] The North Sea transnational grid project. ECN. Available online at: <http://www.nstg-project.nl/> Last accessed: Aug. 2017.
 - [37] We@sea - offshore wind power research. (2009, Dec.). Available online at: <http://www.we-at-sea.org/> Last accessed Aug. 2016.
 - [38] F. J. L. van Hulle. Research line 3: Grid integration of offshore wind power. (2010, Mar.). Available online at: <http://www.we-at-sea.org/library/the-wesea-rd-programme/> Last accessed Aug. 2016.
 - [39] R. Teixeira Pinto, "Multi-terminal dc networks - system integration, dynamics and control," Ph.D. dissertation, Delft University of Technology, 2014.
 - [40] D. Tiku, "dc power transmission: Mercury-arc to thyristor HVdc valves [history]," *IEEE Power and Energy Magazine*, vol. 12, no. 2, pp. 76–96, Mar. 2014.
 - [41] S. P. Teeuwssen, A. Chaudhry, G. Love, R. Sherry, and R. de Silva, "Dynamic performance of the upgraded 1400 MW New Zealand HVDC project," in *proc. 2012 IEEE Power and Energy Society General Meeting*, San Diego, CA, Jul., 22–26, 2012.
 - [42] J.-E. Skog, H. van Asten, T. Worzyk, and T. Andersröd, "NorNed – World's longest power cable," in *Cigré Session*, Paris, France, Aug., 22–27, 2010.
 - [43] J.-E. Skog, K. Koreman, B. Pääjärvi, T. Worzyk, and T. Andersröd, "The NorNed HVDC cable link a power transmission highway between Norway and the Netherlands," in *ENERGEX 2006*, Stavanger, Norway, Jun., 12–15, 2006.
 - [44] G. Asplund, K. Eriksson, and K. Svensson, "HVDC light - DC transmission based on voltage sourced converters," *ABB Rev*, no. 1, pp. 4–9, 1998.
 - [45] Y. Makino. Compendium of all HVDC projects. (2016) Cigré SC B4. Available online at: <http://b4.cigre.org/Publications/Other-Documents/Compendium-of-all-HVDC-projects> Last accessed: Jul. 2017.
 - [46] S. Cole and R. Belmans, "Transmission of bulk power," *IEEE Ind. Electron. Mag.*, vol. 3, no. 3, pp. 19–24, Sep. 2009.
 - [47] C. Du, E. Agneholm, and G. Olsson, "Comparison of different frequency controllers for a VSC-HVDC supplied system," *IEEE Trans. Power Del.*, vol. 23, no. 4, pp. 2224–2232, Oct. 2008.
 - [48] B. Jacobson, Y. Jiang-Häfner, P. Rey, G. Asplund, M. Jeroense, A. Gustafsson, and M. Bergkvist, "HVDC with voltage source converters and extruded cables for up to ± 300 kV and 1000 MW," in *41st International Conference on Large High Voltage Electric Systems, CIGRE 2006*, Paris, France, Aug., 27 – Sep., 1 2006.
 - [49] S. Dodds, B. Railing, K. Akman, B. Jacobson, T. Worzyk, and B. Nilsson, "HVDC VSC (HVDC light) transmission – operating experiences," in *proc. Cigré session B4-203*, Paris, France, Aug., 22–27, 2010.
 - [50] R. Marquardt, A. Lesnicar, and J. Hildinger, "Modulares stromrichterkonzept für netzkupplungsanwendung bei hohen spannungen," in *ETG-Fachtagung*, Bad Nauheim, Germany, Apr., 23–24, 2002.
 - [51] L. Franquelo, J. Rodriguez, J. Leon, S. Kouro, R. Portillo, and M. Prats, "The age of multilevel converters arrives," *Industrial Electronics Magazine, IEEE*, vol. 2, no. 2, pp. 28–39, June 2008.
 - [52] E. Solas, G. Abad, J. A. Barrena, A. Carear, and S. Aurtenetxea, "Modulation of modular multilevel converter for HVDC application," in *proc. 14th Int. Power Electronics and Motion Control Conf. (EPE/PEMC)*, Ohrid, Macedonia, Sep., 6–8, 2010, pp. T2–84–T2–89.
 - [53] A. Hassanpoor, S. Norrgrä, and M. Lindgren, "Switching pattern optimisation algorithm for modular multilevel converters," in *proc. 40th annual conf. of the IEEE Industrial Electronics Society (IECON)*, Dallas, TX, Sep., 28–29, 2014.
 - [54] P. Haugland, "It's time to connect - technical description of HVDC light technology," pp. –, Dec. 2012. Available online at: <https://library.e.abb.com> Last accessed: Aug. 2016.
 - [55] M. Davies, M. Dommashchik, J. Dorn, J. Lang, D. Retzmann, and D. Soerangr, "HVDC PLUS – basics and principle of operation," Siemens AG, Erlangen, Germany, technical article, Aug. 2011, last accessed Aug. 2016. Available online at: www.siemens.com/energy/hvdcplus
 - [56] "Product catalogue: HVDC solutions," 2015. Available online at: <http://www.gegridsolutions.com/alstomenergy/grid/products-services/product-catalogue/electrical-grid-new/hvdc/hvdc-solutions/index.html> Last accessed Aug. 2016.
 - [57] H. Saad, X. Guillaud, J. Mahseredjian, S. Denetière, and S. Nguefeu, "MMC capacitor voltage decoupling and balancing controls," in *proc. IEEE Power Energy Society General Meeting*, Denver, CO, Jul., 26–30, 2015, pp. 704–712.
 - [58] H. Saad, J. Mahseredjian, S. Denetière, and S. Nguefeu, "Interactions studies of HVDC–MMC link embedded in an AC

- grid," *Electr. Power Syst. Res.*, vol. 138, pp. 202–209, 2016, special Issue: Papers from the 11th International Conference on Power Systems Transients (IPST).
- [59] J. Hu, K. Xu, L. Lin, and R. Zeng, "Analysis and enhanced control of hybrid-MMC-based HVDC systems during asymmetrical DC voltage faults," *IEEE Trans. Power Del.*, vol. 32, no. 3, pp. 1394–1403, Jun. 2017.
 - [60] L. Zhang, L. Harnefors, and H.-P. Nee, "Power-synchronization control of grid-connected voltage-source converters," *IEEE Trans. Power Syst.*, vol. 25, no. 2, pp. 809–820, May 2010.
 - [61] T. Ackermann, Ed., *Wind Power in Power Systems*, 2nd ed. Chichester, UK: John Wiley & Sons, Ltd, Apr. 2012.
 - [62] S. Heier, *Grid integration of wind energy conversion systems*, 3rd ed. Chichester, UK: John Wiley & Sons, Ltd, Jun. 2014.
 - [63] A. Nordmann. Illustration of a wind turbine. (2007, Feb.). Available online at: https://en.wikipedia.org/wiki/Wind_power Last accessed: Aug. 2017.
 - [64] H. Polinder, F. F. A. Van Der Pijl, G.-J. De Vilder, and P. Tavner, "Comparison of direct-drive and geared generator concepts for wind turbines," *IEEE Trans. Energy Convers.*, vol. 21, no. 3, pp. 725–733, 2006.
 - [65] S. A. Papathanassiou and M. P. Papadopoulos, "Mechanical stresses in fixed-speed wind turbines due to network disturbances," *IEEE Trans. Energy Convers.*, vol. 16, no. 4, pp. 361–367, Dec. 2001.
 - [66] K. Wong, S. Ho, and K. Cheng, "Direct torque control of a doubly-fed induction generator with space vector modulation," *Electr. Power Comp. Syst.*, vol. 36, no. 12, pp. 1337–1350, 2008.
 - [67] J. Fletcher and J. Yang, *Introduction to the Doubly-Fed Induction Generator for Wind Power Applications, Paths to Sustainable Energy*. IN TECH Open Science, 2010, ch. 14, pp. 259–278.
 - [68] I. Erlich, J. Kretschmann, J. Fortmann, S. Mueller-Engelhardt, and H. Wrede, "Modeling of wind turbines based on doubly-fed induction generators for power system stability studies," *IEEE Trans. Power Syst.*, vol. 22, no. 3, pp. 909–919, 2007.
 - [69] H.-S. Ko, G.-G. Yoon, N.-H. Kyung, and W.-P. Hong, "Modeling and control of DFIG-based variable-speed wind-turbine," *Electr. Power Syst. Res.*, vol. 78, no. 11, pp. 1841–1849, 2008.
 - [70] V. Yaramasu, B. Wu, P. C. Sen, S. Kouro, and M. Narimani, "High-power wind energy conversion systems: State-of-the-art and emerging technologies," *Proc. IEEE*, vol. 103, no. 5, pp. 740–788, May 2015.
 - [71] A. D. Hansen and G. Michalke, "Modelling and control of variable-speed multi-pole permanent magnet synchronous generator wind turbine," *Wind Energy*, vol. 11, no. 5, pp. 537–554, 2008.
 - [72] W. Hu, Y. Wang, W. Yao, J. Wu, H. Zhang, and Z. Wang, "An efficient experimental method for high power direct drive wind energy conversion systems," in *proc. IEEE Power Electronics Specialists Conference, PESC 2008.*, Rhodes, Greece, Jun., 15–19, 2008, pp. 3955–3959.
 - [73] A. Miller, E. Muljadi, and D. Zinger, "A variable speed wind turbine power control," *IEEE Trans. Energy Convers.*, vol. 12, no. 2, pp. 181–186, 1997.
 - [74] V. Akhmatov, "Variable-speed wind turbines with doubly-fed induction generators. part I: Modelling in dynamic simulation tools," *Wind Engineering*, vol. 26, no. 2, pp. 85–108, 2002.
 - [75] L. Holdsworth, X. Wu, J. Ekanayake, and N. Jenkins, "Comparison of fixed speed and doubly-fed induction wind turbines during power system disturbances," *IEE Proceedings: Communications*, vol. 150, no. 3, pp. 343–352, 2003.
 - [76] Cigré WG B4.55, "HVDC connection of offshore wind power plants," May 2015, Cigré technical brochure 619.
 - [77] J. G. Slootweg, "Wind power, modelling and impact on power system dynamics," Ph.D. dissertation, Delft University of Technology, the Netherlands, 2003.
 - [78] E. Muljadi, C. Butterfield, A. Ellis, J. Mechenbier, J. Hochheimer, R. Young, N. Miller, R. Delmerico, R. Zavadil, and J. Smith, "Equivalentencing the collector system of a large wind power plant," in *Power Engineering Society General Meeting, 2006. IEEE*, 2006.
 - [79] T. K. Vrana, J. Beerten, R. Belmans, and O. B. Fosso, "A classification of DC node voltage control methods for HVDC grids," *Electric Power Systems Research*, vol. 103, pp. 137–144, 2013.
 - [80] J. Thomas, S. Poullain, and A. Benchaib, "Analysis of a robust DC-bus voltage control system for a VSC transmission scheme," in *proc. AC-DC Power Transmission*, no. 485. London, UK: IEE, Nov., 28–30, 2001, pp. 119–124.
 - [81] L. Xu and B. Andersen, "Grid connection of large offshore wind farms using HVDC," *Wind Energy*, vol. 9, no. 4, pp. 371–382, 2006.
 - [82] B. Silva, C. L. Moreira, L. Seca, Y. Phulpin, and J. A. P. Lopes, "Provision of inertial and primary frequency control services using offshore multiterminal HVDC networks," *IEEE Trans. Sustainable Energy*, vol. 3, no. 4, pp. 800–808, Oct. 2012.
 - [83] C. Barker and R. Whitehouse, "Autonomous converter control in a multi-terminal HVDC system," in *proc. 9th IET International Conference on AC and DC Power Transmission*, London, UK, Oct., 19–21 2010.
 - [84] T. M. Haileselassie and K. Uhlen, "Impact of DC line voltage drops on power flow of MTDC using droop control," *IEEE Trans. Power Syst.*, vol. 27, no. 3, pp. 1441–1449, Aug. 2012.
 - [85] J. Beerten, S. Cole, and R. Belmans, "Modeling of multi-terminal VSC HVDC systems with distributed DC voltage control," *IEEE Trans. Power Syst.*, vol. 29, no. 1, pp. 34–42, Jan. 2014.
 - [86] T. M. Haileselassie, A. G. Endegnanew, and K. Uhlen, "Secondary control in multi-terminal VSC-HVDC transmission system," in *proc. IEEE Power Energy Society General Meeting*, Denver, CO, Jul., 26–30 2015, pp. 3577–3581.
 - [87] R. Pinto, P. Bauer, S. Rodrigues, E. Wiggelinkhuizen, J. Pierik, and B. Ferreira, "A novel distributed direct-voltage control strategy for grid integration of offshore wind energy systems through MTDC network," *IEEE Trans. Ind. Electron.*, vol. 60, no. 6, pp. 2429–2441, Jun. 2013.
 - [88] R. Irnawan, F. F. da Silva, C. L. Bak, and T. C. Bregnhøj, "A categorization of converter station controllers within multi-terminal DC transmission systems," in *IEEE/PES Transmission and Distribution Conference and Exposition (T & D)*, Dallas, TX, May, 3–5, 2016.
 - [89] K. Sakamoto, M. Yajima, T. Ishikawa, S. Sugimoto, T. Sato, and H. Abe, "Development of a control system for a high-performance self-commutated AC/DC converter," *IEEE Trans. Power Del.*, vol. 13, no. 1, pp. 225–232, Jan. 1998.
 - [90] R. T. Pinto, S. Rodrigues, P. Bauer, and J. Pierik, "Description and comparison of DC voltage control strategies for offshore MTDC networks: Steady-state and fault analysis," *EPE Journal*, vol. 22, no. 4, pp. 31–39, 2012.
 - [91] F. Gonzalez-Longatt and J. M. Roldan, "Effects of dc voltage control strategies of voltage response on multi-terminal HVDC following a disturbance," in *proc. 47th International Universities Power Engineering Conference (UPEC)*, London, UK, Sep., 4–7, 2012, pp. 1–6.

- [92] P. Chodura, M. Gibescu, W. L. Kling, and R. A. A. de Graaff, "Investigation of the impact of embedded VSC-HVDC active and reactive power control on power system stability," in *proc. 2015 IEEE Eindhoven PowerTech*, Eindhoven, the Netherlands, Jun., 29 – Jul., 2 2015, pp. 3370–3375.
- [93] O. A. Urquidez and L. Xie, "Singular value sensitivity based optimal control of embedded VSC-HVDC for steady-state voltage stability enhancement," *IEEE Trans. Power Syst.*, vol. 31, no. 1, pp. 216–225, Jan. 2016.
- [94] N. T. Trinh, I. Erlich, M. Zeller, and K. Wuerflinger, "Utilization of embedded VSC-MTDC system for supporting power flow during primary frequency control," in *2016 Power Systems Computation Conference (PSCC)*, Genoa, Italy, Jun., 20–24 2016.
- [95] A. Bayo-Salas, J. Beerten, J. Rimez, and D. V. Hertem, "Analysis of control interactions in multi-infeed VSC HVDC connections," *IET Generation, Transmission Distribution*, vol. 10, no. 6, pp. 1336–1344, Apr. 2016.
- [96] X. Ni, A. M. Gole, C. Zhao, and C. Guo, "An improved measure of ac system strength for performance analysis of multi-infeed HVDC systems including VSC and LCC converters," *IEEE Trans. Power Del.*, vol. PP, no. 99, pp. 1–1, 2017.
- [97] R. Irnawan, F. F. da Silva, C. L. Bak, and T. C. Bregnhøj, "An initial topology of multi-terminal HVDC transmission system in europe: A case study of the North-Sea region," in *2016 IEEE International Energy Conference (ENERGYCON)*, Leuven, Belgium, Apr., 4–8 2016.
- [98] F. F. da Silva. The COBRACable research project. (2016). Available online at: <http://www.cobracable.et.aau.dk/> Last accessed: Aug. 2017.
- [99] COBRACable. Energinet, TenneT. Available online at: <http://www.cobracable.eu/> Last accessed: Aug. 2017.
- [100] Estlink. (2006) ABB. Available online at: <http://new.abb.com/systems/hvdc/references/estlink> Last accessed: Aug. 2017.
- [101] East-West interconnector. EIRGrid Group. Available online at: <http://www.eirgridgroup.com/customer-and-industry/interconnection/> Last accessed: Aug. 2017.
- [102] The INELFE baixas-santa llogaia interconnection. Available online at: <https://www.inelfe.eu/en> Last accessed: Aug. 2017.
- [103] Aachen liège electric grid overlay. Elia. Available online at: <http://www.elia.be/en/projects/grid-projects/alegro/alegro-content> Last accessed: Aug. 2017.
- [104] "European union projects of common interest in energy," Jan. 2014. Available online at: http://ec.europa.eu/energy/sites/ener/files/documents/2013_pci_projects_country.pdf Last accessed: Oct. 2016.
- [105] J. Binkai and W. Zhixin, "The key technologies of VSC-MTDC and its application in china," *Renewable and Sustainable Energy Reviews*, vol. 62, pp. 297–304, 2016.
- [106] B. Gummell, J. Dorn, D. Retzmann, and D. Soerangr, "Prospects of multilevel VSC technologies for power transmission," in *proc. Transmission and Distribution Conference and Exposition, 2008 IEEE/PES*, Chicago, IL, Apr. 21–24, 2008, pp. 1–16.
- [107] S. Wenig, M. Goertz, M. Suriyah, and T. Leibfried, "Active DC fault management of a bipolar full-bridge MMC-HVDC scheme with metallic return," in *2016 IEEE International Energy Conference (ENERGYCON)*, Leuven, Belgium, Apr., 4–8, 2016.
- [108] Q. Du, "VSC-HVDC for industrial power systems," Ph.D. dissertation, Chalmers University Of Technology, Göteborg, Sweden, 2007.
- [109] J. Morren and S. W. H. de Haan, "Ridethrough of wind turbines with doubly-fed induction generator during a voltage dip," *IEEE Trans. Energy Convers.*, vol. 20, no. 2, pp. 435–441, Jun. 2005.
- [110] I. Erlich, H. Wrede, and C. Feltes, "Dynamic behavior of dfig-based wind turbines during grid faults," in *proc. 4th Power Conversion Conference-NAGOYA, PCC-NAGOYA*, Kempen, Germany, 2007, pp. 1195–1200.
- [111] K. Skaloumpakas, J. C. Boemer, E. van Ruitenbeek, M. Gibescu, and M. A. M. M. van der Meijden, "Response of low voltage networks with high penetration of photovoltaic systems to transmission network faults," in *3rd Renewable Power Generation Conference (RPG 2014)*, Naples, Italy, Sep., 25–26 2014.
- [112] J. C. Boemer, B. G. Rawn, M. Gibescu, M. A. M. M. van der Meijden, and W. L. Kling, "Response of wind power park modules in distribution systems to transmission network faults during reverse power flows," *IET Renewable Power Generation*, vol. 9, no. 8, pp. 1033–1042, 2015.
- [113] S. Liu, T. Bi, K. Jia, and Q. Yang, "Coordinated fault-ride-through strategy for doubly-fed induction generators with enhanced reactive and active power support," *IET Renewable Power Generation*, vol. 10, no. 2, pp. 203–211, 2016.
- [114] A. Dimov and S. Bolik, "Wind turbine manufacturers observation regarding reactive power support and control requirements," *IET Renewable Power Generation*, vol. 11, no. 4, pp. 539–544, 2017.
- [115] European Commission, "Establishing a network code on requirements for grid connection of high voltage direct current systems and direct current-connected power park modules," Commission Regulation (EU) 2016/1447, Aug. 2016. Available online at: <http://data.europa.eu/eli/reg/2016/1447/oj> Last accessed: Nov. 2016.
- [116] J. B. Ekanayake, L. Holdsworth, and N. Jenkins, "Comparison of 5th order and 3rd order machine models for doubly fed induction generator (DFIG) wind turbines," *Electr. Power Syst. Res.*, vol. 67, no. 3, pp. 207–215, Dec. 2003.
- [117] F. Shewarega and I. Erlich, "Simplified modeling of VSC-HVDC in power system stability studies," in *proc. 19th IFAC World Congress*, vol. 19, Cape Town, South Africa, Aug., 24–29 2014, pp. 9099–9104.
- [118] J. Beerten, S. D'Arco, and J. A. Suul, "Identification and small-signal analysis of interaction modes in VSC MTDC systems," *IEEE Trans. Power Del.*, vol. 31, no. 2, pp. 888–897, Apr. 2016.
- [119] V. Blasko and V. Kaura, "A new mathematical model and control of a three-phase AC-DC voltage source converter," *IEEE Trans. Power Electron.*, vol. 12, no. 1, pp. 116–123, 1997.
- [120] L. Harnefors, "Control of VSC-HVDC Transmission," tutorial presented at the IEEE Power Electronics Specialists Conference, Rhodes, Greece, Jun. 15–19 2008.
- [121] M. Hoeijmakers, "Modelling of AC machines," Apr. 2004, EPP, EW1, TU Delft.
- [122] A. Gole, V. K. Sood, and L. Mootosamy, "Validation and analysis of a grid control system using d-q-z transformation for static converter systems," in *Proc. Canadian Conf. on Electrical and Computer Engineering*, Montréal, CQ, Sep. 17–20, 1989.
- [123] V. Kaura and V. Blasko, "Operation of a phase locked loop system under distorted utility conditions," *IEEE Trans. Ind. Appl.*, vol. 33, no. 1, pp. 58–63, Jan. / Feb. 1997.
- [124] A. Tabesh and R. Iravani, "Multivariable dynamic model and robust control of a voltage-source converter for power system applications," *IEEE Trans. Power Del.*, vol. 24, no. 1, pp. 462–471, Jan. 2009.

- [125] The simulink R2017a documentation: Rate limiter. (2017) Mathworks. Available online at: <http://www.mathworks.com/help/simulink/slref/ratelimiter.html> Last accessed: Aug. 2017.
- [126] J. G. Slootweg, H. Polinder, and W. L. Kling, "Representing wind turbine electrical generating systems in fundamental frequency simulations," *IEEE Trans. Energy Convers.*, vol. 18, no. 4, pp. 516–524, 2003.
- [127] J. Fortmann, S. Engelhardt, J. Kretschmann, C. Feltes, and I. Erlich, "New generic model of DFG-based wind turbines for RMS-type simulation," *IEEE Trans. Energy Convers.*, vol. 29, no. 1, pp. 110–118, Mar. 2014.
- [128] C. Jauch, S. Islam, P. Sørensen, and B. Bak Jensen, "Design of a wind turbine pitch angle controller for power system stabilisation," *Renewable Energy*, vol. 32, no. 14, pp. 2334–2349, 2007.
- [129] E. A. Bossanyi, "Wind turbine control for load reduction," *Wind Energy*, vol. 6, no. 3, pp. 229–244, 2003.
- [130] J. Feltes, R. Hendriks, S. Stapleton, R. Voelzke, B. Lam, and N. Pfunter, "Twixt land and sea: Cost-effective grid integration of offshore wind plants," *IEEE Power Energy Mag.*, vol. 10, no. 2, pp. 53–61, Mar. 2012.
- [131] B. Singh, "Introduction to FACTS controllers in wind power farms: A technological review," *International Journal of Renewable Energy Research*, vol. 2, no. 2, pp. 166–212, 2012.
- [132] L. Stendius and P. Sandeberg, "Large scale offshore wind power energy evacuation by HVDC light," in *Proc. European Wind Energy Conference*, Brussels, Belgium, Apr. 2008.
- [133] L. Harnefors, Y. Jiang-Hafner, M. Hyttinen, and T. Jonsson, "Ride-through methods for wind farms connected to the grid via a VSC-HVDC transmission," in *Proc. Nordic Wind Power Conference*, Roskilde, Denmark, Nov. 1–2, 2007.
- [134] A. Arulampalam, G. Ramtharan, N. Caliao, J. B. Ekanayake, and N. Jenkins, "Simulated onshore-fault ride through of offshore wind farms connected through VSC HVDC," *Wind Engineering*, vol. 32, no. 2, pp. 103–114, 2008.
- [135] L. Xu, B. R. Andersen, and P. Cartwright, "VSC transmission operating under unbalanced AC conditions – analysis and control design," *IEEE Trans. Power Del.*, vol. 20, no. 1, pp. 427–434, 2005.
- [136] C. Feltes, H. Wrede, F. Koch, and I. Erlich, "Fault ride-through of DFIG-based wind farms connected to the grid through VSC-based HVDC link," in *Proc. 16th Power Systems Computation Conference*, Glasgow, Scotland, Jul. 14–18, 2008.
- [137] L. Xu, L. Yao, and C. Sasse, "Grid integration of large DFIG-based wind farms using VSC transmission," *IEEE Transactions on Power Systems*, vol. 22, no. 3, pp. 976–984, 2007.
- [138] J. Morren, S. W. H. de Haan, W. L. Kling, and J. A. Ferreira, "Wind turbines emulating inertia and supporting primary frequency control," *IEEE Trans. Power Syst.*, vol. 21, no. 1, pp. 433–434, 2006.
- [139] S. K. Chaudhary, R. Teodorescu, P. Rodriguez, and P. C. Kjaer, "Chopper controlled resistors in VSC-HVDC transmission for WPP with full-scale converters," in *2009 IEEE PESIAS Conference on Sustainable Alternative Energy (SAE)*, Valencia, Spain, Sep., 28–30 2009, pp. 176–183.
- [140] S. Nanou and S. Papathanassiou, "Evaluation of a communication-based fault ride-through scheme for offshore wind farms connected through high-voltage DC links based on voltage source converter," *IET Renewable Power Generation*, vol. 9, no. 8, pp. 882–891, 2015.
- [141] U. M. Ascher and L. R. Petzold, *Computer Methods for Ordinary Differential Equations and Differential-Algebraic Equations*. Siam, 1997.
- [142] J. Machowski, J. W. Bailek, and J. R. Bumby, *Power System Dynamics and Stability*. John Wiley & Sons, 1997.
- [143] W. D. Humpage and B. Stott, "Predictor-corrector methods of numerical integration in digital-computer analyses of power-system transient stability," *Proc. of the Institution of Electrical Engineers*, vol. 112, no. 8, pp. 1557–1565, Aug. 1965.
- [144] F. Milano, *Power System Modelling and Scripting*. Springer, 2010.
- [145] J. Marti, "Accurate modelling of frequency-dependent transmission lines in electromagnetic transient simulations," *IEEE Trans. Power App. Syst.*, vol. PAS-101, no. 1, pp. 147–157, Jan. 1982.
- [146] A. A. van der Meer, R. Hendriks, M. Gibescu, and W. L. Kling, "Interfacing methods for combined stability and electromagnetic transient simulations applied to VSC-HVDC," in *Proc. International Conference on Power System Transients*, Delft, the Netherlands, Jun., 14–17, 2011.
- [147] H. Dommel and N. Sato, "Fast transient stability solutions," *IEEE Trans. Power App. Syst.*, vol. PAS-91, no. 4, pp. 1643–1650, July 1972.
- [148] S. Cole, J. Beerten, and R. Belmans, "Generalized dynamic VSC MTDC model for power system stability studies," *IEEE Trans. Power Syst.*, vol. 25, no. 3, pp. 1655–1662, Aug. 2010.
- [149] N. Chaudhuri, R. Majumder, B. Chaudhuri, and J. Pan, "Stability analysis of VSC MTDC grids connected to multimachine AC systems," *IEEE Trans. Power Del.*, vol. 26, no. 4, pp. 2774–2784, Oct. 2011.
- [150] J. Beerten, S. Cole, and R. Belmans, "A sequential AC/DC power flow algorithm for networks containing multi-terminal VSC HVDC systems," in *proc. Power and Energy Society General Meeting*, Minneapolis, MN, Jul., 19–24, 2010.
- [151] J. Beerten, S. Cole, and R. Belmans, "Generalized steady-state VSC MTDC model for sequential AC/DC power flow algorithms," *IEEE Trans. Power Syst.*, vol. 27, no. 2, pp. 821–829, May 2012.
- [152] R. Pandey, "Stability analysis of AC/DC system with multirate discrete-time HVDC converter model," *IEEE Trans. Power Del.*, vol. 23, no. 1, pp. 311–318, Jan. 2008.
- [153] P. Kundur, *Power System Stability and Control*. New York, NY: McGraw-Hill, Inc., 1994.
- [154] A. Gole, R. Menzies, H. Turanli, and D. Woodford, "Improved interfacing of electrical machine models to electromagnetic transients programs," *IEEE Trans. Power App. Syst.*, vol. PAS-103, no. 9, pp. 2446–2451, Sep. 1984.
- [155] "HVDC cable design sheet," New England Clean Power Link Project (Docket 8400, Exhibit TDI-LE-4), Vermont Public Service Board, Dec. 2014. Available online at: <http://psb.vermont.gov/docketsandprojects/electric/8400>
- [156] C. Du, E. Agneholm, and G. Olsson, "VSC-HVDC system for industrial plants with onsite generators," *IEEE Trans. Power Del.*, vol. 24, no. 3, pp. 1359–1366, Jul. 2009.
- [157] P. M. Anderson and A. A. Fouad, *Power System Control and Stability*, 1st ed. Ames, IA: The Iowa State University Press, 1977.
- [158] T. Strasser, M. Stifter, F. Andrén, and P. Palensky, "Co-simulation training platform for smart grids," *IEEE Trans. Power Syst.*, vol. 29, no. 4, pp. 1989–1997, Jul. 2014.
- [159] S. Sicklinger, C. Lerch, R. Wüchner, and K.-U. Bletzinger, "Fully coupled co-simulation of a wind turbine emergency brake maneuver," *Journal of Wind Engineering and Industrial Aerodynamics*, vol. 144, pp. 134–145, 2015, selected papers from the 6th International Symposium on Computational Wind Engineering {CWE} 2014.

- [160] D. Bhor, K. Angappan, and K. M. Sivalingam, "Network and power-grid co-simulation framework for smart grid wide-area monitoring networks," *Journal of Network and Computer Applications*, 2015.
- [161] W. Li, X. Zhang, and H. Li, "Co-simulation platforms for co-design of networked control systems: An overview," *Control Engineering Practice*, vol. 23, pp. 44–56, 2014.
- [162] M. Björkbohm, S. Nethi, L. Eriksson, and R. Jäntti, "Wireless control system design and co-simulation," *Control Engineering Practice*, vol. 19, no. 9, pp. 1075–1086, 2011.
- [163] A. Al-Hammouri, "A comprehensive co-simulation platform for cyber-physical systems," *Computer Communications*, vol. 36, no. 1, pp. 8–19, 2012.
- [164] M. Trcka and J. L. M. Hensen, "Model and tool requirements for co-simulation of building performance," in *Proc. of the 15th IASTED Int. Conf. on Applied Simulation and Modelling*, Rhodes, Greece, Jun., 26–28, 2006.
- [165] J. Fitzgerald, P. G. Larsen, and M. Verhoef, Eds., *Collaborative Design for Embedded Systems*. Springer, 2014. Available online at: <http://www.springer.com/gp/book/9783642541179>
- [166] L. Gheorghe, F. Bouchhima, G. Nicolescu, and H. Boucheneb, "Formal definitions of simulation interfaces in a continuous/discrete co-simulation tool," in *Proc. Seventeenth IEEE International Workshop on Rapid System Prototyping*, Chania, Crete, Greece, Jun., 14–16, 2006, pp. 186–192.
- [167] S. Sicklinger, V. Belsky, B. Engelmann, H. Elmqvist, H. Olsson, R. Wüchner, and K.-U. Bletzinger, "Interface jacobian-based co-simulation," *International Journal for Numerical Methods in Engineering*, vol. 98, no. 6, pp. 418–444, 2014.
- [168] H.-J. Bungartz, F. Lindner, M. Mehl, and B. Uekermann, "A plug-and-play coupling approach for parallel multi-field simulations," *Computational Mechanics*, vol. 55, no. 6, pp. 1119–1129, 2015.
- [169] H. Dommel, "Digital computer solution of electromagnetic transients in single-and multiphase networks," *IEEE Trans. Power App. Syst.*, vol. PAS-88, no. 4, pp. 388–399, Apr. 1969.
- [170] P. Dandeno and P. Kundur, "Simulation of the non-linear dynamic response of interconnected synchronous machines part ii-network solution procedures and comparisons of particular computational methods," *Power Apparatus and Systems, IEEE Transactions on*, vol. PAS-91, no. 5, pp. 2069–2077, sept. 1972.
- [171] W. Janischewskij and P. Kundur, "Simulation of the non-linear dynamic response of interconnected synchronous machines part I-machine modelling and machine-network interconnection equations," *IEEE Trans. Power App. Syst.*, vol. PAS-91, no. 5, pp. 2064–2069, Sep. 1972.
- [172] J. Arrillaga and I. Elamin, "Transient stability performance of a 3-machine system including an h.v. d.c. link," *Proc. Inst. Electr. Eng.*, vol. 123, no. 11, pp. 1239–1244, Nov. 1976.
- [173] J. Arrillaga, H. Al-Khashali, and J. Campos-Barros, "General formulation for dynamic studies in power systems including static convertors," *Proc. Inst. Electr. Eng.*, vol. 124, no. 11, pp. 1047–1052, Nov. 1977.
- [174] G. Carter, C. Grund, H. Happ, and R. Pohl, "The dynamics of AC/DC systems with controlled multiterminal HVDC transmission," *IEEE Trans. Power App. Syst.*, vol. 96, no. 2, pp. 402–413, Mar. 1977.
- [175] P. Mutschler, "Programs for transient studies of generators connected with HVDC converters and their control system," in *6th Power Systems Computation Conference*, Darmstadt, Germany, Aug., 21–25, 1978, pp. 823–827.
- [176] A. Turner, "Modelling techniques for the study of HVDC infeeds to weak AC systems," *IEEE Trans. Power App. Syst.*, vol. PAS-100, no. 7, pp. 3461–3467, Jul. 1981.
- [177] M. Heffernan, K. Turner, J. Arrillaga, and C. Arnold, "Computation of a.c.-d.c. system disturbances - parts I, II, and III. interactive coordination of generator and convertor transient models," *IEEE Trans. Power App. Syst.*, vol. PAS-100, no. 11, pp. 4341–4363, Nov. 1981.
- [178] V. Jalili-Marandi, V. Dinavahi, K. Strunz, J. A. Martinez, and A. Ramirez, "Interfacing techniques for transient stability and electromagnetic transient programs IEEE task force on interfacing techniques for simulation tools," *IEEE Trans. Power Del.*, vol. 24, no. 4, pp. 2385–2395, Oct. 2009.
- [179] J. Reeve and R. Adapa, "A new approach to dynamic analysis of AC networks incorporating detailed modeling of dc systems - parts I and II," *IEEE Trans. Power Del.*, vol. 3, no. 4, pp. 2005–2019, Oct. 1988.
- [180] G. Anderson, N. Watson, N. Arnold, and J. Arrillaga, "A new hybrid algorithm for analysis of HVDC and FACTS systems," in *proc. Int. Conf. on Energy Management and Power Delivery (EMPD '95)*, vol. 2, Singapore, Nov., 21–23, 1995, pp. 462–467.
- [181] H. Su, K. Chan, and L. Snider, "Evaluation study for the integration of electromagnetic transients simulator and transient stability simulator," *Electric Power Systems Research*, vol. 75, no. 1, pp. 67–78, 2005.
- [182] A. Abur and H. Singh, "Time domain modeling of external systems for electromagnetic transients programs," *IEEE Trans. Power Syst.*, vol. 8, no. 2, pp. 671–679, May 1993.
- [183] K. Chan and L. Snider, "Electromagnetic electromechanical hybrid real-time digital simulator for the study and control of large power systems," in *Proc. International Conference on Power System Technology (PowerCon)*, Perth, Australia, Dec., 4–7, 2000, pp. 783–788.
- [184] B. Kasztenny and M. Kezunovic, "A method for linking different modeling techniques for accurate and efficient simulation," *IEEE Trans. Power Syst.*, vol. 15, no. 1, pp. 65–72, Feb. 2000.
- [185] H. Inabe, T. Futada, H. Horii, and K. Inomae, "Development of an instantaneous and phasor analysis combined type real-time digital power system simulator," in *Proc. Int. Conf. on Power Systems Transients*, New Orleans, LA, Sep., 28–Oct., 2, 2003.
- [186] H. Su, K. Chan, and L. Snider, "Parallel interaction protocol for electromagnetic and electromechanical hybrid simulation," *IEE Proceedings - Generation, Transmission and Distribution*, vol. 152, no. 3, pp. 406–414, May 2005.
- [187] H. Su, K. W. Chan, L. A. Snider, and J. C. Soumagne, "Advancements on the integration of electromagnetic transients simulator and transient stability simulator," in *Proc. of International Conference on Power System Transients*, Montreal, QC, Canada, 2005.
- [188] P. Lehn, J. Rittiger, and B. Kulicke, "Comparison of the ATP version of the EMTP and the NETOMAC program for simulation of HVDC systems," *IEEE Trans. Power Del.*, vol. 10, no. 4, pp. 2048–2053, Oct. 1995.
- [189] X. Lin, A. Gole, and M. Yu, "A wide-band multi-port system equivalent for real-time digital power system simulators," *IEEE Trans. Power Syst.*, vol. 24, no. 1, pp. 237–249, feb 2009.
- [190] U. Annakkage, N. Nair, Y. Liang, A. Gole, V. Dinavahi, B. Gustavsen, T. Noda, H. Ghasemi, A. Monti, M. Matar, R. Iravani,

- and J. Martinez, "Dynamic system equivalents: A survey of available techniques," *IEEE Trans. Power Del.*, vol. 27, no. 1, pp. 411–420, Jan. 2012.
- [191] R. Adapa and J. Reeve, "A new approach to dynamic analysis of AC networks incorporating detailed modeling of DC systems. II. application to interaction of DC and weak AC systems," *IEEE Trans. Power Del.*, vol. 3, no. 4, pp. 2012–2019, Oct. 1988.
- [192] M. Sultan, J. Reeve, and R. Adapa, "Combined transient and dynamic analysis of HVDC and FACTS systems," *IEEE Trans. Power Del.*, vol. 13, no. 4, pp. 1271–1277, Oct. 1998.
- [193] Q. Huang and V. Vittal, "Application of electromagnetic transient - transient stability hybrid simulation to FIDVR study," *IEEE Trans. Power Syst.*, vol. 31, no. 4, p. 2634–2646, Jul. 2016.
- [194] T. Fang, Y. Chengyan, W. Zhongxi, and Z. Xiaoxin, "Realization of electromechanical transient and electromagnetic transient real time hybrid simulation in power system," in *IEEE/PES Transmission and Distribution Conference and Exhibition: Asia and Pacific*, Dalian, China, Aug., 14–18, 2005, pp. 1–6.
- [195] J. Arrillaga and N. R. Watson, *Computer Modelling of Electrical Power Systems*, 2nd ed. Chichester, UK: John Wiley & Sons LTD, 2002.
- [196] J. Grainger and W. D. Stevenson, *Power System Analysis*. New York, NY: McGraw-Hill, 1994.
- [197] P. McLaren and M. Redfern, "Fourier-series techniques applied to distance protection," *Proceedings of the Institution of Electrical Engineers*, vol. 122, no. 11, pp. 1301–1305, Nov. 1975.
- [198] T. Lobos, "Nonrecursive methods for real-time determination of basic waveforms of voltages and currents," *IEE Proc. C, Generation, Transmission and Distribution*, vol. 136, no. 6, pp. 347–352, Nov. 1989.
- [199] K.-F. Eichhorn and T. Lobos, "Recursive real-time calculation of basic waveforms of signals," *IEE proc. C Generation, Transmission and Distribution*, vol. 138, no. 6, pp. 469–470s, Nov. 1991.
- [200] *IEC61400-21 Wind turbines - part 21: Measurement and assessment of power quality characteristics of grid connected wind turbines*, International Electrotechnical Commission Std., 2008.
- [201] S. A. Soman, "Estimation of system frequency," Lecture Slides on Digital Protection of Power Systems - Indian Institute of Technology, Nov. 2010. Available online at: <http://www.nptel.ac.in/courses/108101039/> Last accessed Aug. 2017.
- [202] S. Filizadeh, M. Heidari, A. Mehrizi-Sani, J. Jatskevich, and J. Martinez, "Techniques for interfacing electromagnetic transient simulation programs with general mathematical tools ieee taskforce on interfacing techniques for simulation tools," *IEEE Trans. Power Del.*, vol. 23, no. 4, pp. 2610–2622, Oct. 2008.
- [203] J. R. Marti and J. Lin, "Suppression of numerical oscillations in the EMTP," *IEEE Trans. Power Syst.*, vol. 4, no. 2, pp. 739–747, May 1989.
- [204] ENTSO/e, "Regional investment plan 2015 North Sea region," online, Oct. 2015. Available online at: <http://tyndp.entsoe.eu/reference/#downloads>
- [205] —, "Ten-year network development plan 2016," Dec. 2016. Available online at: <http://tyndp.entsoe.eu/exec-report/Executive-report>
- [206] Norned. (2008) TenneT/StatNett. Available online at: <https://www.tennet.eu/our-grid/international-connections/norned/> Last Accessed: Aug. 2017.
- [207] Noordzeewind. (2007) Shell, Nuon. Available online at: <http://www.noordzeewind.nl/en/> Last Accessed: Aug. 2017.
- [208] Prinses amaliawindpark. (2008) Eneco. Available online at: <https://www.eneco.nl/over-ons/projecten/prinses-amaliawindpark/> Last Accessed: Aug. 2017.
- [209] Britned cable. (2011) BritNed Development Ltd. Available online at: <http://www.britned.com/> Last Accessed: Aug. 2017.
- [210] Gemini offshore wind park. (2007) Northland Power, Siemens, van Oord, HVC. Available online at: <http://ggeminiwindpark.nl/> Last accessed: Aug. 2017.
- [211] Offshore wind farms overview. (2014) 4C Offshore Ltd. Available online at: <http://www.4c offshore.com/windfarms/> Last accessed: Aug. 2017.
- [212] NordLink HVDC power grid interconnection. (2017) ABB. Available online at: <http://new.abb.com/grid/projects/nordlink> Last accessed: Aug. 2017.
- [213] North sea link. National Grid, Statnett. Available online at: <http://northsealink.com/> Last accessed: Aug. 2017.
- [214] Offshore wind energy. (2015) RVO - Netherlands Enterprise Agency. Available online at: <http://offshorewind.rvo.nl/> Last accessed: Aug. 2017.
- [215] SDE+ windenergie op zee. RVO. Available online at: <http://www.rvo.nl/subsidies-regelingen/sde/windenergie-op-zee> Last accessed: Aug. 2017.
- [216] Marien ruimtelijk plan 2020–2026. (2017, May) Belgian Offshore Platform. Available online at: <http://www.belgianoffshoreplatform.be/nl/publications> Last accessed: Aug. 2017.
- [217] Offshore grid development in the North Seas : ENTSO-E views. (2011, Feb.) ENTSO-E. Brussels, Belgium. Available online at: https://www.entsoe.eu/fileadmin/user_upload/_library/position_papers/110202_NSOG_ENTSO-E_Views.pdf
- [218] J. T. G. Pierik, "North Sea transnational grid - wind farm locations and development (WP2)," Energy Research Centre of The Netherlands, Tech. Rep. ECN-E-10-072, Jun. 2012. Available online at: www.nstg-project.nl
- [219] Viking link interconnector. National Grid, Energinet. Available online at: <http://viking-link.com/> Last accessed: Jul. 2017.
- [220] T. Knuppel, J. N. Nielsen, K. Jensen, A. Dixon, and J. Ostergaard, "Small-signal stability of wind power system with full-load converter interfaced wind turbines," *IET Renewable Power Generation*, vol. 6, no. 2, pp. 79–91, Mar.
- [221] A. van der Meer, M. Ndreko, B. R. Rawn, and M. Gibescu, "Dynamic behaviour and transient stability assessment of a North-Sea region case containing VSC-HVDC transmission," Delft University of Technology, Tech. Rep., Apr. 2013, WP 6.2. NSTG Project Technical Report Part II.
- [222] "Zeitreihen zur Entwicklung der erneuerbaren Energien in Deutschland," Feb. 2017. Available online at: http://www.erneuerbare-energien.de/EE/Navigation/DE/Service/Erneuerbare_Energien_in_Zahlen/Zeitreihen/zeitreihen.html Bundesministerium für Wirtschaft und Energie.
- [223] M. Ndreko, "Offshore wind power connected to the dutch transmission system by vsc-hvdc networks: Modeling and stability analysis," Master's thesis, Delft University of Technology, 2012.
- [224] D. Oeding and B. R. Oswald, *Elektrische Kraftwerke und Netze*. Springer, 2011.

Acknowledgement

AC/DC conversion rocks, we know that already from 1970s. That wind energy and hybrid simulation tools are valuable additions to this ensemble I have been experiencing over the past, ehm, nine years. It was a rollercoaster ride of conducting very interesting research, joy, short nights, dead ends, interesting conferences, fantastic colleagues, and which finally ended by this thesis. A thesis that is actually a result of the effort and input of many of you, to whom I would like to express my personal gratitude.

First of all, I would like to thank my promotors prof. M.A.M.M. van der Meijden and prof. dr. J.A. Ferreira for giving me the opportunity to conduct my Ph.D. research. Mart, I will always remember your fruitful reflections about the study assumptions and the relations between the various parts of my research. Braham, I sincerely appreciate the various technical discussion we had throughout my research, sometimes down to the level of substrate and potential barriers of power electronics, seemingly far away from system behaviour but nothing is further from the truth.

Second, I owe a lot of thanks to dr. M. Gibescu. Madeleine, we have been discussing about virtually every tiny detail that's written in this thesis, our papers, and other things that matter in life. By continually challenging my assumptions, methods, approaches you made me an independent researcher, I very much enjoyed working with you!

I would also like to thank the members of the doctoral examination committee for their efforts to scrutinise my thesis, assess it, and for providing valuable feedback improving the quality of the work. This research has been conducted under the umbrella of the North-Sea Transnational Grid research project. In this light, I owe many thanks to Jan Pierik, prof. dr. P. Bauer, and dr. R. Teixeira Pinto for the fruitful cooperation. Ana and Barry, it has been a pleasure working with you, your no-nonsense style helped me with looking things from a different angle. My research has been partially executed at the premises of TenneT TSO B.V. I would like to thank John Zwaal for facilitating this and hosting me at the Grid Strategy department. Kees Jansen and Jorrit Bos, you have been fantastic sparring-partners from the beginning of my stay until the very finalisation of my thesis. I would also take the opportunity to acknowledge Siemens PTI Germany for the provision of an academic testing license of PSS[®]NETOMAC for the duration of my research.

March 2015. The birth of our daughter was eclipsed by the unexpected passing away of prof. W.L. Kling. Marte and I will always cherish Wil's personal congratulations just two days before he died from natural causes. Wil convinced me of going in for Ph.D. research, guided me along the sometimes slippery road that's called science, and revitalised my enthusiasm every time things looked pretty bleak. Our thoughts go to Mirjam; we will never forget Wil his warm and paternal personality.

Many colleagues and friends have been special to me throughout my research. That

especially counts for my paranymfs Ralph Hendriks and Rick van Kessel. Ralph, thanks for the invaluable kick-start you have given me at the very beginning of my Ph.D. You learned me to write papers, basically to write at all, and to set out my research. Oh, and we still have a pending bet about the Zwarte Cross but I lost the exact terms ;-) Rick, our common interest for the /PUB, Jiskefet, science, summer CDs, and Peugeot 206 will never decline.

I'm honoured to have guided M.Sc. students during my research. Chris in offshore VSC-HVDC network controls, Paulo in developing a dynamic VSC-HVDC model in PSS[®]E, Line in scenario development and market analysis of offshore wind power, and last but not least, Mario in model development and stability assessment of AC/VSC-HVDC networks. Thank you very much for the magnificent collaboration during your M.Sc. programme! Mario, you were also a fantastic colleague and friend throughout your Ph.D. research. Thanks for the in-depth discussions about VSC-HVDC and for teaching me the Greek perspective of the present-day problems.

The very diverse discussions with my colleagues at the Intelligent Electrical Power Grids group of the faculty Electrical Engineering, Mathematics, and Computer Science have been very enlightening. I would like to give thanks to dr. J. Rueda Torres and prof. dr. P. Palensky for giving me the opportunity to work on the COBRACable and ERIGrid research projects. My dear office mates Arcadio, Jens, Ilya, Matija, and Ralph were always up for a chat, joke, or technical discussion, which I highly appreciate. dr. J. C. Boemer (Jens), it was a pleasure to host you in Delft occasionally and to have you as a real office mate for over a year. Also thanks for converting me to reactive power support religion ;-) Ellen, Sharmila, Ilona, thank you very much for your secretarial and personal support. Prof. L. van der Sluis, thank you very much for providing the research facilities in the IEPG-group and for the many pleasant discussions we had.

Roy, thank you very much for your support, discussions, pitching tents, fixing bath rooms, etc. *ajetoe buurman!* Rokemeijer, .NL, van Akkeren, gedeeld door drie, Friesland, van Dongen, Putter, Pattie pat, van Dam, Lisse, Bleek, Geljon: *spinnnn*. Anke, Bas, Douwe, Nynke, Halvar, Marianne, Joast, Jitske, Uco, Wendy: I treasure the precious times we have been shaving in Dokkum, throwing axes, dice, cards, you name it. *Das war einmal*, now we're pushing buggies ;-)

My family has been very supportive during my research. Ludo en Henk, thanks for giving me the proper parental boundary conditions; I was glad to let off some steam at Motorherberg Healbird each time I visited you. Johannes, the self-motivation you're showing inspired me a lot over the past years, thanks! Wybren, Bodil, Jessica, Auke, Patricia, Foeke, thanks for your great help! Sietse, Riemke, Sibbe Jan, I very much appreciate your support and thanks for making me a reasonable shepherd, too ;) both cousins, friends, ex-colleagues, and fellow-parents, does that ring a bell? Thanks Jonne and Teec!

And finally a big hug and many kisses to my dear fiancée Marte and our lovely daughter Famke, without whom I couldn't have finished this thesis decently. Thanks for your love, reflections, relativism, sacrifices, and much more. I love it when a plan comes together: a new house, Ph.D. defence, and expecting a baby, all within one month, great! I think we're up for the next challenge, you're still my fiancée, after all :-) Love you!

Thank you, thanks to you all!

Arjen van der Meer

Delft, September 2017

Cirriculum Vitae

Arjen Anne van der Meer was born on July 4th, 1982 in Dokkum, the Netherlands. He attended secondary school at the Piter Jelles College in Leeuwarden, where he graduated in 2000. He studied Physics at the University of Groningen for one year after which he started studying Electrical Engineering at the Leeuwarden University of Applied Sciences (NHL) in 2002. During his B.Sc., he ran an internship at the Physics Shop of the University of Groningen where he investigated the noise generation of onshore wind turbines. He conducted his graduation project at Essent Netwerk Noord, Zwolle, where he was responsible for the development of a substation switching simulator for training purposes. After obtaining his B.Sc. degree in 2006 he joined Delft University of Technology for a M.Sc. in Electrical Engineering. In 2007, he conducted an internship at Enexis, Zwolle, where he assessed directional relay protection schemes for ungrounded medium voltage networks. In 2008, he obtained his M.Sc. degree (cum laude) with a thesis on power hardware-in-the-loop based directional relay co-ordination. In October 2008, he joined the power systems group (now IEPG) of the Electrical Engineering, Mathematics, and Computer Science faculty of TU Delft as a Ph.D. student. His main research topic comprised the modelling and stability impacts of VSC-HVDC connected offshore wind power. During his research, he temporarily stayed at TenneT TSO B.V., Arnhem for developing a dynamic VSC-HVDC model for PSS[®]E. In 2015 he continued at Delft university of Technology as a researcher: on the COBRACable research project in 2015 and on the ERIGrid smart grid project from 2016 onwards. His research interests are power system modelling, simulation, and control, renewable energy resources, power electronics, power system protection, and the roll-out of smart grids. Arjen van der Meer is engaged and has one daughter.

The transition towards a sustainable society calls for the massive deployment of renewable energy sources such as large wind parks located far offshore. High-voltage direct current transmission based on voltage sourced converter technology (VSC-HVDC) offers a wide range of technological benefits that foster the grid integration of offshore wind parks. Coupling AC and HVDC grids comes with significant challenges. Control and system functions, which were formerly separated, interact, especially during faults in the transmission system. Classical (transient stability) modelling and simulation does not suffice and must be made ready for VSC-HVDC.

This Ph.D. thesis answers two questions to master these challenges. First, what is the impact of the operation and control of a, possibly multi-terminal, offshore grid based on VSC-HVDC on the transient stability of the onshore power system? Second, how can we model and simulate these impacts while maintaining the desired simulation accuracy and speed? The results of this thesis facilitate fast and accurate assessment of stability impacts of large transmission systems with a significant proportion of converter-interfaced generation.

